# THE HYDRODYNAMICS OF SHIP SECTIONS ENTERING AND EXITING A FLUID

*A thesis submitted for the degree of Doctor of Philosophy*

by

**Ian Edward Barringer**

**Department of Mathematics & Statistics, Brunel University**

**October 1998**

# Acknowledgement

The author would like to thank his tutor Dr Martin Greenhow for his encouragement, advice and contributions throughout the course of this research, and the Ship Division of Lloyds Register for useful discussions.

This research was financially supported by the Engineering and Physical Sciences Research Council (EPSRC) C.A.S.E Award Scheme with Lloyds Register as the collaborating body.

*Dedicated to the memory of Edward C Fox.*

# Declaration

No part of this thesis has been submitted for a degree to any other university or institution.

# Abstract

We study the hydrodynamics of wedge, knuckle and box cross-sectional profiles undergoing transient extreme motions, in particular forced entry and exit at constant velocity or acceleration. Extensive data for the forces, pressures and free-surface profiles is generated by an extension of a fully-nonlinear boundary-integral method. The code is thoroughly checked by altering the time step and particle spacing on the bodies and Lagrangian free-surface markers, and, for the wedge, checking self-similarity for the infinite Froude number (gravity free) constant velocity entry. Difficulties with inviscid flow around sharp corners are discussed. Results for exit are of particular interest since no zero-gravity approximation is valid and this precludes application of existing slamming theories in reverse. Whilst entry generally gives larger free-surface motions (spray jets), pressures and hence forces, calculation of exit is needed for the velocity of subsequent slamming and so is of practical interest too.

These results are compared with an approximate analytical model, based on Schwarz-Christoffel transformations to calculate the infinite-frequency added mass of the cross-section below the mean water line. For constant acceleration of both entry and exit, the analytical theory is good during the early stages of motion. Later, the assumption of an undisturbed mean water level is clearly violated; the exact calculations show a large amount of draw-down (up-rise), the free-surface making contact with the body well below (above) the mean water level. We therefore examine the effect of reducing (increasing) the submerged body volume to take account of this, which prolongs the agreement between the results considerably and therefore might be used to improve practical calculation of extreme ship motions using existing strip theory codes.

Full sets of numerical data input/output are provided in the appendices, together with some mathematical details. We also speculate on the possible application of John's equation to wedge entry.

# Contents

*Title*

*Acknowledgement* i

*Declaration* ii

*Abstract* iii

**Chapter 1 Introduction** **1**

Statement of the problem 1

Nature of added mass in unbounded fluid 2

Boundary value problem 3

Linear floating body hydrodynamics 6

Wave theories 8

Wave loading on fixed bodies 10

Transient motion problems 12

**Chapter 2 The Fully Non-Linear Calculation** **16**

Problem formulation 16

Numerical method 22

Numerical implementation 32

Verification of numerical results 32

Transient motion 42

**Chapter 3 Analytic Theory** **51**

Wedge theory 51

Box body theory 57

Knuckled body theory 65

**Chapter 4 Body Exit from Initially Calm Water** **72**

Constant acceleration 73

Constant velocity 93

**Chapter 5 Body Entry into Initially Calm Water 121**

Constant acceleration 122

Constant velocity 139

**Chapter 6 Draw-down Analysis 162**

Wedge 164

Box 171

Knuckle 177

**Conclusion 184**

**Recommendations 187**

**Appendix A Numerical Results 188**

**Appendix B Added Mass Derivation from Dipole Moment 197**

**Appendix C Simplification of Added Mass Equations 202**

**Appendix D John's Formula 212**

**Appendix E Program Documentation 222**

*References* 227

# Chapter 1 Introduction

*Definition of problem and a discussion of previous studies.*

## 1.0 Overview

The problem of a body executing large motions near or through a free surface is extremely challenging mathematically: a boundary-value problem can be formulated under the usual assumptions of incompressibility and irrotationality (see 1.1 - 1.3), but the non-linear conditions must be applied on the free surface whose position is not known *a priori* and must be calculated as part of the problem. This suggests some simplification to the problem might be desirable; the usual formulation for floating body hydrodynamics is given in section 1.4, primarily to show how the infinite frequency added mass is related to that of a body in unbounded fluid which is used in the analytical theory of Chapter 3.

For the extreme motions considered here, linearisation is, of course, of very limited validity in general. Section 1.5 therefore reviews non-linear theories of waves (without floating bodies present) which sets the present numerical work in mathematical and historical context. The wave loading from extreme events is reviewed in sections 1.6 and 1.7 where slamming loads are especially considered.

## 1.1 Statement of the problem

The fluid is assumed to be irrotational

$$\nabla \times \mathbf{v} = 0$$

and so we can assume that the velocity vector can be represented by the gradient of a scalar velocity potential $\phi$ which will depend on the space co-ordinates and time. We define

$$\mathbf{v} = \nabla\phi$$

We also assume the fluid is incompressible, which requires

$$\nabla \cdot \mathbf{v} = 0$$

Combining these results we obtain Laplace's equation

$$\nabla^2\phi = 0$$

The problems considered in this thesis are all two-dimensional in the vertical x-y plane. Thus if the velocity vector

$$\mathbf{v} = u(x,y)\hat{i} + v(x,y)\hat{j}$$

then the incompressibility condition states

$$\nabla \cdot \mathbf{v} = \frac{\partial u}{\partial x} + \frac{\partial v}{\partial y} = 0$$

This can be satisfied automatically if we define

$u = \frac{\partial \psi}{\partial y}$ and $v = -\frac{\partial \psi}{\partial x}$ where $\psi$ is a suitably smooth scalar function.

Then $\nabla \cdot \mathbf{v} = \frac{\partial u}{\partial x} + \frac{\partial v}{\partial y} = \frac{\partial^2 \psi}{\partial x \partial y} - \frac{\partial^2 \psi}{\partial x \partial y} = 0$, so the fluid velocity can be written as

$$\mathbf{v} = \frac{\partial \psi}{\partial y}\hat{i} - \frac{\partial \psi}{\partial x}\hat{j} = \nabla \times \psi$$

where $\psi = (0,0,\psi)$ is the stream function.

We may now define the complex potential as

$$\beta(z) = \phi + i\psi$$

where $z = x + iy$ is the complex form of the space co-ordinates, $\phi$ is the velocity potential and $\psi$ is the stream function.

The two velocity components can be obtained by differentiating either of the real functions $\phi$ or $\psi$, so it follows that

$$u = \frac{\partial \phi}{\partial x} = \frac{\partial \psi}{\partial y} \text{ and } v = \frac{\partial \phi}{\partial y} = -\frac{\partial \psi}{\partial x}$$

these are known as the Cauchy-Riemann equations.

So the complex potential $\beta$ is an analytic function of the complex variable $z$, and its derivative gives the complex conjugate of the fluid velocity,

$$\frac{d\beta}{dz} = u - iv .$$

## 1.2 Nature of added mass in unbounded fluid

Physically we interpret the added mass as representing the amount of fluid accelerated by a body moving through the fluid domain. Contrary to real masses, where the mass $m$ is independent of the direction of the acceleration, the added mass will change with the body motion direction. Consider the added mass as a volume of fluid particles that are accelerated with the body. Although in reality the particles will be accelerated to varying degrees dependent on their proximity to the body, we can think of the added mass to be a weighted average of the entire fluid mass. This is made precise by considering the relationship between the added mass and the kinetic energy of the fluid. We define the added mass (see e.g. Newman (1977)) as

$$m_a = \rho \int_S \phi \frac{\partial \phi}{\partial n} dS$$

then from the divergence theorem we can write

$$m_a = \rho \int_S \phi \frac{\partial \phi}{\partial n} dS = \rho \iiint_V \nabla \cdot (\phi \nabla \phi) dV = \rho \iiint_V (\nabla \phi \cdot \nabla \phi) dV$$

since $\nabla^2 \phi = 0$. We assume that $\phi$ vanishes sufficiently quickly at infinity for the integrals to exist.

The kinetic energy of the fluid is

$$T = \frac{1}{2} \rho \iiint_V (U \nabla \phi) \cdot (U \nabla \phi) dV = \frac{1}{2} \rho U^2 \iiint_V \nabla \phi \cdot \nabla \phi dV$$

that is

$$T = \frac{1}{2} U^2 m_a$$

where $U$ is the body velocity.

An additional property of the added mass is its relation to the dipole moment of the body which is the leading order term in the far field. This important fact is demonstrated in Appendix B, also see Newman (1977), and used in Chapter 3.

## 1.3 Boundary value problem

The situation we first consider may be depicted as in Figure 1.1

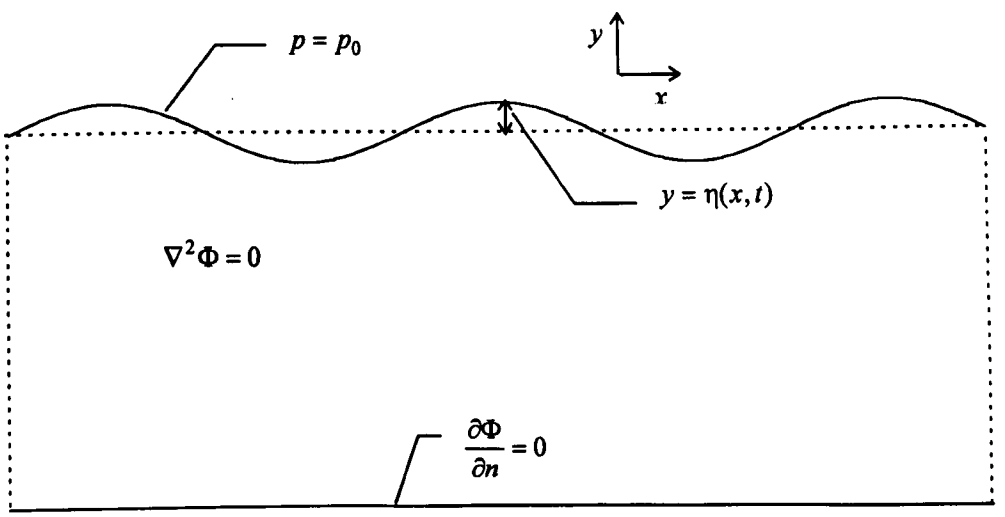


*Figure 1.1 Unbounded ideal fluid and the boundary conditions*

The field equation is Laplace's equation

$$\nabla^2\phi = \frac{\partial^2\phi}{\partial x^2} + \frac{\partial^2\phi}{\partial y^2} = 0 \tag{1.1}$$

which we must solve in the region $-\infty < y < \eta(x,t)$. For simplicity in this section, we assume that $\eta$ is a single-valued function of $x$, i.e. we preclude overturning free-surfaces here.

On the seabed we have a fixed boundary condition on $y = -h$ or we assume that the fluid velocity tends to zero as $y \to -\infty$, that is

$$\frac{\partial\phi}{\partial n} = 0 \text{ on } y = -h \text{ or}$$

$$\nabla\phi \to 0 \text{ as } y \to -\infty. \tag{1.2}$$

To solve for $\phi$ and so for $\mathbf{v}$ requires two boundary conditions linking $\phi$ and $\eta$ at the free surface.

Using Bernoulli's equation for unsteady flow, we can state

$$\frac{\partial\phi}{\partial t} + \frac{p_0}{\rho} + \frac{1}{2}(\nabla\phi)^2 + gy = F(t) \text{ on } y = \eta(x,t)$$

where $p_0$ is constant atmospheric pressure taken as our zero reference i.e. $p_0 = 0$. If we define a new velocity potential

$$\Phi = \phi - \int^t F(\tau)d\tau$$

noting that the velocities are unaffected : $\mathbf{v} = \nabla\Phi = \nabla\phi$, then we obtain

$$\frac{\partial\Phi}{\partial t} + \frac{1}{2}(\nabla\phi)^2 + gy = 0 \text{ on } y = \eta(x,t) \tag{1.3}$$

This is the dynamic boundary condition.

We note that the free surface moves with the fluid and any particle in the free-surface will remain in the free-surface for all time $t > 0$. This can be stated as

$$\frac{D}{Dt}\{y - \eta(x,t)\} = 0$$

that is

$$\frac{\partial\Phi}{\partial y} - \frac{\partial\eta}{\partial t} - \frac{\partial\Phi}{\partial x}\frac{\partial\eta}{\partial x} = 0 \text{ on } y = \eta(x,t) \tag{1.4}$$

This is the kinematic boundary condition.

Equations (1.1), (1.2), (1.3) and (1.4) combined with a suitable far field condition constitute a boundary value problem for the velocity potential $\Phi$. These boundary conditions are applied to the function $y = \eta(x,t)$ and require non-linear solutions. To simplify the task of solving the boundary-value problem, ship hydrodynamicists usually linearise the boundary conditions as follows.

If we assume that both the amplitude and wavelength are small in comparison with the depth of the fluid then we may linearise the boundary conditions by taking $|\eta|$, $|\nabla\eta|$ and $|\nabla\Phi|$ to be small. We then retain linear terms and discard all quadratic terms and higher, reducing the conditions to

$$\frac{\partial\Phi}{\partial t} + g\eta = 0 \text{ on } y = 0 \tag{1.5}$$

and

$$\frac{\partial\Phi}{\partial y} - \frac{\partial\eta}{\partial t} = 0 \text{ on } y = 0 \tag{1.6}$$

We can eliminate the surface elevation from (1.5) and (1.6) to obtain a single mixed boundary condition

$$\frac{\partial^2\Phi}{\partial t^2} + g\frac{\partial\Phi}{\partial y} = 0 \text{ on } y = 0 \tag{1.7}$$

Hence, the linearised boundary value problem is defined by (1.1), (1.2), (1.7) and a suitable radiation condition (here $\frac{\partial\Phi}{\partial x} - iK\Phi \to 0$ as $x \to \infty$): $\frac{\partial\Phi}{\partial n} = 0$ on any rigid boundary, such as the seabed for finite depth water (or $\nabla\Phi \to 0$ as for infinitely deep water).

The heuristic approach above can be made rigorous by Taylor expanding the boundary conditions about the undisturbed free-surface position, see e.g. Dean & Dalrymple (1984). Hence equations (1.5)-(1.7) represent conditions for the first-order problem in wave steepness. Dean & Dalrymple (1984), Newman (1977) and many other books give the solution for monochromatic waves moving in the positive x-direction as $\Phi = \frac{iAg}{\omega}e^{kz}e^{i(kx-\omega t)}$ where $k$ and $\omega$ are related by the dispersion relation $\omega^2/g = k$ for infinitely deep water or $\omega^2/g = k\tanh(kh)$ for finite depth water.

## 1.4 Linear floating body hydrodynamics

We now introduce a floating body into the fluid domain

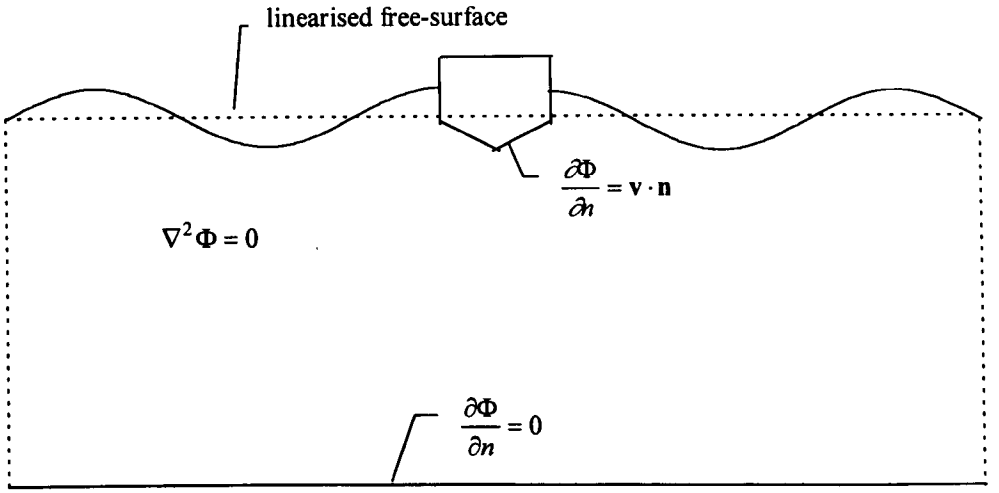


*Figure 1.2 Body in the linearised fluid domain*

A new boundary condition is required on the body matching the normal velocities of the fluid and body surface:

$$\frac{\partial \Phi}{\partial n} = \mathbf{v} \cdot \mathbf{n}$$

Although this condition looks linear, it is in fact non-linear since it must be applied on the moving body surface. For consistency with the linearisation of the free-surface ship hydrodynamicists usually apply this condition on the mean body position resulting in a fully-linear problem.

We now consider the motion of the body. In two-dimensions the body has three modes of motion: vertical (heave), horizontal (sway) and rotational (roll). For three-dimensional models there are a further three modes (surge, yaw and pitch) that will not be considered here.

In general our system consists of a body moving in a fluid with waves incident upon it, represented diagrammatically in Figure 1.3. The great advantage of linearising the boundary value problem is that this general system can be decomposed into: a fixed body with waves incident upon it (Figure 1.4), a body in heave motion radiating waves (Figure 1.5), a body in sway motion radiating waves (Figure 1.6), and a body in roll motion radiating waves (Figure 1.7).

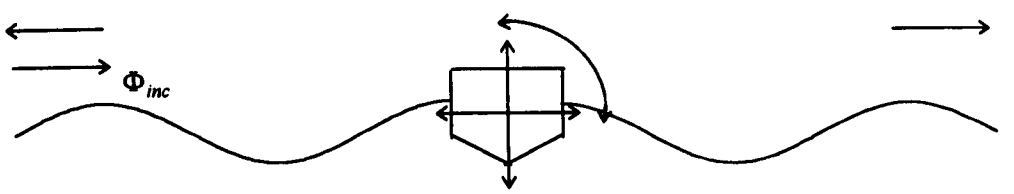


*Figure 1.3 Three modes of motion for two-dimensional body in waves*

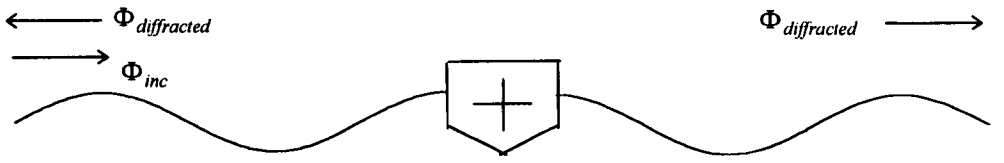


*Figure 1.4 Fixed body in waves: Diffraction problem*

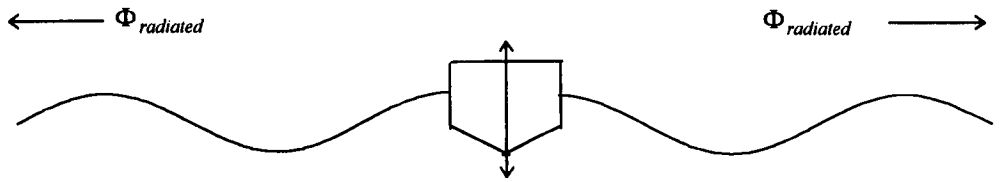


*Figure 1.5 Body in heave motion: Radiation problem*

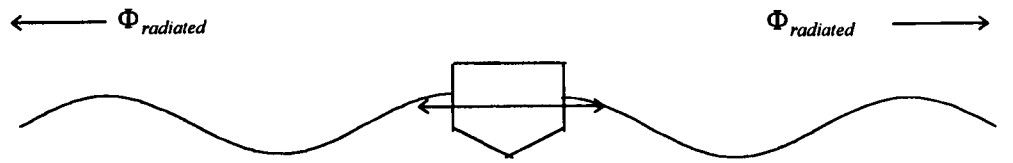


*Figure 1.6 Body in sway motion: Radiation problem*

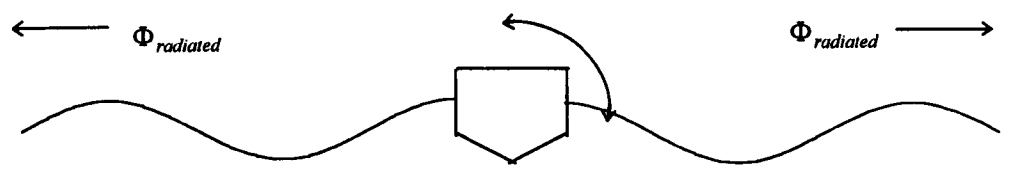


*Figure 1.7 Body in roll motion: Radiation problem*

We can state the total velocity potential as the sum

$$\Phi = \Phi_{incident} + \Phi_{diffracted} + \sum_{j=1}^{3} x_j \Phi_j = \Phi_{scattered} + \sum_{j=1}^{3} x_j \Phi_j$$

where $x_j \Phi_j = \Phi_{radiated}$ for each mode of motion, so that $\Phi_j$ is the radiation potential generated by a body moving with unit velocity amplitude.

The equation of motion of a ship in the $i$ direction can be defined as

$$F_i = \sum_{j=1}^{3} m_{ij}\ddot{x}_j + d_{ij}\dot{x}_j + (k_{ij} + B_{ij})x_j = \rho \int_{S_B} \frac{\partial \Phi}{\partial t} n_i dS$$

where $m_{ij}$ is the inertia, $d_{ij}$ is the applied damping, $k_{ij}$ is the applied spring, $B_{ij}$ is the buoyancy, $S_B$ is the body surface and $n_i$ is the components of the normal vector.

If we consider the contributions from the radiated waves we have

$$F_{radiated_i} = \rho \int_{S_B} \frac{\partial \Phi_j}{\partial t} n_i dS$$

is the force in the $i$ direction due to unit velocity movement in the $j$ direction. This is equal to a force in phase with the acceleration and a force in phase with the velocity, so

$$F_{radiated_i} = \sum_{j=1}^{3} -m_{a_{ij}} \ddot{x}_j - b_{ij} \dot{x}_j$$

and the equation of motion becomes

$$F_i - F_{radiated_i} = F_{scattered_i} = \sum_{j=1}^{3} (m_{ij} + m_{a_{ij}}) \ddot{x}_j + (d_{ij} + b_{ij}) \dot{x}_j + (k_{ij} + B_{ij}) x_j$$

The nature of the boundary-value problem for radiation shows the connection between this frequency-dependent added mass and that of a body for unbounded fluid. The boundary condition (1.7) with the assumed time dependence $\Phi = \phi e^{i\omega t}$ gives

$$-\omega^2 \phi + g \frac{\partial \phi}{\partial y} = 0 \text{ on } y = 0 \qquad (\text{or } -k\phi + \frac{\partial \phi}{\partial y} = 0 \text{ in deep water})$$

so for infinite frequency we get $\phi = 0$ on $y = 0$. Thus translational heave modes correspond to a double (reflected) body moving in unbounded fluid, see Newman (1977).

## 1.5 Wave theories

For the entry and exit problems considered here it is clearly necessary to go beyond the above linear theory. It is therefore worthwhile to examine existing non-linear theories of waves. Wave theories may be divided into two categories - steady and unsteady. The theory for steady waves is much more advanced than for unsteady waves, because we can move with the wave's phase velocity effectively freezing the free-surface. This simplifies the mathematics; the free-surface becomes a steady streamline on which the stream function $\psi$ is constant. Using this fact, Dean (1965) formulated his stream function theory by expanding $\psi$ as a Fourier series, each of the terms satisfying Laplace's equation, the bottom boundary condition and periodicity. Since the kinematic free-surface boundary condition is satisfied exactly this leaves the dynamic boundary condition to determine the unknown coefficients in the Fourier series (for details see Dean & Dalrymple (1984)). Another related approach, which uses the velocity potential $\phi$ instead of the stream function $\psi$ is that of Chaplear (1961) but this requires consideration of both free-surface boundary conditions.

Although generally applicable to any water depth, wavelength and wave height, the stream function formulation does not converge for short wave components because of exponentially large factors in the Fourier expansion. Rienecker & Fenton (1981) include such behaviour in a formalism which is

uniformly convergent. As such this numerical method supersedes all previous theories from the practical point of view, at least for steady waves.

For unsteady waves there is no such convenient reference frame. Bridging these two categories is the linear perturbation analysis of Longuet-Higgins (1978 a & b), which treats time dependent perturbations about the steady, but non-linear, wave solution given by series expansion methods, see especially Williams (1985). More recently Longuet-Higgins & Dommermuth (1997) and Longuet-Higgins & Tanaka (1997) have studied perturbations which are localised around the wave crest and are thought to lead to whitecapping.

Unsteady waves require more sophisticated mathematical techniques. Analytical techniques are almost non-existent apart from simple linear superposition of Airy wave components, see Newman (1977). We are therefore forced to rely on numerical methods for accurate information and checking these against the analytical results for steady waves and accurate unsteady wave experiments. Steady wave theories provide a good check on numerical results from programs designed for unsteady waves.

The first successful model of an overturning wave was that of Longuet-Higgins & Cokelet (1976). Prior to this work, computations based on a grid discretisation throughout the entire fluid were far too computationally expensive to resolve the crest well enough for overturning. Longuet-Higgins & Cokelet's major contribution was to realise that the complex potential $\beta$ is an entire function of $z$ and so the fluid region can be specified by contour integrals around the fluid boundaries (a consequence of Cauchy's theorem). Cokelet (1978) went on to look at the internal flow field in the breaking region, while New (1983) has given very accurate dynamics of the free-surface particles. Another interesting feature is the use of Lagrangian marked particles which tend to cluster in regions of sharp curvature, just where they are required.

Longuet-Higgins & Cokelet's method works in a transformed plane since for periodic waves this closes the contour of integration. For finite-depth studies the fluid occupies an annulus in the transformed plane, New, McIver & Peregrine (1985). A more direct approach, which is more suitable for engineering purposes, is the physical-plane solution of Vinje & Brevig (1981a). Another development, Dommermuth et al (1988) and Greenhow & Lin (1985), is that of a "numerical wave tank" in which waves are generated by a prescribed arbitrary wavemaker motion. Dommermuth et al (1988) compare the resulting waves directly with those in a real wave tank with the same wavemaker motion. One outstanding difficulty is how to apply radiation conditions at the other end of the tank, see Cointe et al (1988).

All the above methods are restricted to two-dimensional flow. Three-dimensions has seen limited progress, with notable contributions from Isaacson (1981), Xu & Yue (1992) and Baker, Merion & Orzag (1981). The latter is applied in two-dimensions but is extendable to three.

## 1.6 Wave loading on fixed bodies

The destructive power of large waves is of major concern and an understanding of the loads induced is essential to the design and operation of offshore structures. These waves give rise to slamming or impact loads of short duration and large pressures at initial contact with the structure followed by engulfment forces as the wave passes over it. The physical and mathematical modelling and experimentation involved in determining the fluid loading is different for these two phases. Also the effect upon the structure is likely to be different. The slamming or impact forces are important locally, giving rise to local damage, crack propagation and fatigue problems, and are related to the crest impact velocity of the wave. The engulfment forces are important globally, giving rise to overall motion of the body and are related to the dynamics of the entire wave. The models for impact and engulfment are different and we concentrate on each separately.

There have been very few experiments performed in deep sea at full scale, a notable exception being Kjeldsen (1981) who measured impacts on an oil rig and various measurements of ship slamming pressures. The situation for coastal structures is more advanced, see e.g. Partensky (1988) and Blackmore & Hewson (1984).

During impact on a body we may ignore gravity since the local accelerations of the fluid particles exceed $g$ by substantial factors (Cooker (1990) quotes theoretical results of 2000-3000 $g$). This greatly simplifies the mathematical modelling, usually to one involving the momentum transfer of an equivalent (added) mass of water moving with the relative speed of impact between the body. On the other hand the short duration and high magnitude of the impact peak presents a considerable experimental challenge. Notwithstanding this, there is a considerable body of literature on these measurements, in contrast to the easier engulfment problem that has very little coverage. The scaling-up of the impact is difficult because the initial stages and hence rise time and magnitude of the peak may be influenced by the cushion of air between the body and the free-surface, and the compressibility of the water, see Moutzouris (1979), Lundgren (1969) and Scott (1975). Such effects are most significant when the body and free surface align; we call this flat water entry.

Flat water entry of cylinders can occur when the body is aligned with the water surface in the impact zone. This can either occur for horizontal cylinders in the surf zone (between the trough and crest elevations), see Kaplan & Silbert (1976) and Campbell & Weynberg (1980), or for vertical or almost vertical cylinders in very steep waves, see e.g. Takagi et al (1986), Tanimoto et al (1986) and particularly the very detailed results of Zhou et al (1991). (Note: this effect is different from "ringing" caused by high frequency resonance of the structure with higher harmonic components of steep waves see Chaplin et al (1997).) Campbell & Weynberg's results show that exact alignment is not necessary for impacts, and that a strip theory may be used to evaluate the body forces during impact, at least for free-surface/cylinder axis angles up to 8 degrees. This motivates and justifies the strip theory approach of this thesis. For flat water entry, it is possible to give the pressure profile around the body during submergence for some shapes; for a flat plate see Wagner (1932), Chuang (1967) and Howison et al

(1991) who applies the flat plate model to wedges, Greenhow (1987) and Zhao & Faltinsen (1993) for wedges, Greenhow & Li (1987) and Greenhow & Moyo (1997) for cylinders.

Flat water entry of a wall, where the wave form is almost exactly aligned with the wave front, gives the largest impact pressures. The subject has been extensively studied for application to coastal defences and a good review, extensive numerical calculations and a useful analytical model can be found in Cooker (1990) and Zhang et al (1996). In the latter and in Peregrine & Thais (1996) the effect of compressing pockets of air is considered.

The problem of engulfment has not received so much attention as the impact problem. Although of lower magnitude, these forces last considerably longer and thus can give rise to large motions and/or mooring forces.

The general problem of extreme wave loading has also been studied to some extent. The usual procedure is to ignore the wave/body interaction non-linearities completely. Forces are then given for Morison's equation where the drag and inertia coefficients are those measured in unbounded fluid, whereas the fluid velocity and acceleration field are given by the equivalent linear design wave. This has been shown to be justified for two-dimensional bodies submerged by about two body radii, see Vinje & Brevig (1981 b). On the other hand, the body's effect on the wave can be strong, see Brevig et al (1981), Skourup & Jonsson (1992) and Miyata & Lee (1990). Another approach is to consider the wave's non-linear velocity and acceleration fields as input to Morison type calculations, see Rainey (1989) for results correct to second order in the Stokes' expansion, and Chaplin (1984) and (1988) for experimental results.

Engulfment problems can be divided up into two types, relative entry and relative exit; for both types there are two sources of non-linearity, due to the free-surface, and due to the wetted body shape changing appreciably. The conventional approach, as in Kaplan & Silbert (1976), is to equate this problem to the similar problem of slamming at the same relative entry velocity. Experiments show this is valid if the wavelength is greater than 40 body diameters. The approach then ignores gravity and solves for the added masses of the double-body problem with a line of equipotential ($\phi = 0$ at the undisturbed free-surface position). In the vertical motion problem, this corresponds to translation, while in the horizontal motion the image motion opposes that of the body - a type of shearing mode, see section 1.4 and Newman (1977).

For relative exit (defined as moving closer to, or upwards through the free-surface) the validity of the double-body model is open to doubt since now gravity must be important, see Greenhow (1993). Øristland (1987) obtains reasonable agreement between numerical and experimental results by leaving out the slamming terms ($v^2$) altogether. This does not conserve energy however, see Cross (1993). The disagreement between the experimental results and theory is not unexpected, since the approximation of the free-surface as a line of equipotential is no longer valid, and so the choice of added mass coefficient is inappropriate. Some exact calculations supporting this viewpoint are given in Greenhow (1988). Indeed it is seen that the so-called slamming ($v^2$) terms may actually give rise to forces in the wrong

direction in some cases. A primary aim of this thesis is to examine the use of such added mass models for ship sections.

## 1.7 Transient motion problems

When a body impacts an initially calm water surface, impulse or slamming loads with high pressure occur. This work seeks to quantify these pressure distributions, the forces on the body and the resulting fluid motion. It is motivated by Lloyds Register and their interest in the slamming of ship bows as they exit and re-enter the water in heavy seas. Although the study presented is concerned with slamming loads on ship hulls, the findings are also useful in the study of slamming on the underside of the deck between the hulls of multi-hull vessels. The two-dimensional interaction between solid bodies and the free-surface also has more general application to many areas of engineering, especially in ocean and coastal engineering. Examples in these fields include the effect of waves on breakwaters and wave energy devices, wave loading in the splash zone on the cross-members oil rigs, marine operations where bodies are lowered through the free-surface by crane, extreme loading (such as those arising from an earthquake) on floating bridges and dams, as well as the aforementioned ship slamming and extreme ship motions. In the case of ship slamming the magnitude and distribution of the pressure can be sufficient to deform the bow area quite severely, as has been recorded by Yamamoto et al (1985).

The physical and mathematical modelling of the system is complex as we must include body elasticity, air and air/water mixture compressibility effects, at least in the early stages of impact, and viscous effects causing vortex shedding in the later stages. The experimentalist also faces additional problems of sensitivity to initial conditions and the repeatability of the early stages. All of the above situations can be considered by assuming that they are equivalent to the entry of a body into calm water with velocity equal to the relative velocity of the body and the moving surface. Such an assumption has been justified for fixed cylinders being engulfed in waves by Ridley (1982) and is expected to hold when the body velocity greatly exceeds the fluid velocities within the wave, as is the case for free-fall lifeboats for example. Early work focussed on modelling the fluid/structure interaction via added mass considerations. Even today this forms the basis of most practical calculation methods. The energy in the fluid boundary, see Bassett (1888) and Greenhow and Li (1987) and this gives rise to inviscid forces which are proportional to the body velocity squared; this makes it difficult or impossible to separate viscous loading (also $\propto v^2$ according to Morison's equation) which requires Reynolds' scaling, from inviscid loading, which requires Froude scaling. Obviously this makes interpretation of data from model experiments problematical.

Slamming for a wedge has been extensively studied more exactly by Wagner (1932), Garabedian (1953) and Mackie (1969). Armand & Cointe (1986), Cointe (1991) and Howison, Ockendon & Wilson (1991) who have further developed and extended Wagner's theory by using matched asymptotic expansions for impacting bodies with small deadrise angles. Dobrovol'skaya (1969) presented similarity solutions for wedges forced through the free-surface at a constant velocity. The solution has application to any deadrise angle $\alpha$, however it is not in explicit form and numerical results are only

presented for $\alpha \leq 30°$. Hughes (1972) gave results for $\alpha = 45°$ whilst Zhao & Faltinsen (1993) covered the entire range of $\alpha$ (see also Keady (1998) for further discussion and downloadable Matlab code). In this sense, the zero gravity entry of a wedge is now solved. Furthermore, Fraenkel & McLeod (1997) proved the existence and uniqueness of Dobrovol'skaya's similarity solution for all $\alpha$. A useful review of slamming is given by Korobkin & Pukhnochov (1988).

These analytical techniques are only successful for rather simple geometries for the flow domain. It was not until the work of Nichols & Hirt (1977) that numerical solutions of more general fluid/structure interactions that included time dependence and gravity were practical, this was achieved by discretisation of the whole fluid domain. The early stages of water entry of a cylinder were modelled with some success but the method was computationally expensive and unsuitable for more general problems.

On the other hand the linearised frequency domain model used in early papers by Dean (1948), Ursell (1950), Ogilvie (1963), Evans et al (1979) and others analytically solved the steady-state sinusoidal problems of waves diffracting over a fixed body and of a moving body radiating waves. By convolution, the transient motion problem can also be solved semi-analytically. The diffraction and radiation problems have also been solved to second order in wave steepness by Ogilvie (1963) and Wu (1993).

For our purposes, however, we require a method that incorporates the full non-linearity of the free-surface boundary conditions and applies the body condition on the actual body position rather than on the mean position of the body surface. The latter requirement implies that any series expansion method that applies the boundary conditions only on the initial body position will only be valid for a short time after the beginning of the motion. King & Needham (1994) apply such a series expansion method to an impulsively started vertical wavemaker moving with constant velocity or constant acceleration. Similarly Tyvand & Miloh (1995 a, b) offer a solution for a submerged circular cylinder.

If the entry velocity is small we can assume the free-surface displacements are small and linearise the free-surface condition and keep the body boundary conditions exact, Chapman (1979) uses such a method. Alternatively, Borg (1957) considers a slender wedge (large deadrise angle) so that even at high velocity the free-surface displacements will remain small. Both Moran (1965) and Mackie (1962 & 1965) also use this slenderness assumption.

To manage high speed entry of non-slender wedges Wagner's (1932) approach (see also von Karman (1929), Pierson (1951) and Fabula (1957)) is to equate the body force with the rate of change of the body's added mass as it enters the water multiplied by its velocity. This simple approach is widely used and can be implemented for a variety of body shapes: cylinders in Faltinsen et al (1977), spheres in Miloh (1981), cones in Shiffman & Spencer (1951) and boxes in Riabouchinski (1920). We can also take the free-surface up-rise into account using Wagner's (1932) approximate method. The wedge entry problem is modelled by an expanding flat plate where the width is defined by the instantaneous waterline of the body during penetration. The solution results in the pressure distribution on the wetted

wedge surface. At the two ends of the plate the fluid is infinite and so Wagner's equations are invalid here and require matching to a local jet solution (see Wagner (1932) or Howison et al (1991) for a modern treatment), but they do predict the maximum pressure some way from the wedge vertex as has been observed for small deadrise angles by Chuang (1967). However it is overly simplistic to approximate a wedge by a flat plate for intermediate deadrise angles.

Practical application of these theories is limited to either low speed, slender body, zero-gravity or self-similar situations. This changed when Longuet-Higgins & Cokelet (1976) formulated the problem as a boundary-value problem that only required us to solve on the free-surface boundary. The contour of integration is closed by a conformal map that ensures periodicity and maps large depths to the origin. A Green's function technique is applied in this mapped plane that results in a Fredholm integral equation of the first kind for the unknown normal fluid velocity at the free-surface. When we map back to the physical plane the method gives spectacular results. Vinje & Brevig (1981 a, b) extended and enhanced this method using Cauchy's theorem in the physical, rather than mapped plane. Further work by Brevig et al (1981), Telste (1987), Greenhow (1987), Terent'ev (1991), Hepworth (1991) and Greenhow (1993) has produced the numerical method for non-surface-piercing bodies. The numerical method for surface piercing bodies of Vinje & Brevig (1981a) described in Chapter 2 gives accurate results so long as the deadrise angle is greater than 45 degrees. Using another numerical scheme, Zhao & Faltinsen (1993) have given accurate results for the body forces and pressures when the deadrise angle is smaller, but their numerical scheme cuts off any ejected spray jets. This is not detrimental to the calculation of the body forces since the jets are thin and their internal pressure is almost atmospheric. A similar procedure has been used in Chapter 6.

The complex potential model of the flow region has two other benefits. Firstly, simple functions can be used to model flows: for example, $\ln z$ will model a source, sink or vortex, the sign of the coefficient of $\ln z$ defining which; $e^{-ikz}$ produces linearised water waves with a wavenumber of $k$, and examples of its use can be found in Patterson (1976) or Milne-Thompson (1986). Secondly, we can conformally map one fluid flow to another. Consequently we may map the flow around a body to uniform flow in another plane. This assists in the calculation of a body's added mass, the large $z$ behaviour can be related to the dipole moment (see Appendix B), making it unnecessary to handle the more complicated local flow around the body. Mappings for simple body shapes can be found in Newman (1977). The Schwartz-Christoffel mapping technique is required for more complicated shapes, implementation of this can also be found in Chapter 3.

Here we will consider only the inviscid loading due to two-dimensional fluid motion in the vertical plane, on wedges, boxes and knuckled bodies moving in initially calm deep water. For the numerical work we do not make any linearising assumptions on the free-surface or body boundary conditions. We study the exit as well as the entry phase; the exit phase is less amenable to analytical treatment (gravity cannot be ignored for example) but it is important since it can give rise to appreciable hydrodynamic forces which may affect the body motion and the subsequent slamming forces and pressures on the next entry phase. A major aim of this thesis is to compare these essentially exact numerical results with those

predicted by simple added mass modelling. The quantification of errors introduced by this analytical model is important since it is believed that only approximate models such as this (rather than full numerical calculations) could be incorporated into practical strip theory models and codes to be used for predicting extremes of displacement, bow acceleration, shear forces and bending moments on a slamming ship in regular and irregular seas, see e.g. Belik, Bishop & Price (1983).

# Chapter 2 The Fully Non-Linear Calculation

*Explanation of the methods used to obtain the numerical results and a verification of the scheme's implementation.*


## Abstract

A derivation of the numerical methods and considerations as to how they are used and implemented on a computer is given. Extensive checking of the numerical code and sensitivity to discretisation is carried out.


## Introduction

Some of the information in this chapter is taken from Vinje & Brevig (1981b). The rest is either derivations of their results or the inclusion of new methods made by either Dr M.J.Greenhow or myself.

The problem is solved as an initial-value problem, given the initial position and velocity potential of the free-surface fluid particles and the body position and velocity. We assume the domain is periodic in space. Using a Cauchy contour integral, with a linear variation of the known part of the complex potential between nodes, we can obtain the unknown part of the complex potential at each time step and march forwards in time.

## Problem Formulation

The problem is considered as a mixed Eulerian/Lagrangian system, so we consider the free surface elevation with reference to a co-ordinate system with a fixed origin at the mean water level. We treat the fluid as homogeneous, incompressible and irrotational so that potential theory governed by Laplace's equation is applicable. The fluid motion is considered in two dimensions only. We will describe the fluid motion using both the velocity potential, $\phi$, and the stream function, $\psi$. We can therefore define the complex potential as

$$\beta(z,t) = \phi(x,y,t) + i\psi(x,y,t) \tag{2.1}$$

where $z = x + iy$.

We can now solve the problem as an initial-value problem given the position and velocity of the body, and the velocity potential and elevation of the free surface particles. The positions of the free-surface particles can be time-stepped using the kinematic boundary condition which states that a particle in the free surface will remain in the free surface. Thus :

$$\frac{Dz}{Dt} = u + iv = \overline{w} \tag{2.2}$$

where the material (or Lagrangian) derivative of any quantity may be related to its Eulerian derivative by :

$$\frac{D(\ )}{Dt} = \frac{\partial(\ )}{\partial t} + \nabla\phi.\nabla(\ )$$

From Bernoulli's equation we can derive the dynamic free-surface boundary condition as follows

$$\frac{\partial\phi}{\partial t} + \frac{p_a}{\rho} + \frac{(\nabla\phi)^2}{2} + gy = F(t)$$

We can absorb $F(t)$ into $\phi$ and we know that $w\overline{w} = (u - iv)(u + iv) = u^2 + v^2 = (\nabla\phi)^2$. Hence the dynamic boundary condition is

$$\frac{\partial\phi}{\partial t} = -\frac{w\overline{w}}{2} - gy - \frac{p_a}{\rho}$$

where $p_a$ is the atmospheric pressure on the free surface. However, we are using a Lagrangian description so we must define the dynamic boundary condition as

$$\frac{D\phi}{Dt} = \frac{w\overline{w}}{2} - gy - \frac{p_a}{\rho} \tag{2.3}$$

using the material derivative. We further assume throughout that $P_a = 0$.

We can find the velocities, $w$, by the differentiation of the complex potential with respect to z, that is

$$w(z,t) = \frac{d\beta(z,t)}{dz} = u(x,y,t) - iv(x,y,t)$$

Since $\beta(z,t)$ is an analytic function of $z$, Cauchy's integral theorem is valid,

$$\oint_C \frac{\phi + i\psi}{z - z_0} dz = 0 \tag{2.4}$$

where $C$ is any closed contour lying within the fluid. We choose $C$ to be the free surface, the wetted surface of the body, the bottom and the two vertical sides of the fluid volume, and we assume $z_0$ is outside the contour $C$.

Now we let $z_0$ approach a point $z_k$ on the contour $C$; in the limit we have

$$\oint_C \frac{\beta}{z - z_0} dz = \oint_{C+C_k} \frac{\beta}{z - z_k} dz = \int_C \frac{\beta}{z - z_k} dz + \int_{C_k} \frac{\beta}{z - z_k} dz = 0 \tag{2.5}$$

where $C_\varepsilon$ is a semicircle of radius ε centred on $z_k$. Along $C_\varepsilon$ we have

$z = z_k + \varepsilon e^{i\alpha}$ and $dz = \varepsilon i e^{i\alpha} d\alpha = (z - z_k) i d\alpha$.

We know by Laurent expansion of the complex potential that

$$\beta(z) = \beta(z_k) + \frac{d\beta(z_k)}{dz} e^{i\alpha}\varepsilon + O(\varepsilon^2) + \ldots$$

So we can state, from the residue theorem

$$\oint_{C_\varepsilon} \frac{\beta(z)}{z - z_k} dz = \int_0^{\alpha_k} \frac{\beta(z_k) + \frac{d\beta(z_k)}{dz} e^{i\alpha}\varepsilon + O(\varepsilon^2) + \ldots}{z - z_k} (z - z_k) i d\alpha$$

$$= i\beta(z_k).\alpha_k + \frac{d\beta(z_k)}{dz} i\varepsilon(e^{i\alpha_k} - 1) + O(\varepsilon^2) + \ldots$$

That is

$$\lim_{\varepsilon \to 0} \oint_{C_\varepsilon} \frac{\beta(z)}{z - z_k} dz = i\alpha_k \beta(z_k) \tag{2.6}$$

where $\alpha_k$ is the angle between the surface either side of point $k$ as shown in Figure 2.1. Analytically this is $\pi$ for any smooth part of the contour, but may be different from $\pi$ numerically as shown.

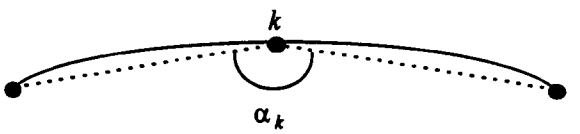


***Figure 2.1** Angle $\alpha_k$ given by the nodal points in the numerical scheme*

If we let $dz$ be replaced by $e^{i\theta} ds$, where $ds$ is a line element of the contour, then substituting (2.6) into (2.5) we obtain

$$-i \oint_C \frac{\beta(z)}{z - z_k} dz = \alpha_k \beta(z_k) - i \int_{C_k} \frac{\beta(z)}{z - z_k} e^{i\theta} ds \tag{2.7}$$

where $C_k$ is the indented contour omitting the singular point $z_k$.

Now, we can set either the real or the imaginary part of (2.7) equal to zero. However, this is not an arbitrary choice without consequences for the numerical scheme, see below. We divide the contour $C$ into two parts, $C_\phi$ and $C_\psi$, where $\phi$ is known on $C_\phi$ and $\psi$ is known on $C_\psi$.

If we assume that $z_k$ is on $C_\psi$, thus $\phi$ is the unknown, we take the real part of (2.7) to be zero giving

$$\begin{aligned}
\mathrm{Re}\left\{-i\oint_C \frac{\beta(z)}{z-z_k}dz\right\} &= \alpha_k\phi(z_k) - \mathrm{Re}\left\{i\int_{C_k}(\phi(s)+i\psi(s))\frac{e^{i\theta}}{z-z_k}ds\right\} \\
&= \alpha_k\phi(z_k) - \mathrm{Re}\left\{\int_{C_k}(\phi(s)+i\psi(s))\frac{ie^{i\theta}}{z-z_k}ds\right\} \\
&= \alpha_k\phi(z_k) - \int_{C_k}\mathrm{Re}\left\{\phi(s)\frac{ie^{i\theta}}{z-z_k}\right\}ds - \int_{C_k}\mathrm{Re}\left\{i\psi(s)\frac{ie^{i\theta}}{z-z_k}\right\}ds \\
&= \alpha_k\phi(z_k) + \int_{C_k}\phi(s)\,\mathrm{Im}\left\{\frac{e^{i\theta}}{z-z_k}\right\}ds + \int_{C_k}\psi(s)\,\mathrm{Re}\left\{\frac{e^{i\theta}}{z-z_k}\right\}ds = 0
\end{aligned}$$

This equation is of the form

$$-\mathrm{Re}\left\{i\oint_C \frac{\beta(z)}{z-z_k}dz\right\} = \alpha_k\phi(z_k) + \int_{C_k}\phi(s)g(z_k,s)ds + j(z_k) = 0 \tag{2.8}$$

where the functions $g$ and $j$ are known.

This is an inhomogeneous Fredholm equation of the second kind. Note that taking the imaginary part of (2.7) when $\phi$ is unknown produces Fredholm integral equation of the first kind, see comments below.

Similarly, if we consider $z_k$ on $C_\phi$, e.g. $\psi$ is the unknown, we put the imaginary part of (2.7) equal to zero and we derive

$$\begin{aligned}
\mathrm{Im}\left\{-i\oint_C \frac{\beta(z)}{z-z_k}dz\right\} &= \alpha_k\psi(z_k) + \mathrm{Im}\left\{-i\int_{C_k}\frac{\beta(z_k)}{z-z_k}e^{i\theta}ds\right\} \\
&= \alpha_k\psi(z_k) + \mathrm{Im}\left\{\int_{C_k}\frac{(\phi(s)+i\psi(s))}{z-z_k} - ie^{i\theta}ds\right\} \\
&= \alpha_k\psi(z_k) + \mathrm{Im}\left\{\int_{C_k}\frac{\phi(s)}{z-z_k} - ie^{i\theta}ds\right\} + \mathrm{Im}\left\{\int_{C_k}\frac{\psi(s)}{z-z_k}e^{i\theta}ds\right\} \\
&= \alpha_k\psi(z_k) - \int_{C_k}\phi(s)\,\mathrm{Re}\left\{\frac{e^{i\theta}}{z-z_k}\right\}ds + \int_{C_k}\psi(s)\,\mathrm{Im}\left\{\frac{e^{i\theta}}{z-z_k}\right\}ds = 0
\end{aligned}$$

Similarly this is of the form

$$\mathrm{Re}\left\{\oint_C \frac{\beta(z)}{z-z_k}dz\right\} = -\alpha_k\psi(z_k) + h(z_k) - \int_{C_k}\psi(s)l(z_k,s)ds = 0 \tag{2.9}$$

with $h$ and $l$ known functions.

Again, this is an inhomogeneous Fredholm integral equation of the second kind. Furthermore the complementary situation when we take the real part of (2.7) when $\psi$ is unknown gives us another Fredholm integral equation of the first kind.

Fredholm integral equations of the first kind do not, generally, have a unique solution; for this reason we are specific about which part of the equation we set equal to zero.

If $z_0 \to z_k$ and $z_k$ is on a smooth part of $C$ and $C_0$ is the indented contour omitting the singular point $z_0$, then

$$\pi\psi(z_0) + \mathrm{Re}\left\{\int_{C_0} \frac{\beta(z)}{z - z_0} dz\right\} = 0 \tag{2.10}$$

when $z_k$ is on $C_\phi$, and

$$\pi\phi(z_0) + \mathrm{Re}\left\{i\int_{C_0} \frac{\beta(z)}{z - z_0} dz\right\} = 0 \tag{2.11}$$

when $z_k$ is on $C_\psi$. Note that in the implemented numerical scheme $\pi$ is replaced by $\alpha_k$ (as shown in Figure 2.1).

Equations (2.10) and (2.11) together form a Fredholm integral equation of the second kind on $C$ that can be solved to obtain the unknown part of $\beta(z) = \phi + i\psi$ on $C$.

In the numerical calculations we use the following approximation to the integral stated in (2.8) and (2.9)

$$\oint_C \frac{\beta(z)}{z - z_k} dz \cong \sum_{j=1}^{N} \Gamma_{k,j}\beta_j$$

where the $\Gamma_{k,j}$ will be explained in the following section (see Numerical Method).

For the same reasons as for $\beta(z)$ we know that $\partial\beta(z,t)/\partial t$ is an analytic function of $z$ inside the fluid domain. Then in a similar manner we can derive from

$$\oint_C \frac{\frac{\partial\phi}{\partial t} + i\frac{\partial\psi}{\partial t}}{z - z_0} dz = 0$$

that when $z_0$ is on $C_\phi$

$$\pi\frac{\partial\psi(x_0,y_0,t)}{\partial t}+\mathrm{Re}\left\{\int_{C_0}\frac{\overline{\frac{\partial\beta(z,t)}{\partial t}}}{z-z_0}dz\right\}=0 \tag{2.12}$$

and when $z_0$ is on $C_\psi$

$$\pi\frac{\partial\phi(x_0,y_0,t)}{\partial t}+\mathrm{Re}\left\{i\int_{C_0}\frac{\overline{\frac{\partial\beta(z,t)}{\partial t}}}{z-z_0}dz\right\}=0 \tag{2.13}$$

From equations (2.12) and (2.13) we can find the derivative of the complex potential with respect to time along the contour.

Now we know the complex potential and its time derivative on the contour, we can find their values inside the same contour if required using

$$\beta(z_0,t)=\frac{1}{2\pi i}\oint_C\frac{\beta(z,t)}{z-z_0}dz \tag{2.14}$$

and

$$\frac{\partial\beta(z_0,t)}{\partial t}=\frac{1}{2\pi i}\oint_C\frac{\overline{\frac{\partial\beta(z,t)}{\partial t}}}{z-z_0}dz \tag{2.15}$$

Also since Cauchy's integral formula can be extended to derivatives, defined as

$$f^{(n)}(z_0)=\frac{n!}{2\pi i}\int_C\frac{f(z)}{(z-z_0)^{n+1}}dz$$

and we know that $w=\frac{d\beta}{dz}$, we conclude

$$w(z_0,t)=\frac{1}{2\pi i}\oint_C\frac{\beta(z,t)}{(z-z_0)^2}dz \tag{2.16}$$

$$\frac{\partial w(z_0,t)}{\partial t}=\frac{1}{2\pi i}\oint_C\frac{\overline{\frac{\partial\beta(z,t)}{\partial t}}}{(z-z_0)^2}dz \tag{2.17}$$

$$\frac{dw(z_0,t)}{dz}=\frac{2}{2\pi i}\oint_C\frac{\beta(z,t)}{(z-z_0)^3}dz \tag{2.18}$$

Higher time derivatives of $\beta(z,t)$ can also be found in the same way, and this opens up the possibility of a multi-step method such as that of Dold and Peregrine (1986) who considered waves evolving

towards breaking. In our case, however, when surface-piercing bodies are involved and undergo large motions, the number of equations changes continuously and a single-step method is therefore far easier to implement on a machine.

We calculate the acceleration of the fluid particles at the free surface from the kinematic boundary condition since

$$a_x(x,y,t)+ia_y(x,y,t)=\frac{Dw(z,t)}{Dt} \tag{2.19}$$

where the subscripts denote the direction of acceleration. Whilst the acceleration inside the contour is calculated using

$$a_x(x,y,t)+ia_y(x,y,t)=\frac{\partial w}{\partial t}+w.\overline{\frac{dw}{dt}} \tag{2.20}$$

The terms on the right hand side can be found using (2.16), (2.17) and (2.18).

The pressure at the free surface is zero in accordance with (2.3), while the pressure inside the contour can be found by a rearrangement of Bernoulli's equation, giving

$$\frac{-p(x,y,t)}{\rho}=\frac{\partial \phi}{\partial t}+\frac{1}{2}w\overline{w}+gy$$

## Numerical Method

We numerically solve equations (2.10), (2.11), (2.12) and (2.13) using the collocation method. The contour $C$ is divided up into a discrete number of points. We shall call these nodes, see Figure 2.2. Either the real or imaginary part of the variables $\beta$, $\frac{\partial \beta}{\partial t}$, etc. are known at each of these nodes.

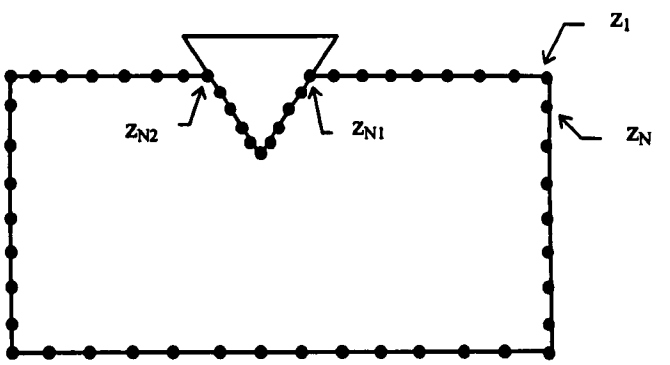


*Figure 2.2 Node allocation along the contour at t=0*

Between the nodal points we assume that $\beta$ and $\frac{\partial \beta}{\partial t}$ vary linearly in $z$. We can then write $\beta(z)$ as

$$\beta(z) = \frac{z - z_j}{z_{j-1} - z_j}\beta_{j-1} + \frac{z - z_{j-1}}{z_j - z_{j-1}}\beta_j \quad \text{for} \quad z_{j-1} \le z \le z_j$$

$$\beta(z) = \frac{z - z_j}{z_{j+1} - z_j}\beta_{j+1} + \frac{z - z_{j+1}}{z_j - z_{j+1}}\beta_j \quad \text{for} \quad z_j \le z \le z_{j+1}$$

So we can write the complex potential and its time derivative as

$$\beta(z) = \sum_j \Lambda_j \beta_j$$

$$\frac{\partial \beta(z)}{\partial t} = \sum_j \Lambda_j \frac{\partial \beta_j}{\partial t}$$

Where the influence function at node $z_j$ is defined as

$$\Lambda_j(z) = \frac{z - z_{j+1}}{z_j - z_{j+1}} \quad \text{for } z \text{ on } C \text{ between } z_j \text{ and } z_{j+1} \tag{2.21}$$

$$\Lambda_j(z) = \frac{z - z_{j-1}}{z_j - z_{j-1}} \quad \text{for } z \text{ on } C \text{ between } z_{j-1} \text{ and } z_j$$

and zero elsewhere on $C$.

If we now consider the contour integral (2.4) we have

$$\oint_C \frac{\beta(z)}{z - z_k} dz = \oint_C \frac{\sum_j \Lambda_j \beta_j}{z - z_k} dz = \sum_j (I1_{k,j} + I2_{k,j})\beta_j$$

where

$$I1_{k,j} = \int_{z_{j-1}}^{z_j} \frac{z - z_{j-1}}{z_j - z_{j-1}} \cdot \frac{1}{z - z_k} dz = \frac{1}{z_j - z_{j-1}} \left[ z + z_k \ln(z - z_k) - z_{j-1} \ln(z - z_k) \right]_{z_{j-1}}^{z_j} = \frac{z_k - z_{j-1}}{z_j - z_{j-1}} \ln\left( \frac{z_j - z_k}{z_{j-1} - z_k} \right) + 1$$

$$I2_{k,j} = \int_{z_1}^{z_{j+1}} \frac{z - z_{j+1}}{z_j - z_{j+1}} \cdot \frac{1}{z - z_k} dz = \frac{1}{z_j - z_{j+1}} \left[ z + z_k \ln(z - z_k) - z_{j+1} \ln(z - z_k) \right]_{z_1}^{z_{j+1}} = \frac{z_k - z_{j+1}}{z_j - z_{j+1}} \ln\left( \frac{z_{j+1} - z_k}{z_j - z_k} \right) - 1$$

We can now introduce the function

$$\Gamma_{k,j} = I1_{k,j} + I2_{k,j} = \frac{z_k - z_{j-1}}{z_j - z_{j-1}} \ln\left( \frac{z_j - z_k}{z_{j-1} - z_k} \right) + \frac{z_k - z_{j+1}}{z_j - z_{j+1}} \ln\left( \frac{z_{j+1} - z_k}{z_j - z_k} \right) \tag{2.22}$$

However, because $\lim_{z \to 0} (z \ln \frac{1}{z}) = 0$ some special cases must be explicitly considered for this function (2.22) as follows

$$k = j-1 \Rightarrow \Gamma_{j-1,j} = \frac{z_{j-1} - z_{j+1}}{z_j - z_{j+1}} \ln \frac{z_{j+1} - z_{j-1}}{z_j - z_{j-1}}$$

$$k = j+1 \Rightarrow \Gamma_{j+1,j} = \frac{z_{j+1} - z_{j-1}}{z_j - z_{j-1}} \ln \frac{z_j - z_{j+1}}{z_{j-1} - z_{j+1}}$$

$$k = j \Rightarrow \Gamma_{j,j} = \ln \frac{z_{j+1} - z_j}{z_{j-1} - z_j}$$

Finally we note that when $j = 1 \Rightarrow j-1 = N$ and when $j = N \Rightarrow j+1 = 1$ , see Figure 2.2.

So we can write

$$\oint_C \frac{\beta(z)}{z - z_k} dz \approx \sum_j \Gamma_j(z_{j-1}, z_j, z_{j+1}, z_k) \beta_j(z_j, t) \tag{2.23}$$

and similarly

$$\oint_C \frac{\frac{\partial \beta(z)}{\partial t}}{z - z_k} dz \approx \sum_j \Gamma_j(z_{j-1}, z_j, z_{j+1}, z_k) \frac{\partial \beta_j(z_j, t)}{\partial t} \tag{2.24}$$

where $z_k$ is the node in question.

When we solve the equations (2.23) and (2.24) we take the real and imaginary parts as specified by equations (2.10), (2.11), (2.12) and (2.13). Since we know $\phi$ on the free surface (see (2.3)) then the free surface is part of $C_\phi$ .

The body surface is part of $C_\psi$, which can be explained by considering the kinematic boundary condition on the body, that is

$$\frac{\partial \psi}{\partial s} = \vec{v}.\vec{n} \tag{2.25}$$

where $\vec{v}$ is the body velocity at the point in question. We can express this in terms of the velocity of the centre of gravity, $\vec{v}_0$, and the rotational velocity of the body, $\dot{\theta}$ . So

$$\vec{v} = \vec{v}_0 + \dot{\theta}\hat{k} \times \vec{\rho}$$

where $\vec{\rho} = (x - x_0)\hat{i} + (y - y_0)\hat{j}$ is the radius vector from the centre of gravity $(x_0, y_0)$ to the point $(x, y)$, and $\hat{k}$ is a third dimensional vector for calculation purposes only (coming out of the page in Figure 2.3).

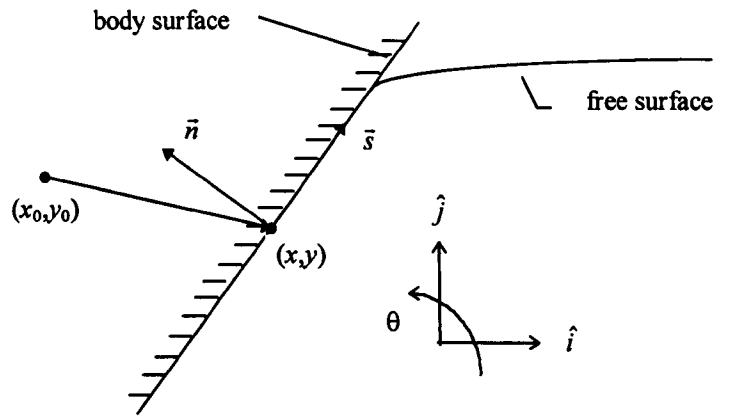


***Figure 2.3*** *Vectors acting upon a body node (x, y).*

If we define $\vec{n} = \hat{k} \times \vec{s}$ then we can deduce

$$d\psi = (\vec{v} \cdot \vec{n})d\vec{s} = \vec{v} \cdot (\hat{k} \times d\vec{s}) = -(\vec{v} \times \hat{k}) \cdot d\vec{s} = -(\vec{v}_0 \times \hat{k} + \dot{\theta}\vec{\rho}) \cdot d\vec{s}$$

Changing to Cartesian co-ordinates this is

$$d\psi = -\dot{y}_0 dx + \dot{x}_0 dy - \dot{\theta}[(x - x_0)dx + (y - y_0)dy]$$

since $\vec{v}_0 = \dot{x}_0\hat{i} + \dot{y}_0\hat{j}$ . We now integrate this to obtain

$$\psi = \dot{x}_0(y - y_0) - \dot{y}_0(x - x_0) - \frac{1}{2}\dot{\theta}R^2 + \psi_0(t)$$

where $R^2 = (x - x_0)^2 + (y - y_0)^2$ and $\psi_0(t)$ is an arbitrary time-dependent constant which we shall set equal to zero. We know from the definition of the material derivative that

$$\frac{D\psi}{Dt} = \frac{\partial\psi}{\partial t} + \vec{v} \cdot \nabla\psi$$

Now

$$\frac{\partial\psi}{\partial t} = -\frac{\partial\dot{y}_0}{\partial t}(x - x_0) - \dot{y}_0\frac{\partial(x - x_0)}{\partial t} + \frac{\partial\dot{x}_0}{\partial t}(y - y_0) + \dot{x}_0\frac{\partial(y - y_0)}{\partial t} - \frac{1}{2}R^2\frac{\partial\dot{\theta}}{\partial t} - \frac{1}{2}\dot{\theta}\frac{\partial R^2}{\partial t}$$

$$= -\ddot{y}_0(x - x_0) - \dot{y}_0(\dot{x} - \dot{x}_0) + \ddot{x}_0(y - y_0) + \dot{x}_0(\dot{y} - \dot{y}_0) - \frac{1}{2}R^2\ddot{\theta} - \dot{\theta}[(x - x_0)(\dot{x} - \dot{x}_0) + (y - y_0)(\dot{y} - \dot{y}_0)]$$

$$\frac{\partial\psi}{\partial t} = -\ddot{y}_0(x - x_0) - \dot{y}_0\dot{x} + \ddot{x}_0(y - y_0) + \dot{x}_0\dot{y} - \frac{1}{2}R^2\ddot{\theta} - \dot{\theta}[(x - x_0)(\dot{x} - \dot{x}_0) + (y - y_0)(\dot{y} - \dot{y}_0)] \tag{2.26}$$

and

$$\begin{aligned}\nabla\psi &= \frac{\partial\psi}{\partial x}\hat{i} + \frac{\partial\psi}{\partial y}\hat{j} \\ &= (-\dot{y}_0 - \dot{\theta}(x - x_0))\hat{i} + (\dot{x}_0 - \dot{\theta}(y - y_0))\hat{j} \\ \vec{v} &= \dot{x}\hat{i} + \dot{y}\hat{j} \\ &= (\dot{x}_0 - \dot{\theta}(y - y_0))\hat{i} + (\dot{y}_0 + \dot{\theta}(x - x_0))\hat{j}\,.\end{aligned}$$

Hence

$$\nabla\psi = -\dot{y}\hat{i} + \dot{x}\hat{j}\,.$$

So

$$\vec{v}\cdot\nabla\psi = -\dot{x}_0\dot{y} + \dot{y}_0\dot{x} + ((x - x_0)\dot{x} + (y - y_0)\dot{y})\dot{\theta}\,.$$

So we obtain the material derivative explicitly as

$$\frac{D\psi(x,y,t)}{Dt} = \ddot{x}_0(y - y_0) - \ddot{y}_0(x - x_0) - \frac{1}{2}R^2\ddot{\theta} + \dot{\theta}[(x - x_0)\dot{x}_0 + (y - y_0)\dot{y}_0] \tag{2.27}$$

The bottom of the fluid domain forms a streamline where $\psi$ and $\frac{\partial\psi}{\partial t}$ are constant, and is part of $C_\psi$. The vertical boundaries connecting the bottom and the free surface can be regarded as neither a part of $C_\phi$ and of $C_\psi$ since both $\phi$, $\frac{\partial\phi}{\partial t}$, $\psi$ and $\frac{\partial\psi}{\partial t}$ are unknown here. We therefore assume that the problem is periodic in space, and hence only $\phi$ and $\frac{\partial\phi}{\partial t}$ or $\psi$ and $\frac{\partial\psi}{\partial t}$ may be regarded as unknowns at all nodes. So for each node an equation of the form (2.10), (2.11), (2.12) or (2.13) may be established. In the calculations presented here, the vertical boundaries are placed a great distance from the body and so the assumed periodicity does not affect the calculations.

We can now solve the system of linear equations to obtain $\beta$ and $\frac{\partial\beta}{\partial t}$ at all nodes on the contour $C$.

To calculate the accelerations we must calculate the forces and moments acting upon the body. These in turn are calculated by integrating the pressures along the wetted surface of the body, assuming (again) a linear variation between nodes. We find the pressure at each node using Bernoulli's equation

$$\frac{p_j}{\rho} = -\frac{w_j\overline{w}_j}{2} - gy_j - \frac{\partial\phi_j}{\partial t} \tag{2.28}$$

So if we require the pressure distribution on the wetted surface of the body, we need to find $\frac{\partial\phi}{\partial t}$. Since we know $\psi$, and can find $\frac{\partial\psi}{\partial t}$ from (2.26), on the wetted body. Consider

$$\oint_C \frac{\frac{\partial \phi}{\partial t} + i\frac{\partial \psi}{\partial t}}{z - z_k} dz \cong \sum_{j=1}^{N} \Gamma_{k,j}(z_{j-1}, z_j, z_{j+1}, z_k) \frac{\partial \beta_j}{\partial t} = 0 \tag{2.29}$$

On the free surface we know $\phi$ and $w = {}^{d\phi}/_{dz}$, so we can use

$$\frac{\partial \phi_j}{\partial t} = -\frac{w_j \overline{w}_j}{2} - g y_j - \frac{p_a}{\rho} \tag{2.30}$$

to find $\frac{\partial \phi_j}{\partial t}$. Along the vertical boundaries we do not know $\phi$ and $\psi$, or $\frac{\partial \phi}{\partial t}$ and $\frac{\partial \psi}{\partial t}$, but they can be found using periodicity. If we consider the three of the infinite array of domains side by side, we know $\phi$ on the vertical boundaries of the centre domain, and $\psi$ on the two either side, then we must know $\phi$ and $\psi$ on the common boundaries. A numerical approach to this is presented later.

Along the bottom $\psi$ is unknown but constant, and can therefore be assumed to be zero. This implies that $\frac{\partial \psi}{\partial t} = 0$ here also

We stated earlier that we use (2.26) to find $\frac{\partial \phi}{\partial t}$. However we do not know the accelerations $(\ddot{x}_0, \ddot{y}_0, \ddot{\theta})$ at this stage, so to solve (2.29) we split (2.26) into four parts, these being

$$\frac{\partial \psi_j}{\partial t} = \frac{\partial \psi_{j1}}{\partial t} + \ddot{x}_0 \frac{\partial \psi_{j2}}{\partial t} + \ddot{y}_0 \frac{\partial \psi_{j3}}{\partial t} + \ddot{\theta} \frac{\partial \psi_{j4}}{\partial t}$$

where

$$\frac{\partial \psi_{j1}}{\partial t} = -\dot{y}_0 \dot{x}_j + \dot{x}_0 \dot{y}_j - \dot{\theta}[(x_j - x_0)(\dot{x}_j - \dot{x}_0) + (y_j - y_0)(\dot{y}_j - \dot{y}_0)]$$

$$\frac{\partial \psi_{j2}}{\partial t} = (y_j - y_0)$$

$$\frac{\partial \psi_{j3}}{\partial t} = -(x_j - x_0)$$

$$\frac{\partial \psi_{j4}}{\partial t} = -\frac{1}{2} R_j^{\,2}$$

We then solve the linear system of four equations

$$\sum_{j=1}^{N} \Gamma_{k,j} \left( \frac{\partial \phi_{jn}}{\partial t} + i \frac{\partial \psi_{jn}}{\partial t} \right) = 0 \quad \text{for} \quad n = 1,4 \tag{2.31}$$

i.e. $Ax_n = b_n$ for $n = 1,4$

It is useful to note that the coefficient matrix $A$ (in $Ax_n = b_n$ for $n = 1,4$) used to solve the above is the same as that used to solve (2.23).

We calculate $\frac{\partial \phi_{j1}}{\partial t}$ using (2.30), all others (n=2,4) we set to zero. Each of the four sub-problems is unphysical, but the whole solution formed by adding the sub-problems is seen to satisfy all the physical boundary conditions.

The solution of this system can then be used to calculate the pressure along the wetted surface (between points $N1$ and $N2$ in Figure 2.2) as

$$\begin{aligned} p_{j1} &= -x_{j1} - \frac{1}{2} w_j \overline{w}_j - g y_j \quad \text{for} \quad j = N1, N2 \\ p_{jn} &= -x_{jn} \qquad\qquad\qquad\quad \text{for} \quad n = 2,4 \end{aligned}$$

If we now calculate the hydrodynamic forces and moments for each of these pressures ( $F_{xn}, F_{yn}, M_n$ ), the following system of equations can be stated

$$\begin{aligned} &F_{x1} + F_{x2}\ddot{x}_0 + F_{x3}\ddot{y}_0 + F_{x4}\ddot{\theta} = m\ddot{x}_0 \\ &F_{y1} + F_{y2}\ddot{x}_0 + F_{y3}\ddot{y}_0 + F_{y4}\ddot{\theta} - mg = m\ddot{y}_0 \\ &M_1 + M_2\ddot{x}_0 + M_3\ddot{y}_0 + M_4\ddot{\theta} = I\ddot{\theta} \end{aligned} \tag{2.32}$$

This gives us the translational and rotational accelerations of the body. The total solution of (2.31) can be written as

$$x_j = x_{j1} + \ddot{x}_0 x_{j2} + \ddot{y}_0 x_{j3} + \ddot{\theta} x_{j4}$$

and the pressure as

$$p_j = p_{j1} + \ddot{x}_0 p_{j2} + \ddot{y}_0 p_{j3} + \ddot{\theta} p_{j4}$$

For a time-stepping algorithm to work, $w(z,t)$ must be calculated along the free surface. If we calculate $w$ from (2.3) we find it is singular when $\beta$ varies linearly between nodes. So instead we calculate $w$ using a central differentiation method. At a node $j$ we state

$$\left(\frac{\partial \beta}{\partial z}\right)_j = a_{j-1}\beta_{j-1} + a_j\beta_j + a_{j+1}\beta_{j+1} - E \tag{2.33}$$

where $E$ is an error term. If we use Taylor's theorem to expand the complex potential about $z_j$ we have

$$\begin{aligned} \beta_{j-1} &= \sum_{n=0}^{\infty} \frac{\beta_j^{(n)}}{n!} (z_{j-1} - z_j)^n \\ \beta_{j+1} &= \sum_{n=0}^{\infty} \frac{\beta_j^{(n)}}{n!} (z_{j+1} - z_j)^n \end{aligned} \tag{2.34}$$

Substituting (2.34) into (2.33), we can then deduce.

$$\left(\frac{\partial\beta}{\partial z}\right)_j = (a_{j-1}+a_j+a_{j+1})\beta_j + \{a_{j-1}(z_{j-1}-z_j)+a_{j+1}(z_{j+1}-z_j)\}\left(\frac{\partial\beta}{\partial z}\right)_j$$
$$+\frac{1}{2}\{a_{j-1}(z_{j-1}-z_j)^2+a_{j+1}(z_{j+1}-z_j)^2\}\left(\frac{\partial^2\beta}{\partial z^2}\right)_j + \sum_{n=3}^{\infty}\frac{\beta_j^{(n)}}{n!}\{a_{j-1}(z_{j-1}-z_j)^n+a_{j+1}(z_{j+1}-z_j)^n\}$$

So we can conclude that

$$\begin{aligned}
&a_{j-1}+a_j+a_{j+1}=0\\
&a_{j-1}(z_{j-1}-z_j)+a_{j+1}(z_{j+1}-z_j)=1\\
&a_{j-1}(z_{j-1}-z_j)^2+a_{j+1}(z_{j+1}-z_j)^2=0\\
&-\sum_{n=3}^{\infty}\frac{\beta_j^{(n)}}{n!}\{a_{j-1}(z_{j-1}-z_j)^n+a_{j+1}(z_{j+1}-z_j)^n\}=E
\end{aligned}$$

So the solution of the linear system of equations is

$$\begin{aligned}
a_{j-1} &= \frac{z_{j+1}-z_j}{(z_{j+1}-z_j)(z_{j+1}-z_j)-(z_{j-1}-z_j)^2}\\
a_{j+1} &= \frac{z_{j-1}-z_j}{(z_{j-1}-z_j)(z_{j+1}-z_j)-(z_{j+1}-z_j)^2}\\
a_j &= -a_{j-1}-a_{j+1}
\end{aligned} \tag{2.35}$$

At the endpoints of the free surface we can still use the central differentiation scheme by considering the periodicity of the system. We allow the points to join up; thus the last free surface point in one domain is the first free surface point in the next. Hence

$$\begin{aligned}
z_p &= z_1+(z_{N3-1}-z_{N3})\\
z_m &= z_{N3}-(z_1-z_2)
\end{aligned}$$

So we may say

$$\begin{aligned}
a_{1-1} &= \frac{z_2-z_1}{(z_2-z_1)(z_p-z_1)-(z_p-z_1)^2}\\
a_{1+1} &= \frac{z_p-z_1}{(z_p-z_1)(z_2-z_1)-(z_2-z_1)^2}\\
a_{N3-1} &= \frac{z_m-z_{N3}}{(z_m-z_{N3})(z_{N3-1}-z_{N3})-(z_{N3-1}-z_{N3})^2}\\
a_{N3+1} &= \frac{z_{N3-1}-z_{N3}}{(z_{N3-1}-z_{N3})(z_m-z_{N3})-(z_m-z_{N3})^2}
\end{aligned}$$

Thus we have fully-defined the complex velocity $w$. We use this same scheme to calculate the acceleration by replacing $\frac{\partial\beta}{\partial z}$ with $\frac{\partial^2\beta}{\partial z^2}$.

We determine the body motion using

$$\begin{aligned} m\ddot{x} &= F_x \\ m\ddot{y} &= F_y \\ I\ddot{\theta} &= M \end{aligned} \tag{2.36}$$

with reference to the centre of gravity. The forces are calculated as before. To integrate equations (2.36) and equations (2.2) and (2.3) in time we use Hamming's fourth-order predictor/corrector method with a Runge-Kutta starting routine. This method is remarkably stable and is described as follows.

### *Time Stepping Procedure*

To step forward in time we must find numerical methods to solve

$$\begin{aligned} \frac{Dz}{Dt} &= u + iv \\ \frac{D\phi}{Dt} &= \frac{1}{2} w \cdot \overline{w} - gy - \frac{p_a}{\rho} \end{aligned} \tag{2.37}$$

We use a second-order Runge-Kutta and Hamming's fourth-order predictor/corrector to do this, see Gerald & Wheatley (1994).

### Second-Order Runge-Kutta Algorithm

The solution of the differential equation

$$\dot{y}(t) = \frac{dy(t)}{dt} = f\big(y(t)\big)$$

is found as

$$y_{n+1} = y_n + \frac{1}{2}\Delta t\big(k_1 + k_2\big)$$

where

$$\begin{aligned} y_n &= y(t_n) \\ \Delta t &= t_{n+1} - t_n \\ k_1 &= f\big(y_n\big) = \dot{y}_n \\ k_2 &= f\big(y_n + \Delta t \cdot k_1\big) = f\big(\bar{y}_{n+1}\big) = \dot{\bar{y}}_{n+1} \end{aligned}$$

That is, we use Euler's method to predict a value of $y_{n+1}$.

The truncation error is of the form $e_t = K\Delta t^3 + O\big(\Delta t^4\big)$, where $K$ depends upon $f\big(y(t)\big)$ and its higher-order derivatives.

### Hamming's Fourth Order Predictor/Corrector

This multi-step method requires four starting values for $y$ and $f(y)$. These values are calculated from the Runge-Kutta method above. The algorithm may be stated as

1. Calculate the starting values $y_n$ and $f_n$ for $n = 0,3$.

2. Calculate the predictor

$$P_{n+1} = y_{n-3} + \frac{4}{3}\Delta t\left(2\dot{y}_n - \dot{y}_{n-1} + 2\dot{y}_{n-2}\right)$$

3. Calculate the modifier

$$M_{n+1} = P_{n+1} - \frac{112}{121}\left(P_n - C_n\right) \text{ where } \left(P_4 - C_4\right) = 0$$

4. Calculate the time derivative of the modified predictor

$$\dot{\bar{y}}_{n+1} = f\left(M_{n+1}\right)$$

5. Calculate the corrector

$$C_{n+1} = \frac{1}{8}\left[9y_n - y_{n-2} + 3\Delta t\left(\dot{\bar{y}}_{n+1} + 2\dot{y}_n - \dot{y}_{n-1}\right)\right]$$

6. Calculate the final value at $t_n + \Delta t$

$$y_{n+1} = C_{n+1} + \frac{9}{121}\left(P_{n+1} - C_{n+1}\right)$$

Note that the method has a local truncation error of $O\left(\Delta t^5\right)$.

## *Numerical Solutions*

The numerical solutions of (2.14) to (2.18) are found from

$$\beta(z_0,t) = \frac{1}{2\pi i}\oint_C \frac{\beta(z,t)}{z - z_0}dz \cong \sum_j \Gamma_j\left(z_{j-1}, z_j, z_{j+1}, z_0\right)\beta_j\left(z_j, t\right)$$

$$\frac{\partial\beta(z_0,t)}{\partial t} = \frac{1}{2\pi i}\oint_C \frac{\dfrac{\partial\beta(z,t)}{\partial t}}{z - z_0}dz \cong \sum_j \Gamma_j\left(z_{j-1}, z_j, z_{j+1}, z_0\right)\frac{\partial\beta_j}{\partial t}\left(z_j, t\right)$$

$$w(z_0,t) = \frac{1}{2\pi i}\oint_C \frac{\beta(z,t)}{\left(z - z_0\right)^2}dz \cong \sum_j \Gamma 2_j\left(z_{j-1}, z_j, z_{j+1}, z_0\right)\beta_j\left(z_j, t\right)$$

$$\frac{\partial w(z_0,t)}{\partial t} = \frac{1}{2\pi i}\oint_C \frac{\dfrac{\partial\beta(z,t)}{\partial t}}{\left(z - z_0\right)^2}dz \cong \sum_j \Gamma 2_j\left(z_{j-1}, z_j, z_{j+1}, z_0\right)\frac{\partial\beta_j}{\partial t}\left(z_j, t\right)$$

$$\frac{dw(z_0,t)}{dt} = \frac{2}{2\pi i}\oint_C \frac{\beta(z,t)}{\left(z - z_0\right)^3}dz \cong \sum_j \Gamma 3_j\left(z_{j-1}, z_j, z_{j+1}, z_0\right)\beta_j\left(z_j, t\right)$$

where

$$\Gamma_j = \frac{z_0 - z_{j-1}}{z_j - z_{j-1}} \ln \frac{z_j - z_0}{z_{j-1} - z_0} + \frac{z_0 - z_{j+1}}{z_j - z_{j+1}} \ln \frac{z_{j+1} - z_0}{z_j - z_0}$$

$$\Gamma 2_j = \frac{1}{z_j - z_{j-1}} \ln \frac{z_j - z_0}{z_{j-1} - z_0} + \frac{1}{z_j - z_{j+1}} \ln \frac{z_{j+1} - z_j}{z_j - z_0}$$

$$\Gamma 3_j = \frac{1}{2}\left[ \frac{1}{(z_j - z_0)^2} \left( \frac{z_{j-1} - 2z_j + z_0}{z_j - z_{j-1}} + \frac{2z_j - z_{j+1} - z_0}{z_j - z_{j+1}} \right) + \frac{1}{(z_j - z_{j-1})(z_{j-1} - z0)} - \frac{1}{(z_j - z_{j+1})(z_{j+1} - z_0)} \right]$$

Derivation of these functions may be found in Vinje & Brevig (1981a).

## Numerical Implementation

The above numerical scheme was originally implemented by Vinje & Brevig using FORTRAN 77. Enhancements have since been made by Dr M Greenhow and myself. These have included routines to handle forced motion, the distribution of points for different body shapes and the tailoring of output making it more amenable to spreadsheet input.

The program accepts input from a data file (wed.dat) describing the initial conditions of the body and parameters required to time step the numerical scheme.

Output is in the form of six files

1. wed.out - original output file as defined by Vinje & Brevig, it remains purely for reasons of backward compatibility.
2. wed.plt - a brief summary of the run for each time step.
3. wed.dep - the body depth, velocity and acceleration for each step in both x and y directions.
4. wed.for - the force on the body in the x and y direction and the body moment.
5. wed.sur - co-ordinates of each point (node) for every time step, this is used to obtain the surface profiles.
6. wed.pre - pressure at each point (node) for every time step, this is used to obtain the pressure profiles.

## Verification of Numerical Results

There is a dual purpose to the work that has been completed for this section. The main objective was to ensure that the results from the Vinje & Brevig code could be relied upon. The second purpose is to decide upon an optimum or at least viable set of input variables. The data input to the program contains many variables, some of which have a significant impact on the accuracy of the run. Especially significant are the variables concerned with point distribution; we can define the number of

points on the surface / body and the distribution ratio for the surface / body. These play a significant role since they specify the extent to which the program can numerically resolve the particle motions and hence the forces experienced by the body.

We shall use two methods to ensure the program is working correctly, self-similarity and variable sensitivity.

### *Self-similarity*

Produce a sufficiently long lasting high velocity, zero gravity run that will enable us to compare medium and large time data. Self-similarity, as explained in Chapter 6, requires

$$\lambda z(s,t) = z(\lambda s, \lambda t) = z(\varsigma, \tau)$$

where $\varsigma = \lambda s$ and $\tau = \lambda t$.

In our case we demonstrate this self-similarity by comparing the surface profile A at $t = a$ with the surface profile B at $t = b$. For surface profile B we set $b = a/2$ and double the $x$ and $y$ co-ordinate values. If surface profile B coincides with surface profile A then we have demonstrated self-similarity.

The run under consideration involves a wedge, of half-angle $\pi/10$, entering the fluid domain at $1 ms^{-1}$ (Froude number 0.583). The specific input data is given in Table 2.1, the variables of which are explained later in the Variable sensitivity section and Appendix E. The surface and body have fine discretisation, the time steps are small and the wedge is thin to ensure the model continues for large time. Gravity has been set to zero in this case, as is required for self-similarity.

| | | | | | | | | | |
|---|---|---|---|---|---|---|---|---|---|
| 2000 | 0.001 | 0.1 | 14 | 0 | 11 | 0 | 10 | 0 | 10 |
| 0 | 1 | 0 | 1000 | 1000 | | | | | |
| (0.0,0.29) | (0.0,-1.0) | 0 | 0 | (0.0,0.29) | | | | | |
| 20 | 10 | 80 | | | | | | | |
| 1 | 0 | 0 | | | | | | | |
| 0.0075 | 0.001 | | | | | | | | |
| 0 | 0 | 0 | | | | | | | |
| 0.85 | | | | | | | | | |
| 80 | | | | | | | | | |
| 0.95 | 0.3 | 1 | 18 | 36 | | | | | |

*Table 2.1 Input data required to produce run suitable for self-similarity study*

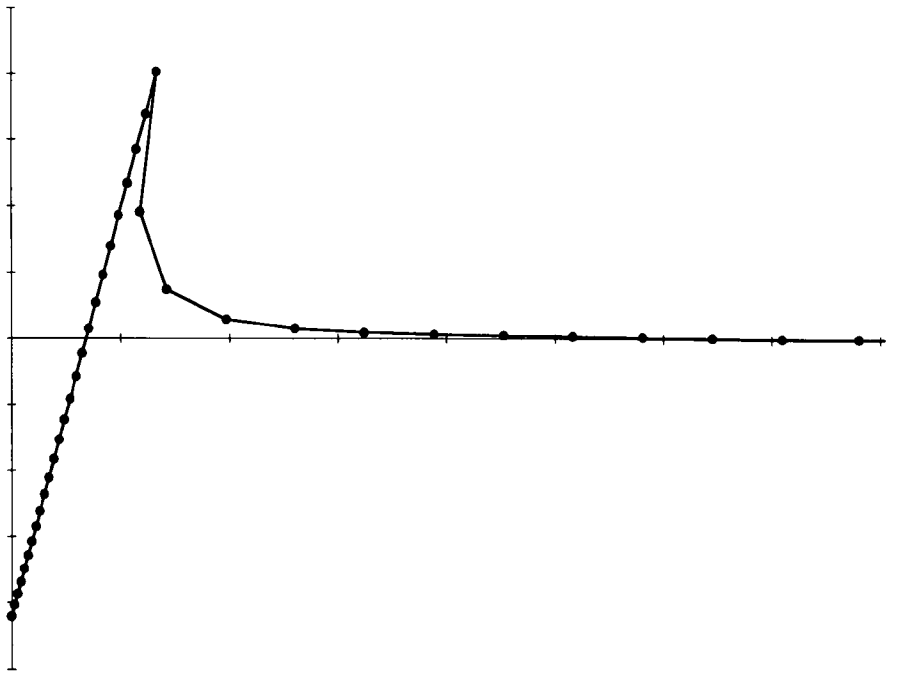

*Graph 2.1 Surface profile of entering wedge for t=0.2*

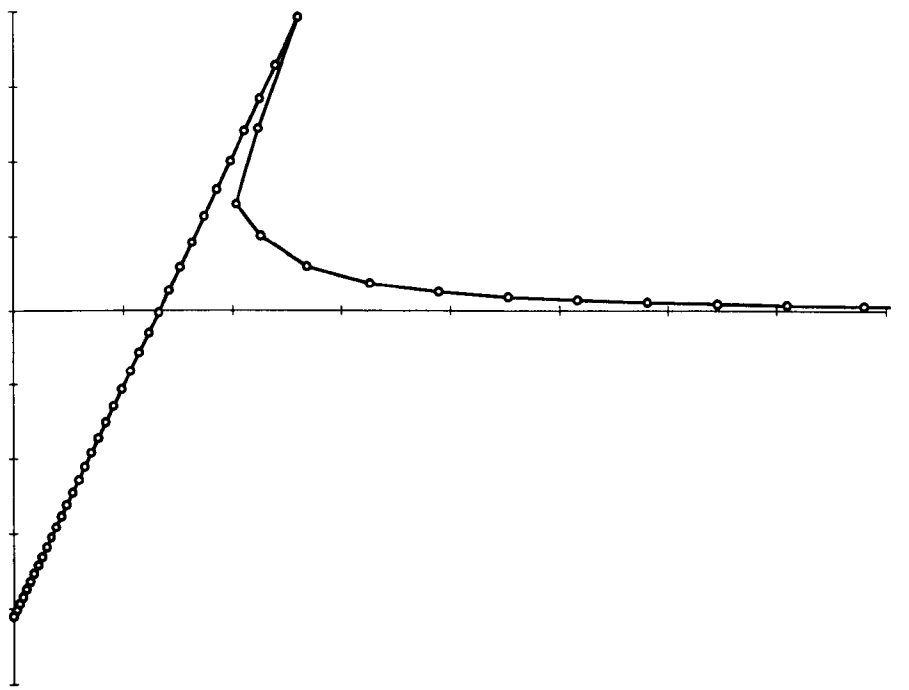

*Graph 2.2 Surface profile of entering wedge for t=0.4*

The surface profiles produced for time $t = 0.2$ and $t = 0.4$ are presented in Graph 2.1 and Graph 2.2 respectively. The surface profile of $t = 0.2$, with $x$ and $y$ values doubled, is overlaid on the surface profile from Graph 2.2 and presented on Graph 2.3.

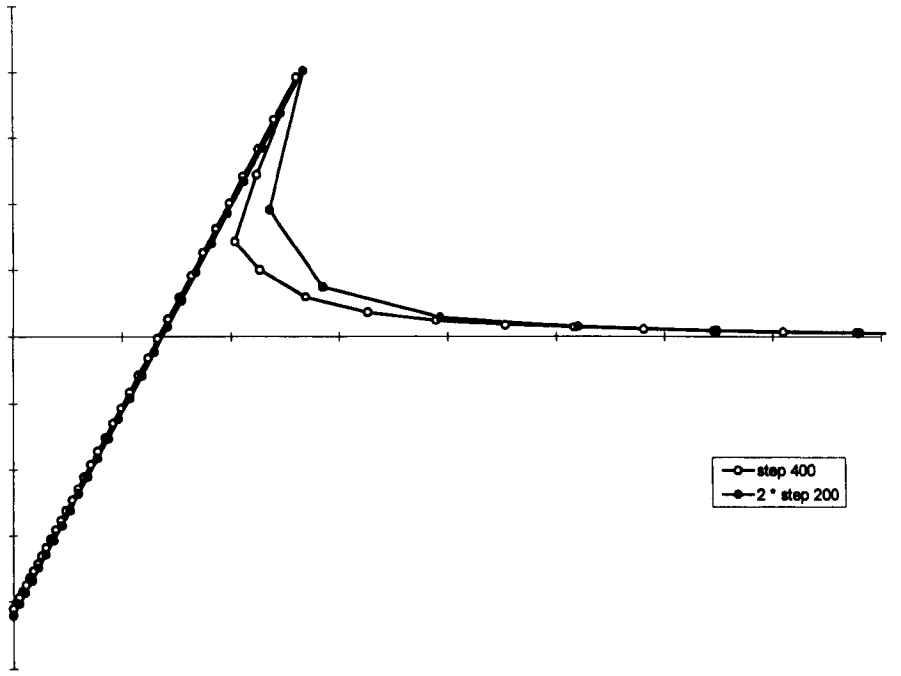


*Graph 2.3 Surface profiles demonstrating self-similarity.*

Clearly the model produces self-similar results for the bulk of the flow, but the jet would need further resolution. To explore this we examine the systems sensitivity to resolution variable changes in the following section.

## *Variable sensitivity*

Produce a selection of runs that have all physical variables in common; the differing variables being those that do not change the free-surface profile and pressure distribution but only their resolution along the contour. That is, we can change the number of points on the free surface to increase accuracy but we cannot change the height of the wedge, since this would produce a completely different physical situation that would not allow comparison.

Eight test were carried out for the symmetric exit of a wedge of half angle $\alpha$=30°, and a Froude number of 0.404. The form of the input file (wed.dat) is as follows; the variables to be changed are named:

| | | | | | | | | | |
|---|---|---|---|---|---|---|---|---|---|
| 200 | DT | 0.1 | 14 | 0 | 11 | 1 | 10 | 0 | 10 |
| 0 | 1 | 0 | 3.0 | 1.0 | | | | | |
| (0.0,-0.05) | (0.0,0.2) | 0 | 0 | (0.0,-0.05) | | | | | |
| 4 | 1 | NF | | | | | | | |
| 1 | 0 | 0 | | | | | | | |
| 0 | 10 | | | | | | | | |
| 0.000388437 | 0.001 | 0 | | | | | | | |
| RATIO | | | | | | | | | |
| NBODY | | | | | | | | | |
| RATBOD | 0.025 | 0.1 | 30 | 60 | | | | | |

The named variables represent

| | |
|---|---|
| DT | The time step |
| NF | The number of points on the free surface |
| RATIO | The distribution ratio of points on the free surface |
| NBODY | The number of points on the body |
| RATBOD | The distribution ratio of points on the body |

These variables were varied in the runs to produce a range of results. If the program numerics are stable then the results should all be the same (to within a certain degree of accuracy, allowing for round-off errors). The data table for the runs listing the variable values and the respective run name is presented as:

| | Test 1 | Test 2 | Test 3 | Test 4 | Test 5 | Test 6 | Test 7 | Test 8 |
|---|---|---|---|---|---|---|---|---|
| DT | 0.005 | 0.005 | 0.02 | 0.01 | 0.01 | 0.01 | 0.01 | 0.01 |
| NF | 70 | 70 | 70 | 80 | 76 | 76 | 70 | 90 |
| RATIO | 0.83 | 0.83 | 0.83 | 0.95 | 0.89 | 0.8 | 0.83 | 0.9 |
| NBODY | 20 | 30 | 20 | 20 | 20 | 20 | 20 | 30 |
| RATBOD | 0.9 | 0.9 | 0.95 | 0.9 | 0.9 | 0.8 | 0.9 | 0.9 |

The differing step size means that the results can only be compared at certain intervals, where the times all coincide. Some of the runs did not last for very many time steps, due to the point distributions being poor. However, the runs are still a good test since if the numerics at the beginning, before breakdown at some localised part of the free surface, still agree with the other runs, then the program is giving accurate results. From the data produced from the program, the graphs of the surface profiles at certain depths (where all runs coincide, except those that did not run long enough) and the graph of the forces experienced by the wedge were produced, a selection of which follows. The axes of the graphs, x and y, are non-dimensionalised with respect to the submerged depth of the body when in equilibrium. All values given are non-dimensionalised as follows

- Time - multiplied by $\sqrt{\frac{g}{d_e}}$ where $d_e$ is the body draft at equilibrium and $g$ is gravity.
- Depth - divided by $d_e$ .
- Velocity - divided by $\sqrt{gd_e}$ .
- Acceleration - divided by $g$.

- Pressure - divided by $d_e g\rho$.
- Force - divided by the buoyancy force given by $\rho g\forall$ where $\forall$ is the submerged volume at equilibrium.

The wedge is exiting the fluid so we will expect any difference to occur as the wedge vertex gets closer to the surface, since there will be fewer points on the wedge and thus poorer resolution. If you study Graph 2.4, Graph 2.5 and Graph 2.6 you will note that all the curves superimpose one-another. The points do not coincide, but we would not expect them to since the number of points and the distances between them vary for each run.

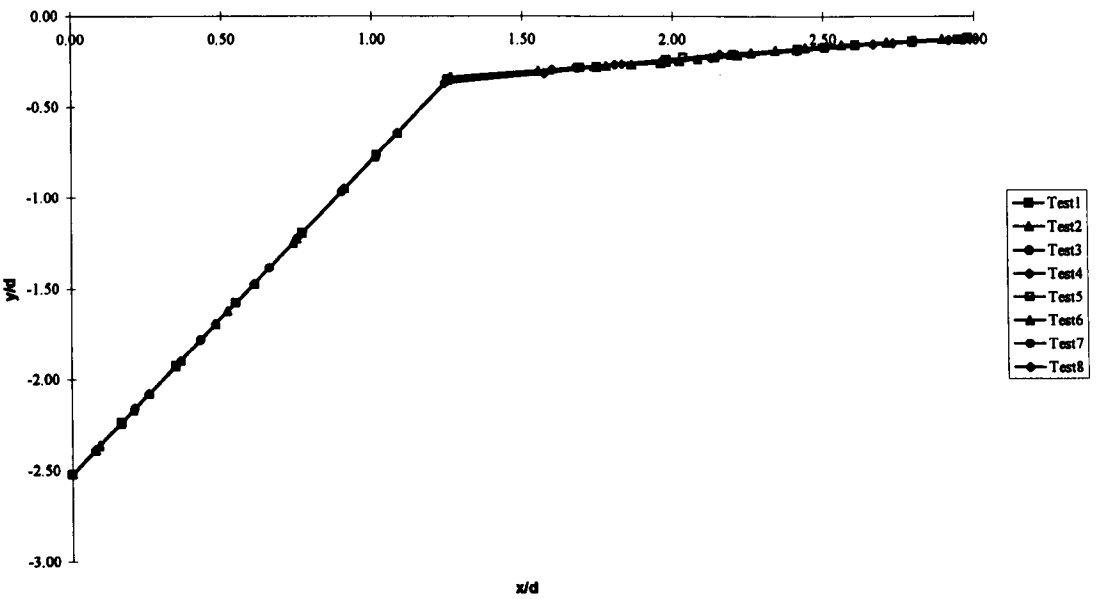


***Graph 2.4** Surface profile for a exiting wedge at a depth of y/d=0.063/0.025=2.52.*

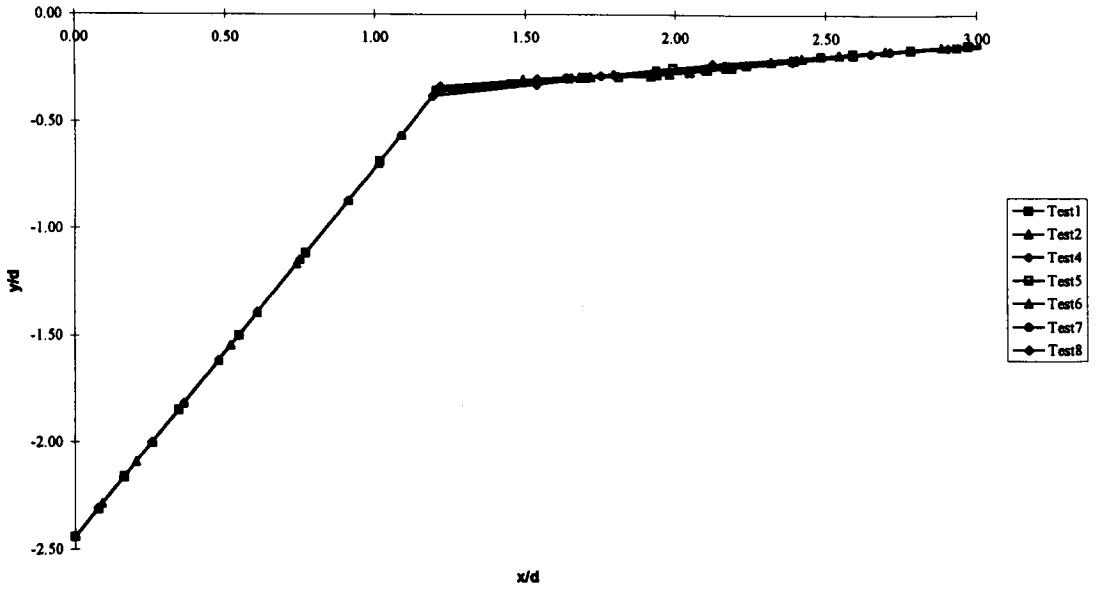


***Graph 2.5** Surface profile of a exiting wedge at a depth of y/d=0.061/0.025=2.44.*

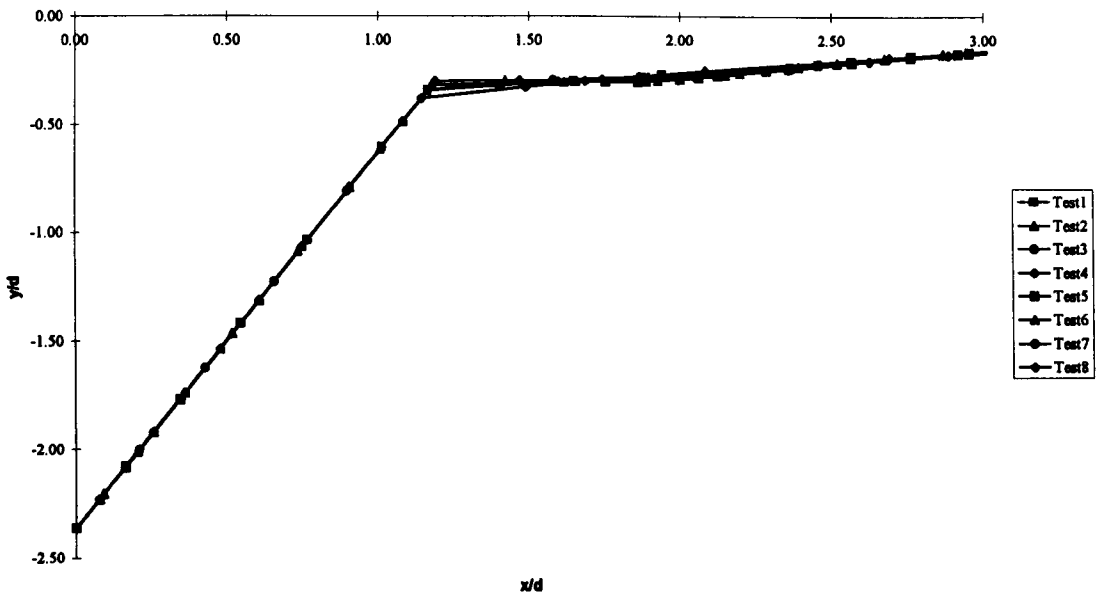


***Graph 2.6** Surface profile to a exiting wedge at a depth of y/d=0.059/0.025=2.36.*

Graph 2.7 has some discrepancies in the surface. Test 3 and Test 8 are showing signs of a jet forming and rushing up the side of the wedge, this will be followed by break down. Test 8 in fact breaks down before the next common time step hence the omission in Graph 2.8. Test 2 is showing similar tendencies. Note the sudden drop in the surface which breaks down before the next common time step.

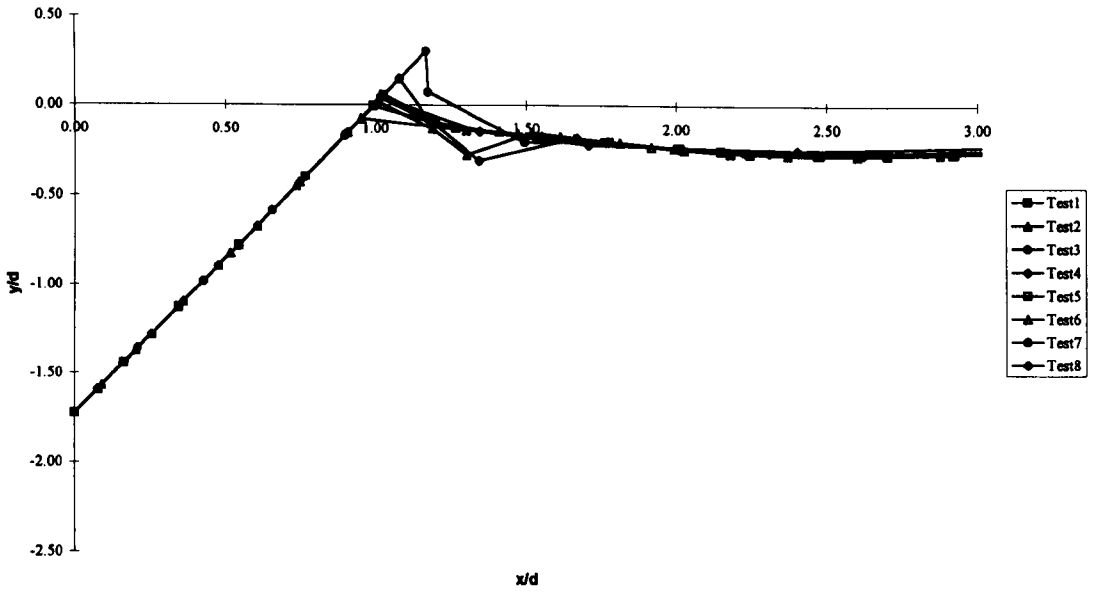


*Graph 2.7 Surface profile of a exiting wedge at a depth of y/d=0.043/0.025=1.72.*

In Graph 2.8 we see the final step of Test 3, as the jet rises up the wedge numerical errors are introduced due to the pressure inversion at the jet tip. These errors are propagated and result in the sudden acceleration of another point downwards, as one can see from the third surface point, breakdown is imminent.

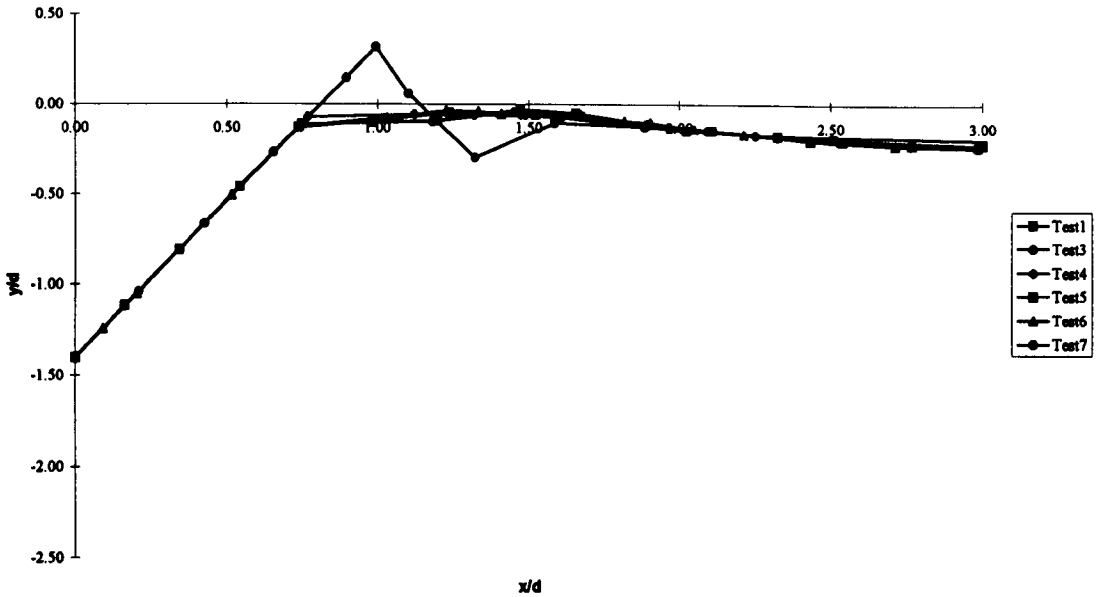


*Graph 2.8 Surface profile of a exiting wedge at a depth of y/d=0.035/0.025=1.4.*

Now the poorly resolved test cases have broken down but we have agreement in the remaining runs. We are left with a well-resolved propagating wave as the wedge nears complete exit.

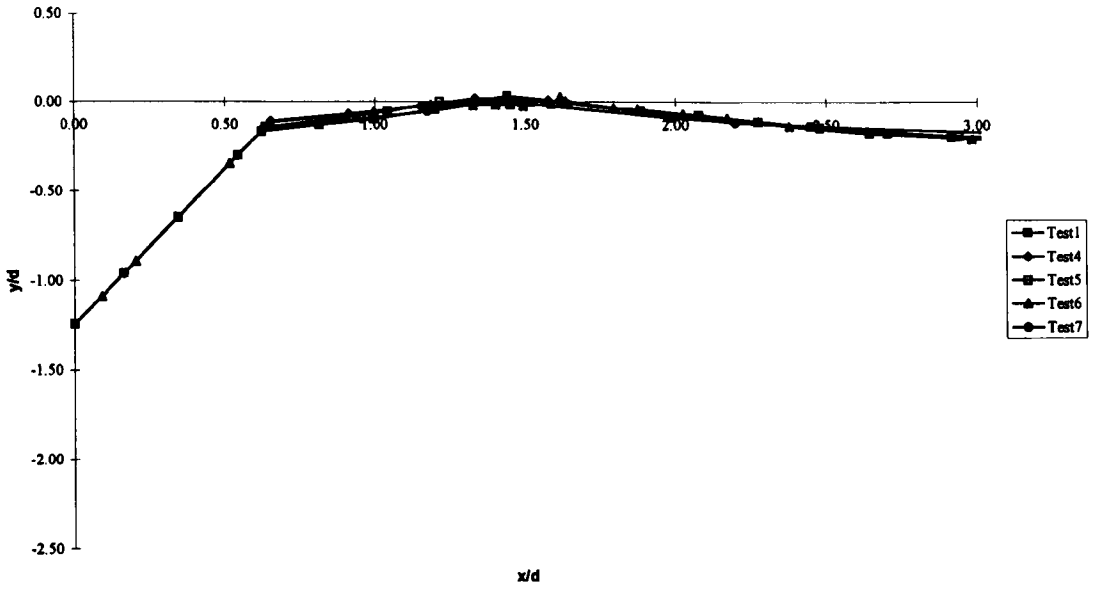


***Graph 2.9** Surface profile of a exiting wedge at a depth of y/d=0.031/0.025=1.24.*

So, generally we have good agreement between the test cases. Can we rely on these cases to demonstrate the consistency of the code? Let us look at the force curve to see if the differences appear there too.

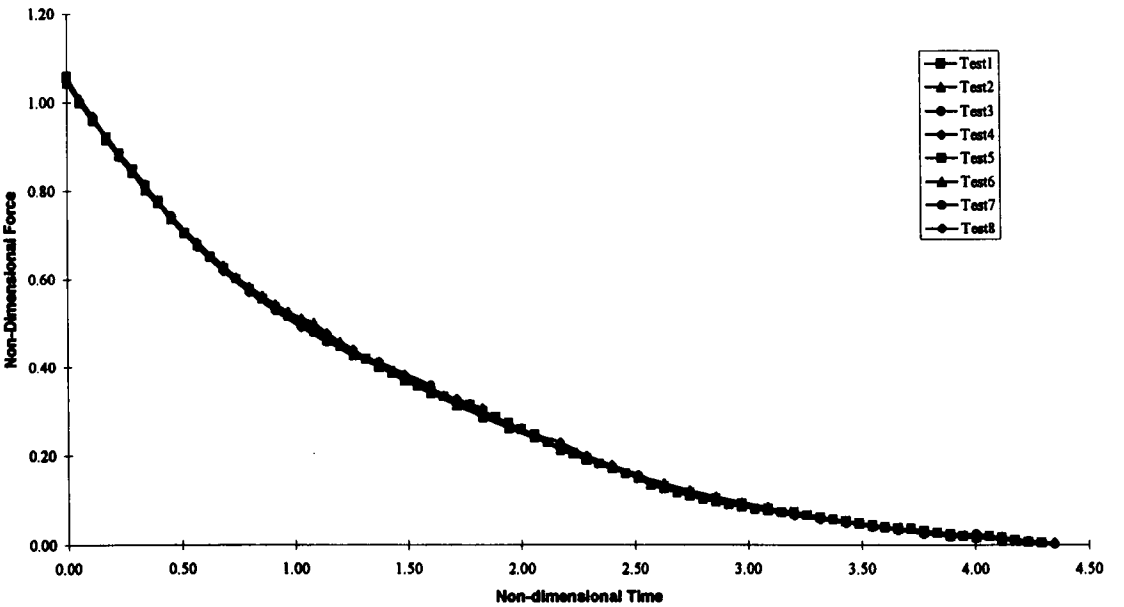


***Graph 2.10** Non-dimensional vertical force experienced by wedge during exit (non-dimensionalised using buoyancy force at initial displacement)*

Looking at the graph we see only slight variations in the global force values (omitting the final values at breakdown which, of course, contain numerical error), so each wedge is undergoing the same basic global interaction with the fluid. Force comparisons, being integrals of the pressure distributions over the entire body, are only a rather crude test of accuracy, but may be all that is needed for most practical

applications. On the other hand, the surface profiles will be affected by the resolution of the points. It is a careful balancing act between the point distribution on the body and on the surface. Test 2 broke down because the point spacing on the body was too cramped compared to that on the surface causing resolution errors. The opposite is true of Test 3 where the surface points are better resolved than those on the body. Since the linear variation that is assumed in $\phi$ will not be a good approximation if the body points are too far apart. Test 8 is a similar case, that is the body is poorly resolved in comparison to the other test cases. If the free surface is poorly resolved, points miss the formation of a wave and "fall through the gap", so we have a single point rising with a wave whilst the others remain still, and this causes a numerical instability. If a surface is too well resolved, we have the situation that small localised jets form rather than a propagating wave which may well be physical, but leads to breakdown. However, the force results testify that the exact resolution of the free surface is not necessary for comparison with the analytic model. Furthermore we can conclude that the code is correct for our purposes and proceed to use the results in the later sections.

The above results show the viability of the code. The exact relationship between free surface and body resolution cannot be specified in general; it will change depending on the system under examination. For instance, Test 1 may be construed as the best resolution for this system (due to its longevity) however it may not be the best for wedge entry, or a transience study. The only way to identify good values for the resolution variables is through trial and error, a continual compare-and-contrast strategy.

## Transient motion

Now we have verified the results obtained from the code we shall proceed to demonstrate the results that can be produced. Under consideration is a body displaced from its equilibrium position then released to move under the influence of gravity alone. For this demonstration of transient motion we shall consider both a wedge and a box body.

The following graphs are a sequence of snapshots of the body and surrounding free surface as the body undergoes transient motion. Accompanying each graph is a table of results describing the body status for each snapshot.

Graph 2.11 to Graph 2.13 depict a wedge undergoing transient motion when released from various displacements from the equilibrium position. Likewise Graph 2.14 to Graph 2.16 depict a box undergoing transient motion.

As a further demonstration of the programs capabilities we also display further data produced for the case considered in Graph 2.14. We present graphs of the pressure profile across the wetted body surface, Graph 2.17, and the vertical forces experienced by the wetted surface, Graph 2.18, during the transient motion. The pressure is non-dimensionalised by dividing by $d_e \rho g$, and the forces are non-dimensionalised using the buoyancy forces at equilibrium $\rho g \forall$.

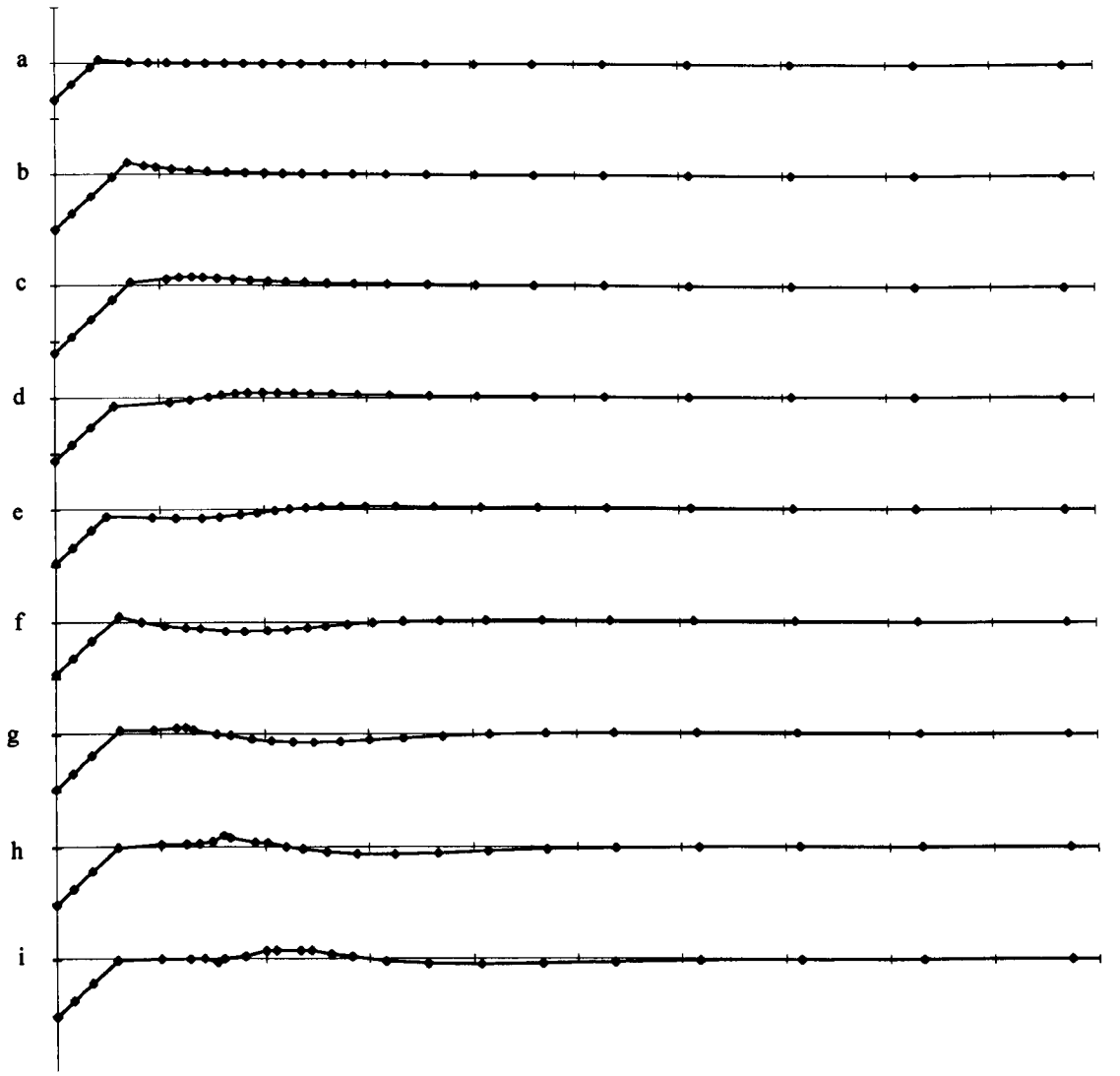


***Graph 2.11*** *Transient motion of a wedge of half angle* $\pi/6$ *(note that the vertical scale is exaggerated). Initially the body is displaced upwards by 0.4 from its equilibrium position and released under the influence of gravity.*(a) *to* (i) *show the progressive motion of the wedge as it oscillates about its equilibrium position and the waves radiated by the body. Each surface profile represents a non-dimensional time step of 0.990. Note the clustering of points in* (i) *this leads to breakdown of the calculation as the nodes intercept one another, this is due to the excessive motion of the wedge a consequence of the large initial displacement. Below is a table of the data for each profile non-dimensionalised as explained previously.*

| | *Time* | *Depth* | *Velocity* | *Acceleration* |
|---|---|---|---|---|
| a | *0.495* | *-0.663* | *-9.567* | *-0.373* |
| b | *1.486* | *-0.989* | *-13.193* | *0.155* |
| c | *2.476* | *-1.196* | *-2.479* | *0.319* |
| d | *3.467* | *-1.123* | *6.853* | *0.094* |
| e | *4.457* | *-0.962* | *4.354* | *-0.166* |
| f | *5.447* | *-0.931* | *-1.233* | *-0.085* |
| g | *6.438* | *-0.986* | *-2.436* | *0.023* |
| h | *7.428* | *-1.029* | *-0.813* | *0.047* |
| i | *8.419* | *-1.028* | *0.728* | *0.029* |

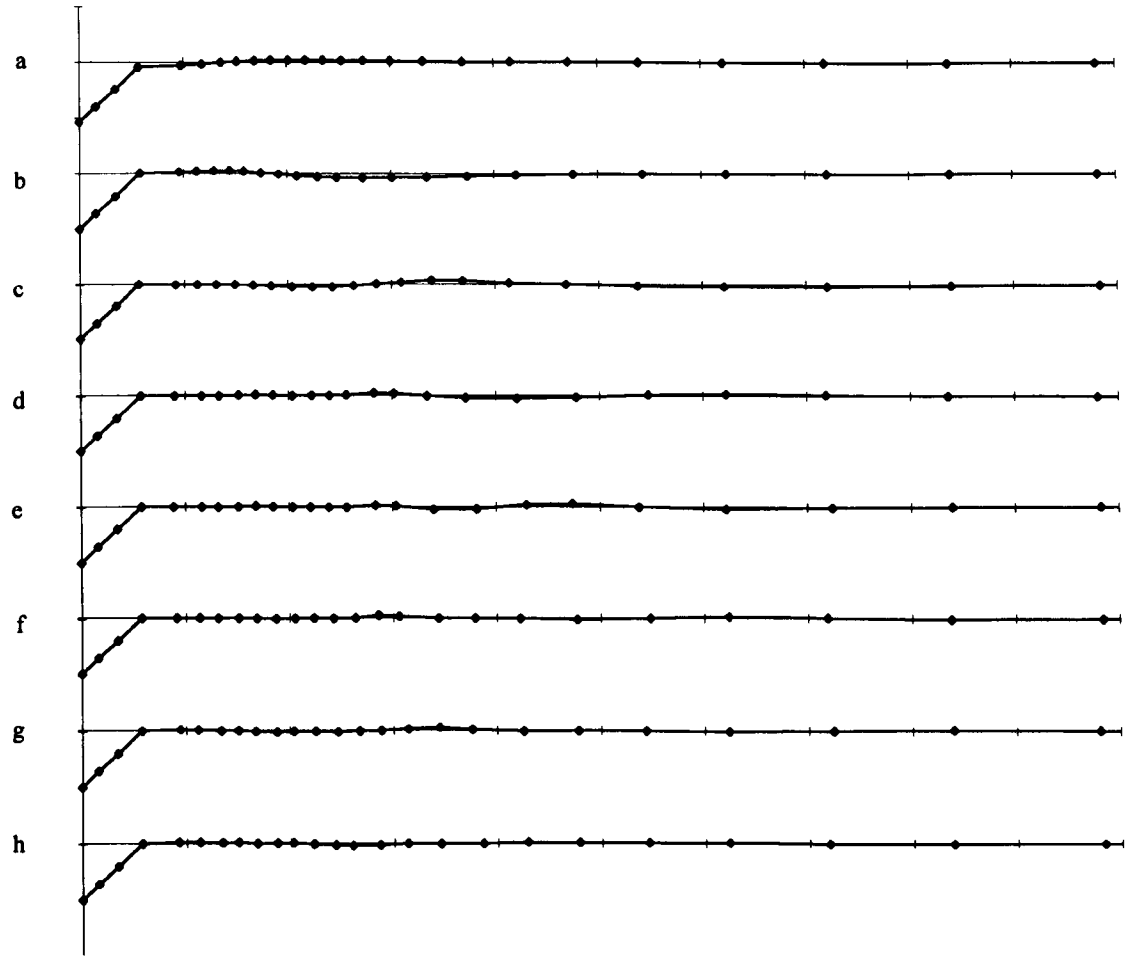


***Graph 2.12*** *Transient motion of a wedge of half angle* $\pi/6$ *(exaggerated vertical scale). Initially the body is displaced upwards by 0.2 from its equilibrium position and released under the influence of gravity.*(a) *to* (h) *show the progressive motion of the wedge as it oscillates about its equilibrium position and the waves radiated by the body. In comparison with Graph 2.11 the amplitude of the radiated waves is small, and the deviation from the equilibrium position is also small, this is due to the relatively small initial displacement. Each surface profile represents a non-dimensional time step of 3.467. Below is a table of the data for each profile non-dimensionalised as explained previously.*

| | *Time* | *Depth* | *Velocity* | *Acceleration* |
|---|---|---|---|---|
| a | *3.467* | *-1.072* | *3.388* | *0.052* |
| b | *6.933* | *-1.004* | *-1.504* | *0.019* |
| c | *10.400* | *-0.988* | *0.034* | *-0.024* |
| d | *13.866* | *-1.003* | *0.157* | *0.003* |
| e | *17.332* | *-0.999* | *-0.300* | *0.001* |
| f | *20.800* | *-0.996* | *-0.095* | *-0.004* |
| g | *24.266* | *-0.998* | *-0.046* | *0.002* |
| h | *27.732* | *-1.01* | *-0.430* | *0.020* |

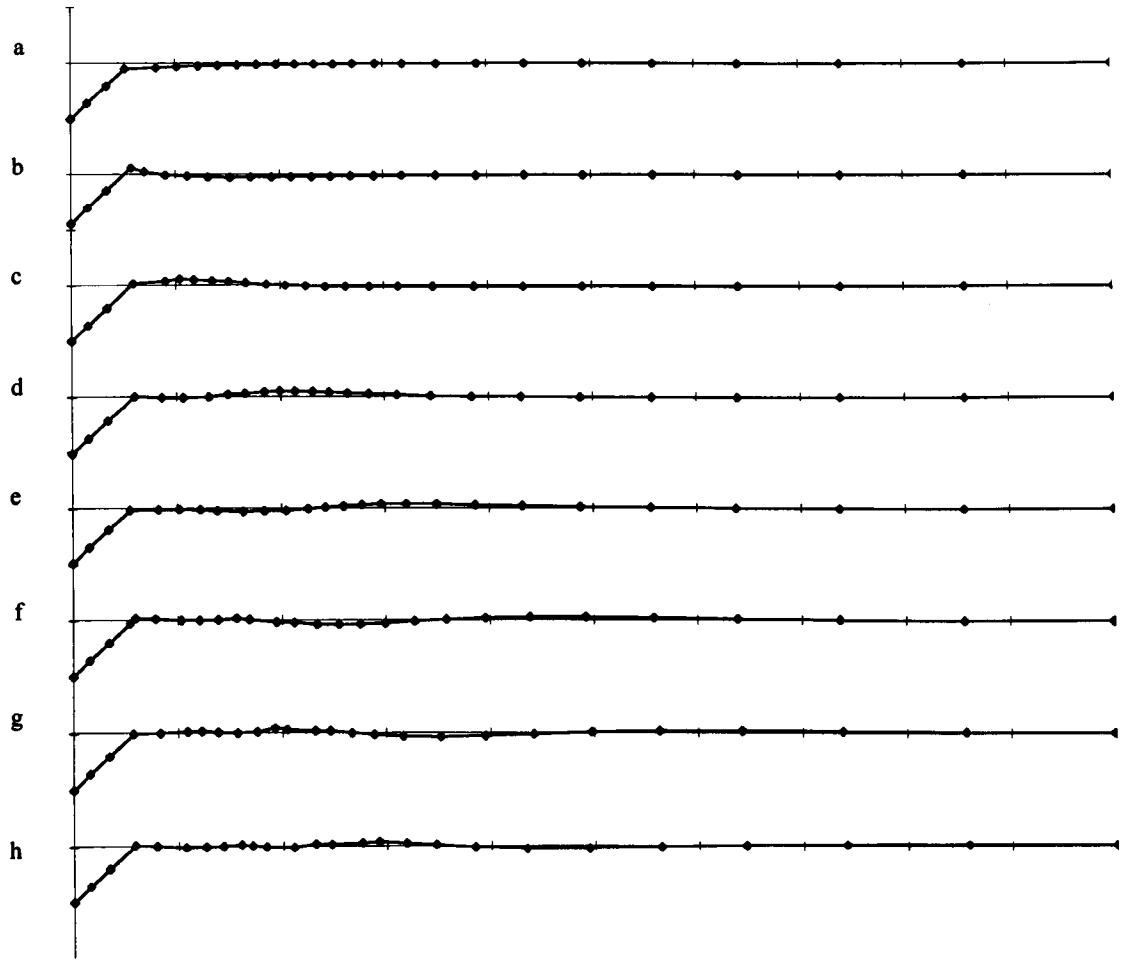


***Graph 2.13*** *Transient motion of a wedge of half angle* $\pi/6$ *(exaggerated vertical scale). Initially the body is displaced downwards by 0.2 from its equilibrium position and released under the influence of gravity.*(a) *to* (h) *show the progressive motion of the wedge as it oscillates about its equilibrium position and the waves radiated by the body. Again, as in Graph 2.12, the amplitudes of the radiated waves are small, and the deviation from the equilibrium position is also small. Each surface profile represents a non-dimensional time step of 1.486. Below is a table of the data for each profile non-dimensionalised as explained previously.*

| | *Time* | *Depth* | *Velocity* | *Acceleration* |
|---|---|---|---|---|
| a | *1.486* | *-1.004* | *7.319* | *-0.067* |
| b | *2.971* | *-0.884* | *-1.183* | *-0.118* |
| c | *4.457* | *-0.996* | *-3.185* | *0.046* |
| d | *5.943* | *-1.036* | *1.132* | *0.057* |
| e | *7.428* | *-0.981* | *0.727* | *-0.049* |
| f | *8.914* | *-0.991* | *-0.663* | *0.004* |
| g | *10.400* | *-1.006* | *-0.167* | *0.001* |
| h | *11.885* | *-1.001* | *0.449* | *0.005* |

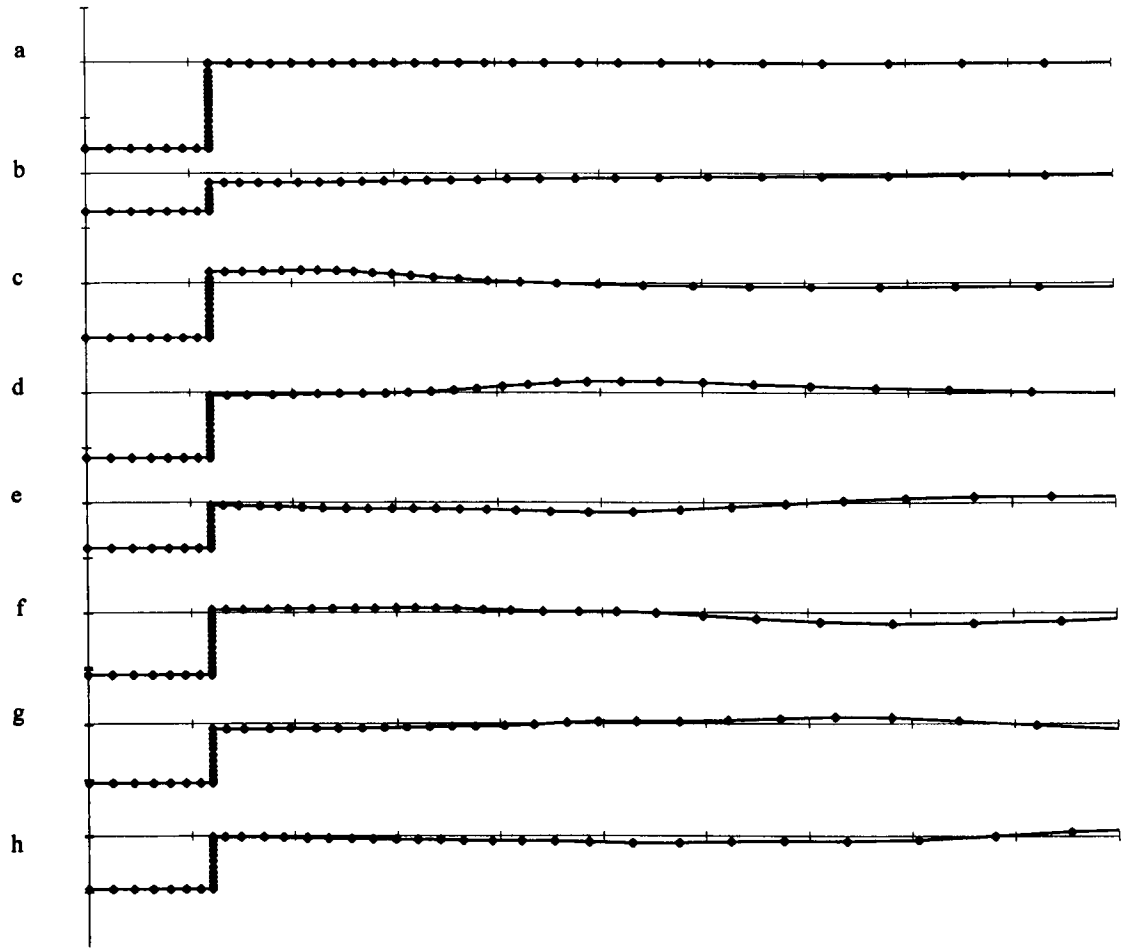


***Graph 2.14*** *Transient motion of a box of aspect ratio beam / draft = 1.2 (vertical scale is exaggerated). Initially the body is displaced downwards by 0.6 from its equilibrium position and released under the influence of gravity.*(a) *to* (h) *show the progressive motion of the box as it oscillates about its equilibrium position and the waves radiated by the body. Each surface profile represents a non-dimensional time step of 3.132. Note there are large amplitude waves away from the body and comparatively minor surface disturbance near the body, this is contrary to the case of a wedge (see Graph 2.11 - Graph 2.13). Below is a table of the data for each profile non-dimensionalised as explained previously.*

| | *Time* | *Depth* | *Velocity* | *Acceleration* |
|---|---|---|---|---|
| a | *0.626* | *-1.553* | *0.585* | *0.218* |
| b | *3.759* | *-0.693* | *0.651* | *-0.197* |
| c | *6.891* | *-0.994* | *-0.890* | *0.030* |
| d | *10.023* | *-1.191* | *0.502* | *0.083* |
| e | *13.155* | *-0.830* | *-0.005* | *-0.103* |
| f | *16.287* | *-1.111* | *-0.347* | *0.058* |
| g | *19.419* | *-0.939* | *0.347* | *0.003* |
| h | *22.551* | *-0.951* | *-0.157* | *-0.039* |

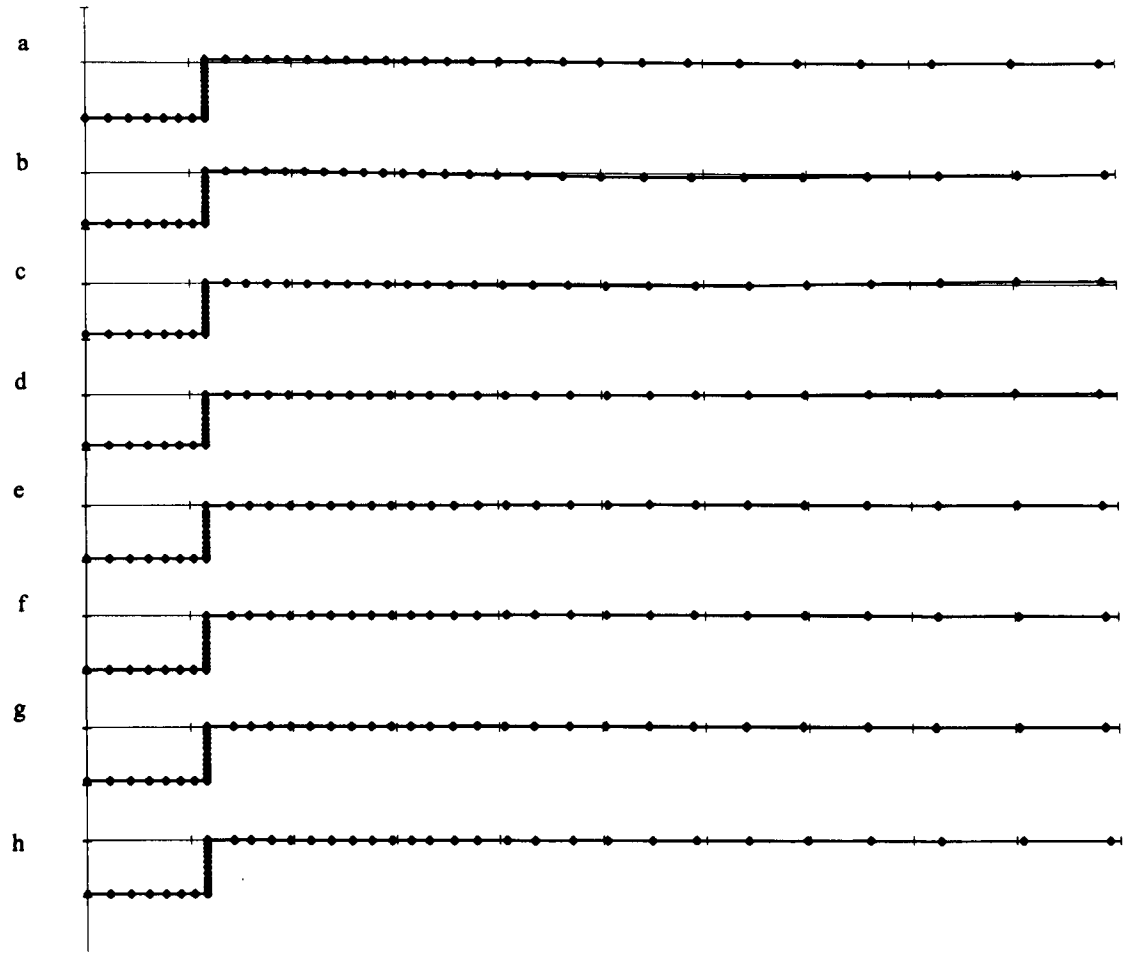


***Graph 2.15*** *Transient motion of a box of aspect ratio beam / draft = 1.2 (vertical scale is exaggerated). Initially the body is displaced upwards by 0.2 from its equilibrium position and released under the influence of gravity.* (a) *to* (h) *show the progressive motion of the box as it oscillates about its equilibrium position and the waves radiated by the body. The wave amplitudes are less that those displayed in Graph 2.14 a result in the decrease in the initial displacement. Each surface profile represents a non-dimensional time step of 7.517. Below is a table of the data for each profile non-dimensionalised as explained previously.*

| | *Time* | *Depth* | *Velocity* | *Acceleration* |
|---|---|---|---|---|
| a | *2.819* | *-1.041* | *-0.444* | *0.032* |
| b | *10.336* | *-0.947* | *-0.216* | *-0.203* |
| c | *17.853* | *-0.941* | *-0.036* | *-0.026* |
| d | *25.370* | *-0.965* | *0.037* | *-0.015* |
| e | *32.887* | *-0.996* | *0.042* | *-0.003* |
| f | *40.404* | *-1.002* | *0.036* | *0.002* |
| g | *47.921* | *-0.984* | *0.004* | *0.001* |
| h | *55.438* | *-1.015* | *-0.020* | *0.004* |

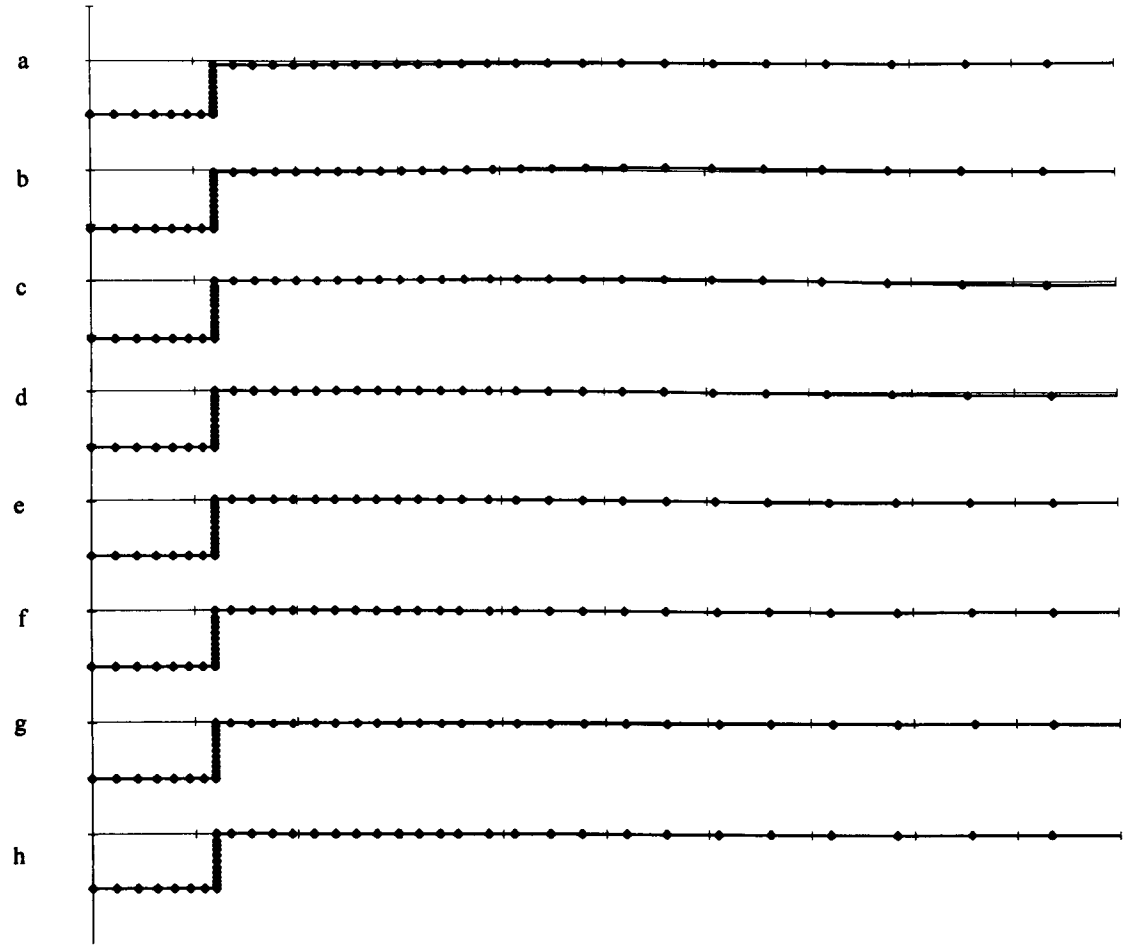


***Graph 2.16*** *Transient motion of a box of aspect ratio beam / draft = 1.2 (vertical scale is exaggerated). Initially the body is displaced downwards by 0.2 from its equilibrium position and released under the influence of gravity.*(a) *to* (h) *show the progressive motion of the box as it oscillates about its equilibrium position and the waves radiated by the body. Again note the lack of surface disturbance as in Graph 2.15. Each surface profile represents a non-dimensional time step of 7.517. Below is a table of the data for each profile non-dimensionalised as explained previously.*

| | *Time* | *Depth* | *Velocity* | *Acceleration* |
|---|---|---|---|---|
| a | *2.819* | *-0.967* | *0.428* | *-0.032* |
| b | *10.336* | *-1.052* | *0.207* | *0.020* |
| c | *17.853* | *-1.057* | *0.035* | *0.024* |
| d | *25.370* | *-1.034* | *-0.035* | *0.014* |
| e | *32.887* | *-1.004* | *-0.038* | *0.003* |
| f | *40.404* | *-0.998* | *-0.035* | *-0.002* |
| g | *47.921* | *-1.015* | *-0.003* | *-0.001* |
| h | *55.438* | *-0.986* | *0.017* | *-0.003* |

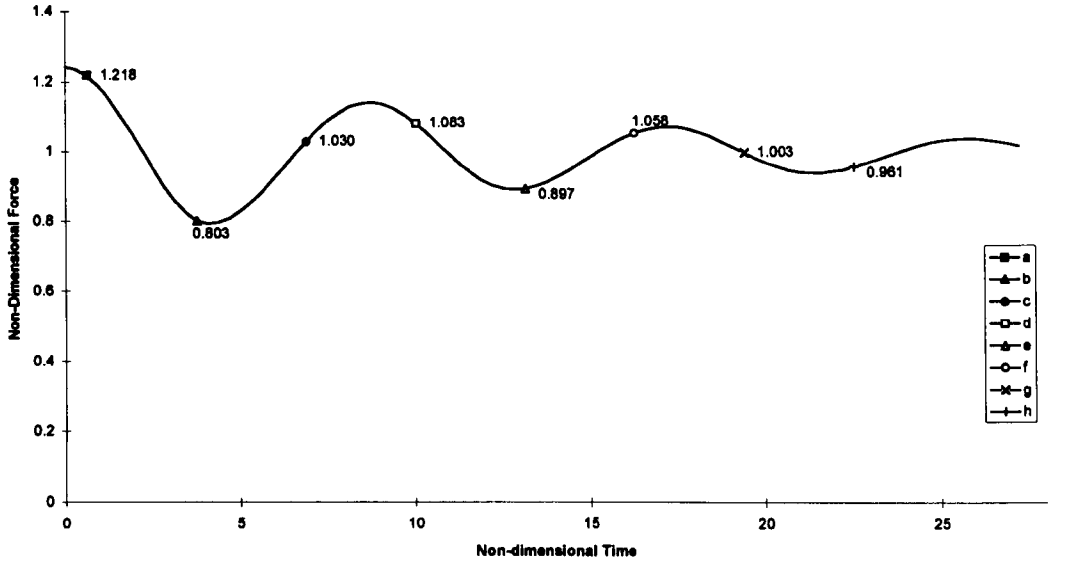


***Graph 2.17*** *Graph of non-dimensional force against time for the transient motion of a box as described in Graph 2.14. The marked points represent the steps presented in Graph 2.14 and the figures beside are the forces on the wetted surface of the body at that time.*

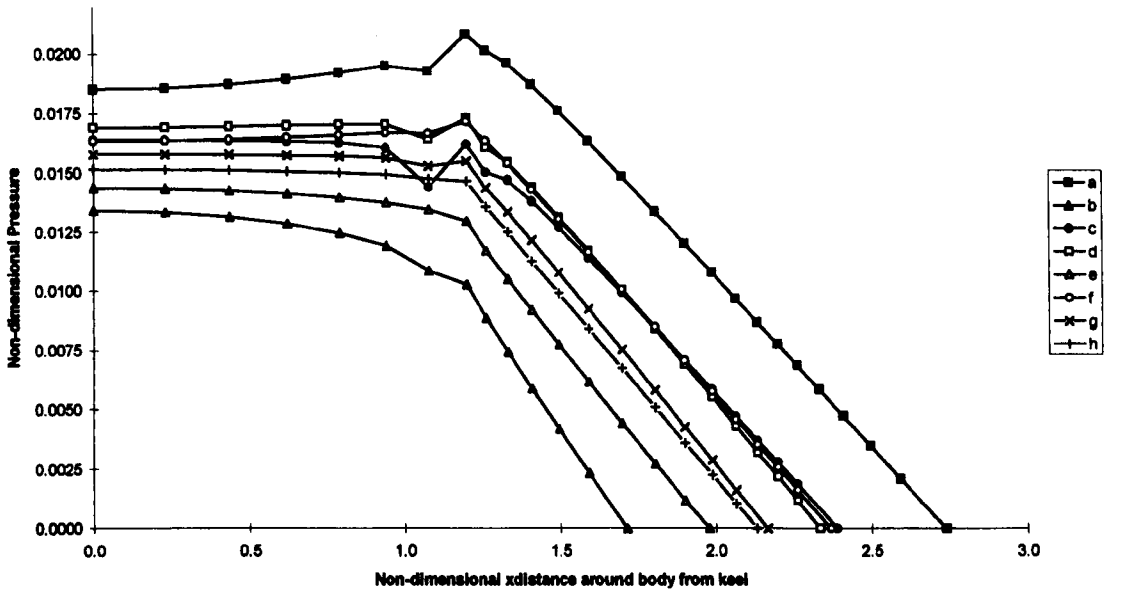


***Graph 2.18*** *The non-dimensional pressure acting at the nodes on the wetted surface of the body. The x axis represents the non-dimensional distance from the centre of the body. Each step in Graph 2.14 has a corresponding pressure curve in the diagram.*

The reader may note the disturbance in the pressure curves at $x = 1$. Calculation of the pressure at the body corners is unreliable due to the integrable singularities present. A full discussion of this problem is given in Chapter 4 and Chapter 5.

## Conclusion

In this chapter we have demonstrated the viability of the fully non-linear numerical theory and its implementation in Fortran. Furthermore, we have presented graphs indicating the capabilities of the code to produce near physical results. In the next chapter we will derive an analytical method to approximate the fully non-linear solution. Chapters 4 and 5 will then compare the theory presented here with that in the following chapter for bodies exiting and entering the fluid domain.

# Chapter 3 Analytic Theory

*A derivation of the analytic theory and approximate added mass used to calculate the forces experienced by a body moving through the fluid domain*


## Abstract

This chapter describes the derivation of the analytic theory as applied to the problem of a body moving in the fluid domain. An explanation is given of the analytical theory and the method of application to the problem.


## Introduction

This chapter is concerned with obtaining an analytical description of a body moving in fluid. The main priority will be the forces acting upon the body. Three systems are under consideration, a wedge, a box and a knuckled body. Each shall be considered separately; although there is some commonality at points in the derivation, it will be repeated for clarity.

We consider each body in motion through a quintessent fluid from a prescribed position. As the body shifts in the fluid domain it experiences hydrostatic and hydrodynamic pressures upon its wetted surface. These are integrated to give hydrostatic and hydrodynamic forces which are due to the interaction with the fluid particles and their subsequent acceleration. An analytical theory is implemented in an attempt to produce a practical method of calculation. The motivation is to develop a simpler theory that is able to calculate the forces experienced by the body without the need for extensive numerical calculations, and which could be included in strip theory codes dealing with large-amplitude (slamming) calculations.

## Wedge Theory

Firstly we consider a wedge with half-angle $\alpha$ (Figure 3.1), initially at a depth $d$, leaving the fluid with constant velocity / acceleration.

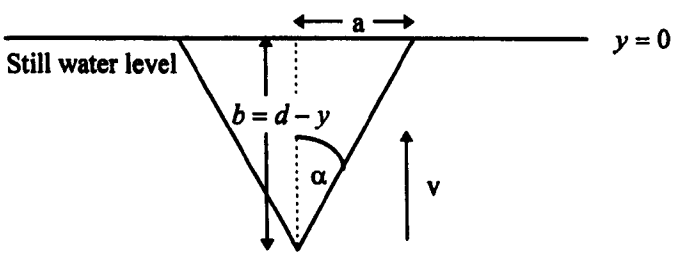


***Figure 3.1** Wedge of half angle α in a state of equilibrium*

This theory consists of the buoyancy force (also known as the hydrostatic force) and the added mass force (referred to as the hydrodynamic force). The buoyancy force is defined as:

$$F_b = \rho g \forall(t) \tag{3.1}$$

where ρ is the body density, g is gravitational acceleration, and $\forall(t)$ is submerged volume, that is, the instantaneous portion of the body below the undisturbed free surface level at $y = 0$. The added mass force is defined from the energy in the fluid/body system. The kinetic energy is

$$T = \frac{1}{2}(m_a + m_b)v^2 \tag{3.2}$$

The potential energy can be defined as

$$V = \int_{-y}^{0} (\rho g \forall - m_b g)dy = (\rho g \forall - m_b g)y \tag{3.3}$$

We set the total energy as

$$L = T + V = \frac{1}{2}(m_a + m_b)\dot{y}^2 + (\rho g \forall - m_b g)y \tag{3.4}$$

Applying Lagrange's equation

$$\frac{\partial L}{\partial y} - \frac{d}{dt}\left(\frac{\partial L}{\partial \dot{y}}\right) = 0$$

Now

$$\frac{\partial L}{\partial y} - \frac{d}{dt}\left(\frac{\partial L}{\partial \dot{y}}\right) = \frac{1}{2}\frac{dm_a}{dy}\dot{y}^2 + (\rho g \forall - m_b g) - \frac{d}{dt}\left(\frac{1}{2}(m_a + m_b)2\dot{y}\right)$$

and

$$\frac{d}{dt}\left(\frac{1}{2}(m_a + m_b)2\dot{y}\right) = (m_a + m_b)\ddot{y} + \frac{dm_a}{dy}\frac{dy}{dt}\dot{y} = (m_a + m_b)\ddot{y} + \frac{dm_a}{dy}\dot{y}^2$$

We find

$$\frac{\partial L}{\partial y} - \frac{d}{dt}\left(\frac{\partial L}{\partial \dot{y}}\right) = -\frac{1}{2}\frac{dm_a}{dy}\dot{y}^2 + (\rho g \forall - m_b g) - (m_a + m_b)\ddot{y} = 0$$

Hence

$$m_b\ddot{y} + m_b g - \rho g \forall = -m_a\ddot{y} - \frac{1}{2}\frac{dm_a}{dy}\dot{y}^2 \tag{3.5}$$

Where the left-hand side is the equation of motion and the right-hand side is the added mass force, $-F_a$. So we state $F_a$ as

$$F_a = \frac{1}{2}\frac{dm_a}{dy}v^2 + m_a\dot{v} \tag{3.6}$$

where $m_a$ is the added mass, $y$ is the vertical axis, and $\dot{y}$ & $\ddot{y}$ are replaced by $v$ & $\dot{v}$ (the vertical velocity and acceleration). Although exact, this is not currently in a form we can utilise because we have no simple means of calculating the added mass exactly. In general the added mass would depend on the entire history of motion (i.e. memory) by the virtue of wave radiation. However analytical progress is possible if we approximate the free surface by a line of equipotential $\phi$=0 on $y = 0$. Such an approximation is essentially pragmatic but does correspond to

i. the initial conditions used for the numerical calculations, meaning that comparisons between analytic and numerical results should agree at $t$=0.

ii. the high-frequency limit for the usual time-independent linear theory used in most seakeeping theories. This can also be thought of as the zero gravity limit used in slamming calculations since the initial local accelerations of spray jets usually greatly exceed $g$.

Then from Wagner (1932) the added mass is :

$$m_a = \rho b^2 G \tan\alpha \tag{3.7}$$

and

$$\frac{dm_a}{dy} = \frac{d}{dy}\left\{\rho b^2 G \tan\alpha\right\} \tag{3.8}$$

where

$$G = \frac{\Gamma\left(1+\frac{\alpha}{\pi}\right)\Gamma\left(\frac{1}{2}-\frac{\alpha}{\pi}\right)}{\Gamma\left(1-\frac{\alpha}{\pi}\right)\Gamma\left(\frac{1}{2}+\frac{\alpha}{\pi}\right)} - 1 \tag{3.9}$$

and $b = d - y$ is the submerged depth of the wedge, where $d$ is initial depth and $y$ is change in depth. The $\Gamma(..)$ are Gamma functions, the evaluation of these Gamma functions is performed using the following identities (see Abramowitz and Stegun (1965)):

$$\Gamma(1+x) = x\Gamma(x) \tag{3.10}$$

$$\Gamma(x)\Gamma(1-x) = \frac{\pi}{\sin \pi x}$$

$$\Gamma(1+x) = 1 + a_1 x + a_2 x^2 + a_3 x^3 + a_4 x^4 + a_5 x^5$$

where

$$a_1 = -0.5748646$$
$$a_2 = 0.9512363$$
$$a_3 = -0.6998588$$
$$a_4 = 0.4245549$$
$$a_5 = -0.1010678$$

Wagner (1932) states his results for $m_a$ without explanation, and it is worth deriving the result here for comparison with the more complicated body geometry considered later. We consider the Schwartz-Christoffel mapping, see e.g. Milne-Thomson (1968).

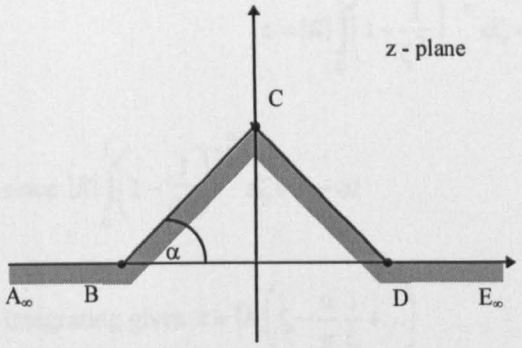


***Figure 3.2*** *Flow past a wedge in the upper half-plane*

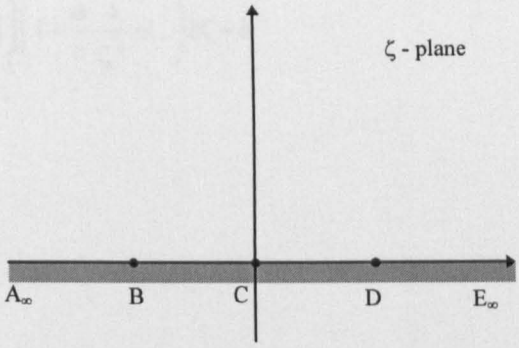


***Figure 3.3*** *Uniform flow in the upper half-plane*

From the Schwartz-Christoffel theorem we can state

$$z = K' \int_0^{\zeta} (\zeta+1)^{\frac{\pi-\alpha}{\pi}-1} (\zeta)^{\frac{\pi+2\alpha}{\pi}-1} (\zeta-1)^{\frac{\pi-\alpha}{\pi}-1} d\zeta + L$$

$$z = K \int_0^{\zeta} \frac{\zeta^{\frac{2\alpha}{\pi}}}{(1-\zeta^2)^{\frac{\alpha}{\pi}}} d\zeta + L$$

At point C: $\zeta = 0,\ z = ai \Rightarrow L = ai$

At point D: $\zeta = 1,\ z = b \Rightarrow b = K \int_0^{1} \frac{\zeta^{\frac{2\alpha}{\pi}}}{(1-\zeta^2)^{\frac{\alpha}{\pi}}} d\zeta + ai$

Using the identity

$$\frac{\Gamma(q)\Gamma(p)}{\Gamma(q+p)} = \int_0^1 t^{q-1}(1-t)^{p-1}\, dt$$

from Abramowitz & Stegun (1965), and the substitution $\zeta = \sqrt{t}$ we can derive

$$b = K\frac{\Gamma\left(\frac{\alpha}{\pi}-\frac{1}{2}\right)\Gamma\left(1-\frac{\alpha}{\pi}\right)}{\sqrt{\pi}} + ai \Rightarrow K = \frac{(b-ai)\sqrt{\pi}}{\Gamma\left(\frac{\alpha}{\pi}-\frac{1}{2}\right)\Gamma\left(1-\frac{\alpha}{\pi}\right)}$$

We now set $K = |K|e^{-i\alpha}$ where $|K| = \frac{b}{\cos\alpha}\frac{\sqrt{\pi}}{\Gamma\left(\frac{\alpha}{\pi}-\frac{1}{2}\right)\Gamma\left(1-\frac{\alpha}{\pi}\right)}$

So we can express

$$z = |K|\int_0^{\zeta}\left(1-\frac{1}{\zeta^2}\right)^{-\frac{\alpha}{\pi}} d\zeta + ai = |K|\int_1^{\zeta}\left(1+\frac{\alpha}{\pi}\frac{1}{\zeta^2}+\ldots\right)d\zeta + b$$

since $|K|\int_0^1\left(1-\frac{1}{\zeta^2}\right)^{-\frac{\alpha}{\pi}} d\zeta = b - ai$

Integrating gives $z = |K|\left(\zeta - \frac{\alpha}{\pi}\frac{1}{\zeta}+\ldots\right)$

Thus $\zeta = z' + \frac{\alpha}{\pi}\frac{1}{z'}+\ldots$ where $z' = \frac{z}{|K|}$ by series reversion.

We require $\beta(z) \to z$ as $z \to \infty$ for unit velocity at $\infty$. So

$$\beta(z) = |K|\zeta = z + |K|^2\frac{\alpha}{\pi}\frac{1}{z}+\ldots$$

The added mass can be derived from the dipole coefficient as explained in Newman (1977) and Appendix B. So taking the coefficient of $1/z$ we can conclude

$$\left(\frac{m_a}{\rho}+\forall\right) = |K|^2\alpha = \frac{(a^2+b^2)\pi\alpha}{\left[\Gamma\left(\frac{\alpha}{\pi}-\frac{1}{2}\right)\Gamma\left(1-\frac{\alpha}{\pi}\right)\right]^2} \quad \text{where } \forall = b^2\tan\alpha \text{ (the body volume)}$$

Using further identities defined in Abramowitz and Stegun (1965) we can obtain the equation

$$\left(\frac{m_a}{\rho}+\forall\right) = b^2\tan\alpha\frac{\frac{\alpha}{\pi}\Gamma\left(\frac{\alpha}{\pi}\right)\Gamma\left(\frac{1}{2}-\frac{\alpha}{\pi}\right)}{\Gamma\left(\frac{\alpha}{\pi}+\frac{1}{2}\right)\Gamma\left(\frac{\alpha}{\pi}+\frac{1}{2}\right)}$$

with minor manipulation we finally obtain equation (3.7) as stated by Wagner (1932). Graph 3.1 depicts the relationship between the added mass, $m_a$, and the wedge half angle, $\alpha$. The added mass is non-dimensionalised in two different manners. On the left we non-dimensionalise with respect to the submerged body depth, *b*.

$$\frac{m_a}{\rho\pi b^2} = \frac{\tan\alpha}{\pi} G$$

On the right we non-dimensionalise with respect to the body half width, $a = b\tan\alpha$. We non-dimensionalise with respect to body half width to allow for comparisons with other body cross sections presented in later sections.

$$\frac{m_a}{\rho\pi a^2} = \frac{G}{\pi}$$

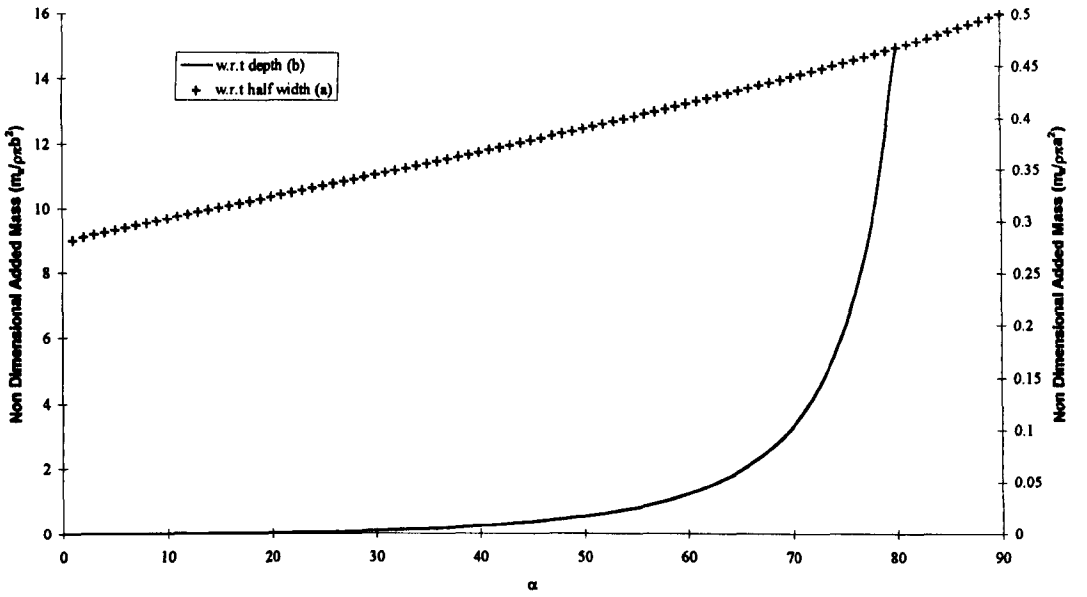


***Graph 3.1** Non-dimensionalised added mass (w.r.t. depth & half width) against half angle α*

We note that the added mass for the wedge approaches $\rho\pi a^2/2$ as $\alpha$ approaches 90 degrees. We expect this result since it is the added mass for a flat plate of half width *a* (equivalent to the displaced mass of a cylinder radius *a*)

Differentiating the added mass with respect to *y*, noting that b is a function of *y* :

$$\frac{dm_a}{dy} = -2\rho bG\tan\alpha \tag{3.11}$$

Hence, by substitution we can obtain the added mass force in a form suitable for comparison with the numerical calculations:

$$F_a = \rho G \tan\alpha \left(-bv^2 + b^2\dot{v}\right) \tag{3.12}$$

The values of $F_a$ and $F_b$ can now be calculated, since the body velocity, v, and hence submergence $(d - y)$ is known for either the constant velocity or constant acceleration cases considered here. The results are calculated for a sufficiently long time period to produce two sets of comparable results from this and the numerical calculations.

## Box Body Theory

So far we have considered a wedge shaped body in the fluid domain. We now extend these theories to the case of a box shaped body.

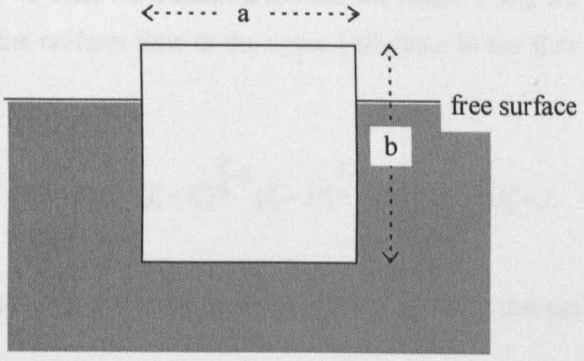


***Figure 3.4*** *Box body in the fluid domain*

We expect this to be a more complex situation for several reasons. In the case of the wedge the submerged body shape is always self-similar, i.e. always a triangle similar to that in the initial conditions (provided the free surface is assumed flat). This is not the case with a box body. As the body moves in the fluid domain so its aspect ratio changes, the limiting case being that of a flat plate on the free surface. Another difference in the analytical models is that the flow around the wedge is regular at the vertex, but singular at the body/free surface intersection points, whereas the box has singularities at the corners but is regular at the body/free surface intersection points. Finally the flat bottom of the box may be expected to have a significant effect on the added mass when it is close to the surface.

To calculate the added mass of a box-body we use a Schwarz-Christoffel transformation. The situation is as follows. We wish to find the transformation that allows us to map the flow around a box-body (Figure 3.5) to that of uniform flow in the upper half-plane (Figure 3.6)

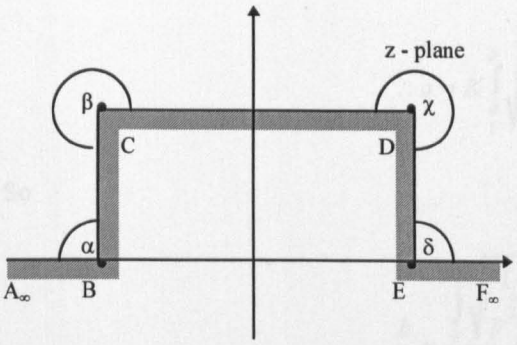


*Figure 3.5 Flow past a box-body in the upper half-plane*

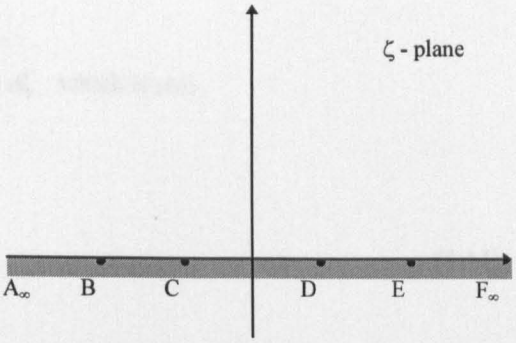


*Figure 3.6 Uniform flow in the upper half-plane*

However, to do this we must work backwards from the result. Using the Schwarz-Christoffel transformation we can map the uniform flow in the upper half-plane to the flow around the body as follows.

$$z = K\int_0^{\zeta}(\zeta - B)^{\frac{\alpha}{\pi}-1}(\zeta - C)^{\frac{\beta}{\pi}-1}(\zeta - D)^{\frac{\chi}{\pi}-1}(\zeta - E)^{\frac{\delta}{\pi}-1}d\zeta + L$$

If we take $B$=-p, $C$=-1, $D$=1 and $E$=p and using the values of $\alpha$, $\beta$, $\chi$, and $\delta$ that can be seen from Figure 3.6. we get

$$z = K\int_0^{\zeta}(\zeta + p)^{\frac{\pi/2}{\pi}-1}(\zeta + 1)^{\frac{3\pi/2}{\pi}-1}(\zeta - 1)^{\frac{3\pi/2}{\pi}-1}(\zeta - p)^{\frac{\pi/2}{\pi}-1}d\zeta + L \tag{3.13}$$

Simplifying

$$z = K\int_0^{\zeta}(\zeta + p)^{-\frac{1}{2}}(\zeta + 1)^{\frac{1}{2}}(\zeta - 1)^{\frac{1}{2}}(\zeta - p)^{-\frac{1}{2}}d\zeta + L$$

$$= K\int_0^{\zeta}\sqrt{\frac{(\zeta^2 - 1)}{(\zeta^2 - p^2)}}d\zeta + L$$

From the diagrams it can be seen that when

$$\text{At } \zeta = 0 \quad z = ai \Rightarrow L = ai$$

$$\text{At } \zeta = 1 \quad z = b + ai = K\int_0^1\sqrt{\frac{\zeta^2 - 1}{\zeta^2 - p^2}}d\zeta + ai \Rightarrow K = \frac{b}{\int_0^1\sqrt{\frac{1-\zeta^2}{p^2 - \zeta^2}}d\zeta} \quad \text{where } |p| > 1$$

$$\text{At } \zeta = p \quad z = b = K\int_0^p\sqrt{\frac{\zeta^2 - 1}{\zeta^2 - p^2}}d\zeta + ai = K\int_1^p\sqrt{\frac{\zeta^2 - 1}{\zeta^2 - p^2}}d\zeta + b + ai$$

$$\Rightarrow -ai = K\int_1^p\sqrt{\frac{\zeta^2 - 1}{\zeta^2 - p^2}}d\zeta$$

$$\therefore a = K\int_1^p \sqrt{\frac{\zeta^2-1}{p^2-\zeta^2}}\,d\zeta \quad \text{which is real}$$

So

$$\frac{b}{a} = \frac{\int_0^1 \sqrt{\frac{1-\zeta^2}{p^2-\zeta^2}}\,d\zeta}{\int_1^p \sqrt{\frac{\zeta^2-1}{p^2-\zeta^2}}\,d\zeta} \tag{3.14}$$

Now, we know

$$z = K\int_0^\zeta \sqrt{\frac{\zeta^2-1}{\zeta^2-p^2}}\,d\zeta + ai = K\int_0^1 \sqrt{\frac{\zeta^2-1}{\zeta^2-p^2}}\,d\zeta + K\int_1^p \sqrt{\frac{\zeta^2-1}{\zeta^2-p^2}}\,d\zeta + K\int_p^\zeta \sqrt{\frac{\zeta^2-1}{\zeta^2-p^2}}\,d\zeta + ai$$

$$= K\int_p^\zeta \sqrt{\frac{\zeta^2-1}{\zeta^2-p^2}}\,d\zeta + b$$

$$= K\int_p^\zeta \left(1-\frac{1}{\zeta^2}\right)^{\frac{1}{2}}\left(1-\left(\frac{p}{\zeta}\right)^2\right)^{-\frac{1}{2}} d\zeta + b$$

Using the following series expansions

$$\left(1-\frac{1}{\zeta^2}\right)^{\frac{1}{2}} = 1-\frac{1}{2\zeta^2}-\ldots\ldots = \sum_{m=0}^{\infty}\left(-\frac{1}{\zeta^2}\right)^m \frac{\prod_{n=0}^{m}\left(\frac{1}{2}-n\right)}{m!} \tag{3.15}$$

$$\left(1-\frac{p}{\zeta^2}\right)^{-\frac{1}{2}} = 1+\frac{p}{2\zeta^2}+\ldots\ldots = \sum_{m=0}^{\infty}\left(-\frac{p}{\zeta^2}\right)^m \frac{\prod_{n=0}^{m}\left(-\frac{1}{2}-n\right)}{m!} \tag{3.16}$$

We can then write

$$z = K\int_p^\zeta \left(1-\frac{1}{2}\frac{1}{\zeta^2}+\ldots.\right)\left(1+\frac{1}{2}\frac{p^2}{\zeta^2}+\ldots.\right)d\zeta + b$$

$$= K\int_p^\zeta \left(1+\frac{1}{2}(p^2-1)\frac{1}{\zeta^2}+\ldots.\right)d\zeta + b$$

$$z \approx K\zeta - K\frac{(p^2-1)}{2}\frac{1}{\zeta}+\ldots.+\text{constant term}$$

So we have, through series reversion

$$\zeta = \frac{z}{K} + \frac{A}{z} + \ldots.$$

$$\zeta = \zeta - \frac{(p^2-1)}{2}\frac{1}{\zeta} + \frac{A}{K\zeta}$$

$$\Rightarrow A = \frac{(p^2-1)}{2}K$$

$$\therefore \zeta = \frac{z}{K} + \frac{(p^2-1)}{2}K\frac{1}{z} + \ldots.$$

We require $\beta(z) \to z$ as $z \to \infty$ ,that is, $\beta(\zeta) \to K\zeta$ as $\zeta \to \infty$ thus,

$$\beta(z) = z + \frac{(p^2-1)}{2}K^2\frac{1}{z} + \ldots.$$

where $\frac{(p^2-1)}{2}K^2$ is the required dipole coefficient needed for the added mass calculation.

This is the flow around the double body

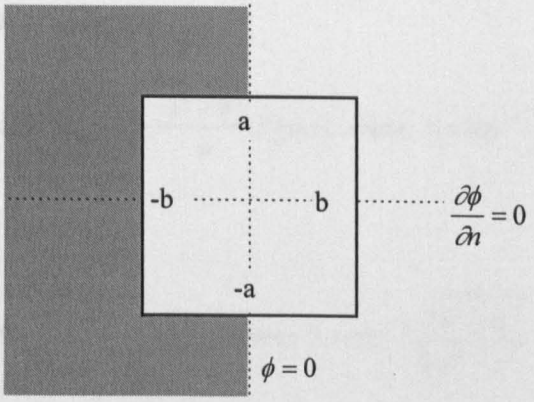


***Figure 3.7*** *Flow around the double body*

So, if subscript $T$ stands for the total double body flow we have

$$\left(\forall_T + \frac{m_{aT}}{\rho}\right) = 2\pi\frac{(p^2-1)}{2}K^2$$

We only require the flow in the shaded region of Figure 3.7, so

$$\frac{m_a}{\rho} = \frac{1}{2}\left\{2\pi\frac{(p^2-1)}{2}K^2 - \forall_T\right\} = \pi\frac{(p^2-1)}{2}K^2 - \forall$$

where $\forall_T = 4ab$ and $\forall = 2ab$ . Hence

$$\frac{m_a}{\rho 2ab} = \frac{\pi(p^2-1)K^2}{4ab} - 1$$

However, this formula is not particularly useful since $b$ varies with time, thus the following is used

$$\frac{m_a}{\rho\pi a^2} = \frac{(p^2-1)K^2}{2a^2} - \frac{2b}{\pi a} \tag{3.17}$$

The whole double-body flow formula (as it appears in Riabouchinski (1920)) can be obtained by multiplying (3.17) through by a factor of 2.

Substituting in for the previously calculated values $K$, $b$ and $a$ we obtain

$$\frac{m_a(p)}{\rho\pi a^2} = \frac{(p^2-1)}{2\left[\int_1^p \sqrt{\frac{\zeta^2-1}{p^2-\zeta^2}}\,d\zeta\right]^2} - \frac{2}{\pi}\left[\frac{\int_0^1 \sqrt{\frac{1-\zeta^2}{p^2-\zeta^2}}\,d\zeta}{\int_1^p \sqrt{\frac{\zeta^2-1}{p^2-\zeta^2}}\,d\zeta}\right] \tag{3.18}$$

provided $|p|>1$.

We can convert this form, containing complicated integrals, into an elliptic integral form. From Gradshteyn and Ryzhik (1994) we state

$$\int_0^u \sqrt{\frac{b^2-x^2}{a^2-x^2}}\,dx = aE(\eta,t) - \frac{a^2-b^2}{a}F(\eta,t) \text{ where } \eta = \sin^{-1}\frac{u}{b} \text{ and } t = \frac{b}{a}$$

and

$$\int_u^a \sqrt{\frac{x^2-b^2}{a^2-x^2}}\,dx = aE(\lambda,q) - \frac{b^2}{a}F(\lambda,q) \text{ where } \lambda = \sin^{-1}\sqrt{\frac{a^2-u^2}{a^2-b^2}} \text{ and } q = \frac{\sqrt{a^2-b^2}}{a}$$

we can deduce

$$\int_0^1 \sqrt{\frac{1^2-x^2}{p^2-x^2}}\,dx = pE(\frac{\pi}{2},\frac{1}{p}) - \frac{p^2-1^2}{p}F(\frac{\pi}{2},\frac{1}{p})$$

$$\int_1^p \sqrt{\frac{x^2-1^2}{p^2-x^2}}\,dx = pE(\frac{\pi}{2},\frac{\sqrt{p^2-1}}{p}) - \frac{1}{p}F(\frac{\pi}{2},\frac{\sqrt{p^2-1}}{p})$$

Now $E(\frac{\pi}{2},k) = E(k)$ and $F(\frac{\pi}{2},k) = K(k)$ where $k$ is the modulus. Also if $k' = \sqrt{k^2-1}$, $E'(k) = E(k')$ and $K'(k) = K(k')$. Then setting $k = \frac{\sqrt{p^2-1}}{p} \Rightarrow p = \sqrt{\frac{1}{1-k^2}}$ we can derive

$$\int_0^1 \sqrt{\frac{x^2-1}{p^2-x^2}}dx = \sqrt{\frac{1}{1-k^2}}E'(k) - k^2\sqrt{\frac{1}{1-k^2}}K'(k)$$

$$\int_1^p \sqrt{\frac{1-x^2}{p^2-x^2}}dx = \sqrt{\frac{1}{1-k^2}}E(k) - \sqrt{1-k^2}K(k)$$

If we now consider the parameter $m$ rather than the modulus $k$, which by definition

$$E(\varphi,k) = \int_0^{\varphi}\sqrt{1-k^2\sin^2\theta}d\theta \text{ and } E(\varphi/m) = \int_0^{\varphi}\sqrt{1-m\sin^2\theta}d\theta \text{ where } m = k^2$$

and similarly for K, then we can find

$$\frac{\int_0^1 \sqrt{\frac{1-x^2}{p^2-x^2}}dx}{\int_1^p \sqrt{\frac{x^2-1}{p^2-x^2}}dx} = \frac{E'(k)-k^2K'(k)}{E(k)-(1-k^2)K(k)} = \frac{E'(m)-mK'(m)}{E(m)-(1-m)K(m)}$$

$$\frac{p^2-1}{\int_1^p \sqrt{\frac{x^2-1}{p^2-x^2}}dx} = \frac{k^2}{\left[E(k)-(1-k^2)K(k)\right]^2} = \frac{m}{\left[E(m)-(1-m)K(m)\right]^2}$$

Hence

$$\frac{m_a(p)}{\rho\pi a^2} = \frac{(p^2-1)}{2\left[\int_1^p \sqrt{\frac{\zeta^2-1}{p^2-\zeta^2}}d\zeta\right]^2} - \frac{2}{\pi}\left[\frac{\int_0^1 \sqrt{\frac{1-\zeta^2}{p^2-\zeta^2}}d\zeta}{\int_1^p \sqrt{\frac{\zeta^2-1}{p^2-\zeta^2}}d\zeta}\right]$$

becomes

$$\frac{m_a}{\rho\pi a^2} = \frac{m}{2\left[E(m)-(1-m)K(m)\right]^2} - \frac{2}{\pi}\left[\frac{E'(m)-mK'(m)}{E(m)-(1-m)K(m)}\right] \tag{3.19}$$

This is, in fact, the half body form of the equations for the added mass of a box stated in Riabouchinski (1920), as discussed in the following section.

If we consider the graph of this against a non-dimensional ratio of $b/a$ we have Graph 3.2.

Again we note that if we let depth $b$ approach zero then so to does $b/a$, once again we have the situation of a flat plate and $m_a = \rho\pi a^2/2$. So the theory is consistent with flat plate and wedge theory. We also comment on the range of results we are most concerned with. These will be most specifically in the range $0 < b/a < 2$, since if we are considering cases based on real world examples, a ship cross-

section will always fall below $b = 2a$ (except for the bow cross-section of some military ships). The minimum of zero allows for the (almost) complete exit of the body from the fluid.

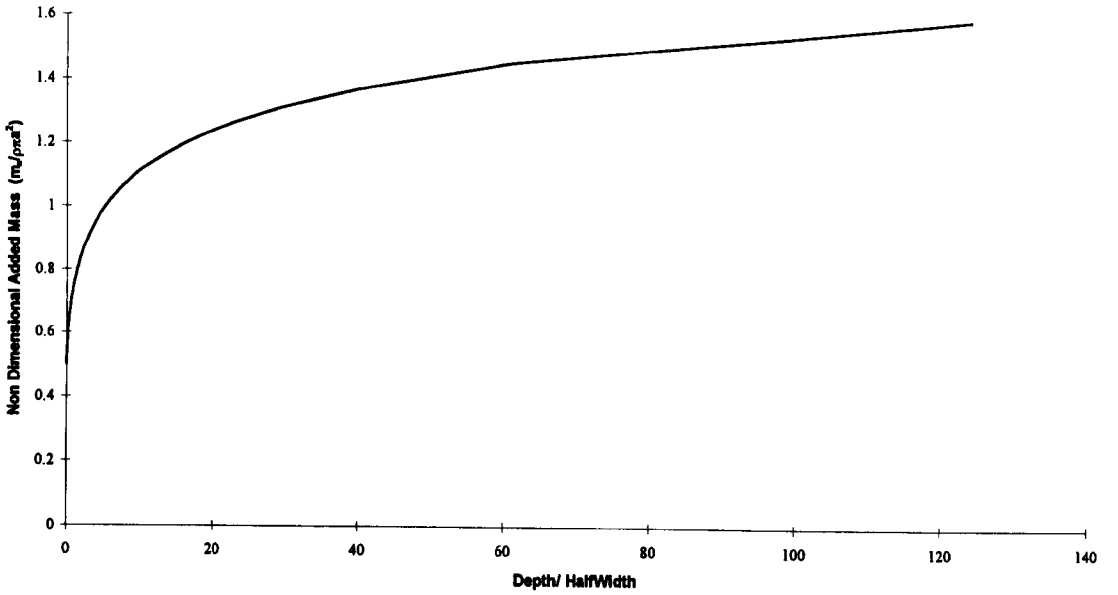


***Graph 3.2** Non-dimensional added mass against non-dimensional body ratio for changing box-body cross section*

## *The Riabouchinski Method*

Riabouchinski (1920) states that the added mass of a box body is

$$\frac{M}{M_0} = \frac{m}{(E(m)-(1-m).K(m))^2} - \frac{4}{\pi}\frac{d}{l} \tag{3.20}$$

Where $M$ is the added mass, $M_0 = 2\pi(l/2)^2$ is used to non-dimensionalise the added mass, $E$ is a complete elliptic integral of the first kind and $K$ is a complete elliptic integral of the second kind defined (see Abramowitz & Stegun (1965)) as

$$K(m) = \int_0^1 ((1-t)(1-mt))^{-1/2}\,dt$$

$$E(m) = \int_0^1 (1-t)^{-1/2}(1-mt)^{1/2}\,dt$$

$\alpha$ being the modular angle, $d$ is the box depth and $l$ is the box width as seen in Figure 3.8

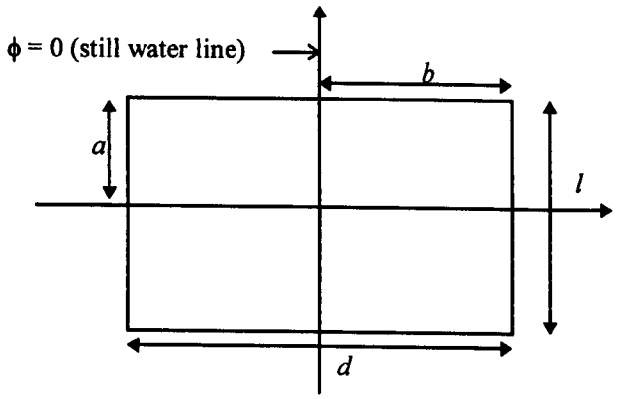


***Figure 3.8*** *Description of box-body according to Riabouchinski*

The distances $a$ and $b$ in Figure 3.8 are the variables referred to in the added mass calculations (see Figure 3.7).

The body ratio, $d/l$, referred to in (3.20) is related to parameter m by

$$\frac{d}{l} = \frac{E(1-m) - mK(1-m)}{E(m) - (1-m)K(m)} \tag{3.21}$$

Comparing this with the second part of (3.19) shows they are the same, considering the identities $E'(m) = E(1-m)$ and $K'(m) = K(1-m)$, so that (3.20) is double (3.19). Since we have verified our derivation with that of an independent theory we shall proceed with our equation for the added mass of the half body as given in (3.19).

## *Comparison of theory*

Now, to be able to compare the analytical theory with the numerical results we have obtained we need to dispose of this parameter $m$. As seen from the previous equations, both the added mass and the body dimension ratio are dependent on the parameter $m$ and this makes direct application of the added mass theory, which needs the depth derivative of $m_a$ also, very cumbersome. We circumvent this problem with help from Mathematica® (see Appendix C).

We then obtain a fitted expression of practical use for the non-dimensional added mass

$$\frac{m_a}{\rho\pi a^2} = M_a = 0.505589 + 0.26405\sqrt{\frac{y}{a}} - 0.0251687\frac{y}{a} + 0.00104839\left(\frac{y}{a}\right)^{\frac{3}{2}} - 0.000014487\left(\frac{y}{a}\right)^2 \tag{3.22}$$

where $b$ has been replaced with the variable $y$ and $a$ is considered constant. (3.22) is a reasonable approximation of the exact value of $m_a$ over the range $0 < \frac{b}{a} < 2$ as can been seen from Graph 3.3.

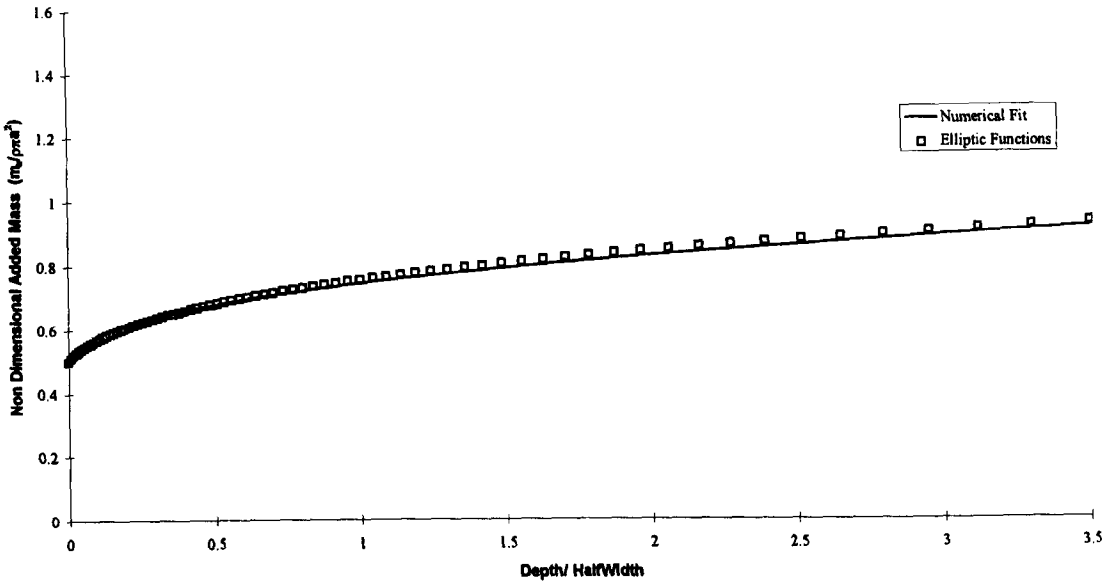


***Graph 3.3*** *Comparison of exact added mass (Elliptic Functions) and approximated added mass (Numerical Fit) for changing box-body cross section*

The derivative with respect to the depth variable is therefore approximated by :

$$\frac{dM_a}{dy} = 0.132025\frac{1}{\sqrt{ay}} - \frac{0.0251687}{a} + \frac{0.001572585}{a}\sqrt{\frac{y}{a}} - 0.000028974\frac{y}{a^2} \tag{3.23}$$

These can be substituted into the added mass force equation

$$F_a = \frac{1}{2}\frac{dm_a}{dy}\dot{y}^2 + m_a\ddot{y}$$

where $y$ is the depth variable.

## Knuckled Body Theory

The previous two sections present theories for the generic geometries of a wedge and a box. Here we look at a more specific "ship-shaped" pentagonal geometry, in accordance with discussions with Lloyds Register.

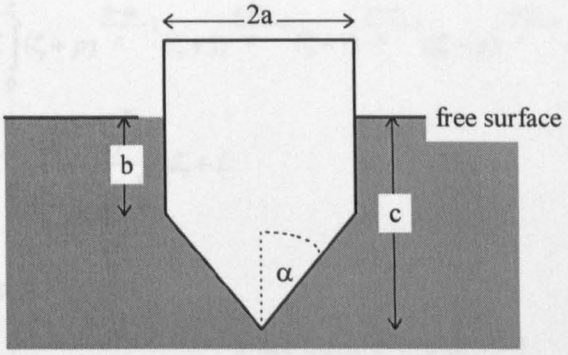


***Figure 3.9*** *Knuckle body in the fluid domain*

Analytically this body has some of the difficulties of both the bodies considered previously, as expected, since the knuckled body can be considered a composite of a box and a wedge. Again we have two singularities one at each knuckle, the flow over the vertex and at the body/free surface intersection points is regular. The problem of the flat bottom no longer arises. We do however have to consider the final calculation of the added mass force in two parts; we need an expression for the added mass of the knuckle body whilst $b > 0$, but once $b = 0$, we need only consider the (already known) added mass of a wedge, since what is above the free surface is of no hydrodynamic consequence. Using the slightly more complicated Schwartz-Christoffel transformation described below we calculate an integral representation of the added mass of this pentagonal body, and evaluate these integrals to obtain equations comparable to the numerical solution.

The body, for the purposes of the Schwartz-Christoffel transformation, is treated as a hexagon (see Figure 3.10) to ensure $\phi = 0$ on the vertical axis represents our approximate free surface. This does not affect the final results but makes analytical progress possible. As in the previous sections we use the Schwartz-Christoffel transformation to map the flow past the half body to that of a uniform flow, the two planes being as follows

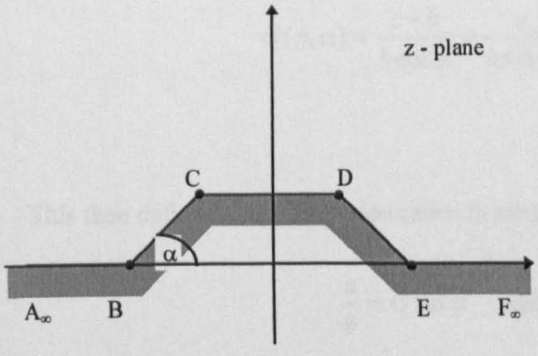


***Figure 3.10*** *Flow past a pentagonal body in the upper half-plane*

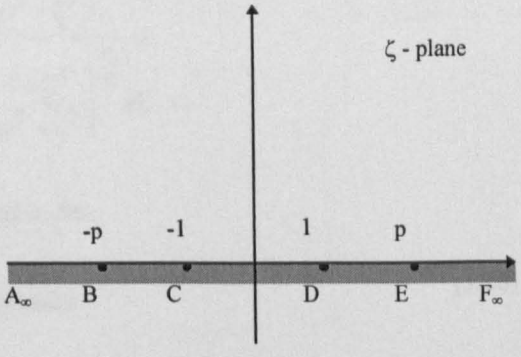


***Figure 3.11*** *Uniform flow in the upper half-plane*

By the standard transformation we can write

$$z = K\int_0^{\zeta}(\zeta+p)^{\frac{\pi-\alpha}{\pi}-1}(\zeta+1)^{\frac{\pi+\alpha}{\pi}-1}(\zeta-1)^{\frac{\pi+\alpha}{\pi}-1}(\zeta-p)^{\frac{-\pi\alpha}{\pi}-1}d\zeta + L$$

$$z = K\int_0^{\zeta}\frac{(\zeta^2-1)^{\frac{\alpha}{\pi}}}{(\zeta^2-p^2)^{\frac{\alpha}{\pi}}}d\zeta + L$$

At $\zeta = 0\ z = ia \Rightarrow L = ia$

At $\zeta = 1\ z = b+ia \Rightarrow K = \dfrac{b}{\int_0^1 \frac{(1-\zeta^2)^{\frac{\alpha}{\pi}}}{(p^2-\zeta^2)^{\frac{\alpha}{\pi}}}d\zeta}$ which is real provided $p > 1$

At $\zeta = p\ z = c \Rightarrow c = K\int_0^{p}\frac{(\zeta^2-1)^{\frac{\alpha}{\pi}}}{(\zeta^2-p^2)^{\frac{\alpha}{\pi}}}d\zeta + ia$

$$c = b + ia + K\int_1^{p}\frac{(\zeta^2-1)^{\frac{\alpha}{\pi}}}{(p^2-\zeta^2)^{\frac{\alpha}{\pi}}}e^{-i\alpha}d\zeta$$

So taking the real and imaginary parts of the above we have

$$K\int_1^{p}\left(\frac{\zeta^2-1}{p^2-\zeta^2}\right)^{\frac{\alpha}{\pi}}d\zeta = \frac{c-b}{\cos\alpha} = \frac{a}{\sin\alpha} \tag{3.24}$$

The above can also be expressed as a ratio, G(p,α), as follows

$$G(p,\alpha) = \frac{c-b}{b\cos\alpha} = \frac{a}{b\sin\alpha} = \frac{\int_1^{p}\left(\frac{\zeta^2-1}{p^2-\zeta^2}\right)^{\frac{\alpha}{\pi}}d\zeta}{\int_0^{1}\left(\frac{1-\zeta^2}{p^2-\zeta^2}\right)^{\frac{\alpha}{\pi}}d\zeta} \tag{3.25}$$

This then defines body dimension ratios in terms of p and α. So

$$\frac{a}{b} = G\sin\alpha \quad \text{and} \quad \frac{c}{b} = G\cos\alpha \tag{3.26}$$

Note the similarities between the above derivation and that shown in the previous section.

Now we can state that,

$$z = K\int_p^{\zeta}\left(\frac{\zeta^2-1}{\zeta^2-p^2}\right)^{\frac{\alpha}{\pi}}d\zeta + ia + c - ia$$

This can be expanded into

$$\left(\frac{\zeta^2-1}{\zeta^2-p^2}\right)^{\frac{\alpha}{\pi}}=\left(1-\frac{1}{\zeta^2}\right)^{\frac{\alpha}{\pi}}\left(1-\frac{p^2}{\zeta^2}\right)^{\frac{-\alpha}{\pi}}=\left(1-\frac{\alpha}{\pi}\frac{1}{\zeta^2}+\ldots\right)\left(1+\frac{\alpha}{\pi}\frac{p^2}{\zeta^2}+\ldots\right)$$

Thus

$$z=K\int_p^{\zeta}1+\frac{\alpha}{\pi}\frac{1}{\zeta^2}(p^2-1)+\ldots d\zeta+c \tag{3.27}$$

Integrating (3.27) gives

$$z\approx K\zeta-K\frac{\alpha}{\pi}(p^2-1)\frac{1}{\zeta}+\ldots+\text{constant term}$$

Reverting the above to obtain

$$\zeta=\frac{z}{K}+\frac{A}{z}+\ldots=\zeta-\frac{\alpha}{\pi}(p^2-1)\frac{1}{\zeta}+\frac{A}{K\zeta}+\ldots$$

$$\Rightarrow A=\frac{\alpha}{\pi}(p^2-1)K$$

$$\Rightarrow\zeta=\frac{z}{K}+\frac{\alpha}{\pi}(p^2-1)\frac{K}{z}+\ldots$$

We require $\beta(z)\to z$ as $z\to\infty$ for unit velocity at $\infty$.

$\Rightarrow\beta(\zeta)\to K\zeta$ as $\zeta\to\infty$

Hence we have

$$\beta(z)\approx z+\frac{\alpha}{\pi}(p^2-1)\frac{K^2}{z}+\ldots \tag{3.28}$$

Where the $1/z$ term in (3.28) is known as the dipole. From the dipole coefficient we can again derive the added mass. Consider the double body in a flow as pictured in Figure 3.12

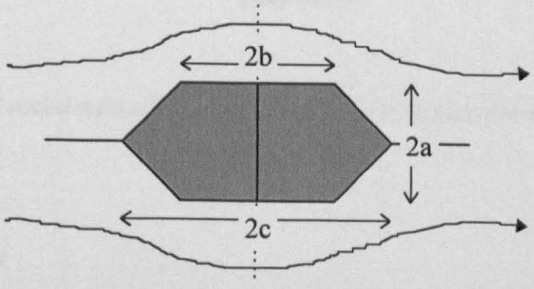


***Figure 3.12*** *Flow past the double body*

Then the added mass can be stated as

$$\left(\forall_T + \frac{m_{aT}}{\rho}\right) = 2\pi\frac{\alpha}{\pi}(p^2 - 1)K^2 \tag{3.29}$$

where $\forall_T = 2a(b+c)$ and $T$ denotes total body flow.

We require the flow around the half body, so set $\forall = a(b+c)$ and we have

$$m_a = \frac{1}{2}\rho\left\{2\alpha(p^2 - 1)K^2 - 2a(b+c)\right\}$$

Non-dimensionalised this becomes

$$\frac{m_a}{\rho\pi a^2} = \frac{\alpha}{\pi}(p^2 - 1)\frac{K^2}{a^2} - \frac{(b+c)}{\pi a} \tag{3.30}$$

A graph of (3.30) plotted against the non-dimensional depth is given in Graph 3.4. You may note that if $\alpha = \pi/2$ in (3.30) then $b$=$c$ and we have the added mass for a box body, as derived in the previous section.

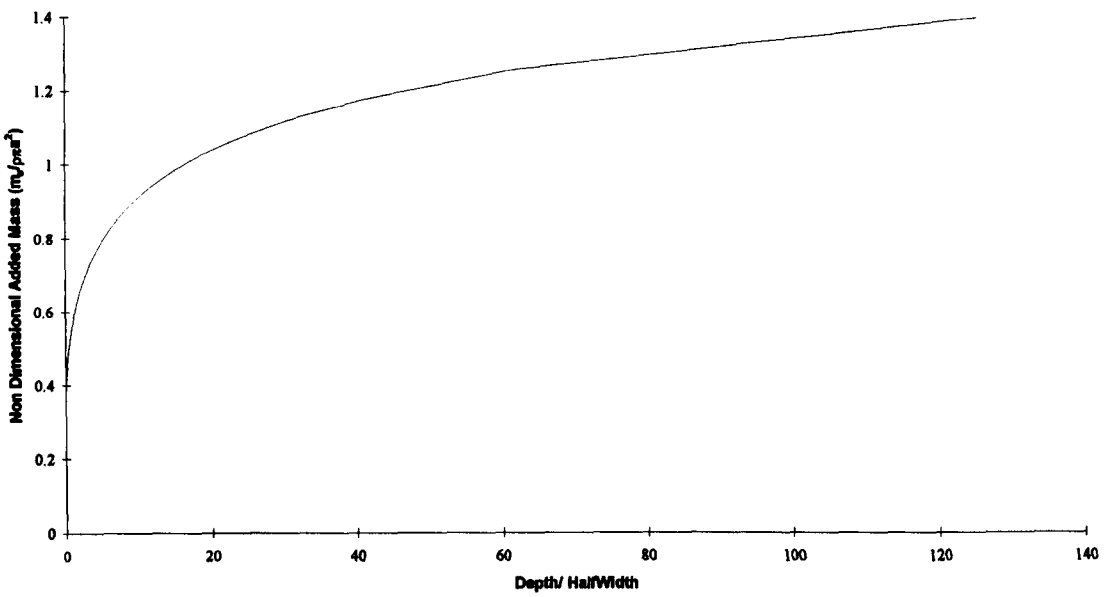


***Graph 3.4*** *Non-dimensional added mass against non-dimensional body ratio for a knuckled body cross section with $\alpha = \pi/4$.*

## *Comparison of theory*

As we noted in the previous section, to be able to compare the analytical theory with the numerical results we must dispose of the parameter, in this case $p$, in the added mass equation. We do this using Mathematica® as explained in Appendix C.

We require an expression dependent on body dimensions as in the previous sections however, here we have three variables $b$, $a$ and $\alpha$. To facilitate a numerical fit we fix $\alpha = \pi/4$, an angle representative of a ship like cross-section. So we get an expression for the added mass that is purely dependent on the body dimensions

$$\frac{m_a}{\rho\pi a^2} = 0.337702 + 0.040939\frac{y}{a} - 0.0148583\left(\frac{y}{a}\right)^2 + 0.207481\sqrt{\frac{y}{a}} - 0.00500196\ln\left(\frac{y\sqrt{2}}{a}\right) \tag{3.31}$$

where depth $b$ has been replaced by the depth variable $y$, and $a$ is treated as constant.

If we inspect the graph of this against a non-dimensional body ratio $b/a$, Graph 3.5.

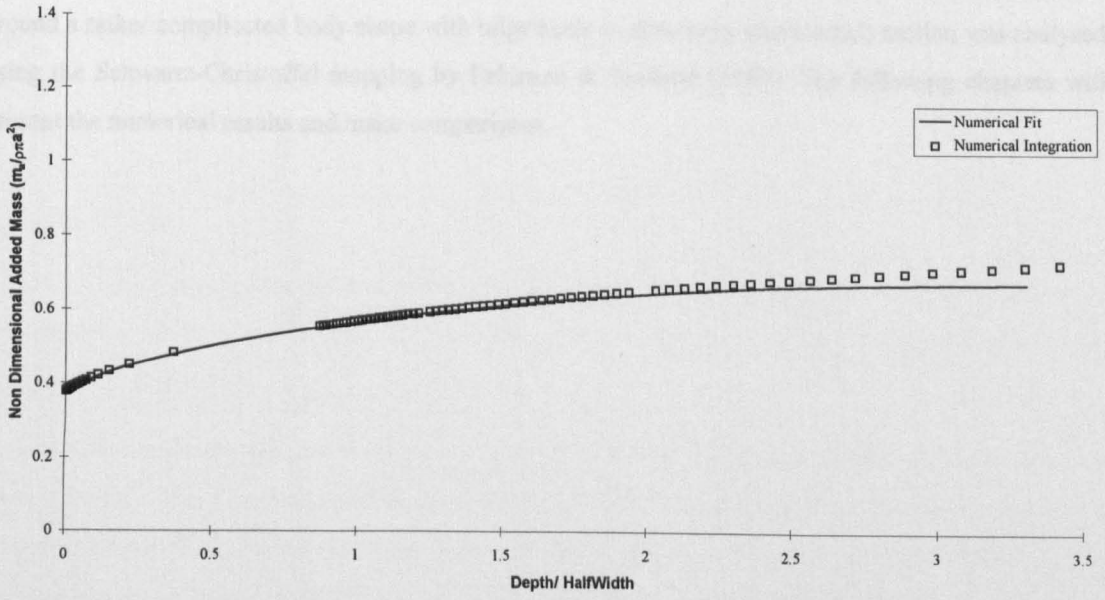


***Graph 3.5*** *Comparison of exact non-dimensional added mass (Numerical Integration) and approximated added mass (Numerical Fit) for a knuckled body cross section with $\alpha=\pi/4$*

The sparsity of points in Graph 3.5 between 0.5 and 1 is a result of the step size used in Mathematica®. Two separate calculations have been performed to produce the results (0 to 1 and 1 upwards) to achieve a denser plot in the 0.5 to 1 range would involve producing a calculation of over 10,000 steps. This is possible but the trend is perfectly apparent without going to such lengths precision.

Note that non-dimensional added mass when $b$=0 is equivalent to that of the wedge when $\alpha$=45, i.e. the knuckled body becomes a wedge when $b$=0.

We also find the derivative of the added mass with respect to $y$

$$\frac{dM_a}{dy} = \frac{0.040939}{a} - 0.0297166\frac{y}{a^2} - \frac{0.103741}{\sqrt{ay}} - 0.00500196\frac{\sqrt{2}}{y} \tag{3.32}$$

These can be substituted into the equation for the added mass force

$$F_a = \frac{1}{2}\frac{dm_a}{dy}\dot{y}^2 + m_a\ddot{y}$$

producing an equation that is comparable to the numerical data.

## Conclusion

We now have the analytic theory for each body shape in a suitable form for comparison with the numerical results obtained from the solution described in Chapter 2. It is worth noting that the method can be extended to even more complicated body shapes. Indeed the vortex shedding flow around a rather complicated body shape with bilge keels in slow sway (horizontal) motion was analysed using the Schwartz-Christoffel mapping by Faltinsen & Sortland (1987). The following chapters will present the numerical results and make comparisons.

# Chapter 4 Body Exit from Initially Calm Water

## *A comparison of numerical and analytic theories used to calculate the forces experienced by a body leaving the fluid domain*


### Abstract

This chapter reviews the application of two non-linear theories, analytical and numerical, to the problem of a body exiting the fluid domain. The objective of this work is to appraise the analytical model and suggest modifications that would allow better approximation of the non-linear method for use in practical calculations such as extreme ship motions and slamming. Presented are the numerical results for constant velocity, and constant acceleration, exit of bodies from the fluid domain. From these results conclusions are drawn, indicating the limitations of the current analytical theory and the future direction of this research. The bodies we consider are those of a wedge, a box and a knuckle (inverted pentagon).


### Introduction

This chapter is concerned with obtaining and comparing data from a full non-linear solution of the body-exit problem and an analytical solution of the same problem. The main priority will be the forces acting on the body.

As the body leaves the fluid domain it experiences hydrostatic and hydrodynamic pressures upon its wetted surface. These are integrated to give hydrostatic and hydrodynamic forces which are due to the interaction with the fluid particles and their subsequent acceleration. The analytical theory is also implemented in an attempt to produce a practical method of calculation, and the two sets of force results are compared. The motivation is to present a simpler theory that is able to calculate the forces experienced by the body without the need for extensive numerical calculations, and which could be included in strip theory codes dealing with large-amplitude (slamming) calculations.

In the following sections we consider the body exiting the fluid at both constant acceleration and constant velocity. For each we examine all body shapes (wedge, box and knuckle) for a variety of initial conditions. Where possible we use comparable initial conditions to allow for comparison between these body shapes.

For each case considered we present four graphs:

1. A comparison of the total vertical force experienced by the body and the buoyancy force. The vertical force is calculated using the fully non-linear numerical method. The buoyancy force is calculated using $\rho g \forall$ where $\forall$ is the time-dependent volume of the body below the initial free surface.

2. We consider the added mass force, $F_a$, and compare it with the difference between the total vertical force and the buoyancy force as considered in the first graph. The intention is to examine whether the added mass force and the buoyancy force together account for the total force given by the fully non-linear calculation.

3. The pressure distribution across the wetted surface of the body as a time-stepped progression. The previous graphs displays the total force acting upon the body, whereas the pressure distribution are presented to illustrate how these forces arise. Each graph contains several time intervals taken over the course of the body motion.

4. The free-surface profiles given at the time intervals used in the pressure distribution.

All graphs are non-dimensional, this is done in the following manner:

- Time - multiplied by $\sqrt{\frac{g}{d_e}}$ where $d_e$ is the draft at equilibrium and g is gravity.
- x and y co-ordinates - divided by $d_e$ .
- Force - divided by the buoyancy force given by $\rho g \forall$ where $\forall$ is the submerged volume at equilibrium.
- Pressure - divided by $d_e \rho g$ .

One of the following parameterises the problem :

- Acceleration - divided by $g$, in the constant acceleration case.
- The Froude number is defined as $\frac{v}{\sqrt{gd_e}}$, where $v$ is the velocity in the constant velocity case.

## Constant acceleration

The following section gives the results produced for constant acceleration of a body from the fluid domain. We consider constant acceleration as a simplification of free motion. Setting acceleration to be constant allows easy comparison of these results with values calculated using the analytical method.

For each body shape we consider constant accelerated exit at $g/5$ and $g/2$.

Tables containing the example numerical results can be found in Appendix A.

## *Wedge*

The first case under consideration is that of constant acceleration at $g/5$ of a wedge with a half angle of 45 degrees, height of 1.7 and an initial vertex depth of -1.67 (where the minus sign indicates below the free surface).

Examining Graph 4.1 we note the curves have similar gradients, until we reach the "blip" around a time of 2.7. As the body exits the fluid so the number of points on the body reduces, when more than one point (actually two, one from either side) is removed due to a large draw-down, or poor discretisation, a small error occurs. The reduction in points on the body is matched by a reduction in the size of the calculation matrix, this in turn results in a blip in the numerical results. A few time steps later we see that the blip has disappeared and the numerics settle down again, producing physically reasonable results.

In Graph 4.2 we see the analytical theory accounts for, at least, the initial difference between the two forces presented in Graph 4.1 as expected since both numerical and analytical theories solve the same boundary value problem initially i.e. a double-body reflection in a line of equipotential. As we progress along the time axis, the two curves become more disparate. This is one of the limitations of the analytical theory. If we again consider the free surface profile, Graph 4.4, we note the movement of the surface near the body is rapid. As we progress in time, so the surface draws down the body. Now the added-mass theory is calculated on the assumption of a fixed free-surface of zero potential (i.e. at the x-axis in Graph 4.4), and so neglects the draw-down. As one can see, at times this will be considerable approximation. Similarly, the buoyancy is calculated using the depth below the initial free-surface (effectively the fixed free-surface of zero potential) and so this force is also compromised by the draw-down. A further analysis of this effect will be given in Chapter 6.

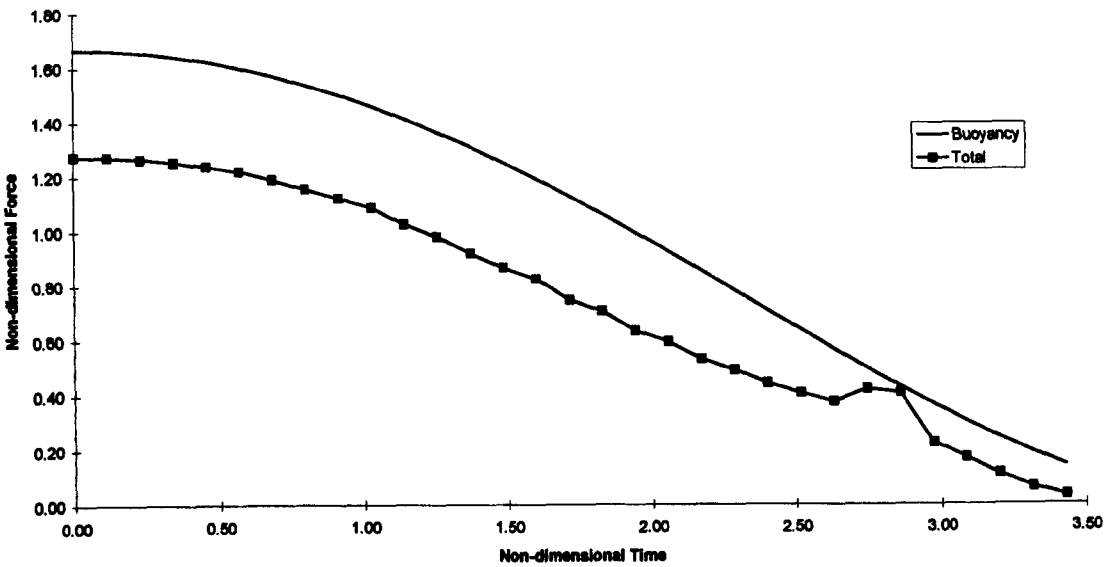


*Graph 4.1 Comparison of total force and buoyancy force for an exiting wedge ($\alpha=\pi/4$, $a/g=0.2$)*

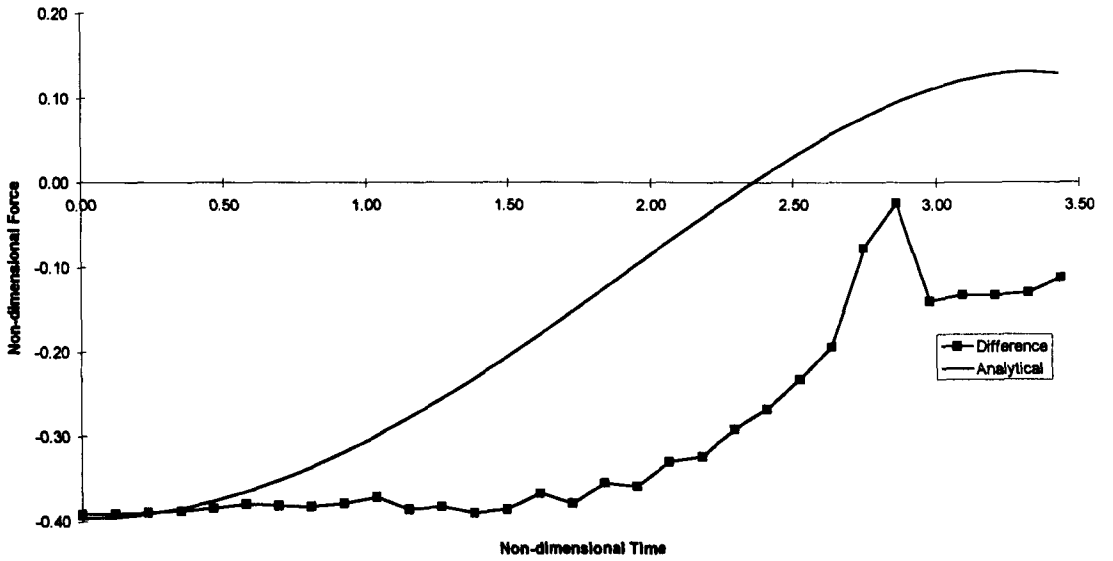


*Graph 4.2 Comparison of analytical added mass and force difference for an exiting wedge ($\alpha=\pi/4$, $a/g=0.2$)*

In Graph 4.3 you will see negative pressures arising near the final steps (i, j and k). This can be attributed to the jet formation shown in Graph 4.4, similar negative pressure effects are noticed in runs with the free surface discretised more finely, see also Greenhow (1987) for the entry case. In Graph 4.4 we have artificially held the jet onto the body by keeping the intersection point in contact with the body by means of implementing the body boundary condition $\frac{\partial \phi}{\partial n} = v_n$. More physically the jet would fall away from the body under the effect of gravity, the particles moving as free projectiles since within the jet the pressure and pressure gradients are small. Therefore, the negative pressures do not arise from numerical inaccuracy but rather from an inappropriate use of the body boundary condition in the jet region.

Graph 4.4 gives the free-surface profiles for the time steps displayed in Graph 4.3. Note the negative pressures correspond with the jet moving up the body. The non-dimensional times for these graphs are given in the following table

| Label | a | b | c | d | e | f | g | h | i | j | k |
|---|---|---|---|---|---|---|---|---|---|---|---|
| Time | 0 | 0.34 | 0.69 | 1.03 | 1.37 | 1.72 | 2.06 | 2.40 | 2.74 | 3.09 | 3.43 |

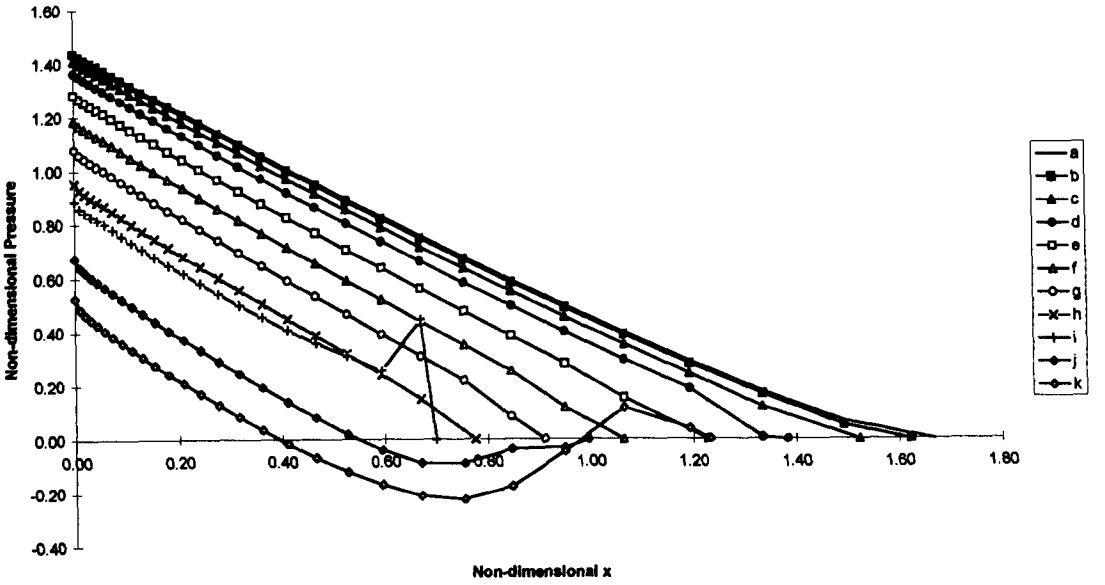


*Graph 4.3 Non-dimensional pressure on half wetted surface of exiting wedge ($\alpha=\pi/4$, $a/g=0.2$)*

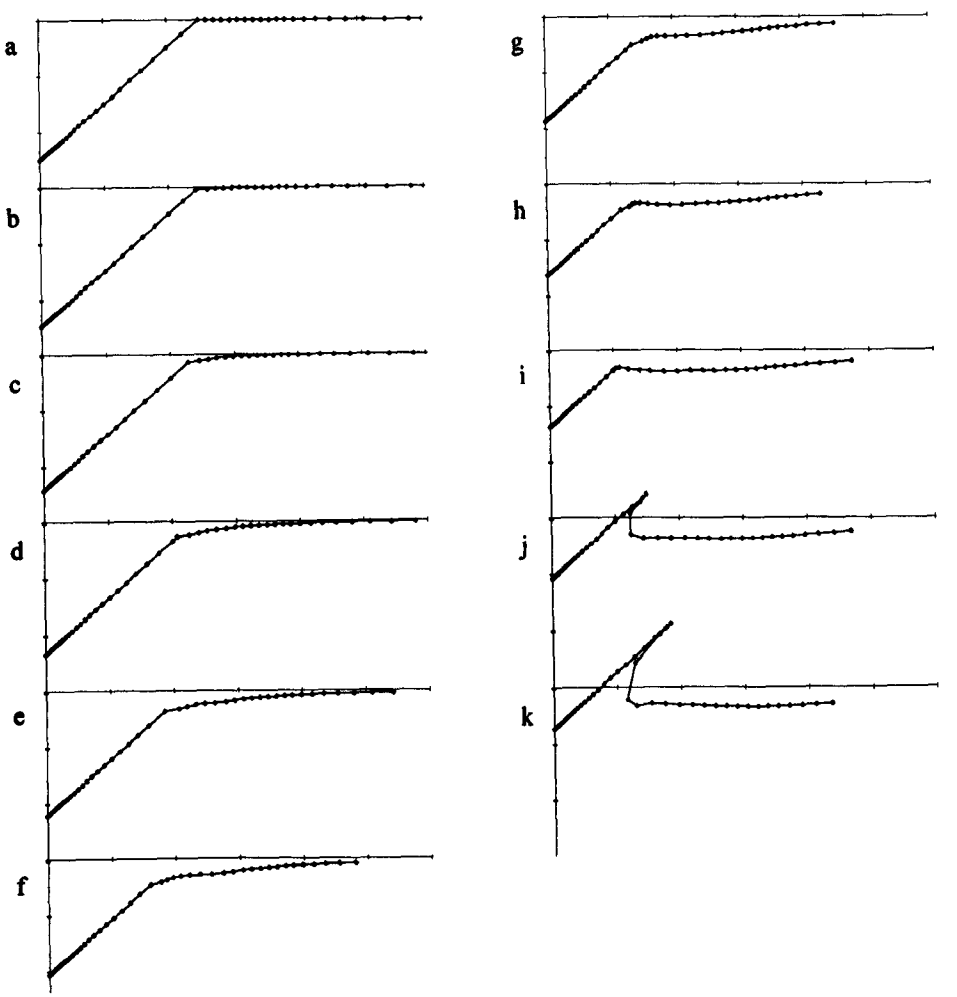


*Graph 4.4 Free surface profile of exiting wedge ($\alpha=\pi/4$, $a/g=0.2$)*

We now consider the same body exiting the fluid at the higher constant acceleration of $g/2$.

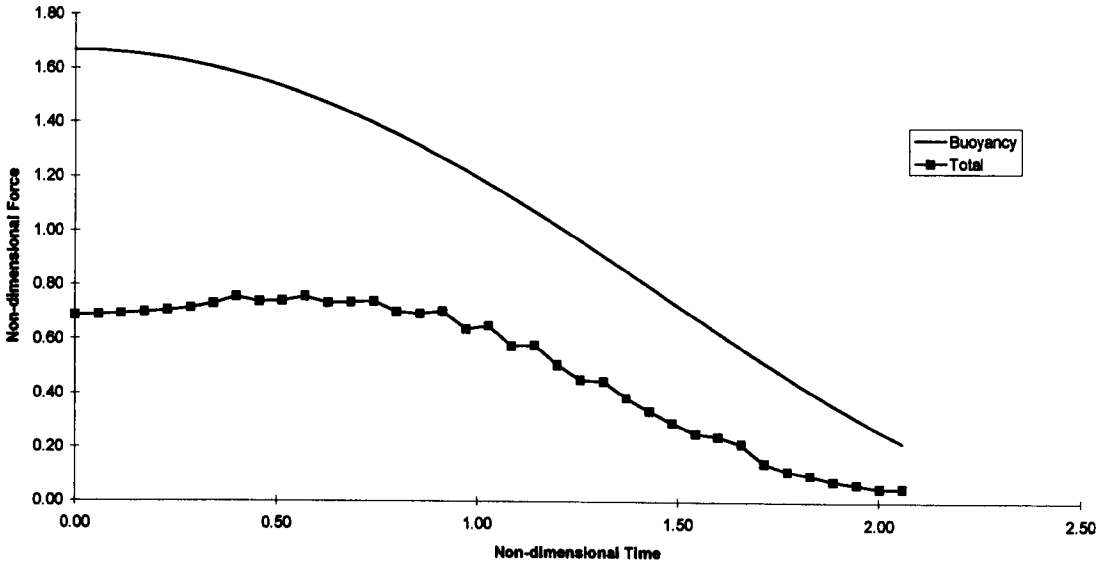


*Graph 4.5 Comparison of total force and buoyancy force of exiting wedge ($\alpha=\pi/4$, $a/g=0.5$)*

The first feature to notice about Graph 4.5 is the greater disparity between the buoyancy force and the total force at time 0, the total force is less than that in the $g/5$ case. So the added-mass component must be considerably larger in this case, which we expect since the acceleration is larger, this is demonstrated explicitly in Graph 4.6.

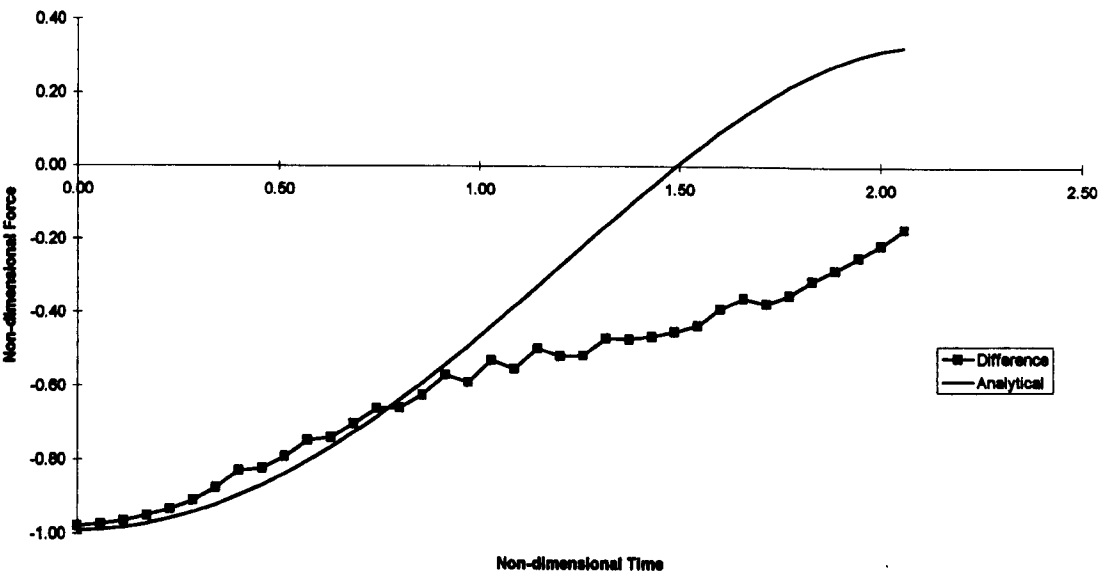


*Graph 4.6 Comparison of analytical added mass and force difference for an exiting wedge ($\alpha=\pi/4$, $a/g=0.5$)*

Here we have agreement between the two theories for a longer period of time. Let us examine the free-surface profiles to see if we can account for this improvement. Looking at Graph 4.8 we see the draw-

down is as severe as that in the $g/5$ case. We conclude that at higher accelerations the added-mass force more accurately approximates the force difference. We attribute this to the relatively smaller contribution from the velocity term which the analytical theory does not predict so well.

| Label | a | b | c | d | e | f | g | h | i | j |
|---|---|---|---|---|---|---|---|---|---|---|
| Time | 0 | 0.23 | 0.46 | 0.69 | 0.91 | 1.14 | 1.37 | 1.60 | 1.83 | 2.06 |

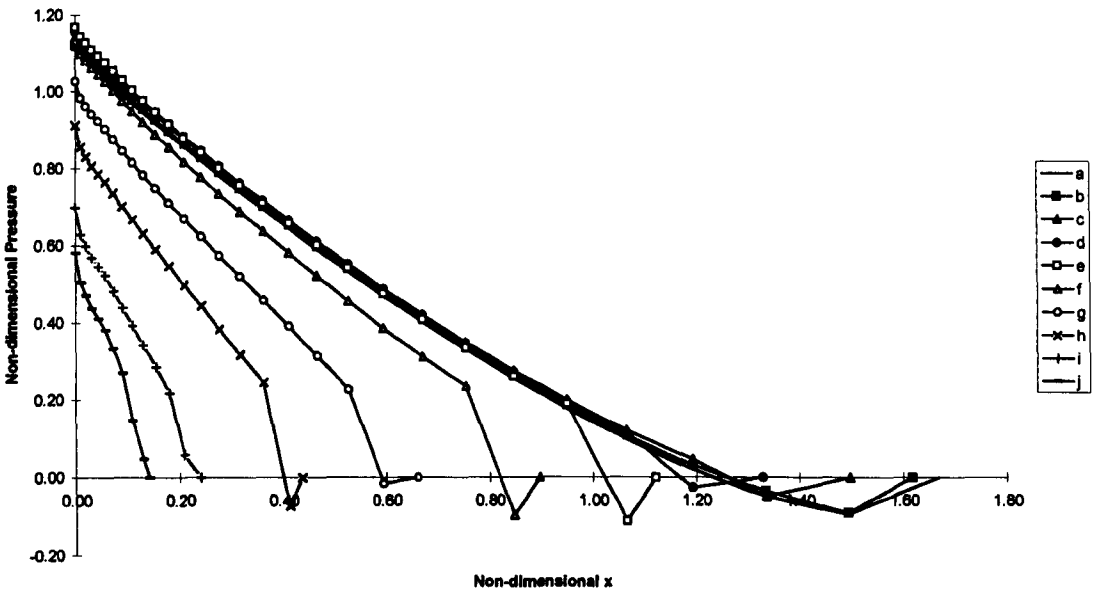


*Graph 4.7 Non-dimensional pressure on half wetted surface of exiting wedge ($\alpha=\pi/4$, $a/g=0.5$)*

This pressure distribution indicates that the penultimate body point (the point before the body/surface interface) has almost continuous negative pressure, a situation normally attributed to jet development. However, the free-surface profiles Graph 4.8, show the negative pressures must be a result of poor numerical discretisation of the very rapid draw down of the free surface near the intersection point, which the numerics are unable to follow accurately enough. In effect, the wetted surface of the wedge is not accurately predicted here, but the pressures and pressure gradient along the wedge surface are both low, so that the force calculations are not significantly affected. The situation is, in fact, rather similar to that of entry, where accurate jet calculation is not needed for force calculations - indeed the calculation of Zhao & Faltinsen (1993) completely removes the jets.

It is also possible that for low enough deadrise angles and high enough velocities, the pressure may actually invert across the free surface, as in the cylinder calculations of Greenhow & Moyo (1997). Since there are significant numerical problems in determining when this happens (the local flow is quite sensitive to discretisation of the draw-down region), an analytical study would be very desirable here. However, as outlined in the introduction, no such theories appear to be available at present.

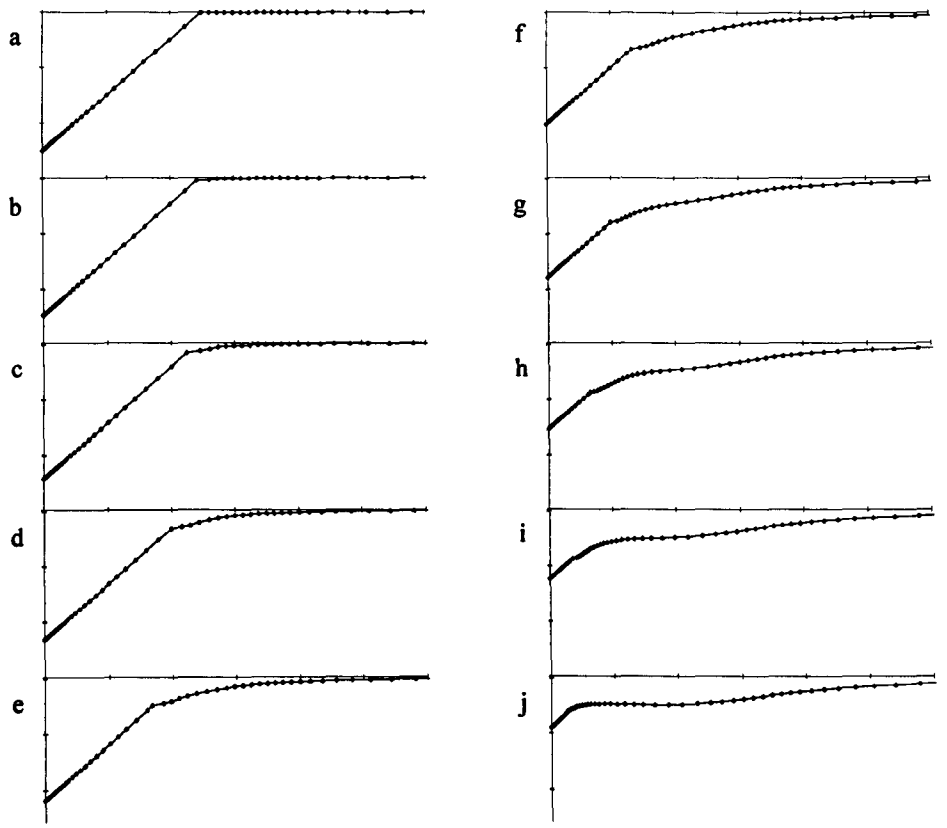


*Graph 4.8 Free-surface profile of exiting wedge ($\alpha=\pi/4$, $a/g=0.5$)*

## *Box*

We now consider a box body of height 1.7, width 2 and an initial depth of -1.63 exiting the fluid domain at a constant acceleration of $g/5$.

Studying Graph 4.9 and Graph 4.10 together we see that the buoyancy and total force have a virtually constant difference (varying by 0.05). The added mass force accounts for this difference well for early times. As we approach complete exit the two curves in Graph 4.10 diverge in opposite directions. Again we can qualify this from the draw-down. As the draw-down increases so the buoyancy force overestimates the actual buoyancy contribution, thus increasing the force difference. This gives the difference curve in Graph 4.10 a negative gradient when in fact it should be positive.

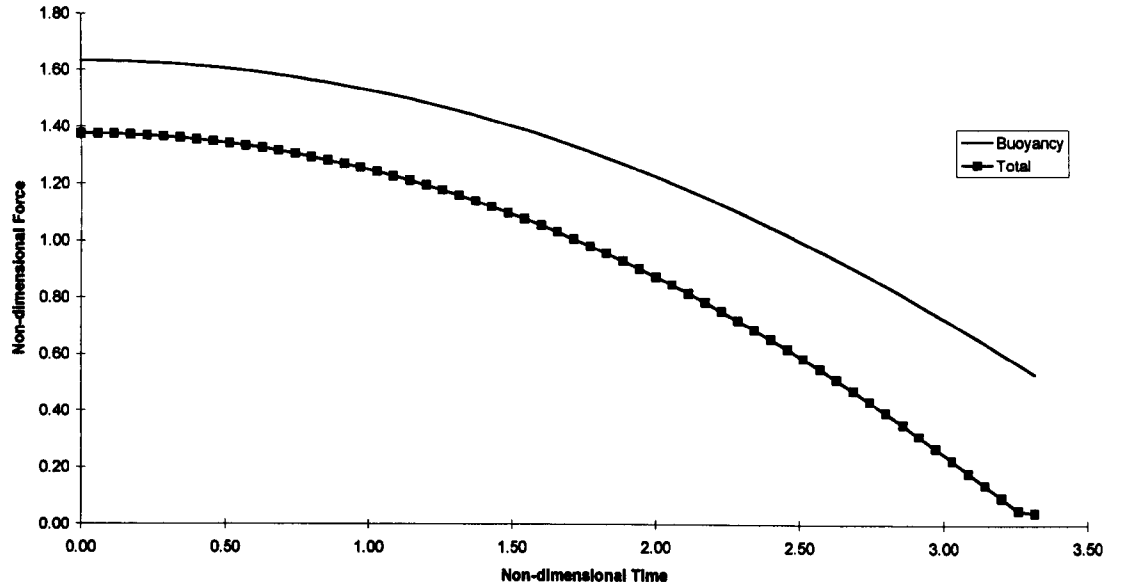


*Graph 4.9 Comparison of total force and buoyancy force for an exiting box (a/g=0.2)*

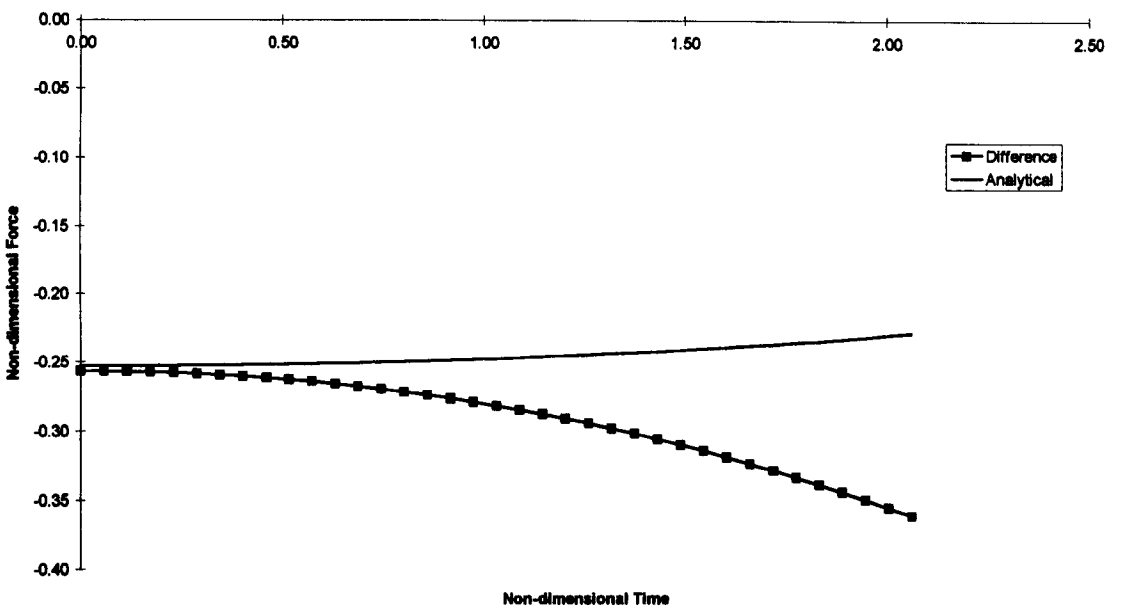


*Graph 4.10 Comparison of analytical added mass and force difference for an exiting box (a/g=0.2)*

Now let us study the pressure distribution. We note the x-axis represents the distance around the body from the keel, that is we measure the perimeter distance from the bottom centre around to the point in question.

First we note the lower pressure trend around 1.00. The first point to drop in pressure is the point before the body corner, the seventh point from the y-axis in Graph 4.12. This is caused by a singularity at the corner. This can be demonstrated as follows.

Consider the mapping $\zeta = z^{2/3}$ the mapped plane would be $\beta(\zeta) = U\zeta$, graphically that is

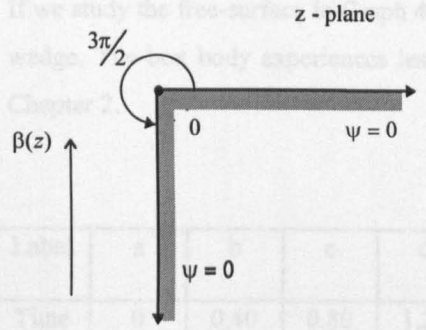


***Figure 4.1*** *Flow past a corner*

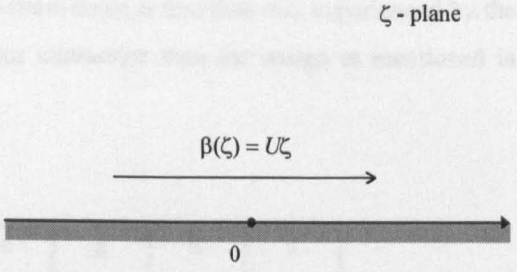


***Figure 4.2*** *Uniform flow in the upper half-plane*

So $\beta(z) = Uz^{2/3}$ which has $\psi = 0$ on $\theta = 0$ and $\psi = 0$ on $\theta = 3\pi/2$ as required.

Note that this flow is only valid locally since $\beta(z) \to \infty$ as $|z| \to \infty$.

Furthermore since

$\beta(z) \sim O(z^{2/3})$ then

$$\frac{d\beta(z)}{dz} \sim O(z^{-1/3}) \Rightarrow v = \overline{\frac{d\beta(z)}{dz}} \sim O(z^{-1/3})$$

So complex velocity is singular.

Though the corner is a singularity we may still calculate forces on the body at this point. Since pressure in steady flow is from the $v^2$ terms in Bernoulli's equation we can deduce $P \sim O(z^{-2/3})$ which is singular.

However, we can still integrate to give a finite force by considering an element between the origin and $z_0$

$$F = \int_0^{z_0} P dz \sim \int_0^{z_0} z^{-2/3} dz \sim O(z_0^{1/3}) \text{ which is finite.}$$

In reality we would get vortex shedding from these corners. The effect of this can be seen on Graph 4.11. At the corner the numerical scheme has attempted to calculate the pressure at the singularity, the curves should actually approach the line keel distance=1 asymptotically. Therefore at the corner we must expect the numerical pressure results, which are based on an inviscid model, to be completely in error. We have clustered the points here to pick up the singular behaviour near the corner correctly, and to highlight this problem with the inviscid formulation. However, the force results, for such sensible body discretisation, may not be particularly sensitive to this very localised error and remain realistic; the difference at $t = 0$ in Graph 4.10 quantifies this error as small for this case (approximately 0.5% of the total body force, 2-3% of the force difference).

If we study the free-surface in Graph 4.12 we notice the draw-down is less than that experienced by the wedge. The box body experiences less local free-surface interaction than the wedge as mentioned in Chapter 2.

| Label | a | b | c | d | e | f | g | h | i |
|---|---|---|---|---|---|---|---|---|---|
| Time | 0 | 0.40 | 0.80 | 1.20 | 1.60 | 2.00 | 2.40 | 2.80 | 3.20 |

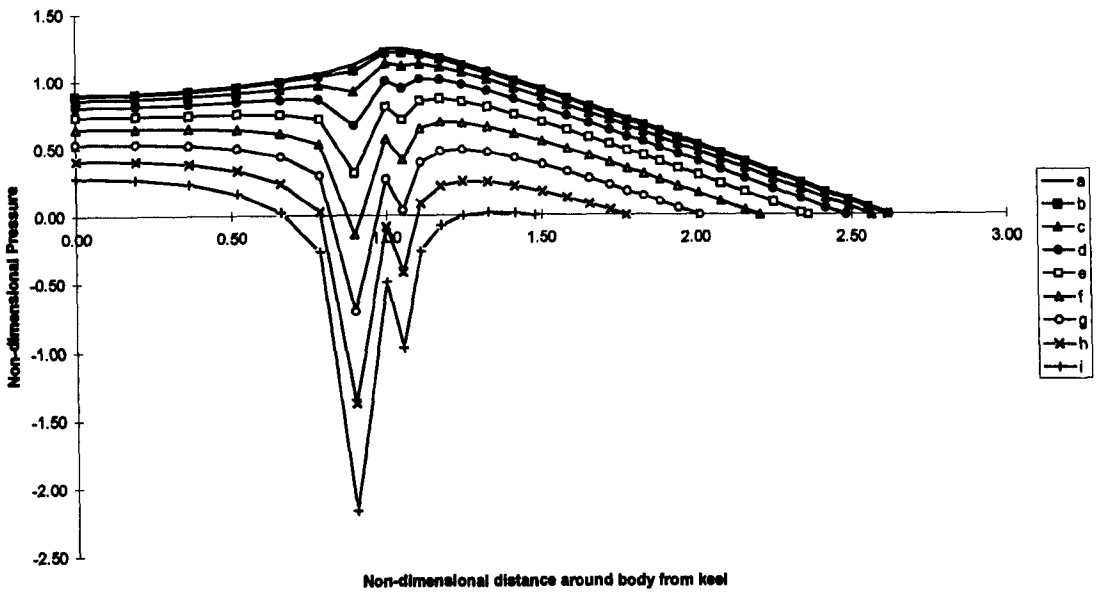


*Graph 4.11 Non-dimensional pressure on half wetted surface of exiting box (a/g=0.2)*

The clustering of points near the corners of the body required to reduce the force error incurred by the presence of a singularity can be seen in Graph 4.12. The points are distributed on the vertical body boundary such that they cluster around the corners and at the boundary midpoint, the latter being implemented for the transient motion case.

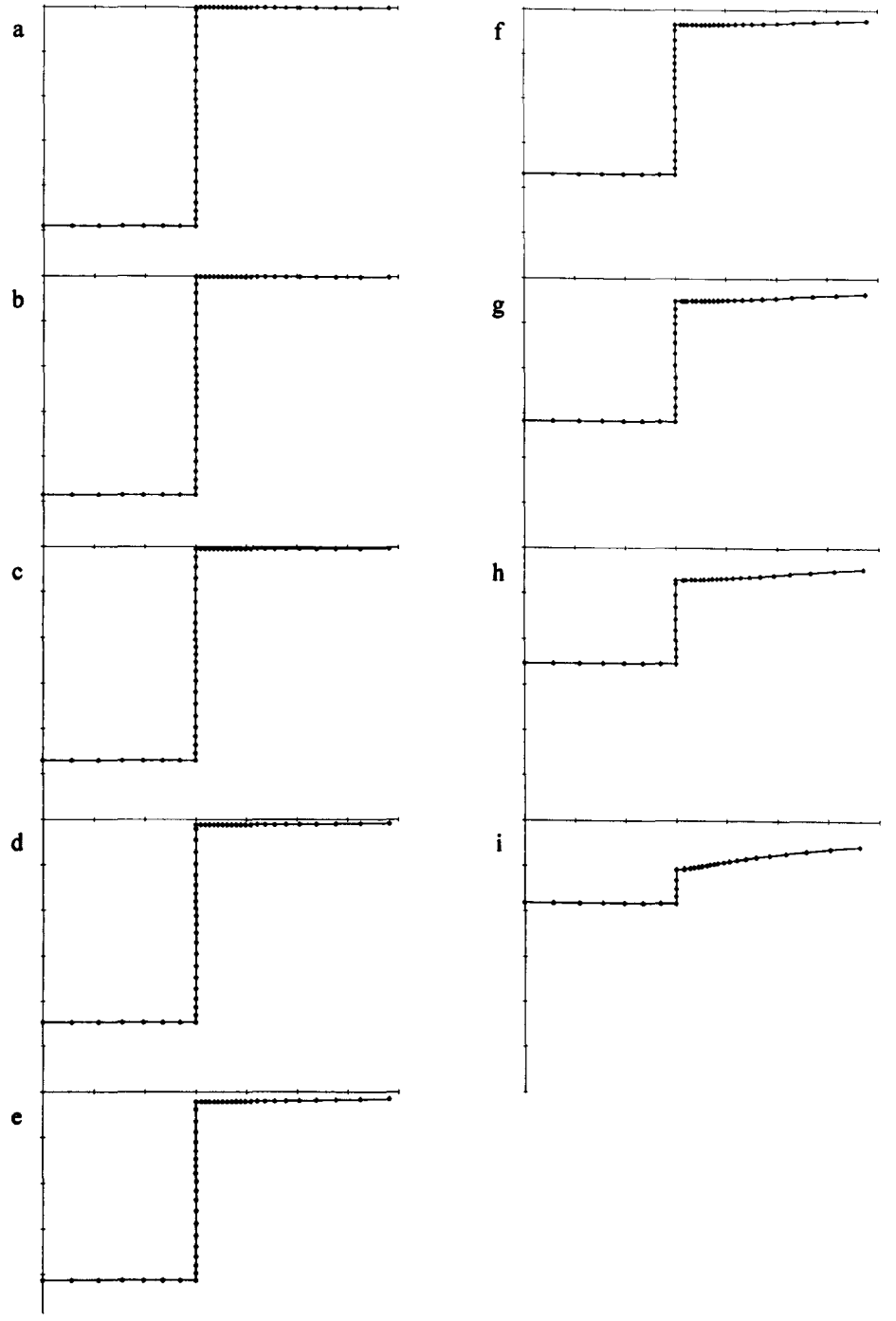


*Graph 4.12 Free-surface profile of exiting box (a/g=0.2)*

Let us consider the same body, this time accelerated at $g/2$. Again the first thing we note is the reduced force due to the high acceleration. Also for the first time we get negative forces near the end of the motion, as can be seen in Graph 4.13. The difference in the gradients of the curves in Graph 4.14 can again be accounted for by the draw-down effect.

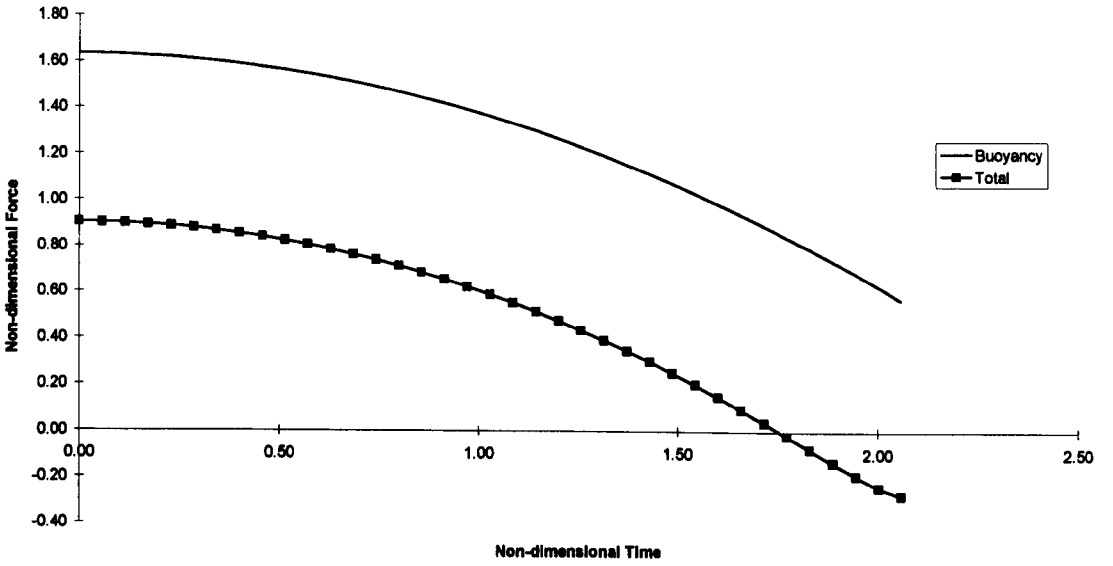


*Graph 4.13 Comparison of total force and buoyancy force for an exiting box (a/g=0.5)*

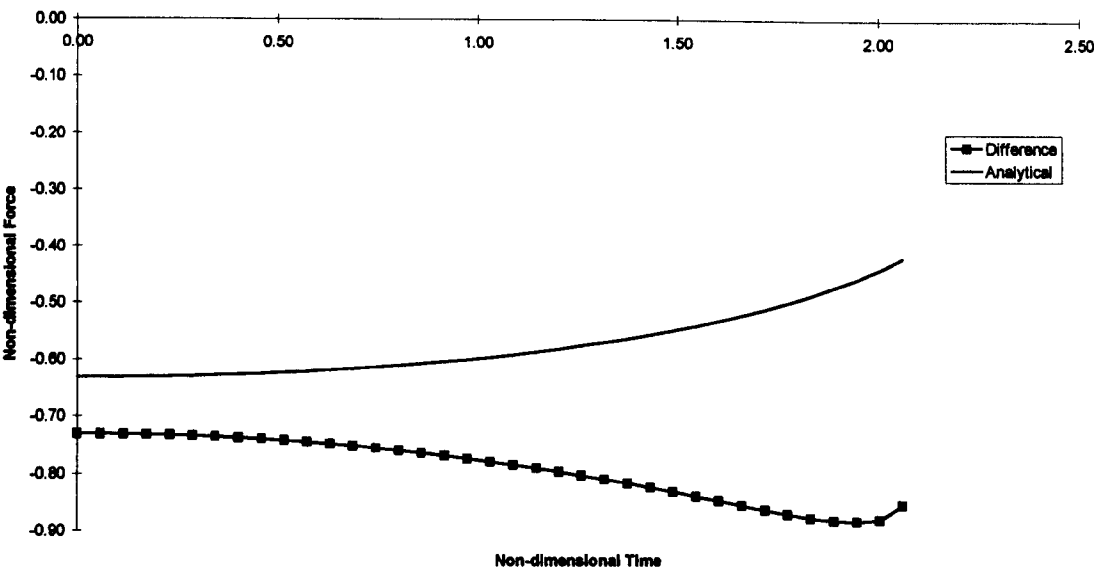


*Graph 4.14 Comparison of analytical added mass and numerical difference for an exiting box (a/g=0.5)*

The discrepancy between the added mass force and the difference force at t=0 is a result of the error in the flow pressure at the body corner. Considering the pressure distribution, Graph 4.15, we see the pressure change near the corner is more noticeable. Although the positive pressures are less than those of the $g/5$ example the negative pressures are larger, this is due to numerical error when the model attempts to resolve the singular pressure on the corner. If we consider the free-surface profile, Graph 4.17, we notice that clustering occurs in the free-surface points on the last three graphs (g, h and i). The negative pressures and forces are correct as far as the model is concerned. However, in reality the inviscid model is invalid since strong vortices will be shed from the sharp corners when the flow starts to move around them. Given this it is pointless to resolve the inviscid flow more accurately, we use the

later stages of the results purely as a comparison with the knuckle body (which also suffers from the same problems although the singularity is not as strong).

| Label | a | b | c | d | e | f | g | h | i |
|---|---|---|---|---|---|---|---|---|---|
| Time | 0 | 0.23 | 0.46 | 0.69 | 0.91 | 1.14 | 1.37 | 1.60 | 1.83 |

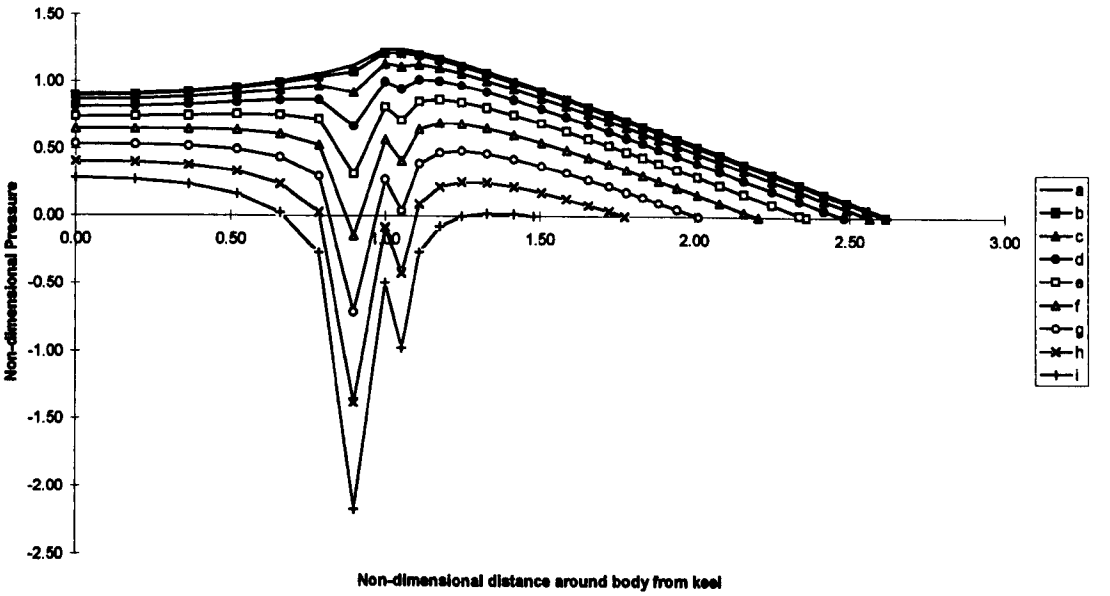


*Graph 4.15 Non-dimensional pressure on half wetted surface of exiting box (a/g=0.5)*

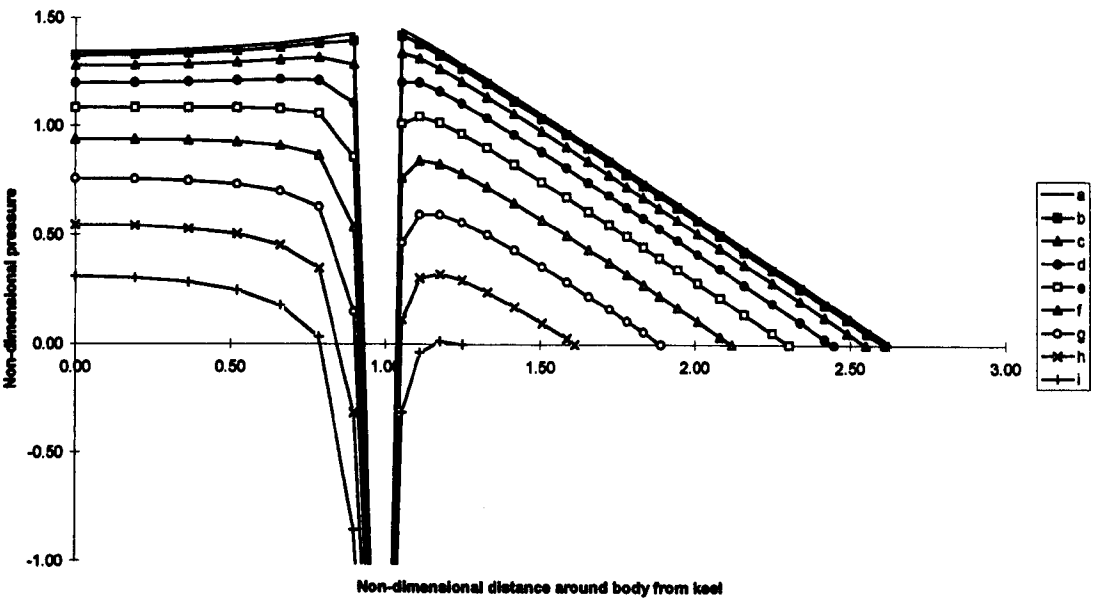


*Graph 4.16 Non-dimensional pressure, including singularity, on half wetted surface of exiting box (a/g=0.5)*

In Graph 4.16 we demonstrate how the pressure curve looks schematically taking the pressure singularity at the corner into account.

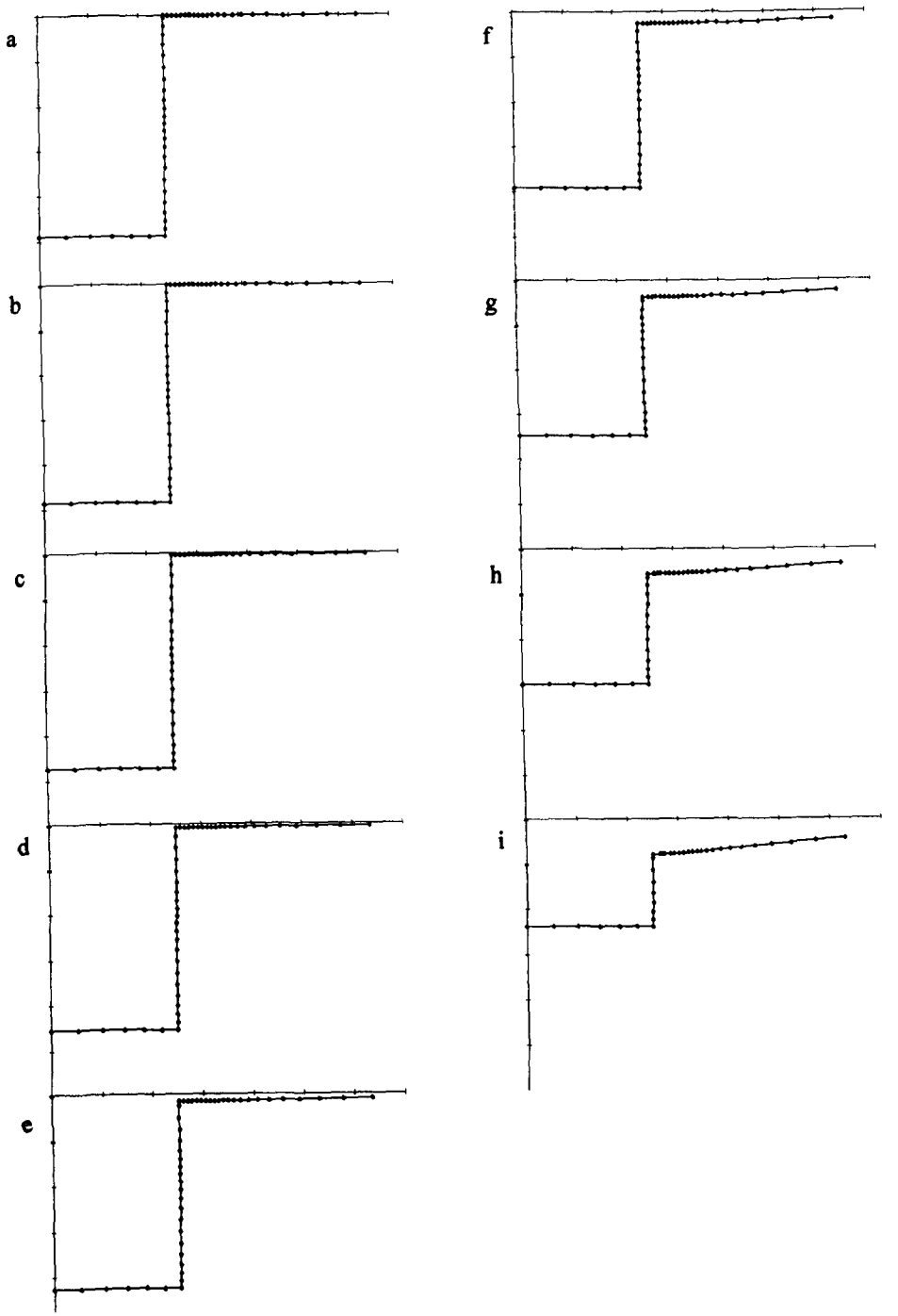


*Graph 4.17 Free-surface profile of exiting box (a/g=0.5)*

### *Knuckle*

We finally consider a knuckled body of total height 2, apex height 1, half angle $\alpha = \pi/4$ and initial depth -1.67.

The first observation when considering the knuckled body is that it consists of two different body shapes, the wedge and the box. Since the final stages of the exit are basically wedge exit albeit with different initial conditions arising from the earlier flow, and we would expect some results to approximate those already presented. The buoyancy and analytical theory is an excellent approximation of the total force for $t < 0.5$ and acceptable for $t < 1.0$, a tendency that was suggested in Graph 4.1 and Graph 4.5. If we consider the free surfaces at this time (h and i on Graph 4.21) we see it is around the zero potential level i.e. a height of zero.

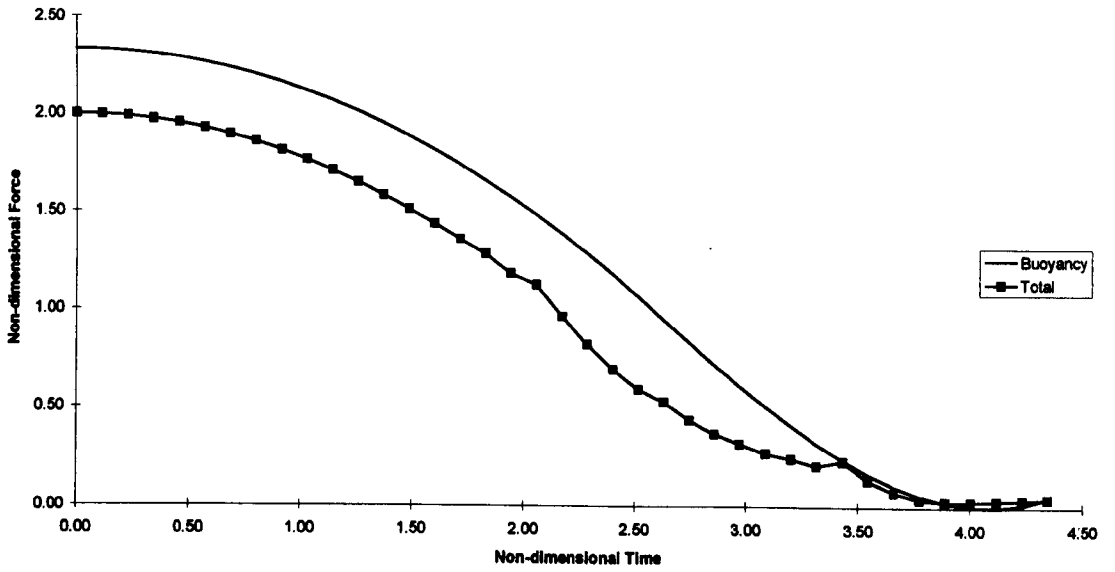


*Graph 4.18 Comparison of total force and buoyancy force for an exiting knuckle (a/g=0.2)*

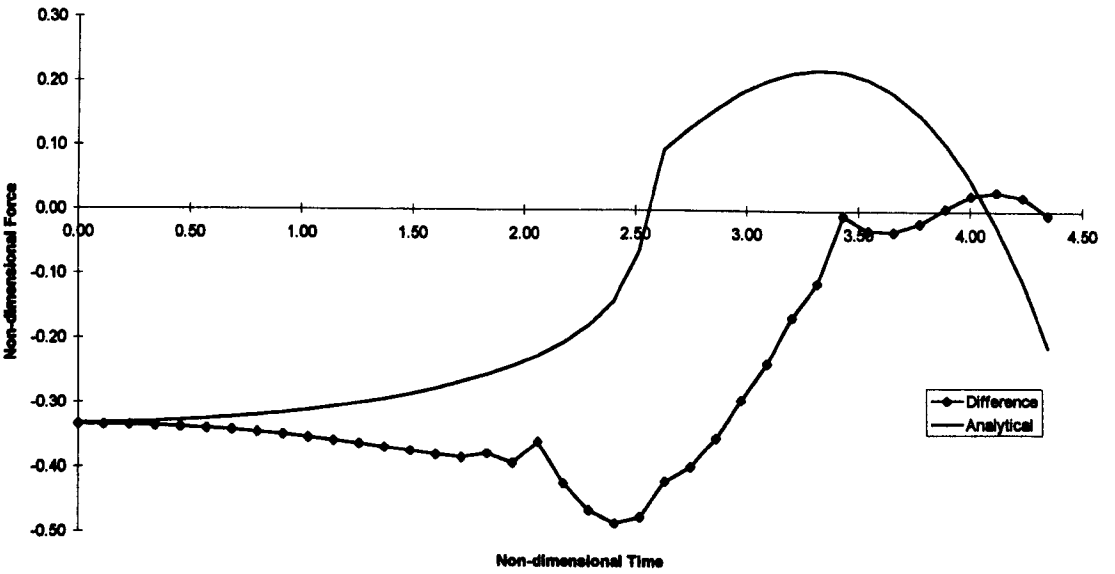


*Graph 4.19 Comparison of analytical added mass and force difference for an exiting knuckle (a/g=0.2)*

The sudden gradient change on the analytical curve just after $t = 2.5$ in Graph 4.19 is caused by the transition from knuckle added mass theory to wedge added mass theory (see Chapter 3 for detail).

There is only a small negative pressure in the final time step as you can see in Graph 4.20 and if we look at Graph 4.21 we see this is due to the beginnings of a jet as the body rises above the mean free surface level and is followed by the free-surface. While some of the upward motion is understandably physical, being similar to a standing wave, the negative pressure indicates the free surface is not drawing fast enough down the body. Better numerical resolution might resolve this problem but since it occurs right at the end of the calculation when the force is insignificant, we have not pursued this.

| Label | a | b | c | d | e | f | g | h | i | j |
|---|---|---|---|---|---|---|---|---|---|---|
| Time | 0 | 0.46 | 0.91 | 1.37 | 1.83 | 2.29 | 2.74 | 3.20 | 3.66 | 4.12 |

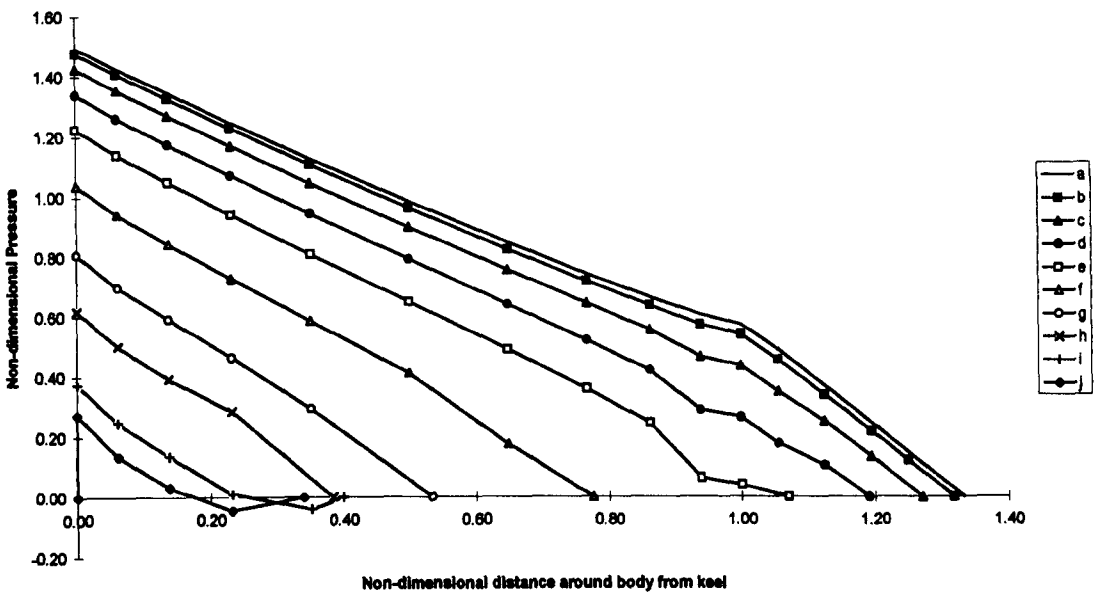


*Graph 4.20 Non-dimensional pressure on half wetted surface of exiting knuckle (a/g=0.2)*

One thing to notice on the free-surface profiles is how the free-surface suddenly draws down as we make the transition from the wall-sided body section to the wedge section.

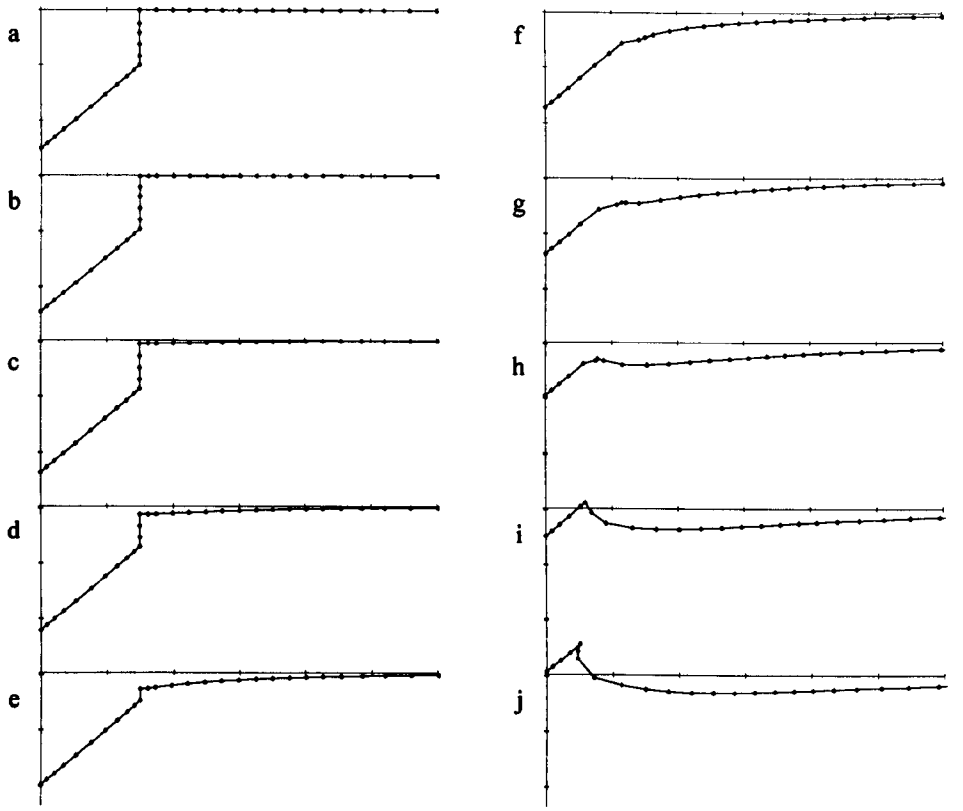


*Graph 4.21 Free-surface profile of exiting knuckle (a/g=0.2)*

Let us follow with the higher acceleration case. The body dimensions and initial depth remain the same but this time the acceleration is $g/2$. Looking at Graph 4.22, we see, as expected, that the total force is less than that experienced by the slower case, and again we see that the tendency is for the analytical theory to approximate the total force better in the final stages as the body nears complete exit. We notice the large "blip" in the results around the time of 1.2. This is caused by the knuckle emergence and hence the disappearance of the weakly singular flow around the knuckle with associated negative pressures, see Graph 4.24. On Graph 4.23 we see an example of excellent approximation by the analytical model for almost half the run time.

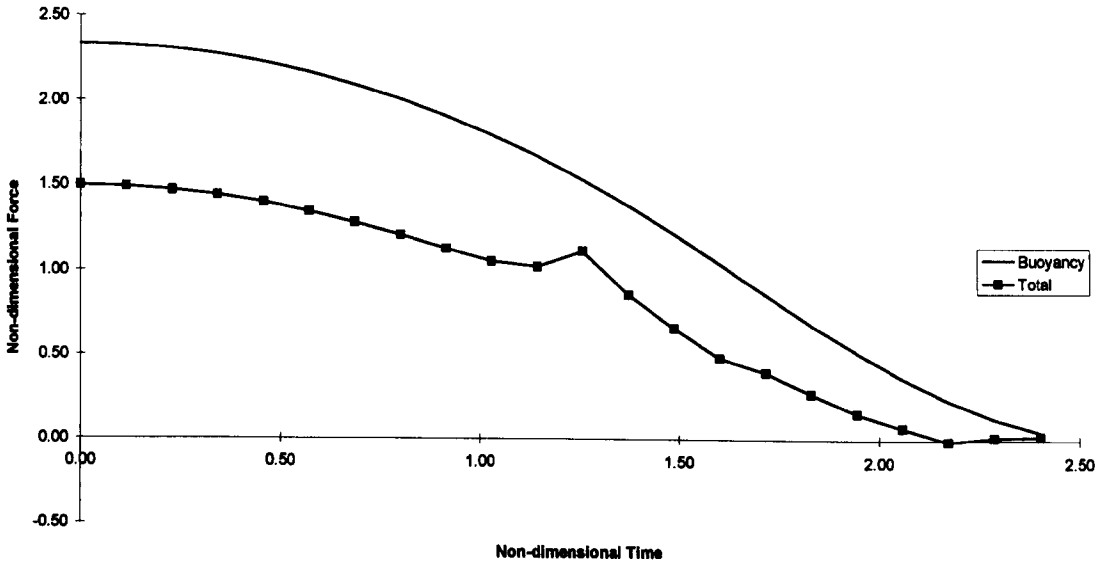


*Graph 4.22 Comparison of total force and buoyancy force for an exiting knuckle (a/g=0.5)*

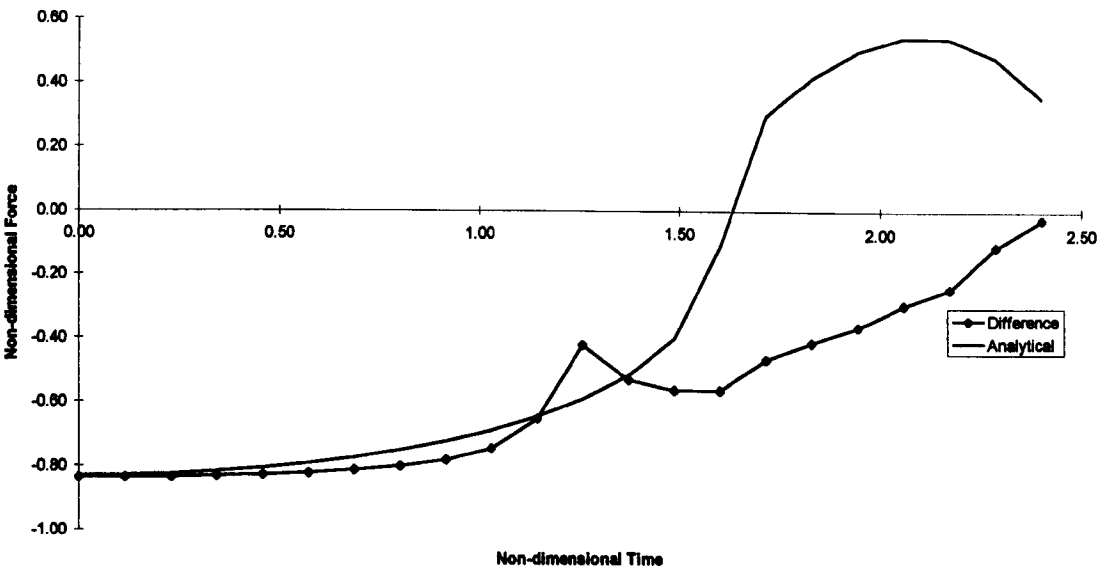


*Graph 4.23 Comparison of analytical added mass and force difference for an exiting knuckle (a/g=0.5)*

We see negative pressures are experience by the body in the later stages of motion. Once again these pressures are centred around the knuckle, that is the gradient change between wall-sided and wedge-sided body. If we study Graph 4.25 we see these pressures arise as the free-surface approaches the corner, as in the box-body case this is caused by a singularity at the knuckle. We therefore generalise the theory we presented in the previous section.

Consider the mapping $\zeta = z^{\alpha}$ the mapped plane would be $\beta(\zeta) = U\zeta$, graphically that is

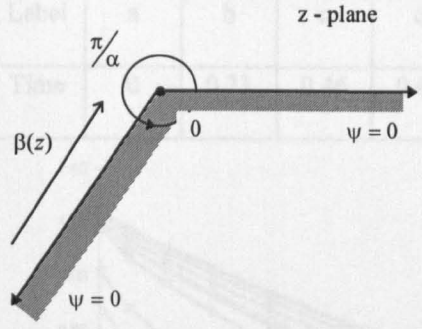


*Figure 4.3 Flow past a knuckle*

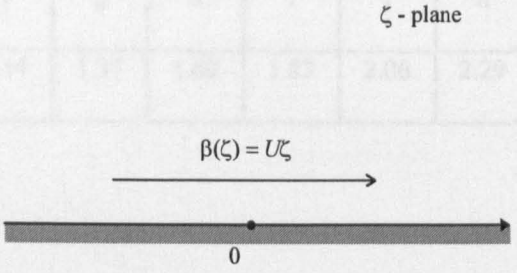


*Figure 4.4 Uniform flow in the upper half-plane*

So $\beta(z) = Uz^{\alpha}$ which has $\psi = 0$ on $\theta = 0$ and $\psi = 0$ on $\theta = \pi/\alpha$ as required.

Note that this flow is only valid locally since $\beta(z) \to \infty$ as $|z| \to \infty$.

Furthermore since

$\beta(z) \sim O(z^{\alpha})$ then

$$\frac{d\beta(z)}{dz} \sim O(z^{\alpha-1}) \Rightarrow v = \overline{\frac{d\beta(z)}{dz}} \sim O(z^{\alpha-1})$$

So $v$ is singular if $\alpha < 0$.

Though the knuckle is a singularity we may still calculate forces on the body at this point. Since pressure in steady flow is from the $v^2$ terms in Bernoulli's equation we can deduce $P \sim O(z^{2(\alpha-1)})$ which is singular if $\alpha < 1$.

However, we can still integrate to give a finite force by considering an element between the origin and $z_0$

$$F = \int_0^{z_0} P dz \sim \int_0^{z_0} z^{2\alpha-2} dz \sim O({z_0}^{2\alpha-1}) \text{ which is finite.}$$

For our particular knuckled body cases we have $\alpha = 4/5 < 1$ and so a singularity exists at the knuckle. So we can expect the pressure at the corner to be incorrect, and is a result of the numerical scheme attempting to calculate pressure at the singularity.

If we consider the final two time steps we see the body has already almost completely exited the fluid domain because the free-surface is well below the zero potential level. The profiles do continue for several more time steps and exhibit the free-surface following the body up, the appearance is that of a jet. However, the results seem spurious for reasons given when discarding the last stage of Graph 4.21 and so they have been omitted here.

| Label | a | b | c | d | e | f | g | h | i | j | k |
|---|---|---|---|---|---|---|---|---|---|---|---|
| Time | 0 | 0.23 | 0.46 | 0.69 | 0.91 | 1.14 | 1.37 | 1.60 | 1.83 | 2.06 | 2.29 |

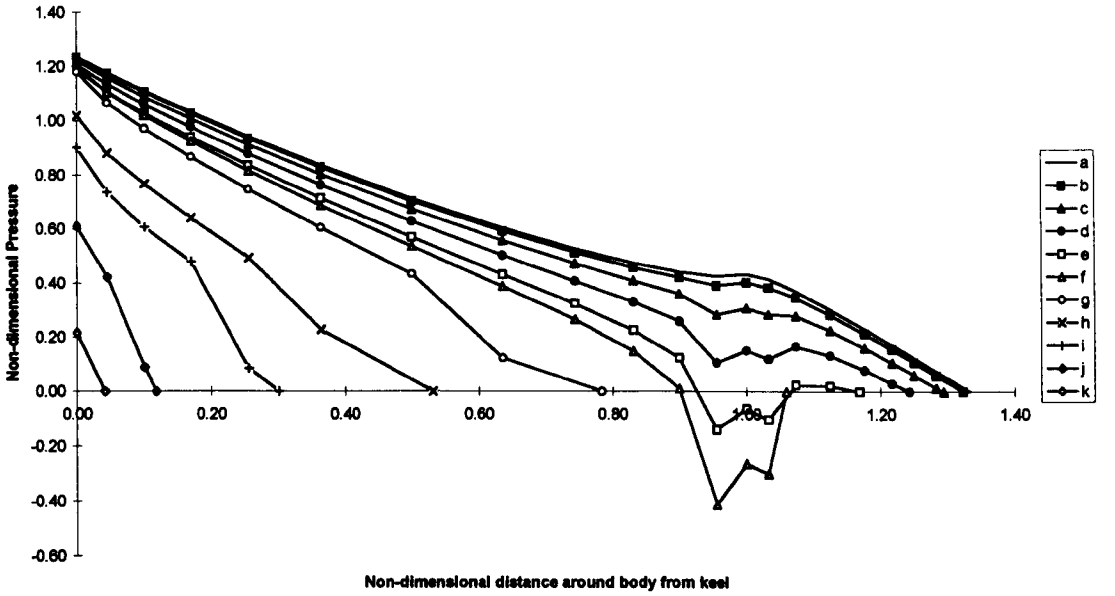


*Graph 4.24 Non-dimensional pressure on half wetted surface of exiting knuckle (a/g=0.5)*

As for the box body we have clustered the points around the knuckled body such that they are denser near the body corners, this can be seen in Graph 4.25. Again this is done with the intention of reducing the force errors caused by the presence of a singularity at the corner.

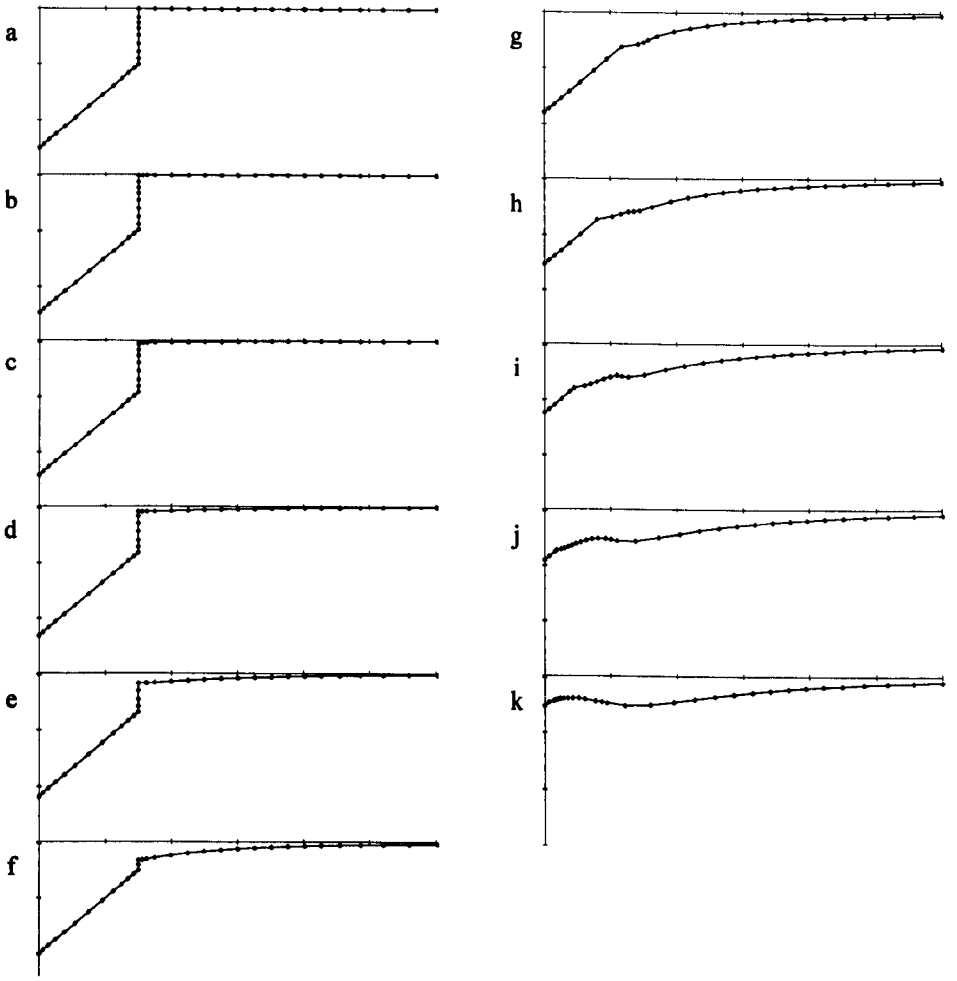


*Graph 4.25 Free-surface profile of exiting knuckle (a/g=0.5)*

## Constant velocity

We switch our attention to the case of constant velocity exit. Since the acceleration is therefore zero, we use this to isolate the contribution of the $\frac{dm_a}{dz}$ portion of the added mass force.

### *Wedge*

We return to the wedge case first. Consider a wedge of half angle $\pi/6$, height 1.7 and initial depth -1.67 exiting the fluid domain at a constant velocity, Froude number 0.117.

First impressions are that the buoyancy performs an excellent job of approximating the total force, although we must remember the velocity is small. Graph 4.27 suggests that the added mass force is a very poor measure for this case, however we should note the size of the force we are considering and compare with those in the previous section.

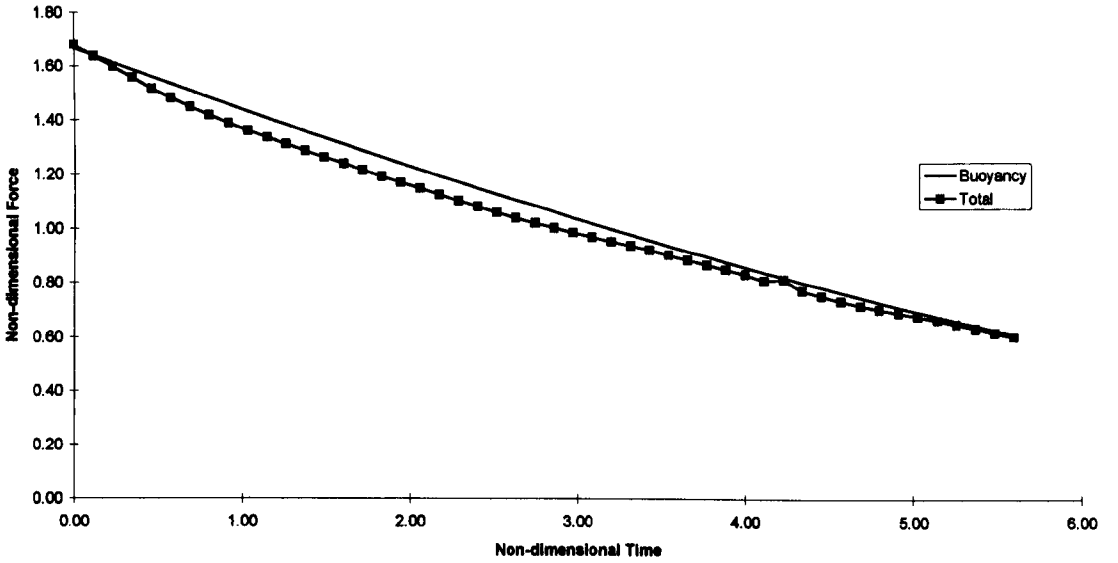


*Graph 4.26 Comparison of total force and buoyancy force for an exiting wedge ($\alpha=\pi/6$, $F_r=0.117$)*

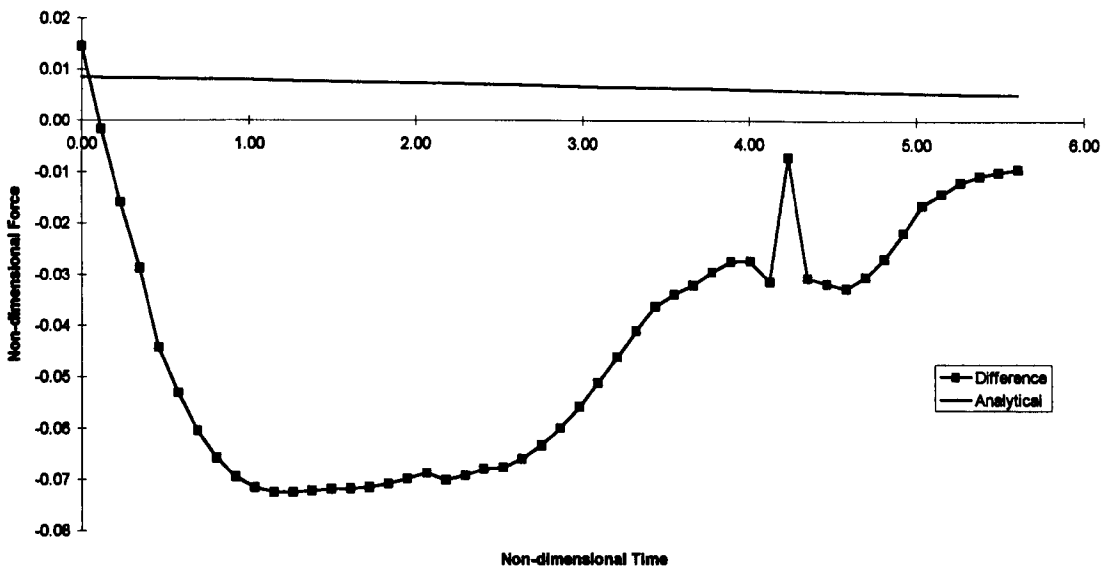


*Graph 4.27 Comparison of analytical added mass and force difference for an exiting wedge ($\alpha=\pi/6$, $F_r=0.117$)*

The pressure distribution in Graph 4.28 is virtually linear, being dominated by hydrostatic pressure. Note the nodal intersection point, at zero pressure, does not have a fixed distance from the keel because it is not fixed on the body as are the other body points within this numerical scheme, but is a free-surface point. Given the very weak hydrodynamic interaction present we have not continued the calculations.

| Label | a | b | c | d | e | f | g | h | i |
|---|---|---|---|---|---|---|---|---|---|
| Time | 0 | 0.69 | 1.37 | 2.06 | 2.74 | 3.43 | 4.12 | 4.80 | 5.49 |

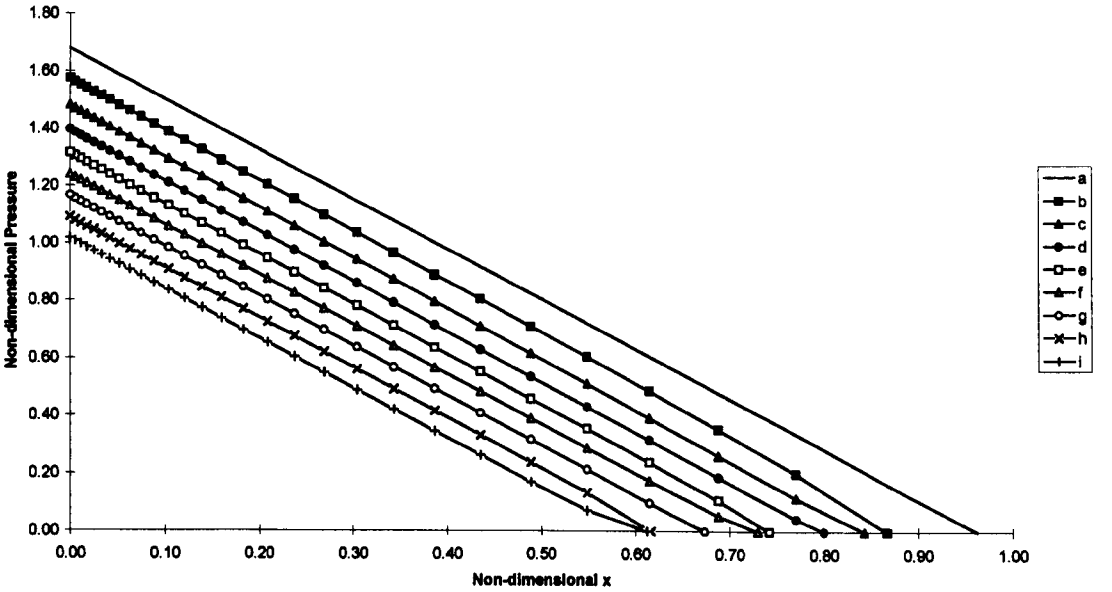


*Graph 4.28 Non-dimensional pressure on half wetted surface of exiting wedge ($\alpha=\pi/6$, $F_r=0.117$)*

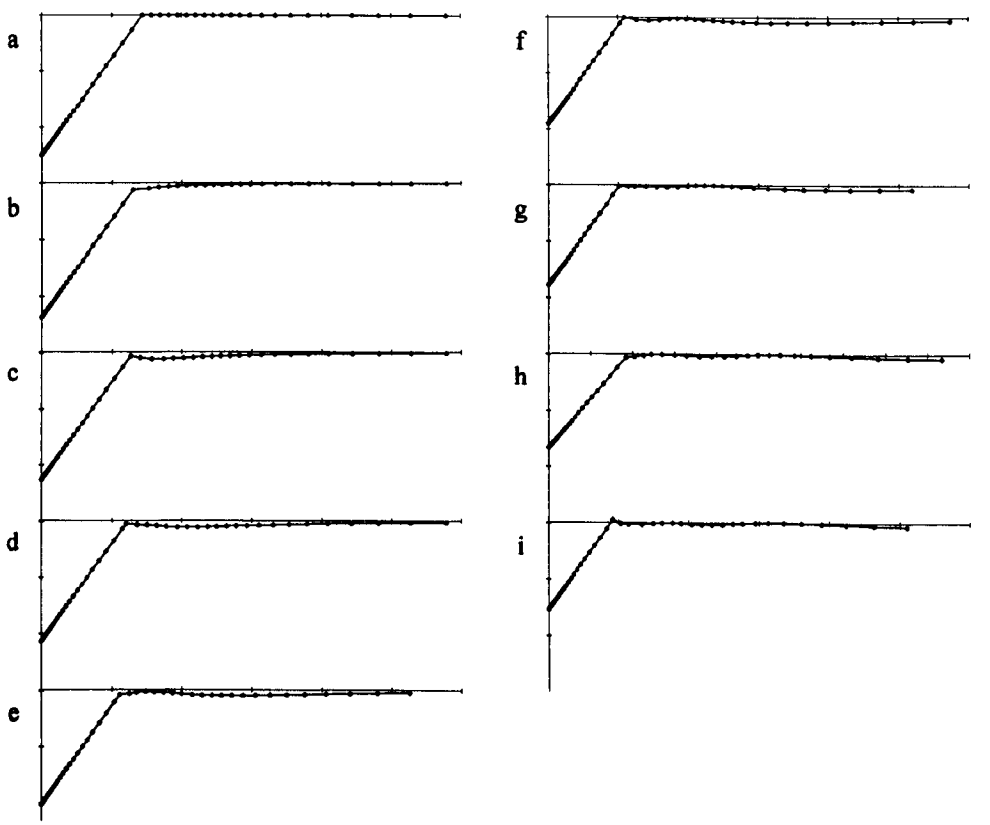


*Graph 4.29 Free-surface profile of exiting wedge ($\alpha=\pi/6$, $F_r=0.117$)*

Now consider a wedge of half angle $\pi/4$, height 1.7 and initial depth -1.0. This body is exiting at twice the speed of the previous example, Froude number 0.233, and is wider, so we can expect stronger hydrodynamic interaction.

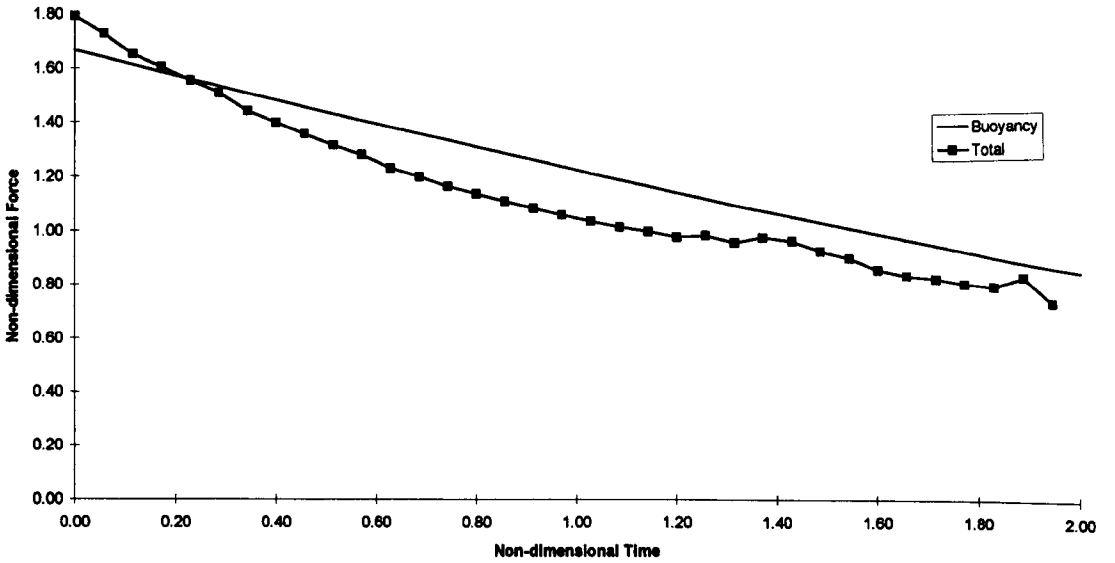


*Graph 4.30 Comparison of total force and buoyancy force for an exiting wedge ($\alpha=\pi/4$, $F_r=0.233$)*

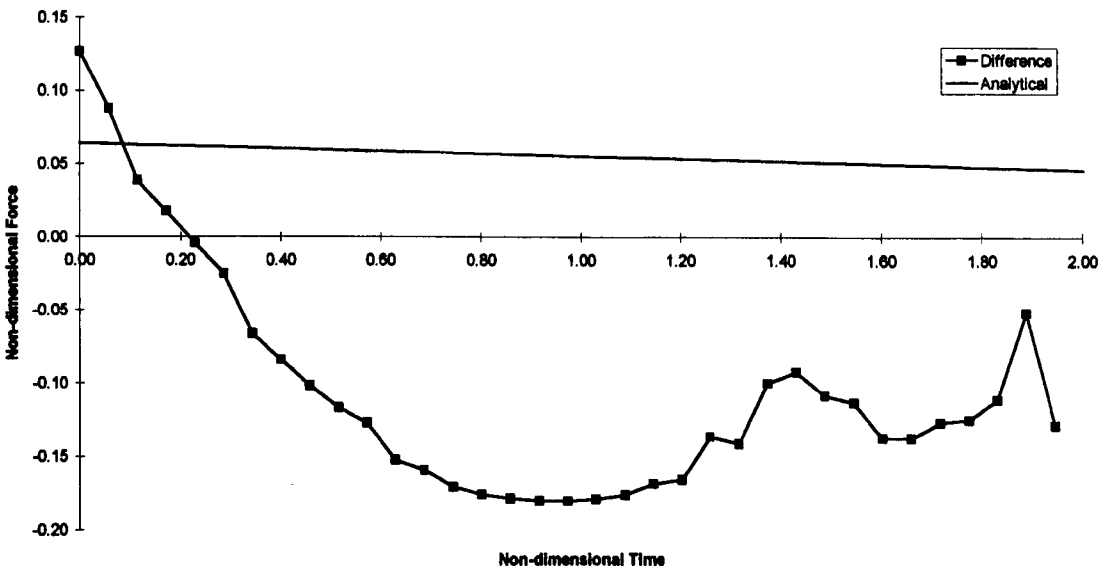


*Graph 4.31 Comparison of analytical added mass and force difference for an exiting wedge ($\alpha=\pi/4$, $F_r=0.233$)*

| Label | a | b | c | d | e | f | g | h | i |
|---|---|---|---|---|---|---|---|---|---|
| Time | 0 | 0.23 | 0.46 | 0.69 | 0.91 | 1.14 | 1.37 | 1.60 | 1.83 |

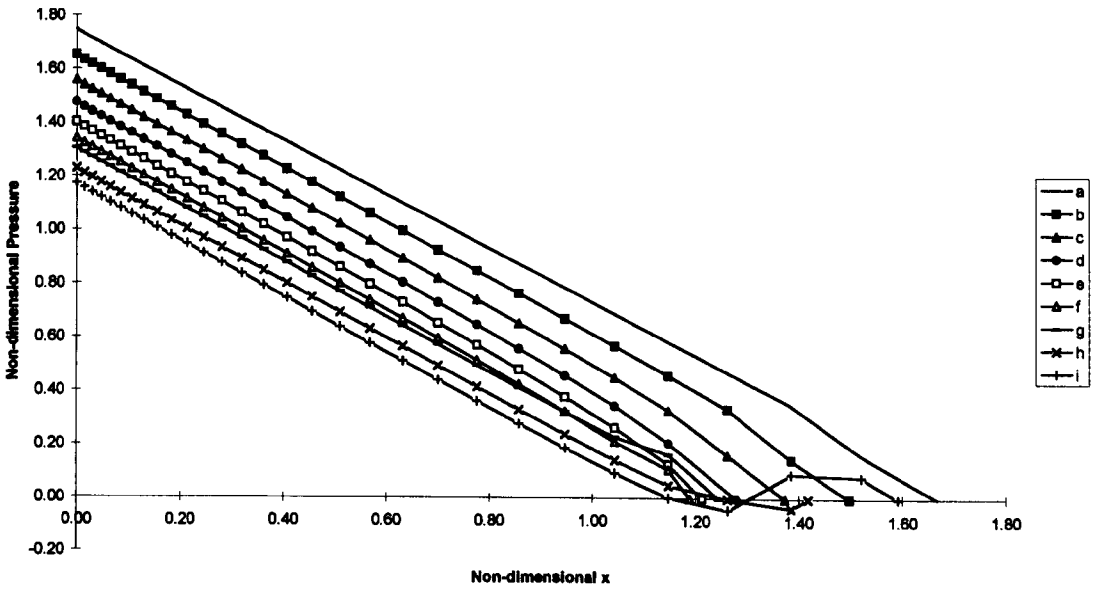


*Graph 4.32 Non-dimensional pressure on half wetted surface of exiting wedge ($\alpha=\pi/4$, $F_r=0.233$)*

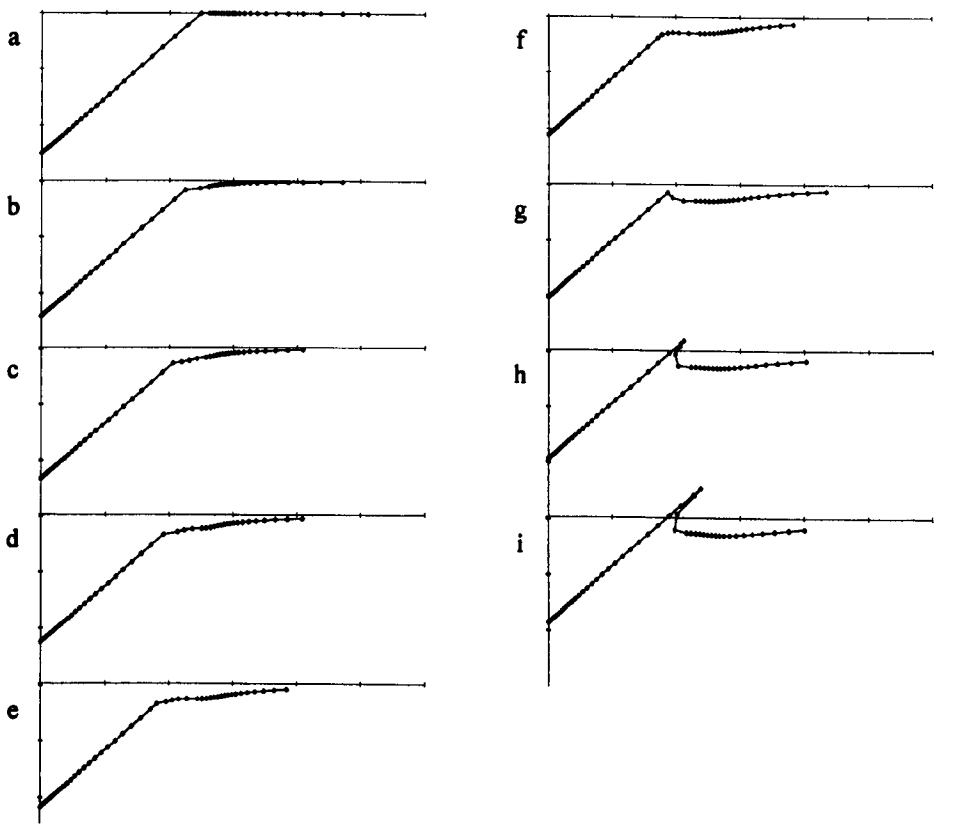


*Graph 4.33 Free-surface profile of exiting wedge ($\alpha=\pi/4$, $F_r=0.233$)*

**Once again, we increase the constant velocity of the wedge, Froude number 0.583.**

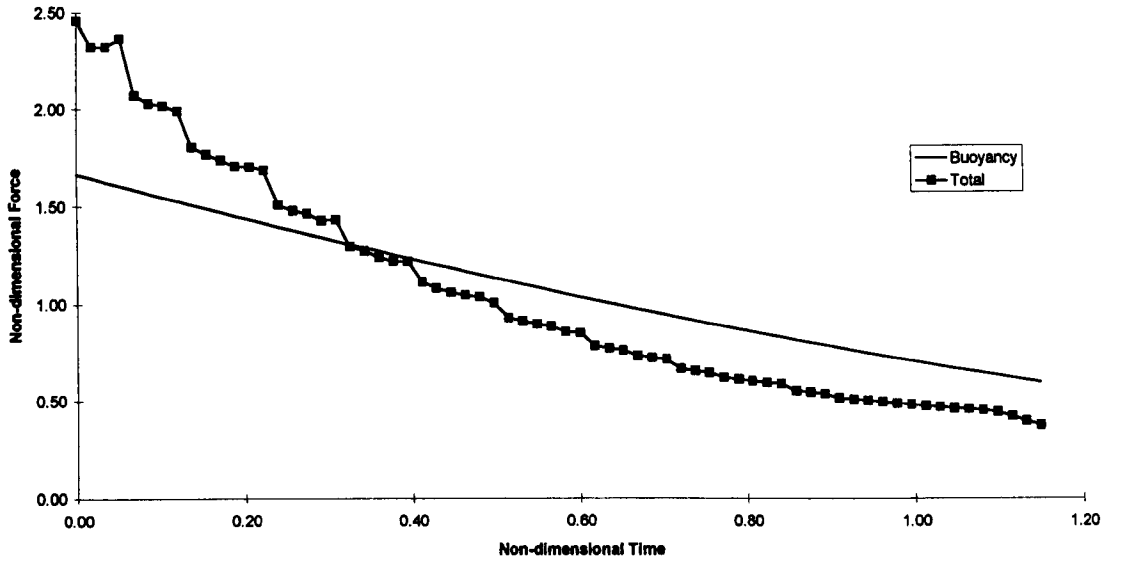


*Graph 4.34 Comparison of total force and buoyancy force for an exiting wedge ($\alpha=\pi/4$, $F_r=0.583$)*

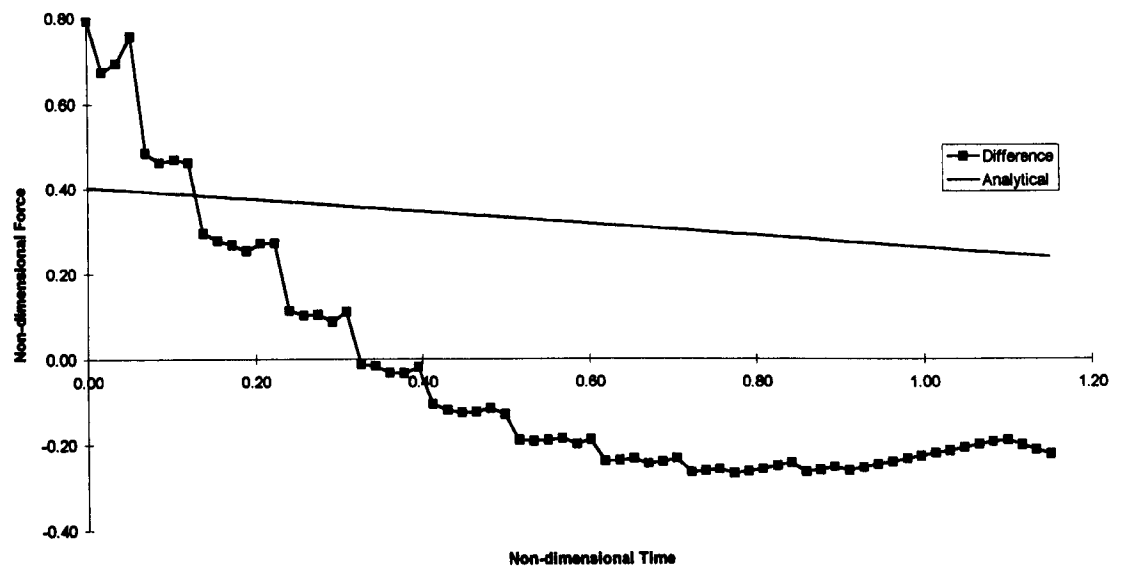


*Graph 4.35 Comparison of analytical added mass and force difference for an exiting wedge ($\alpha=\pi/4$, $F_r=0.583$)*

| Label | a | b | c | d | e | f | g |
|---|---|---|---|---|---|---|---|
| Time | 0 | 0.17 | 0.34 | 0.51 | 0.69 | 0.86 | 1.03 |

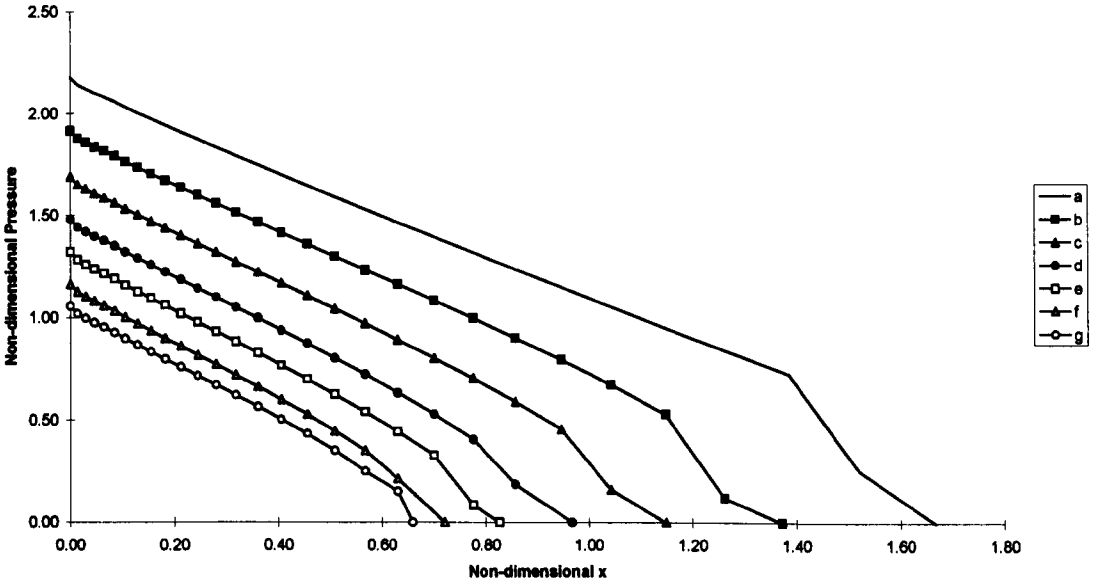


*Graph 4.36 Non-dimensional pressure on half wetted surface of exiting wedge ($\alpha=\pi/4$, $F_r=0.583$)*

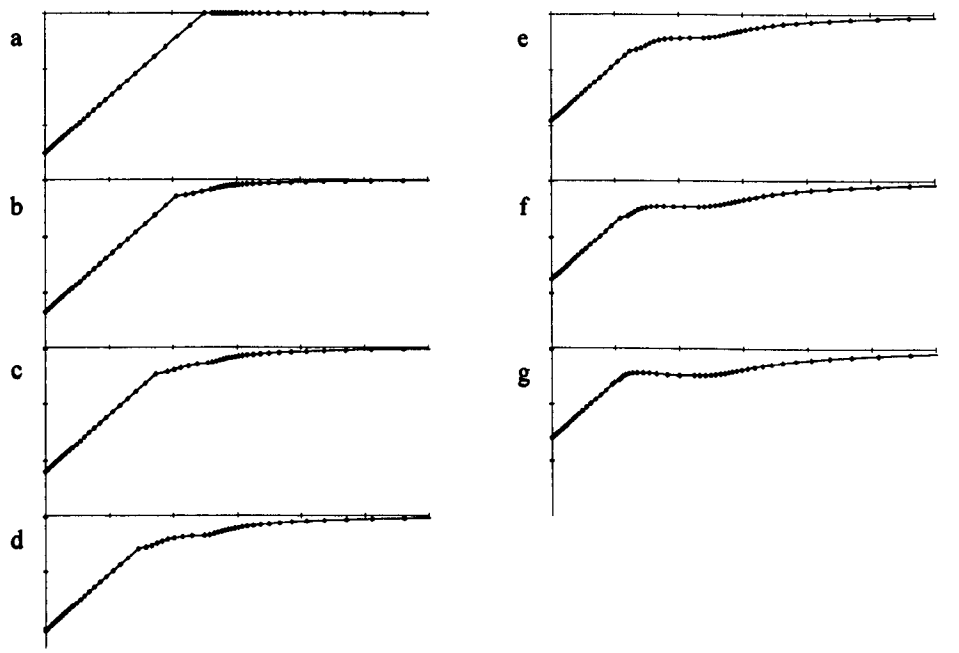


*Graph 4.37 Free-surface profile of exiting wedge ($\alpha=\pi/4$, $F_r=0.583$)*

For the final wedge case under consideration the Froude number is increased to 1.166, double that of the previous example, as an experiment in how far we can "push" the model.

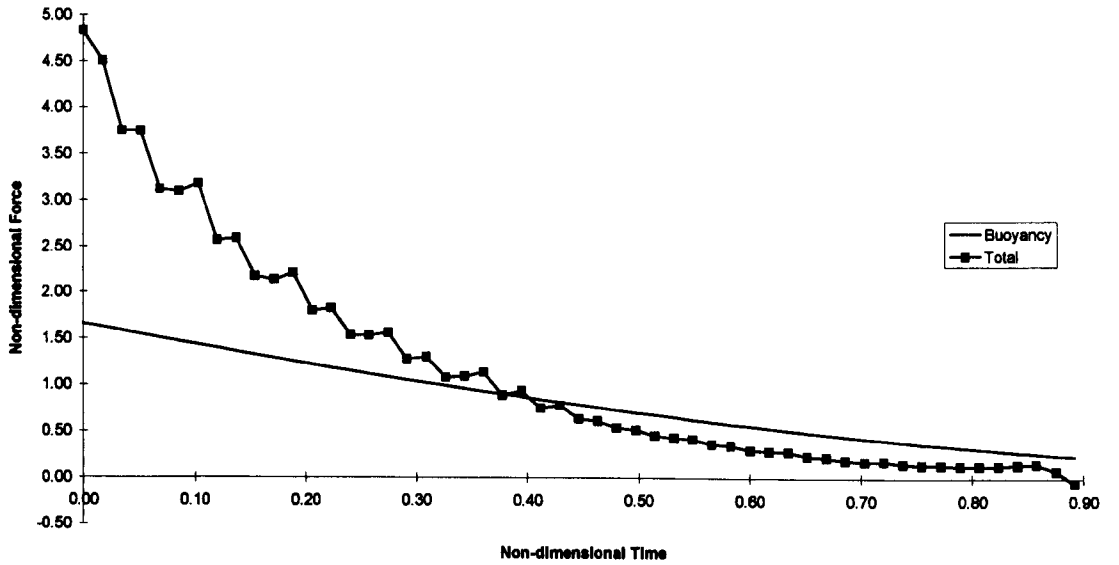


*Graph 4.38 Comparison of total force and buoyancy force for an exiting wedge ($\alpha=\pi/4$, $F_r=1.166$)*

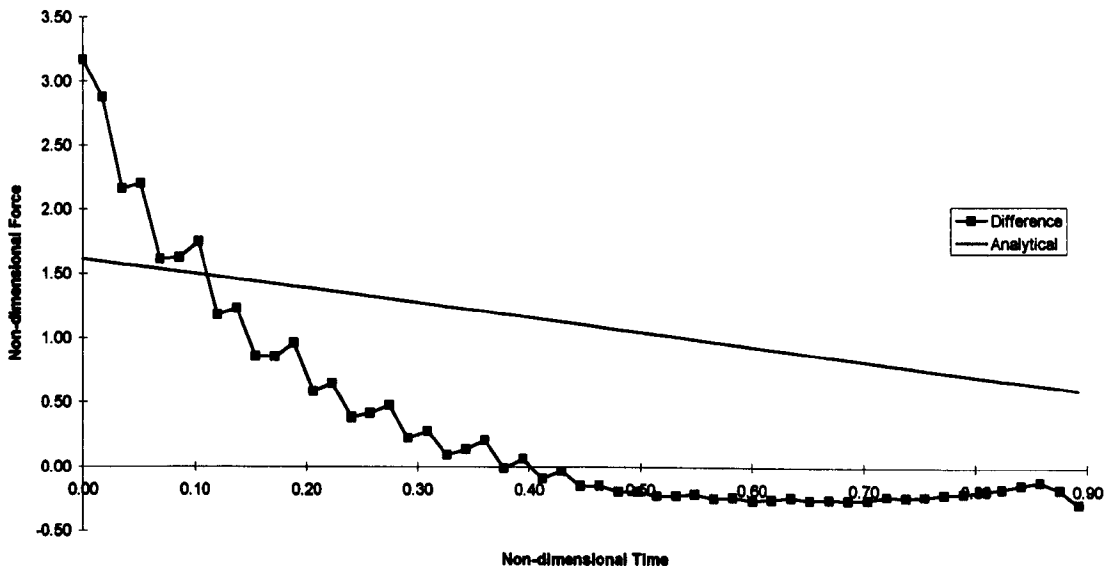


*Graph 4.39 Comparison of analytical added mass and force difference for an exiting wedge ($\alpha=\pi/4$, $F_r=1.166$)*

We see the difference between the analytical theory and the force difference in Graph 4.39 is a lot larger than in previous examples (it has steadily increased). The poor agreement is due to draw-down making $\frac{dm}{dy}$ change more rapidly than we can predict using the model, implying stronger hydrodynamic forces. Refer to Chapter 6 for further investigation into draw-down.

| Label | a | b | c | d | e | f | g | h |
|---|---|---|---|---|---|---|---|---|
| Time | 0 | 0.10 | 0.21 | 0.31 | 0.41 | 0.51 | 0.62 | 0.72 |

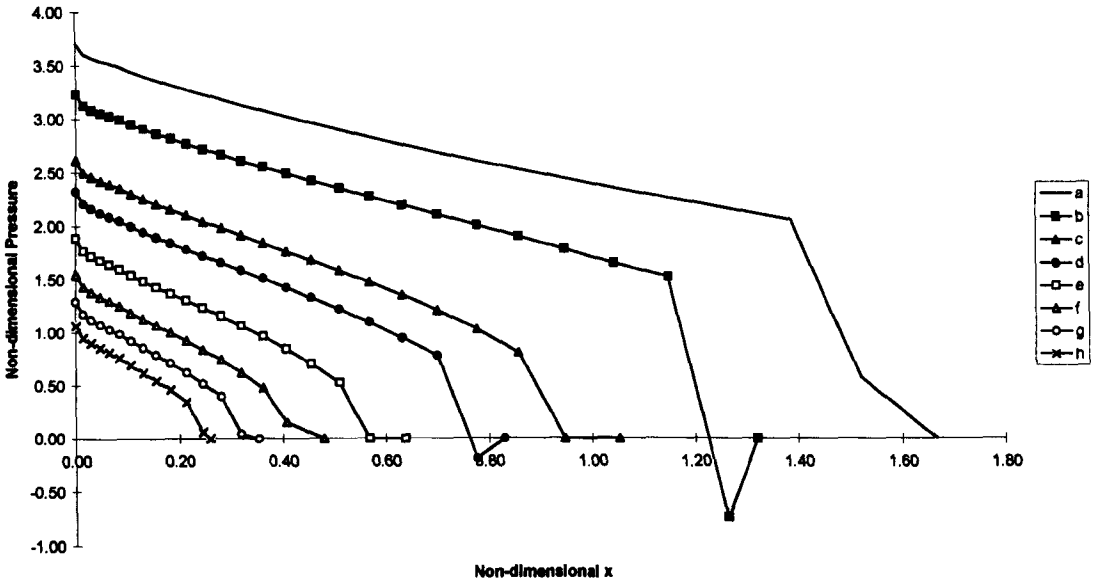


*Graph 4.40 Non-dimensional pressure on half wetted surface of exiting wedge ($\alpha=\pi/4$, $F_r=1.166$)*

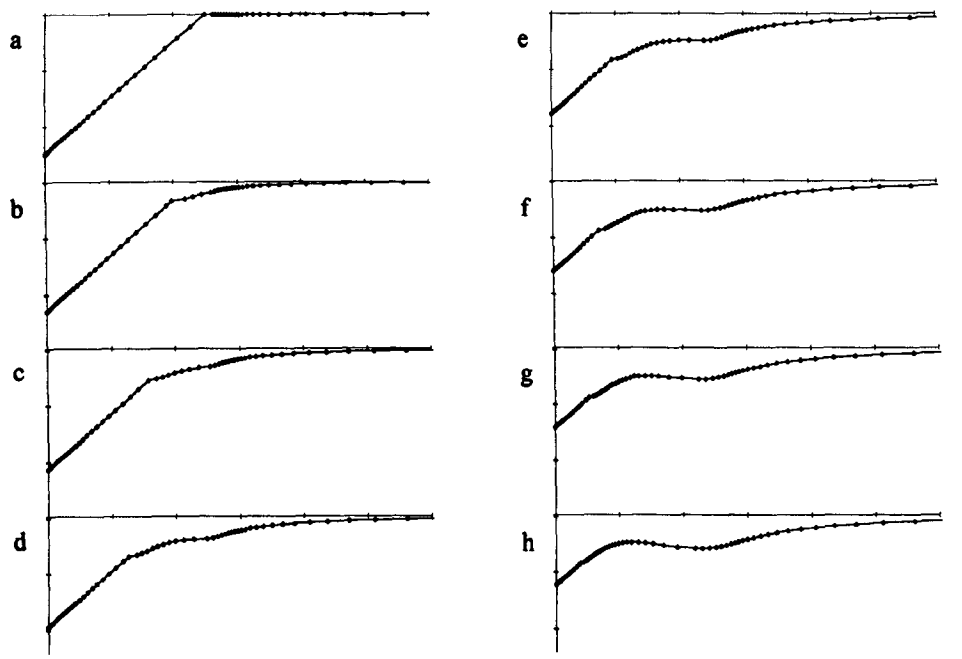


*Graph 4.41 Free-surface profile of exiting wedge ($\alpha=\pi/4$, $F_r=1.166$)*

Although the analytical method does not cope well with the constant velocity wedge exit we have provided a full selection of results for comparison with future work.

### *Box*

We move our attention to the case of a box body exiting the fluid domain. We consider four cases, the first three having Froude numbers equal to those in the first three wedge cases, for the final cases we (as for the wedge) we "push" the model to its limits.

Our first case is that of a box of height 1.7, width 2 and initial depth -1.63, exiting with Froude number 0.117.

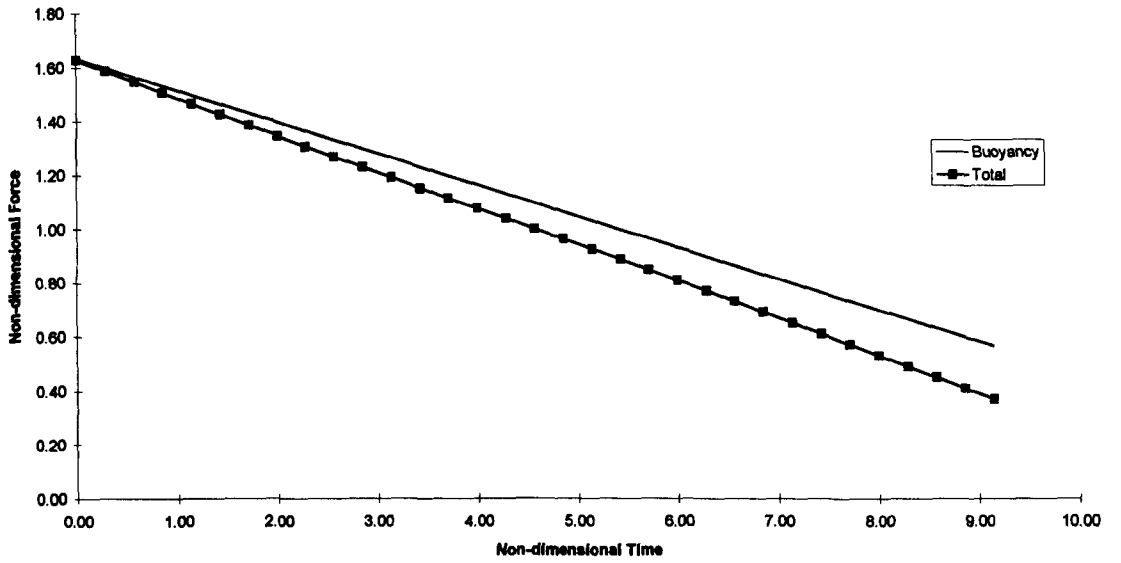


*Graph 4.42 Comparison of total force and buoyancy force for an exiting box ($F_r$=0.117)*

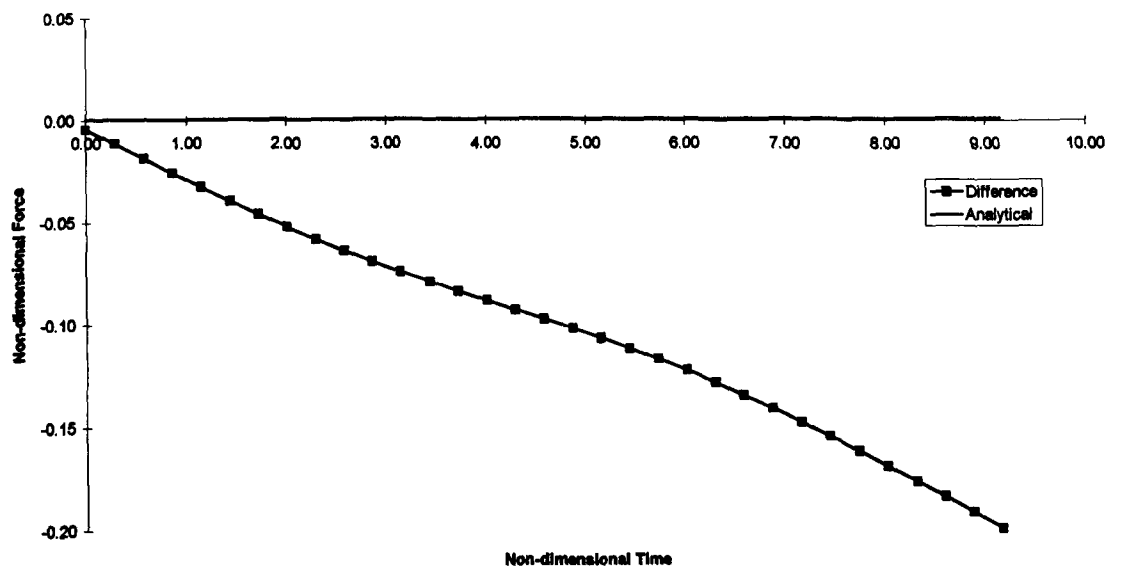


*Graph 4.43 Comparison of analytical added mass and force difference for an exiting box ($F_r$=0.117)*

From the following pressure distribution, Graph 4.44, we see this example is very hydrostatic.

| Label | a | b | c | d | e | f | g | h | i |
|---|---|---|---|---|---|---|---|---|---|
| Time | 0 | 1.14 | 2.29 | 3.43 | 4.57 | 5.72 | 6.86 | 8.01 | 9.15 |

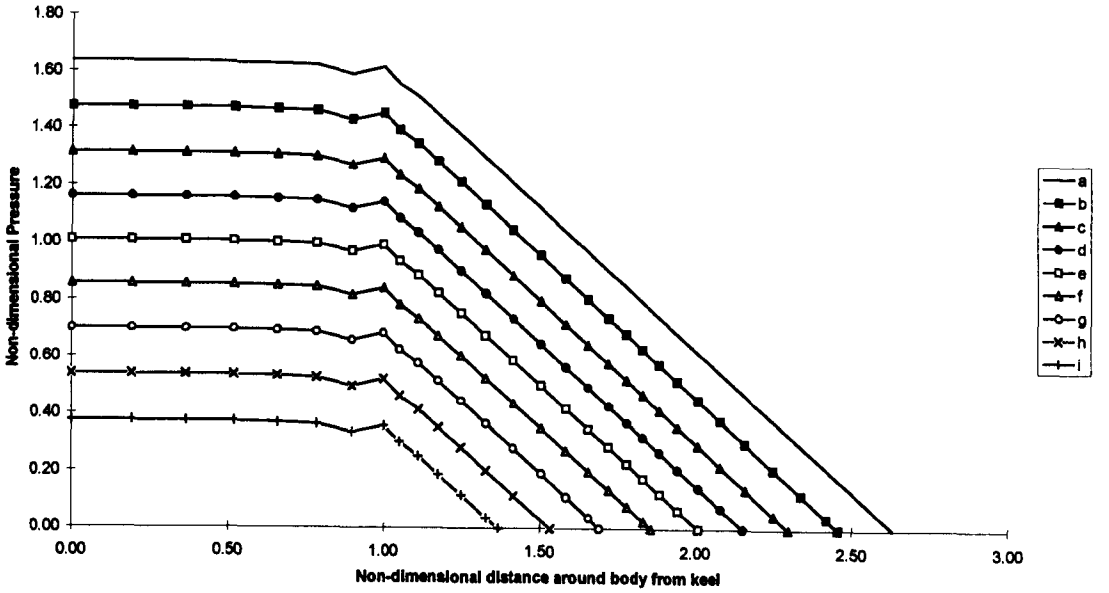


*Graph 4.44 Non-dimensional pressure on half wetted surface of an exiting box ($F_r$=0.117)*

The motion is slow enough that the intersection point moves up the wall side of the body without problems, as is shown by the free-surface profile given in Graph 4.45.

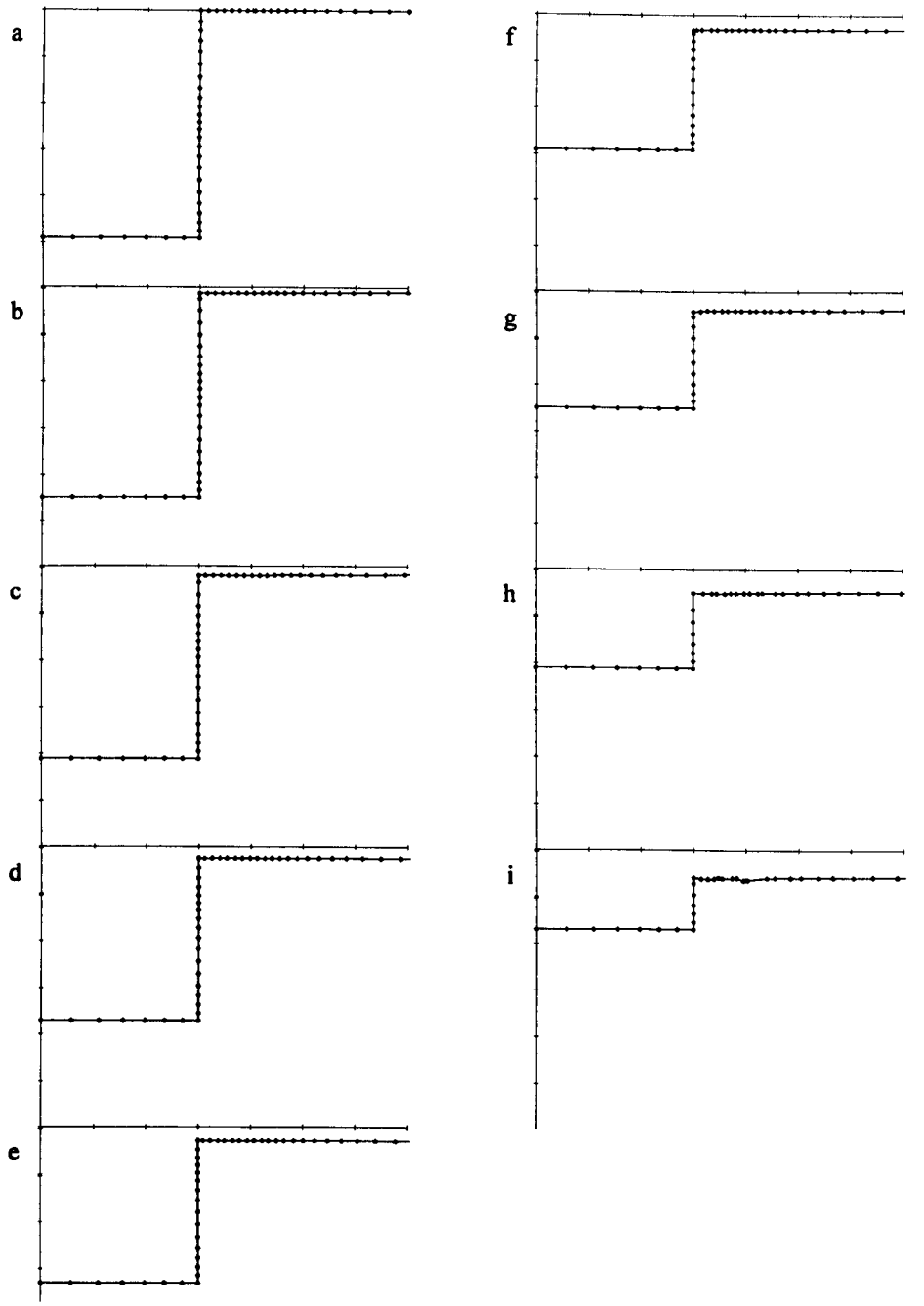


*Graph 4.45 Free-surface profile of exiting box ($F_r$=0.117)*

**We increase the Froude number to 0.233.**

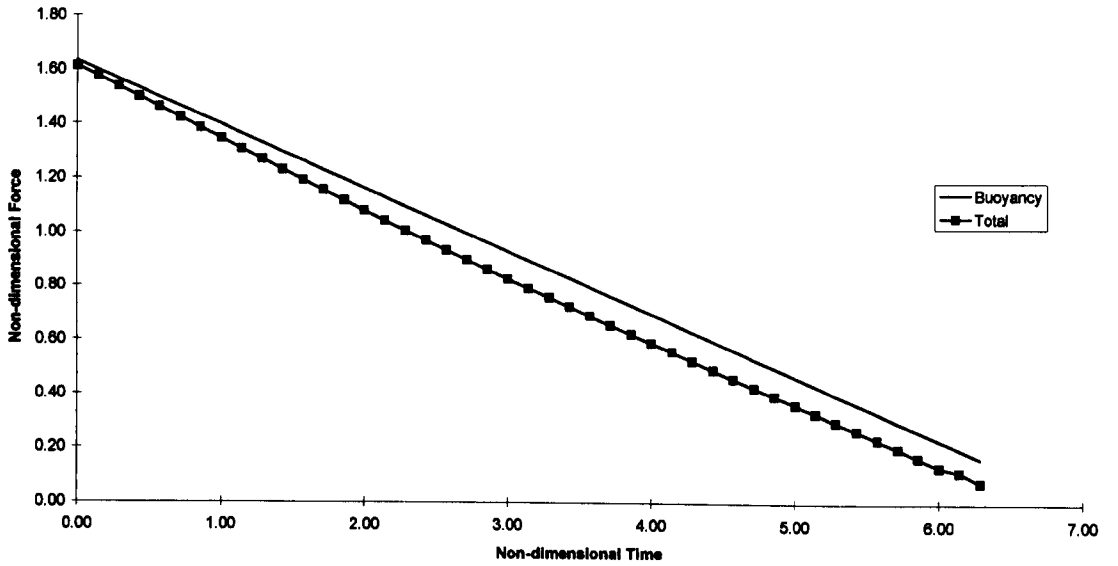


*Graph 4.46 Comparison of total force and buoyancy force for an exiting box ($F_r$=0.233)*

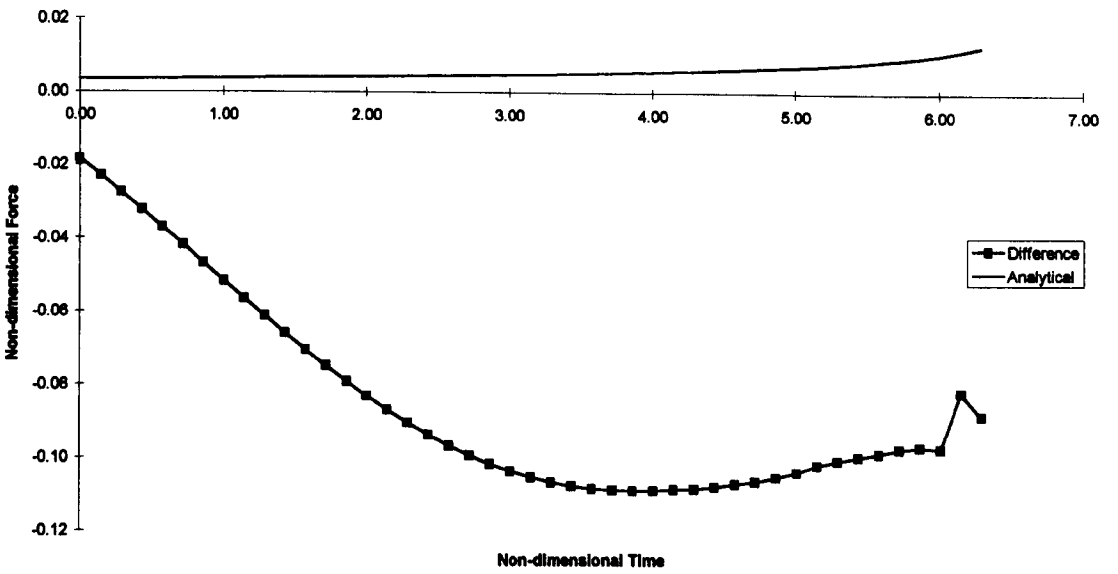


*Graph 4.47 Comparison of analytical added mass and force difference for an exiting box ($F_r$=0.233)*

| Label | a | b | c | d | e | f | g | h | i |
|---|---|---|---|---|---|---|---|---|---|
| Time | 0 | 0.71 | 1.43 | 2.14 | 2.86 | 3.57 | 4.29 | 5.00 | 5.72 |

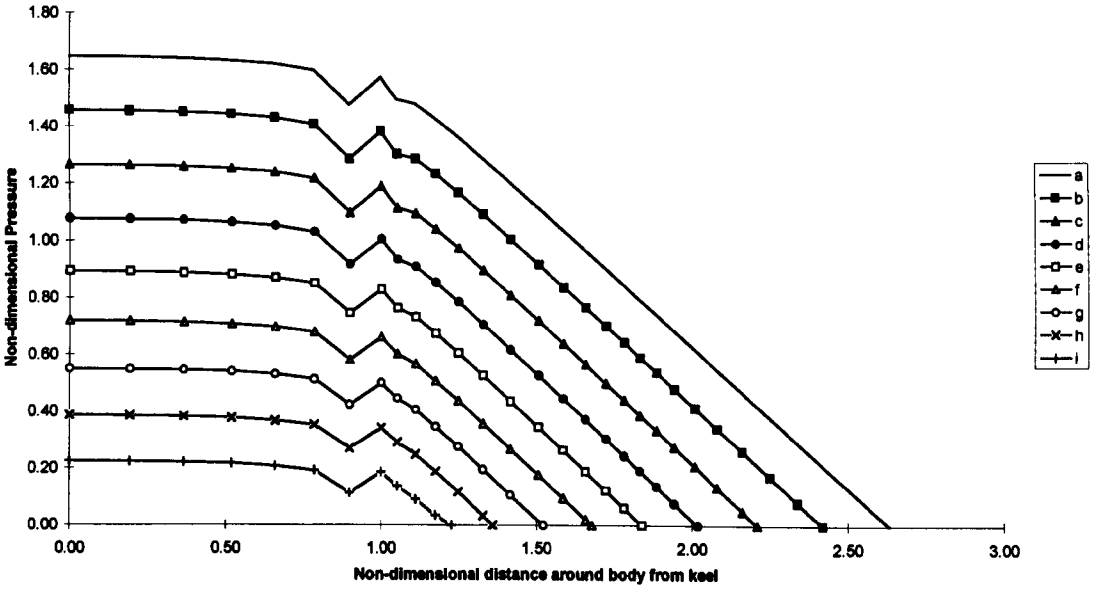


*Graph 4.48 Non-dimensional pressure on half wetted surface of an exiting box ($F_r$=0.233)*

The motion is again uneventful, with just a small draw-down of the free-surface.

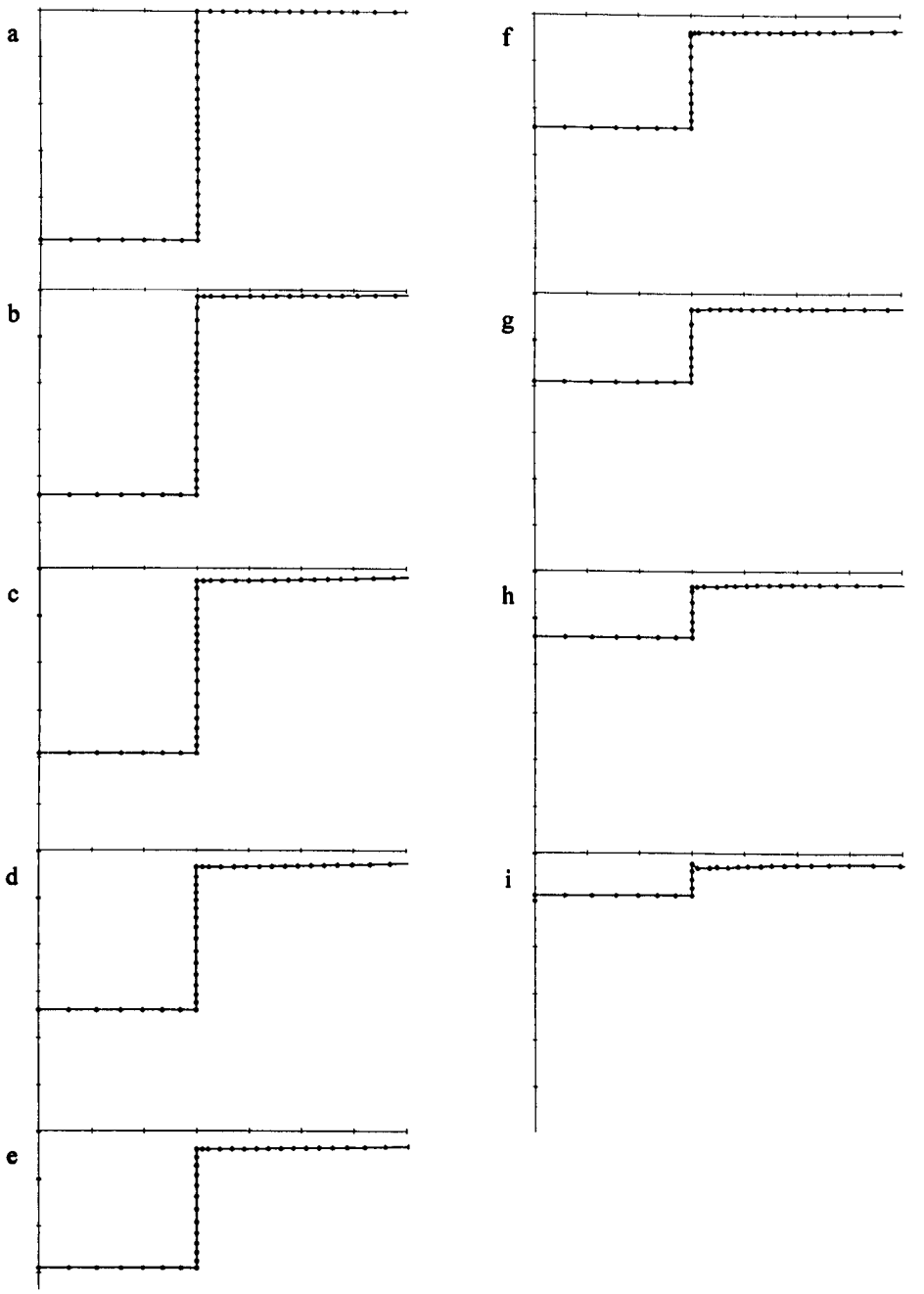


*Graph 4.49 Free-surface profile of exiting box ($F_r$=0.233)*

Taking a larger Froude number, this time 0.583, the motion becomes more interesting.

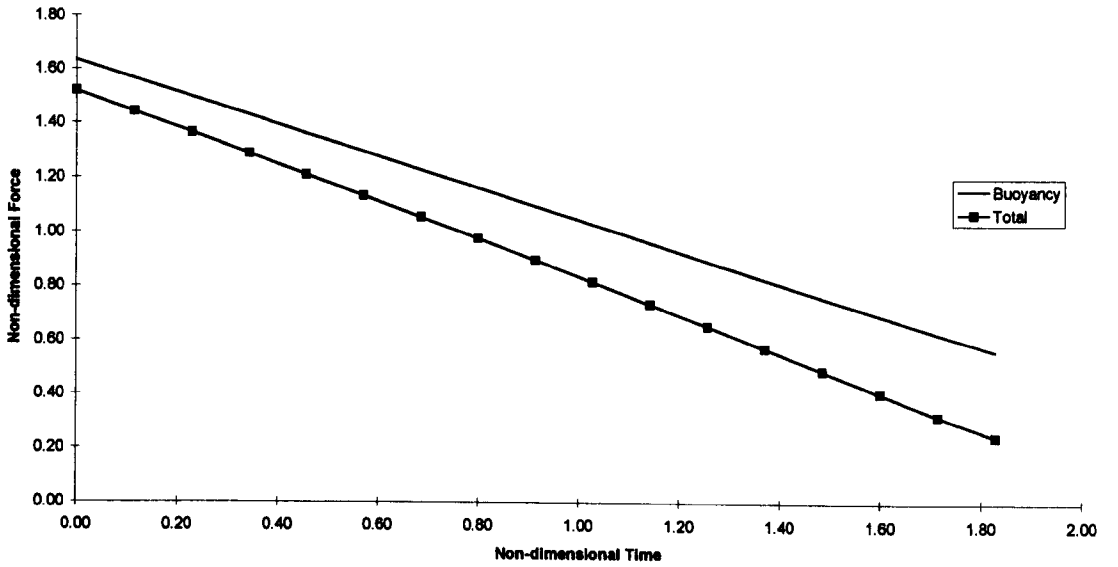


*Graph 4.50 Comparison of total force and buoyancy force for an exiting box ($F_r$=0.583)*

Here we see almost linear force curves, with slightly differing gradients, the overestimate of the buoyancy increasing with time.

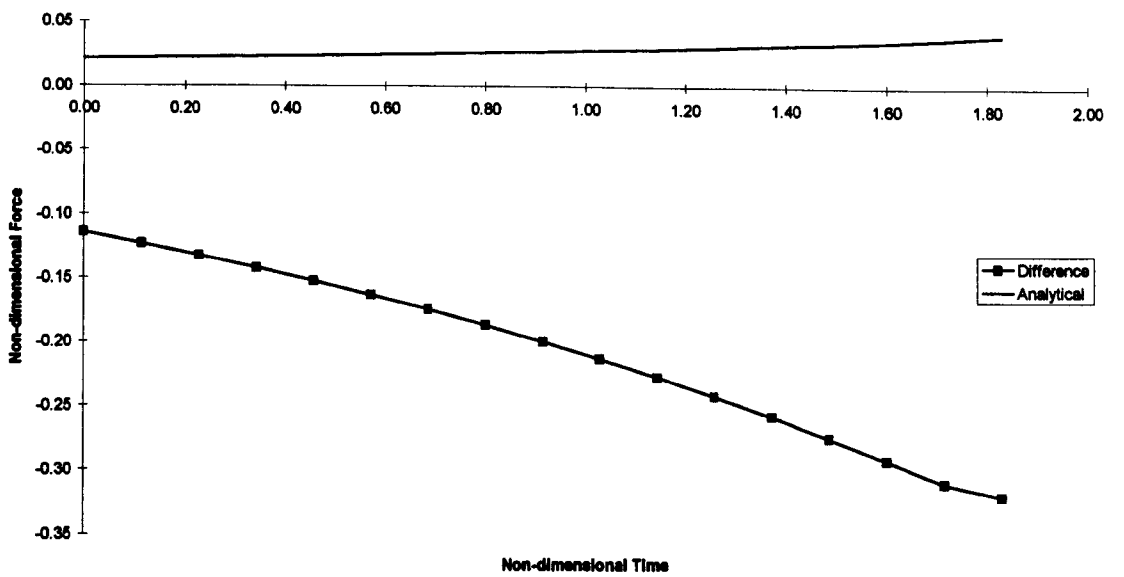


*Graph 4.51 Comparison of analytical added mass and force difference for an exiting box ($F_r$=0.583)*

| Label | a | b | c | d | e | f | g | h | i |
|---|---|---|---|---|---|---|---|---|---|
| Time | 0 | 0.23 | 0.46 | 0.69 | 0.91 | 1.14 | 1.37 | 1.60 | 1.83 |

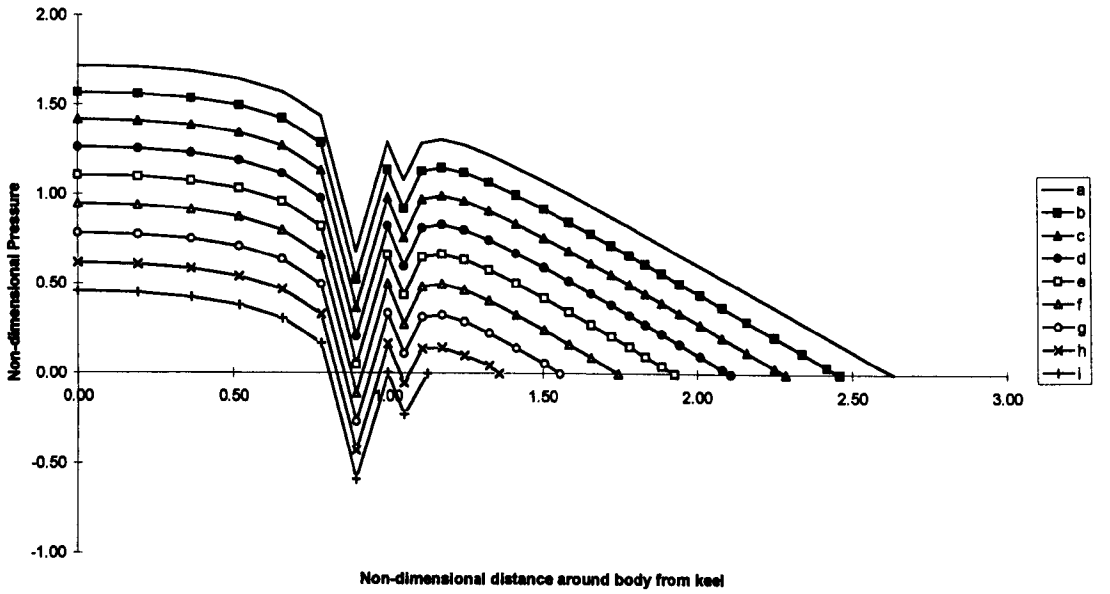


*Graph 4.52 Non-dimensional pressure on half wetted surface of an exiting box ($F_r$=0.583)*

We can see the reason for the buoyancy overestimating the total force when we study the free-surface in Graph 4.53, the draw-down is now quite large, hence the buoyancy should be calculated using the smaller submerged body volume rather than the draft taken from the line of zero potential.

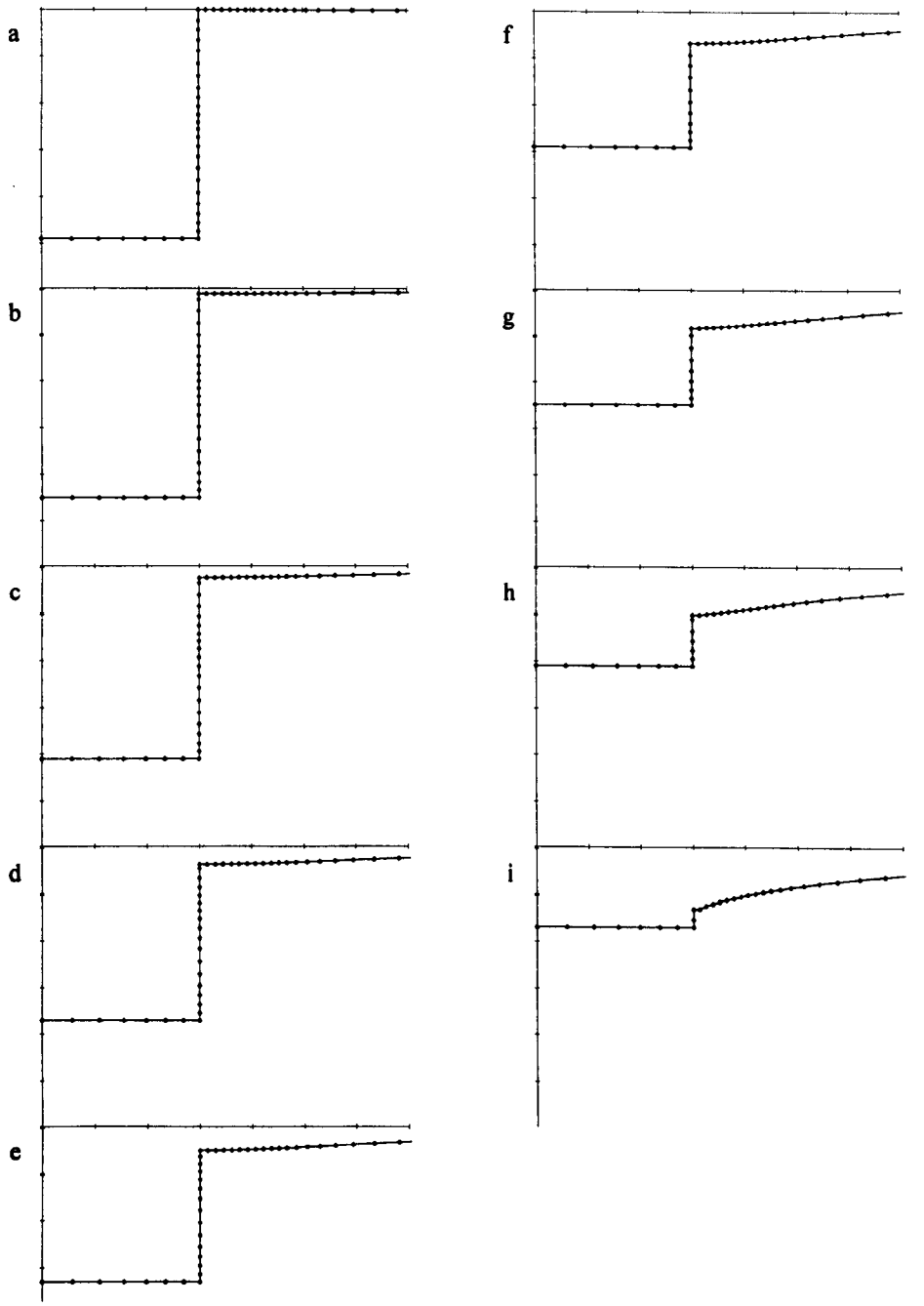


*Graph 4.53 Free-surface profile of exiting box ($F_r$=0.583)*

Now we increase the Froude number to 2.915, to see what effect it has on our model.

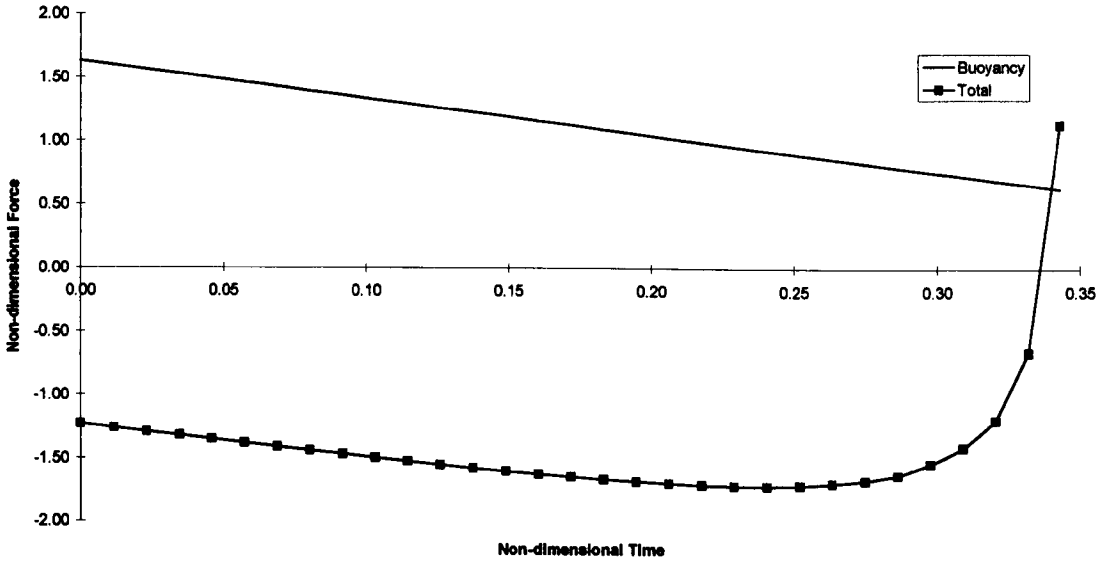


*Graph 4.54 Comparison of total force and buoyancy force for an exiting box ($F_r$=2.915)*

It is immediately apparent that the two forces differ greatly, and we would expect the added mass to play a larger part at such high velocities.

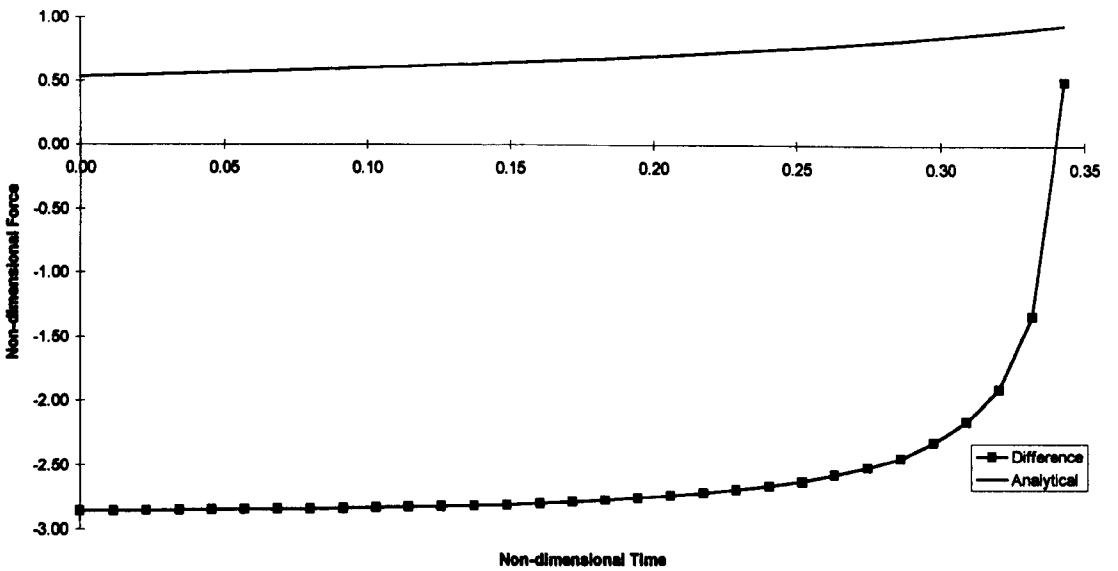


*Graph 4.55 Comparison of analytical added mass and force difference for and exiting box ($F_r$=2.915)*

However, the theory does not account for such a large difference. Considering the pressure distribution we see that there are complications at the corners as expected, resulting in large negative pressures which obviously impact the force calculations given above.

| Label | a | b | c | d | e | f | g | h |
|---|---|---|---|---|---|---|---|---|
| Time | 0 | 0.05 | 0.09 | 0.14 | 0.18 | 0.23 | 0.27 | 0.32 |

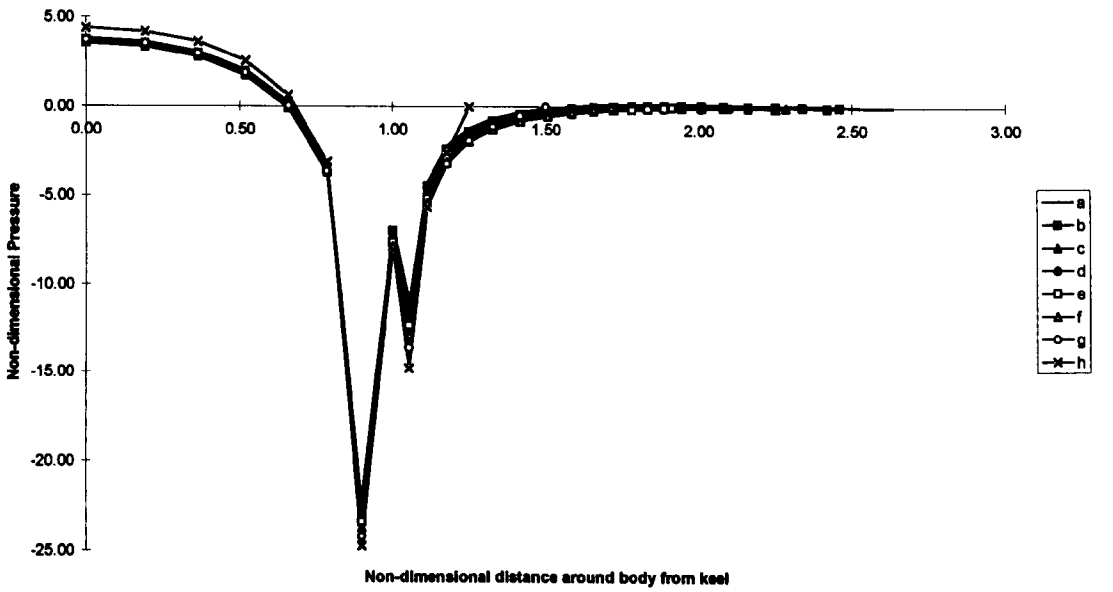


*Graph 4.56 Non-dimensional pressure on half wetted surface of an exiting box ($F_r$=2.915)*

The resolution in Graph 4.56 makes it difficult to separate the results for each time step, so Graph 4.57 provides a closer view.

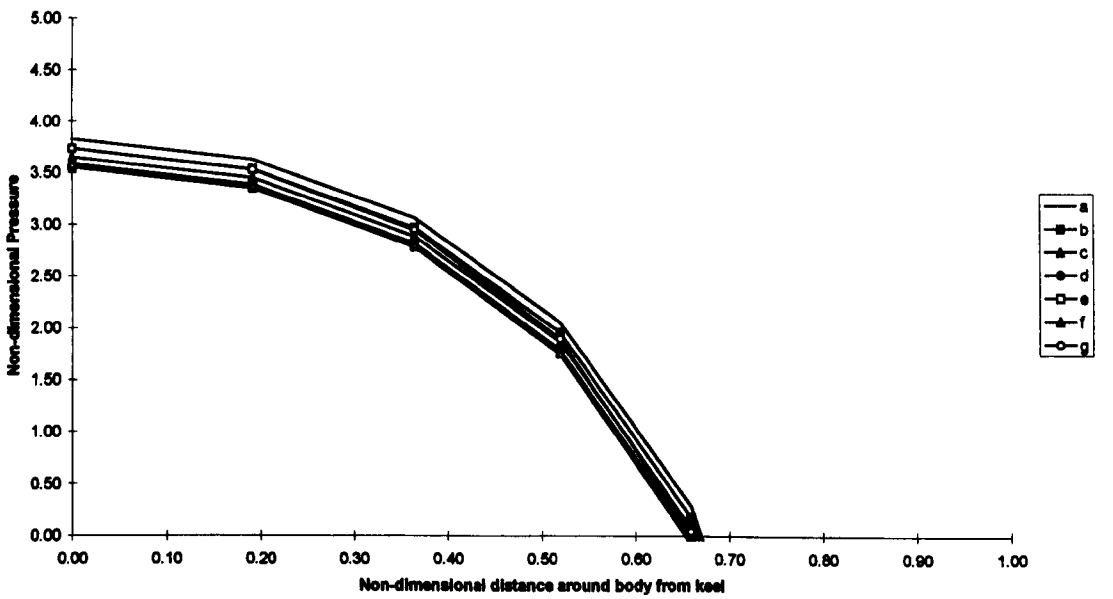


*Graph 4.57 Close-up of Non-dimensional pressure on half wetted surface of an exiting box ($F_r$=2.915)*

The free-surface profile, Graph 4.58, shows the large draw-down involved in such a fast motion, and when considered over such a short time span it is easy to see why the analytical theory has limited applicability.

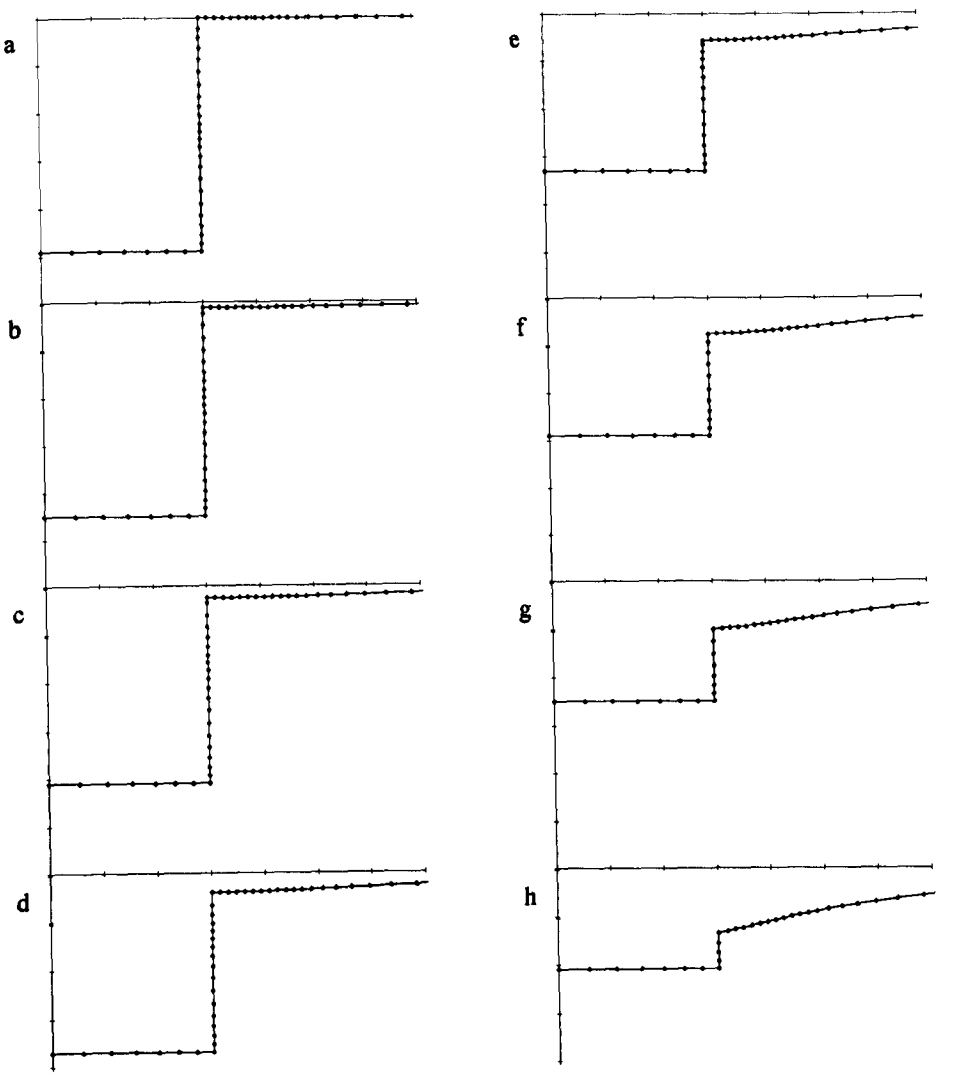


*Graph 4.58 Free-surface profile of exiting box ($F_r$=2.915)*

### *Knuckle*

Finally, we consider a knuckle body exiting the fluid domain. We follow the pattern of results used previously with a body of height 2, vertex height 1, half angle $\pi/4$ and initial depth -1.67 exiting with Froude number 0.117.

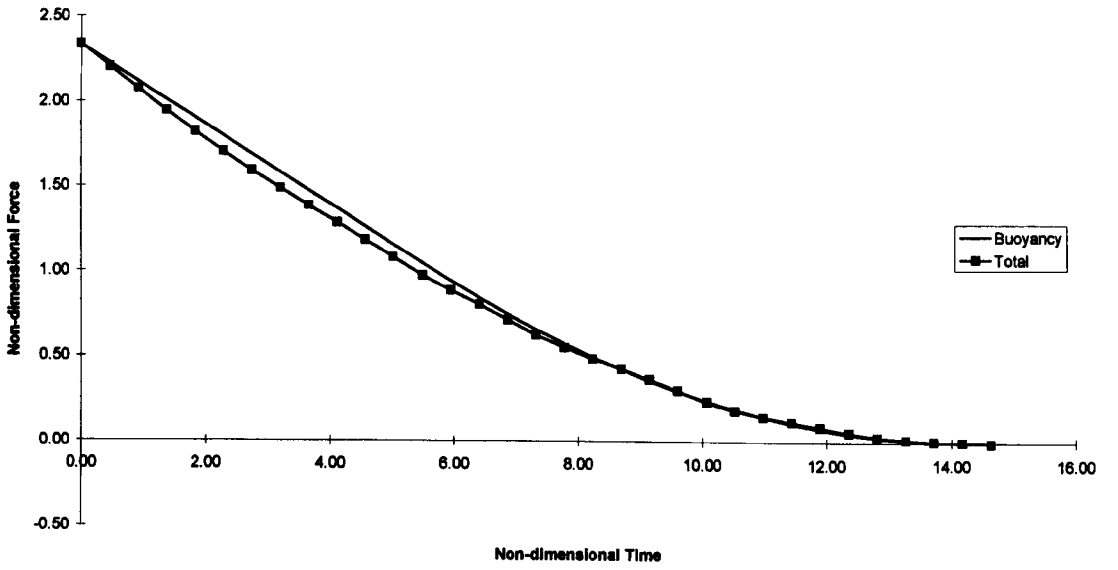


*Graph 4.59 Comparison of total force and buoyancy force for an exiting knuckle ($\alpha=\pi/4$, $F_r=0.117$)*

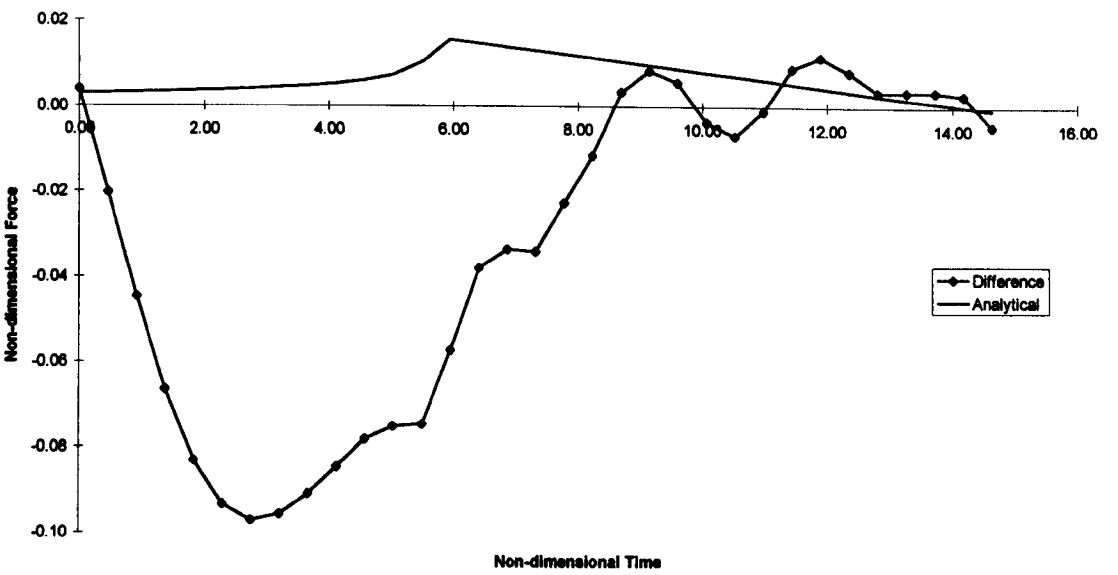


*Graph 4.60 Comparison of analytical added mass and force difference for an exiting knuckle ($\alpha=\pi/4$, $F_r=0.117$)*

The sudden change in gradient at non-dimensional time 6.0 is caused by the transition from knuckle body to wedge as the intersection point passes around the knuckle. Considering such a discontinuity the theory copes well, and achieves a somewhat smoother transition. However, that is offset by the fact that apart from the good initial agreement, the theory underestimates the force difference drastically.

| Label | a | b | c | d | e | f | g | h |
|---|---|---|---|---|---|---|---|---|
| Time | 0 | 1.83 | 3.66 | 5.49 | 7.32 | 9.15 | 10.98 | 12.81 |

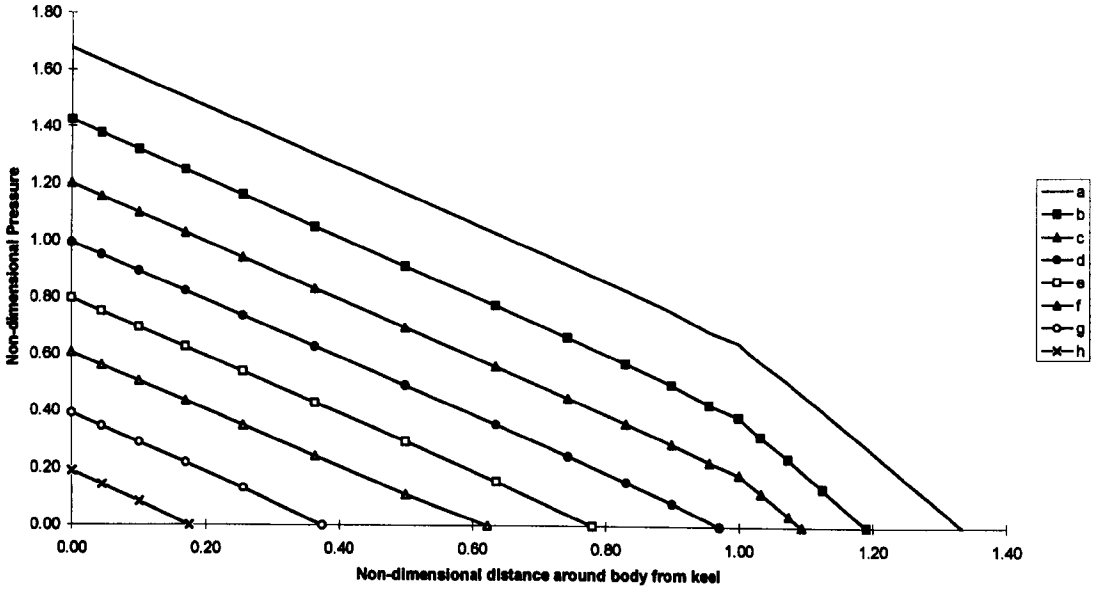


*Graph 4.61 Non-dimensional pressure on half wetted surface of an exiting knuckle ($\alpha=\pi/4$, $F_r=0.117$)*

The free-surface profile is rather uneventful, we note a small draw-down in stage *b*, and some wave propagation that results from this in *c* onwards, as we have already demonstrated in the box body examples.

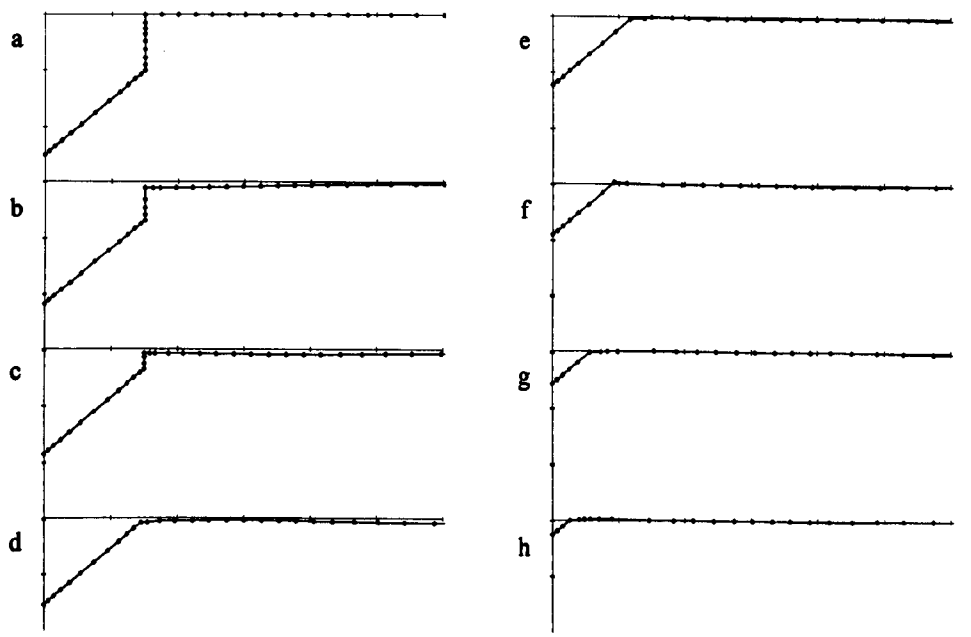


*Graph 4.62 Free-surface profile of exiting knuckle ($\alpha=\pi/4$, $F_r=0.117$)*

**Next the Froude is increased to 0.233.**

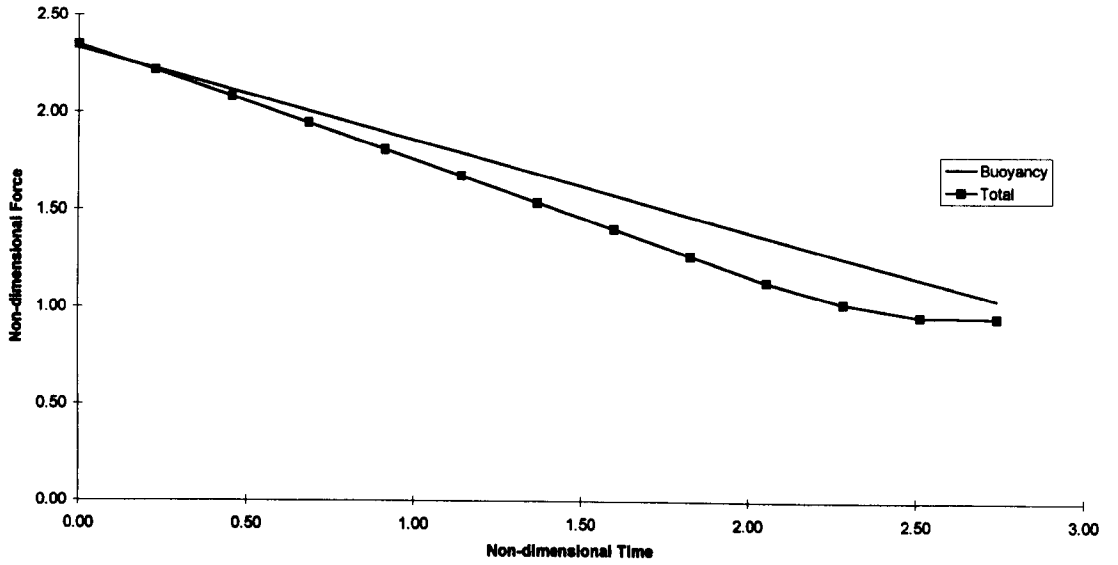


*Graph 4.63 Comparison of total force and buoyancy force for an exiting knuckle ($\alpha=\pi/4$, $F_r=0.233$)*

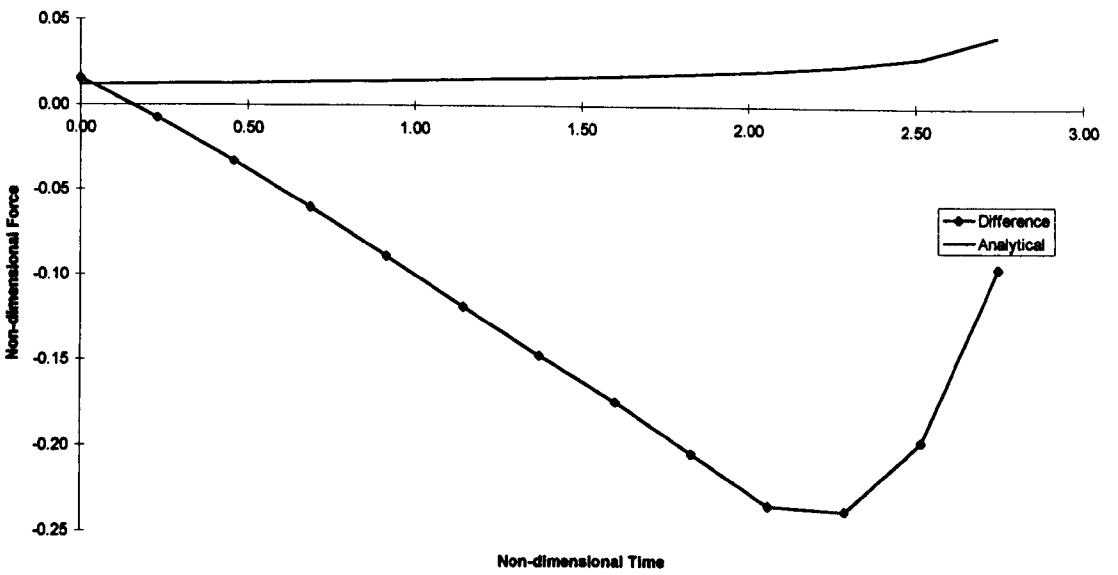


*Graph 4.64 Comparison of analytical added mass and force difference for an exiting knuckle ($\alpha=\pi/4$, $F_r=0.117$)*

Once again initial agreement is good, but the later stages are more disparate than the slower case.

| Label | a | b | c | d | e | f | g |
|---|---|---|---|---|---|---|---|
| Time | 0 | 0.46 | 0.91 | 1.37 | 1.83 | 2.29 | 2.74 |

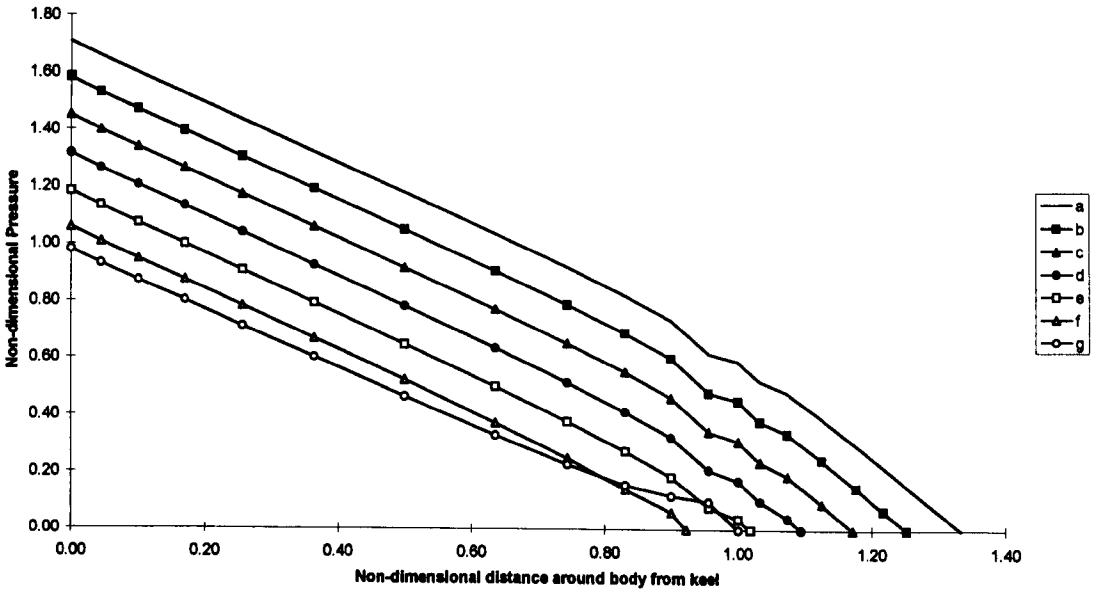


*Graph 4.65 Non-dimensional pressure on half wetted surface of an exiting knuckle ($\alpha=\pi/4$, $F_r=0.233$)*

We see larger movements in the free-surface than in the previous example, rather than propagating waves the intersection point moves down the body (producing the now familiar draw-down) and then begins to follow the body up.

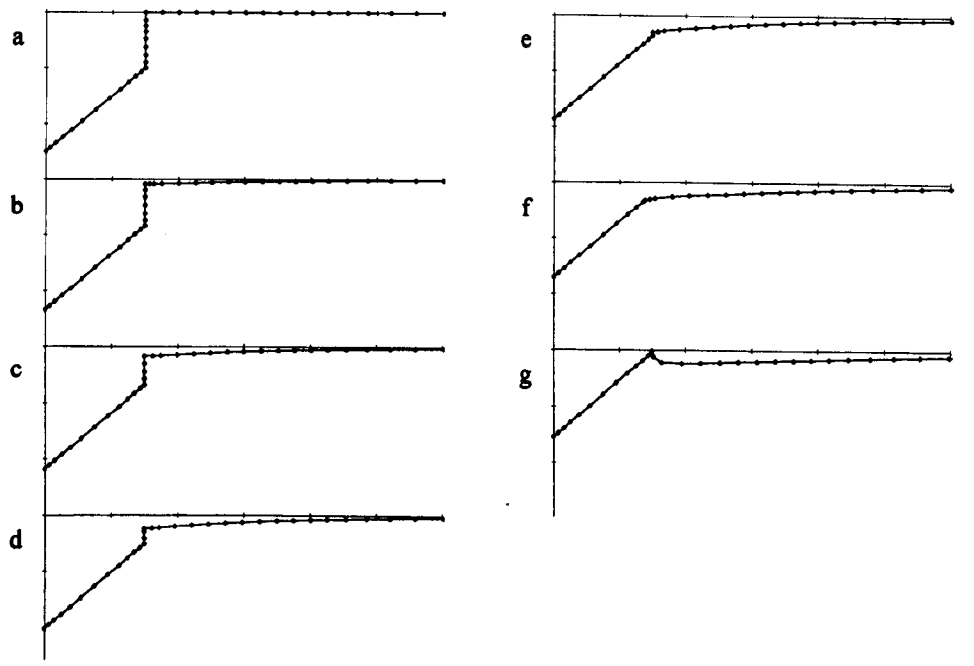


*Graph 4.66 Free-surface profile of exiting knuckle ($\alpha=\pi/4$, $F_r=0.233$)*

Higher Froude numbers proved difficult for the knuckle body exit, so we have taken a step back and slowed the motion to a Froude number of 0.058.

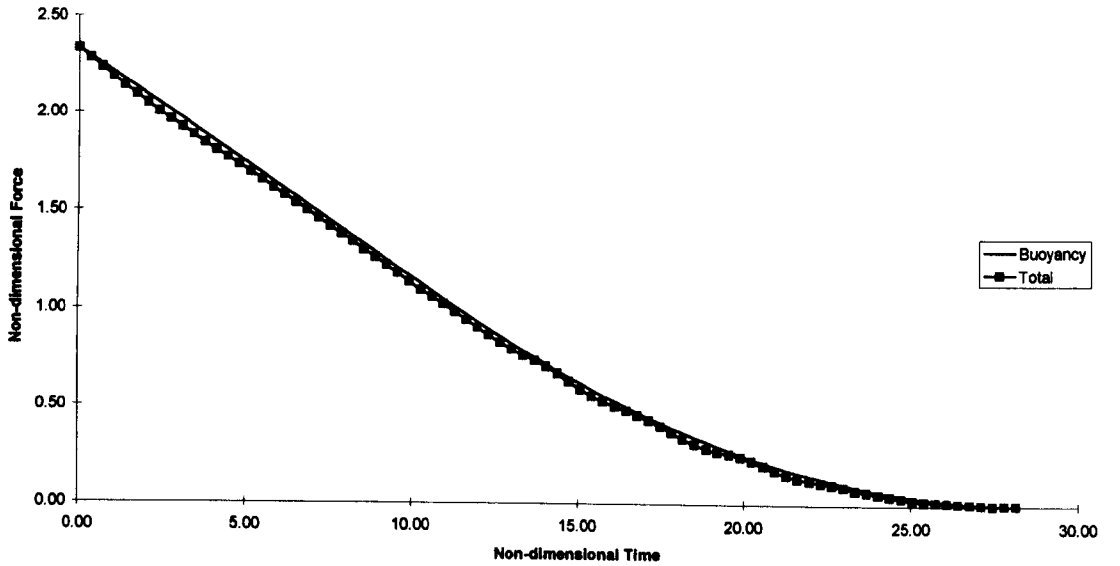


*Graph 4.67 Comparison of total force and buoyancy force for an exiting knuckle ($\alpha=\pi/4$, $F_r=0.058$)*

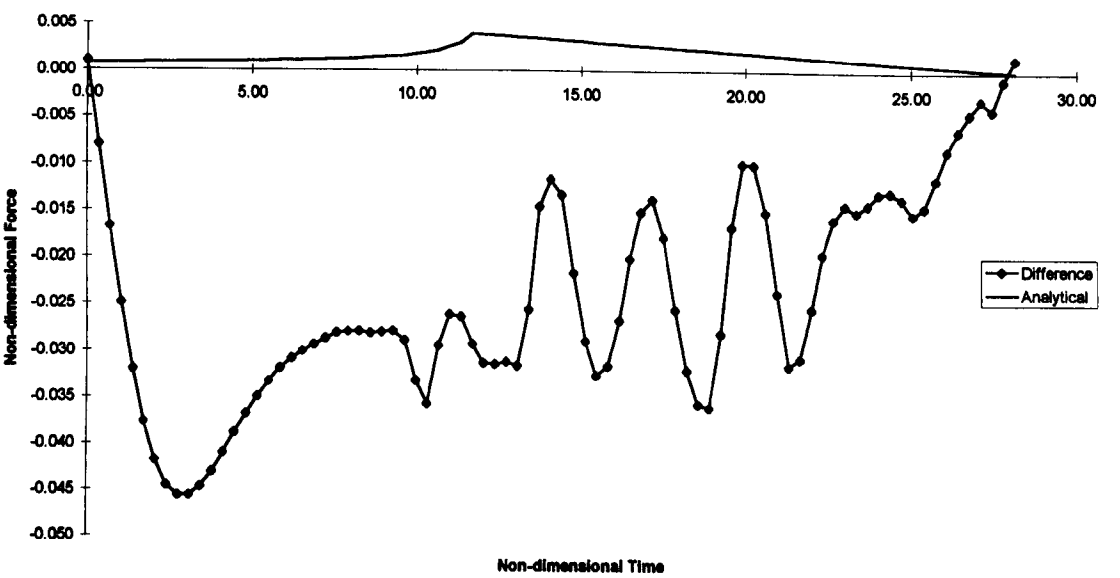


*Graph 4.68 Comparison of analytical added mass and force difference for an exiting knuckle ($\alpha=\pi/4$, $F_r=0.058$)*

We suspect that the curve fluctuation between $t = 10$ and $t = 25$ is caused by a physical occurrence rather than numerical error. To test this we have plotted the locus of the intersection point of the free-surface and the body between these times in Graph 4.69. It is clear from this graph that the fluctuations in the total force, and so the force difference, are a direct result of the intersection point moving up and down the body in a "lapping" motion.

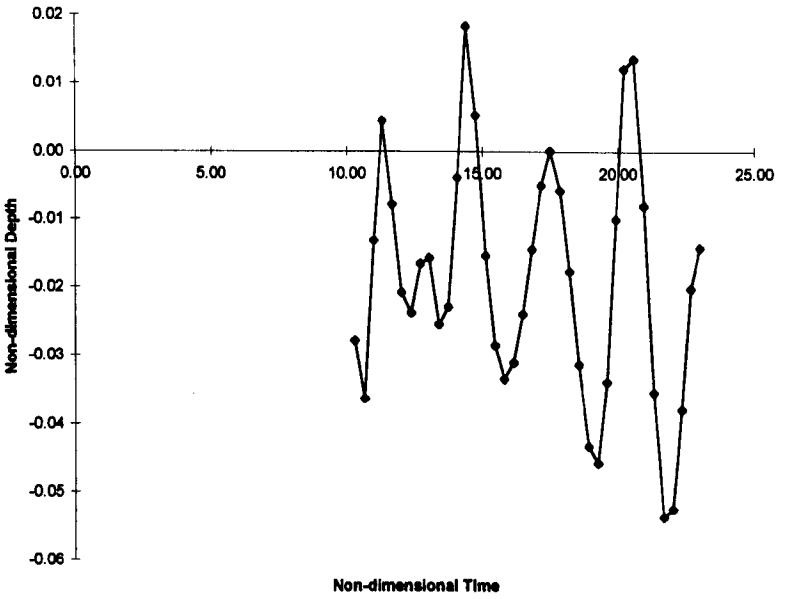


*Graph 4.69 Locus of intersection point for given time*

| Label | a | b | c | d | e | f | g | h | i |
|---|---|---|---|---|---|---|---|---|---|
| Time | 0 | 3.43 | 6.86 | 10.29 | 13.72 | 17.15 | 20.59 | 24.02 | 27.45 |

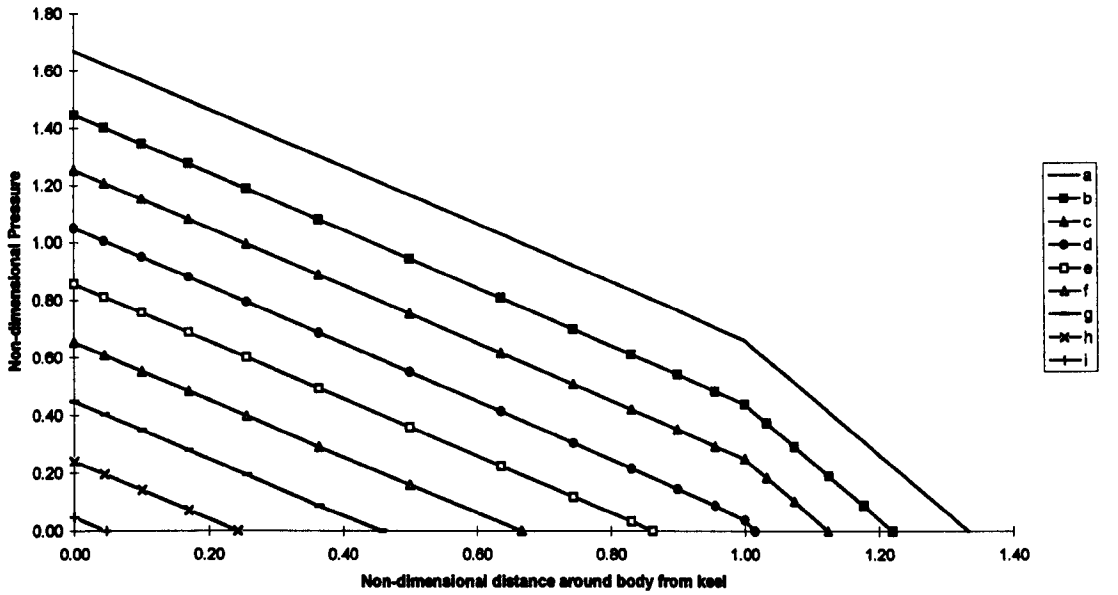


*Graph 4.70 Non-dimensional pressure on half wetted surface of an exiting knuckle ($\alpha=\pi/4$, $F_r=0.058$)*

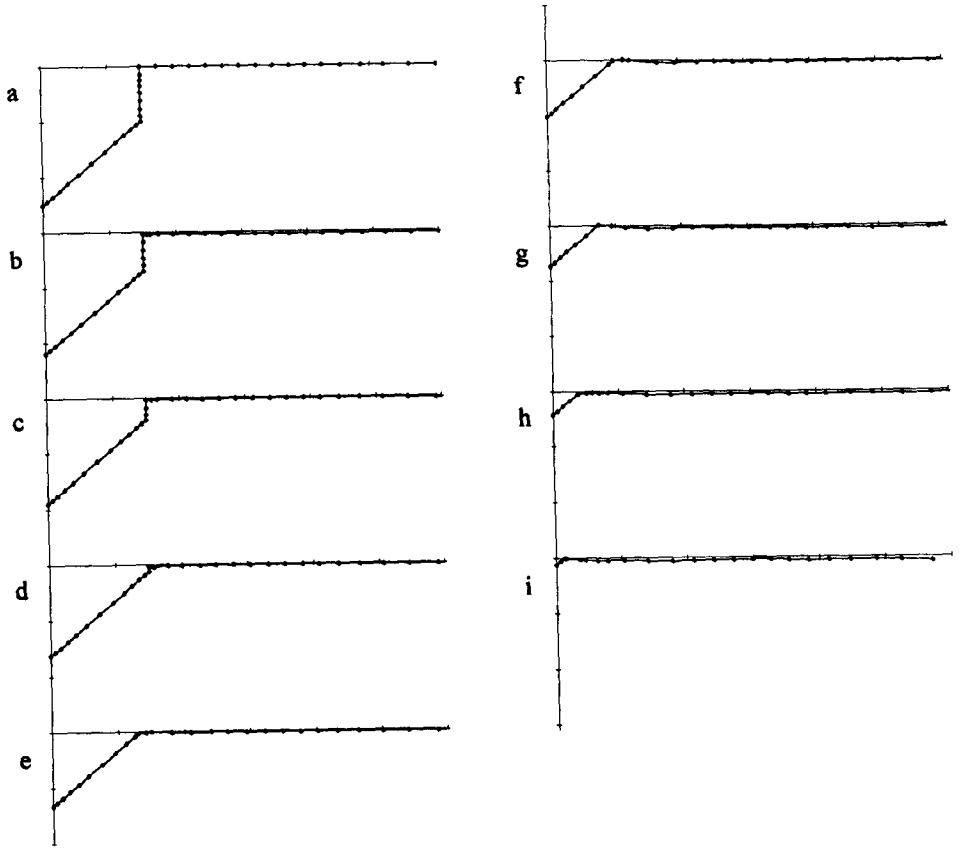


*Graph 4.71 Free-surface profile of exiting knuckle ($\alpha=\pi/4$, $F_r=0.058$)*

## Conclusions

Analysis of the graphs has shown that the theory copes well in the early time steps with accelerated exit of all body forms. Constant velocity exit, however, appears to be more illusive. In both cases the draw-down effect is not included and can account for some of the difference at larger time, refer to Chapter 6 for investigation. The numerical results for the box, and to a lesser extent for the knuckle, obviously do not predict the singular pressures at the corners. However it was shown that this singularity is integrable, and so force comparisons of numerical and analytical results, whilst degraded in some cases, are still possible.

# Chapter 5 Body Entry into Initially Calm Water

## *A comparison of numerical and analytic theories used to calculate the forces experienced by a body entering the fluid domain*


### Abstract

This chapter reviews the application of two non-linear theories, analytical and numerical, to the problem of a body entering the fluid domain. The objective of this work is to appraise the analytical model and suggest modifications that would allow better approximation of the non-linear method for use in practical calculations such as extreme ship motions and slamming. Presented are the numerical results for constant velocity, and constant acceleration, entry of bodies into the fluid domain. From these results conclusions are drawn, indicating the limitations of the current analytical theory and the future direction of this research. The bodies we consider are those of a wedge, a box and a knuckle (inverted pentagon).


### Introduction

This chapter is concerned with obtaining and comparing data from the fully non-linear solution of the body-entry problem and an analytical solution of the same problem. The main priority will be the forces acting on the body.

As the body enters the fluid domain it experiences hydrostatic and hydrodynamic pressures upon its wetted surface. These are integrated to give hydrodynamic forces which are due to the interaction with the fluid particles and their subsequent acceleration. The analytical theory is also implemented in an attempt to produce a practical method of calculation, and the two sets of force results are compared. The motivation is to present a simpler theory that is able to calculate the forces experienced by the body without the need for extensive numerical calculations, and which could be included in strip theory codes dealing with large-amplitude (slamming) calculations.

In the following sections we consider the body entering the fluid at both constant acceleration and constant velocity. For each we examine all body shapes (wedge, box and knuckle) for a variety of initial conditions. Where possible we use comparable initial conditions to allow for comparison between these body shapes.

For each case considered we present four graphs:

1. A comparison of the total vertical force experienced by the body and the buoyancy force. The vertical force is calculated using the fully non-linear numerical method. The buoyancy force is calculated using $\rho g \forall$ where $\forall$ is the time-dependent volume of the body below the initial free surface.

2. We consider the added mass force, $F_a$, and compare it with the difference between the total vertical force and the buoyancy force as considered in the first graph. The intention is to examine whether the added mass force and the buoyancy force together account for the total force given by the fully non-linear calculation.

3. The pressure distribution across the wetted surface of the body as a time stepped progression. The previous graphs displays the total force acting upon the body, the pressure distribution is presented to illustrate how these forces arise. Each graph contains several time intervals taken over the course of the body motion.

4. The free-surface profiles given at the time intervals used in the pressure distribution.

All graphs are non-dimensional, as follows:

- Time - multiplied by $\sqrt{\frac{g}{d_e}}$ where $d_e$ is the submerged depth at equilibrium and g is gravity.
- x and y co-ordinates - divided by $d_e$ .
- Force - divided by the buoyancy force given by $\rho g \forall$ where $\forall$ is the submerged volume at equilibrium.
- Pressure - divided by $d_e \rho g$ .

One of the following parameterises the problem :

- Acceleration - divided by $g$, in the constant acceleration case.
- The Froude number is defined as $\frac{v^2}{\sqrt{g d_e}}$, where $v$ is the velocity in the constant velocity case.

## Constant acceleration

The following section gives the results produced by constant acceleration entry of a body into the fluid domain. We consider constant acceleration as a simplification of free motion. Setting the acceleration to be constant allows easy comparison of these results with values calculated using the analytical method.

For each body shape we consider constant accelerated exit at $g/5$ and $g/2$.

Tables containing the sample numerical results can be found in Appendix A.

## *Wedge*

The first case under consideration is that of constant acceleration at $g/5$ of a wedge with a half angle of 45 degrees, height of 1.7 and an initial vertex depth of -0.33 (where the minus sign indicates below the free surface). Note that this vertex depth introduces a characteristic length scale into the problem, so the resulting flow cannot be self-similar, as in the usual slamming calculations where the body enters the fluid at the vertex tip at $t = 0$. We also have included gravity in the calculations, whereas self-similarity also requires $g = 0$.

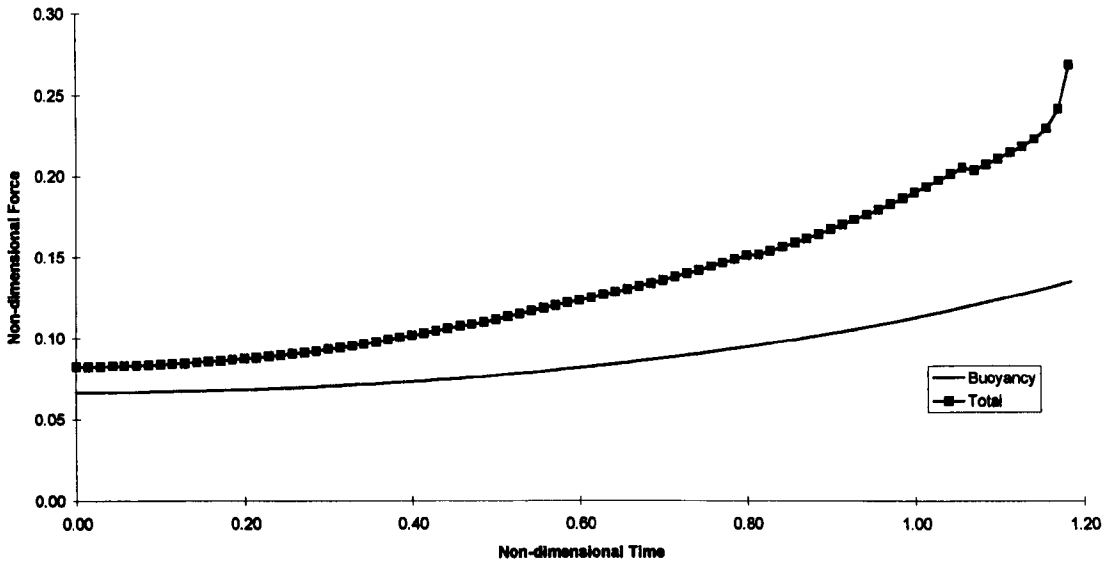


*Graph 5.1 Comparison of Total Force and Buoyancy Force - Entering Wedge ($\alpha=\pi/2$, $a/g=0.2$)*

The gradient of the buoyancy curve in Graph 5.1 does not agree with that of the total force as well as in the exit case. We expect the forces to diverge with time since the body volume increases with time, making larger contributions to the force calculations. We note that the total force overestimates the buoyancy, a consequence of "up-rise" rather than the "draw-down" in the exit case, this will be more pronounced as the body velocity increases.

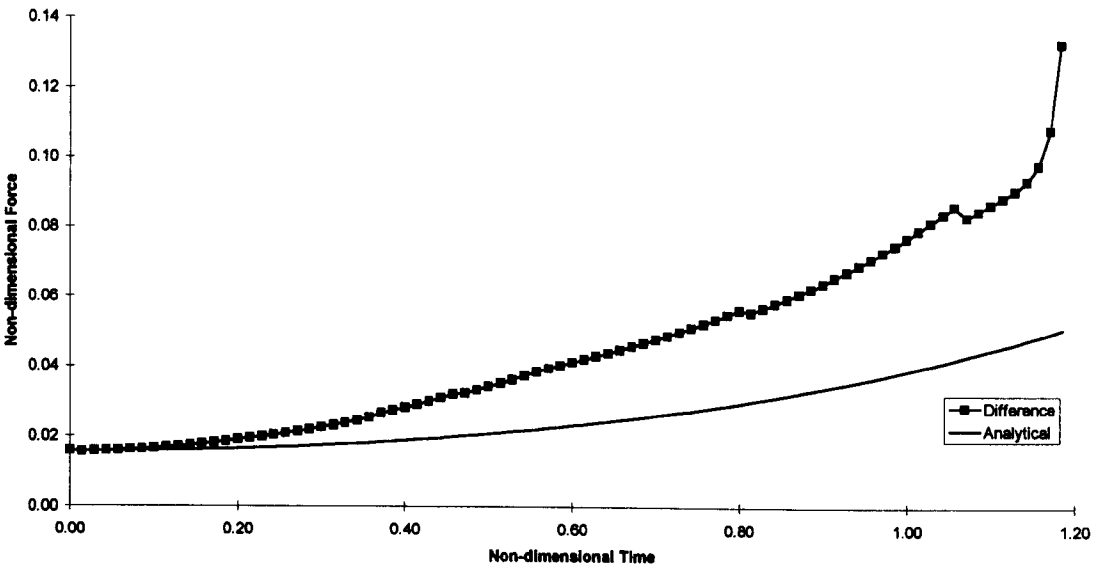


*Graph 5.2 Comparison of Analytical Added Mass and Force Difference - Entering Wedge ($\alpha=\pi/2$, $a/g=0.2$)*

Initial inspection of Graph 5.2 indicates that the added mass theory does not perform as well for entry as for exit. We do have good agreement for small $t$, although the duration of this agreement is shorter than that for exit. This can be attributed to the shorter duration of the complete motion before breakdown. As is evident in Graph 5.4 large surface motions develop more rapidly than in the exit scenario, and as already demonstrated the larger the surface motion the greater the detrimental effects on the added mass theory (since we assume a fixed surface).

Taking pressure calculations at the following non-dimensional times

| Label | a | b | c | d | e | f | g | h | i |
|---|---|---|---|---|---|---|---|---|---|
| Time | 0 | 0.14 | 0.29 | 0.43 | 0.57 | 0.71 | 0.86 | 1.00 | 1.14 |

provides us with a graphical representation of the pressure gradients across the wetted surface of the half-body.

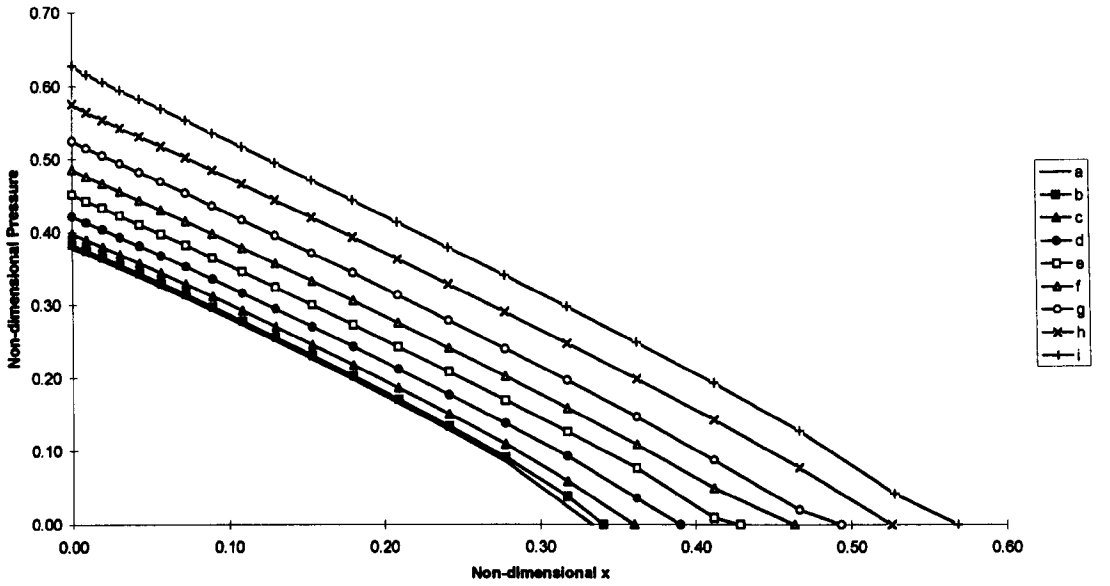


*Graph 5.3 Non-dimensional initial pressure on half wetted surface of entering wedge ($\alpha=\pi/2$, $a/g=0.2$)*

We note the free-surface profiles at these times in Graph 5.4.

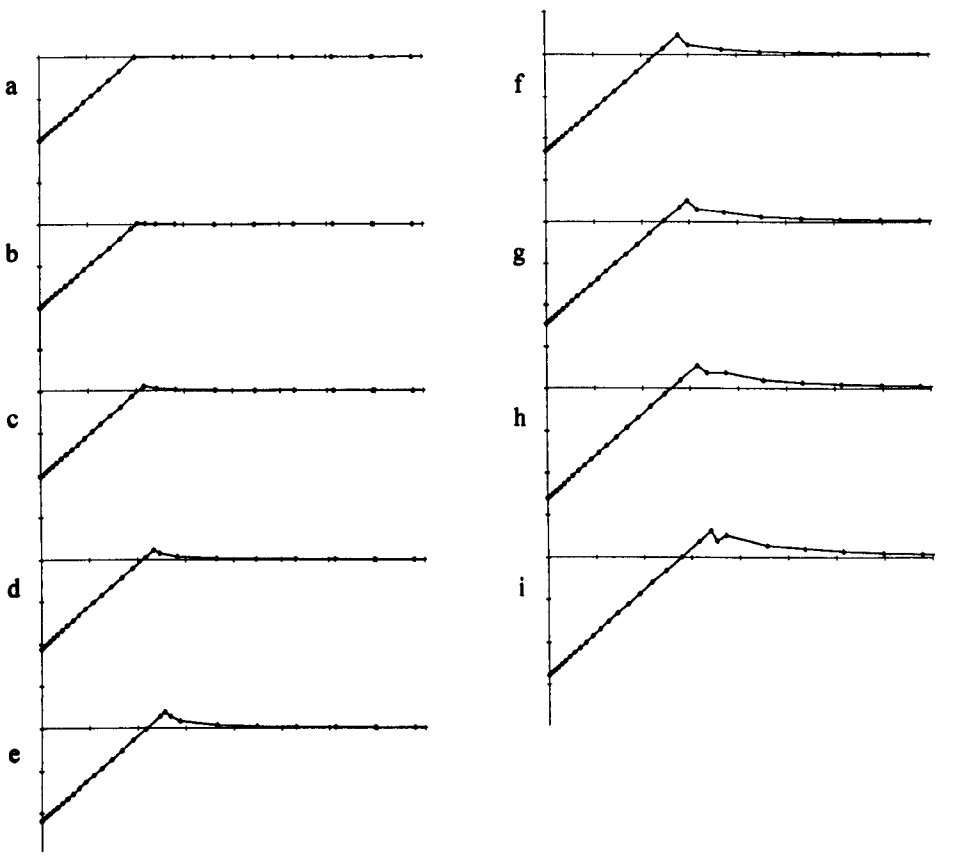


*Graph 5.4 Free-surface profile for entering wedge ($\alpha=\pi/2$, $a/g=0.2$)*

We know consider the same body entering the fluid at the higher constant acceleration of $g/2$.

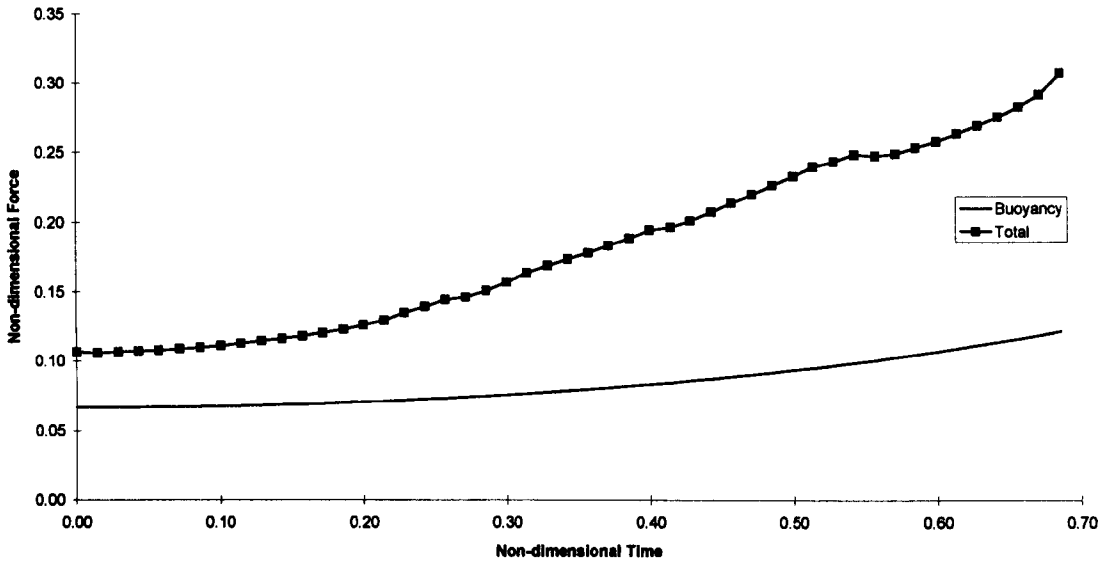


*Graph 5.5 Comparison of Total Force and Buoyancy Force - Entering Wedge ($\alpha=\pi/4$, $a/g=0.5$)*

The forces at $t=0$ are noticeably different in Graph 5.5 a result of the body starting above its equilibrium position. The added mass calculations matches this difference, as we see below

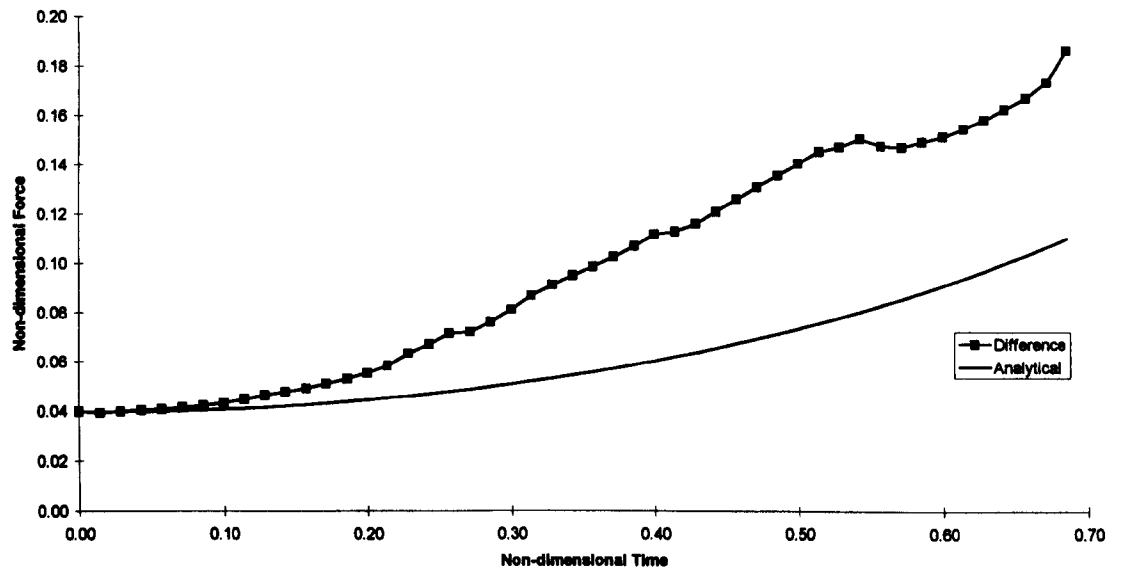


*Graph 5.6 Comparison of Analytical Added Mass and Force Difference - Entering Wedge ($\alpha=\pi/4$, $a/g=0.5$)*

Again, we consider the pressure gradients at the given times

| Label | a | b | c | d | e | f | g | h | i |
|---|---|---|---|---|---|---|---|---|---|
| Time | 0 | 0.09 | 0.17 | 0.26 | 0.34 | 0.43 | 0.51 | 0.60 | 0.69 |

With larger velocity (larger time) we have negative pressures near the free surface, attributable to jet formation. These can be seen in Graph 5.8.

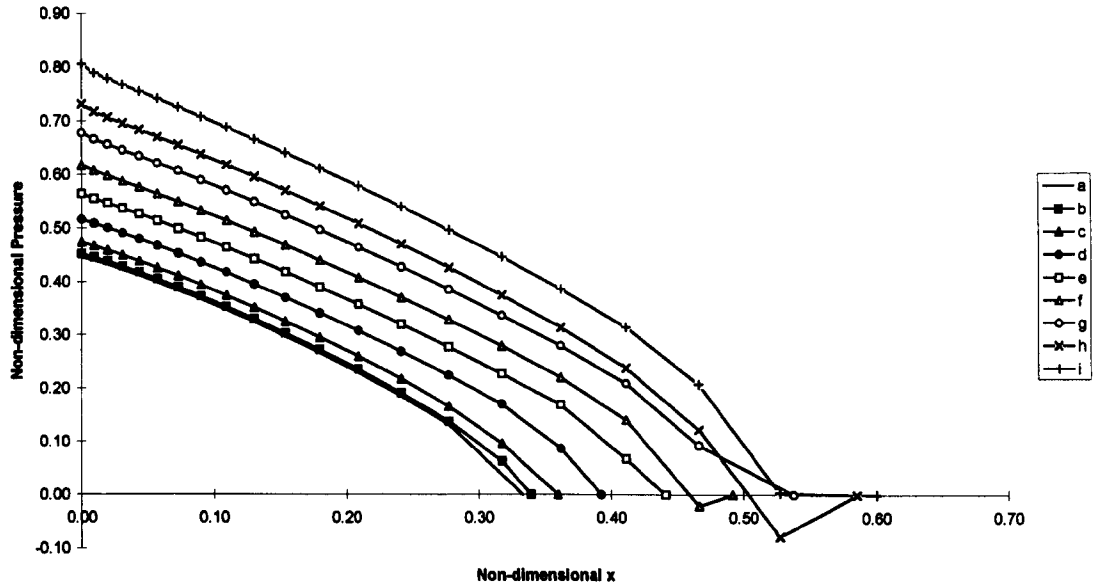


*Graph 5.7 Non-dimensional initial pressure on half wetted surface of entering wedge ($\alpha=\pi/4$, $a/g=0.5$)*

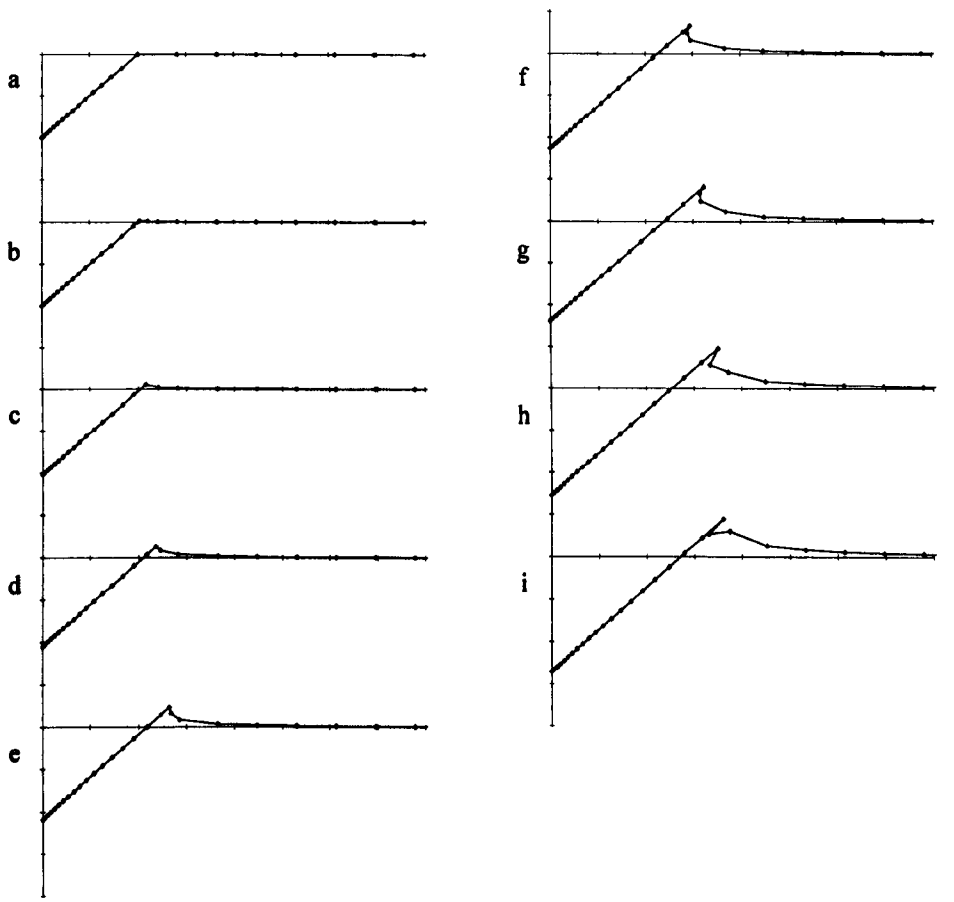


*Graph 5.8 Free-surface profile for entering wedge ($\alpha=\pi/4$, $a/g=0.5$)*

### *Box*

We now consider a box body of height 1.7, width 2 and an initial depth of -0.33 entering the fluid domain at a constant acceleration of $g/5$.

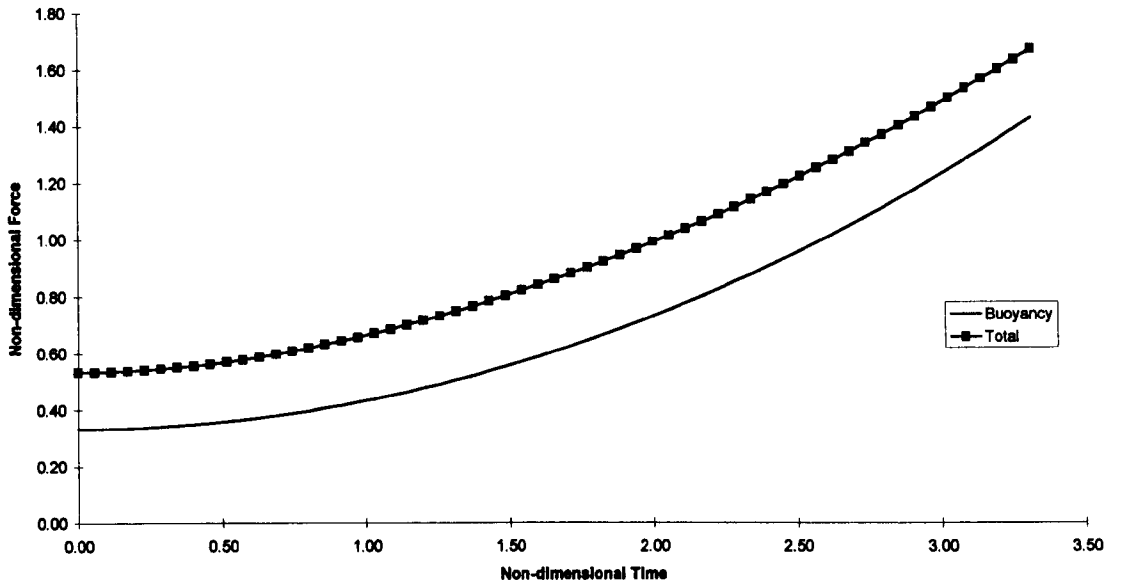


*Graph 5.9 Comparison of Total Force and Buoyancy Force - Entering Box (a/g=0.2)*

The agreement between the gradients of the two curves in Graph 5.9 is an improvement on the wedge entry. The fluid undergoes less violent motion upon entry of a wall-sided body. The added mass force has a very small gradient appearing almost constant.

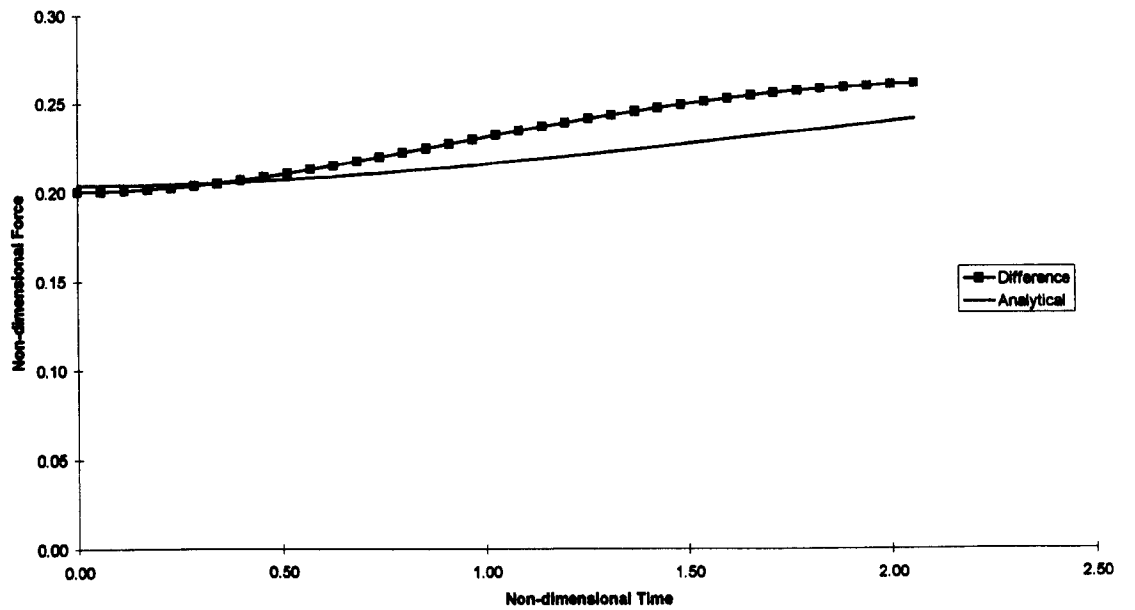


*Graph 5.10 Comparison of Analytical Added Mass and Force Difference - Entering Box (a/g=0.2)*

Considering the pressures at specified times gives a far different picture to those previously seen. We can see the effect the corner plays in the pressure distribution around the wetted surface, an effect already explained in Chapter 4.

| Label | a | b | c | d | e | f | g |
|---|---|---|---|---|---|---|---|
| Time | 0 | 0.46 | 0.91 | 1.37 | 1.83 | 2.29 | 2.74 |

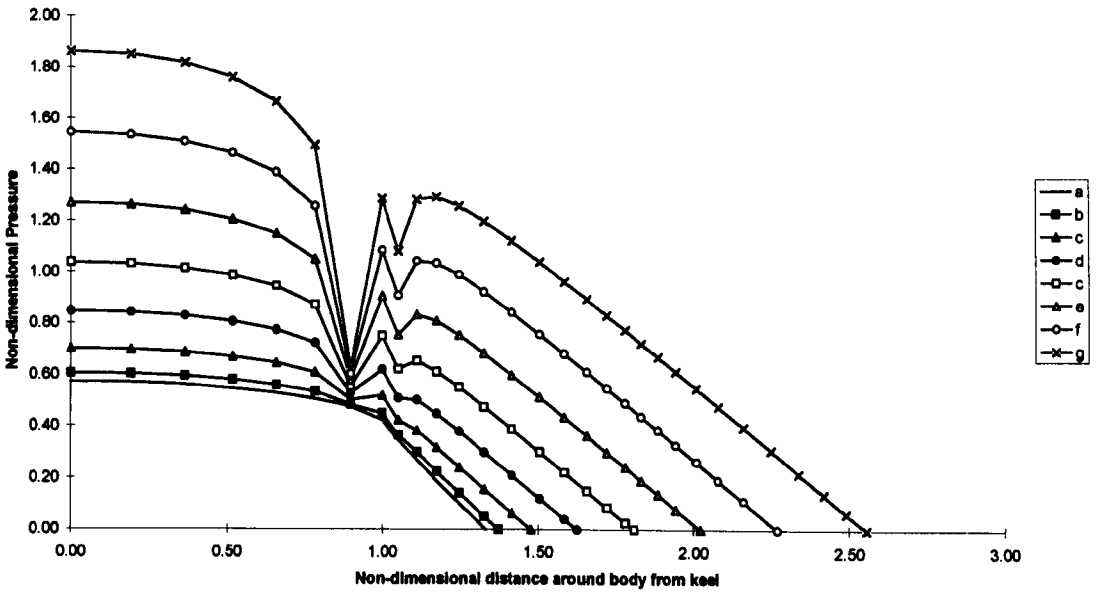


*Graph 5.11 Non-dimensional initial pressure on half wetted surface of entering box (a/g=0.2)*

The free-surface profiles in Graph 5.12 demonstrate a smoother motion. The surface rises more as a step than a jet, the body affects a larger portion of the fluid and its surface (not as localised as the wedge motion) due to the flat bottom.

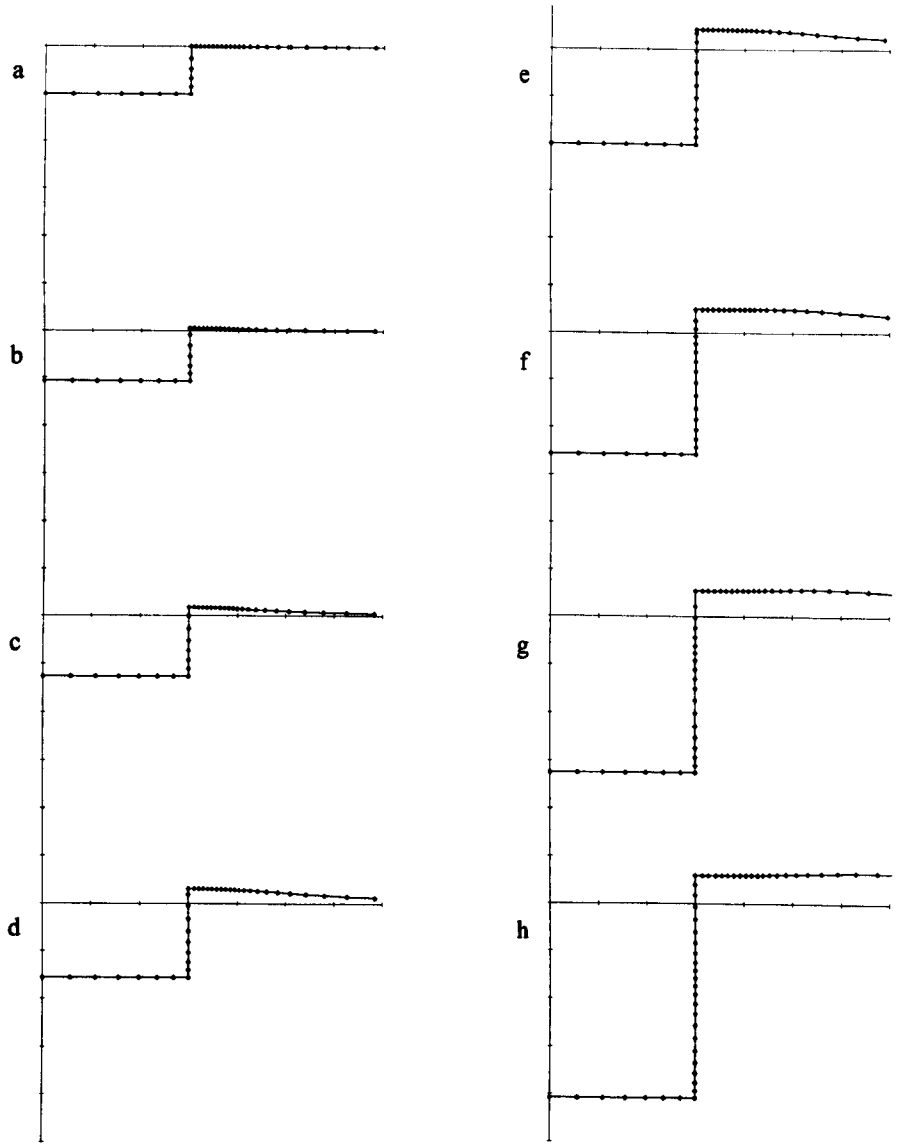


*Graph 5.12 Free-surface profile for entering box (a/g=0.2)*

Let us consider the same body, at an acceleration of $g/2$. The higher acceleration gives rise to larger differences between the two force calculations, but these differences are still accounted for by the added mass for small *t*.

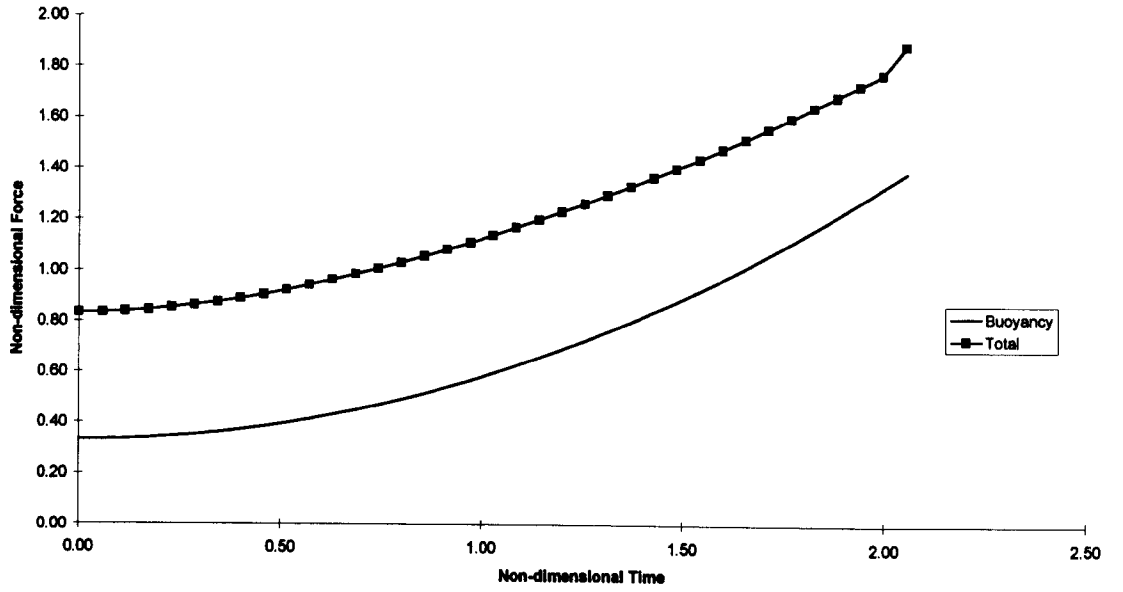


*Graph 5.13 Comparison of Total Force and Buoyancy Force - Entering Box (a/g=0.5)*

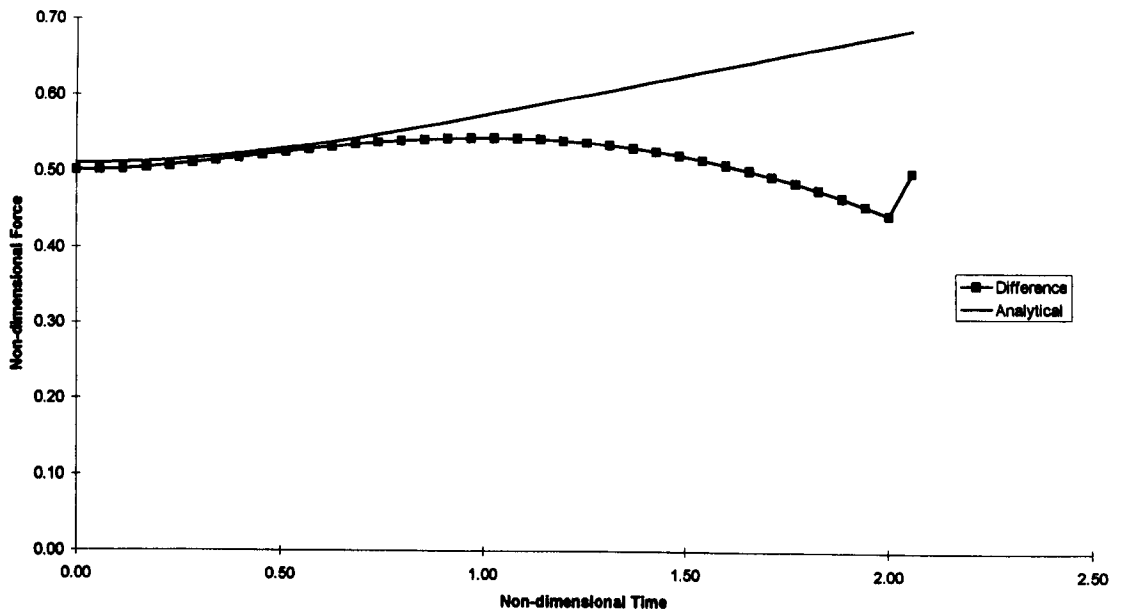


*Graph 5.14 Comparison of Analytical Added Mass and Force Difference - Entering Box (a/g=0.5)*

Consider the pressure at the given times.

| Label | a | b | c | d | e | f | g | h |
|---|---|---|---|---|---|---|---|---|
| Time | 0 | 0.29 | 0.63 | 0.86 | 1.14 | 1.43 | 1.72 | 2.00 |

We see the singularity of the body corner affecting the pressure calculation. As discussed in Chapter 4, the numerical scheme attempts to calculate a pressure value at the singularity which, as you would expect, is wrong.

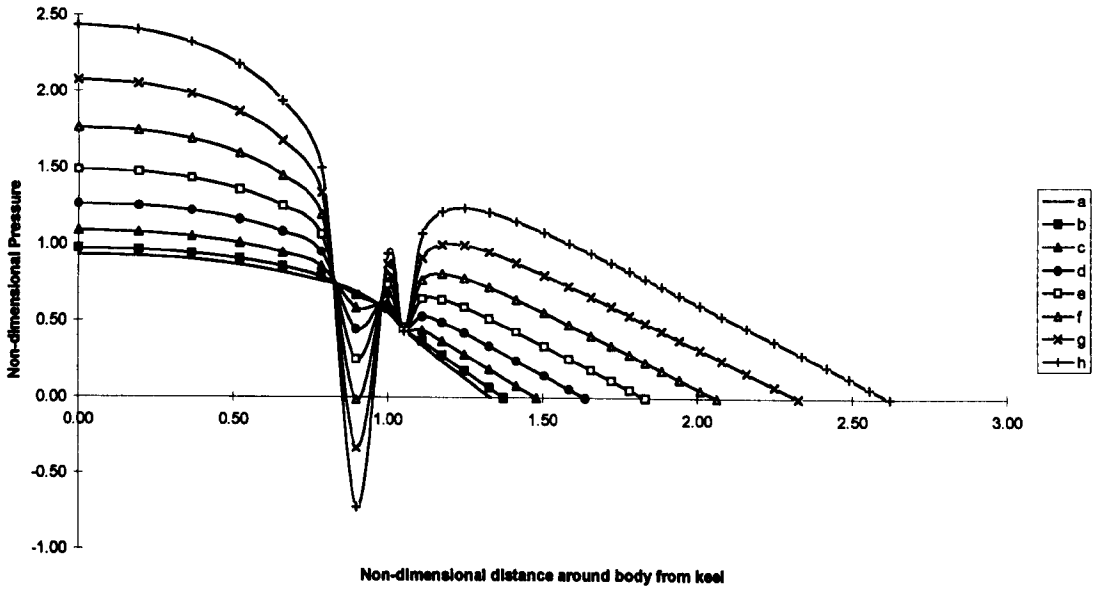


*Graph 5.15 Non-dimensional initial pressure on half wetted surface of entering box (a/g=0.5)*

Again the profiles show the steady rise of the surface, with a slightly more localised effect.

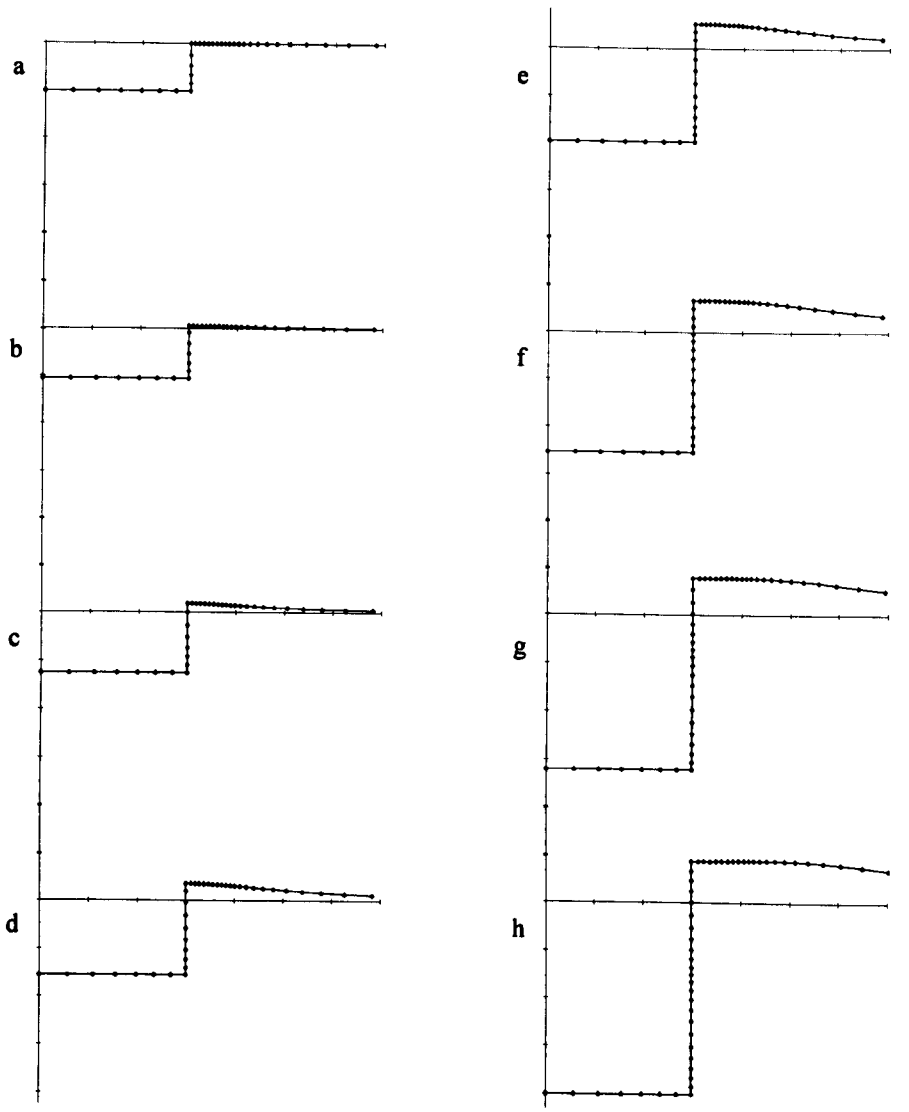


*Graph 5.16 Free-surface profile for entering box (a/g=0.5)*

## *Knuckle*

Finally consider a knuckled body of total height 2, apex height 1, half angle $\pi/4$ and initial depth -1.0. The increased initial submergence is to avoid the problems caused by the intersection point traversing the singularity at the body knuckle.

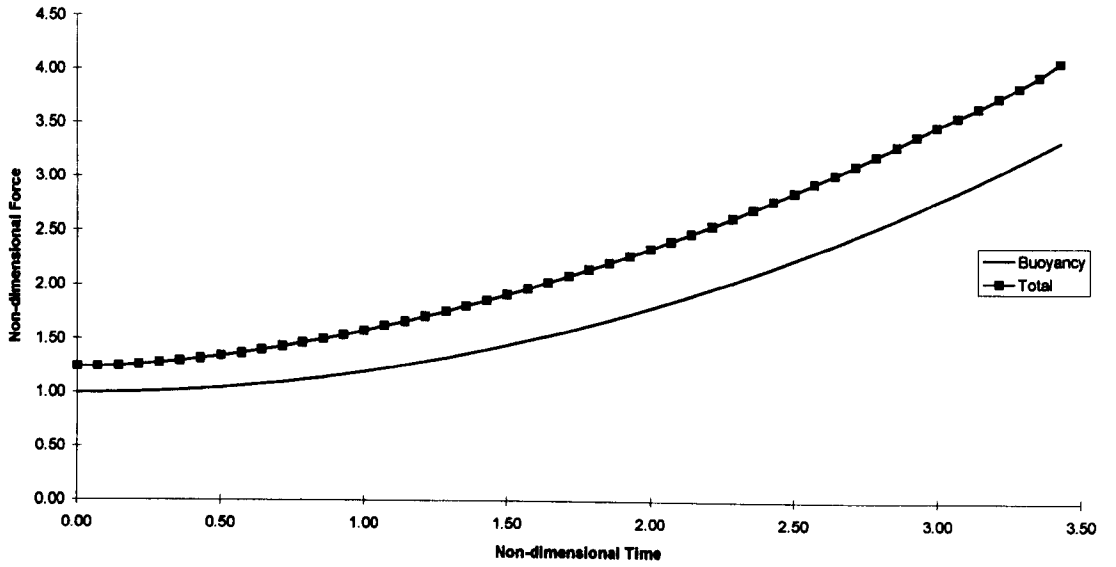


*Graph 5.17 Comparison of Total Force and Buoyancy Force - Entering Knuckle ($\alpha=\pi/4$, $a/g=0.2$)*

The forces correspond with those seen in the case of a box body, again due to the wall sides. However, as can be seen in Graph 5.18 the wedge portion of the body has a noticeable effect on the added mass calculation, producing results that approximate the force difference to a greater extent than those given previously for large $t$.

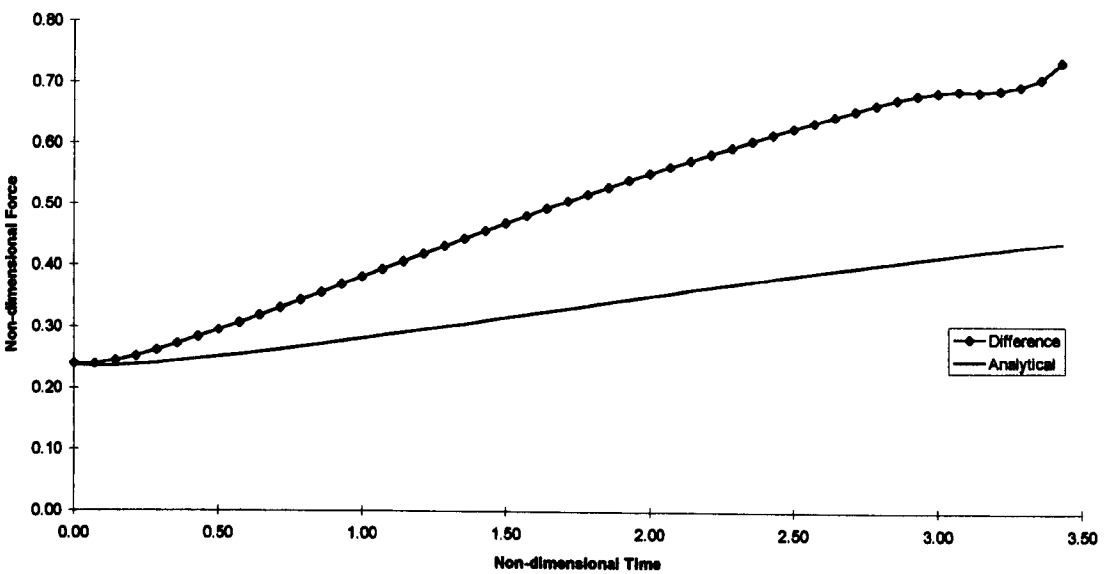


*Graph 5.18 Comparison of Analytical Added Mass and Force Difference - Entering Knuckle ($\alpha=\pi/4$, $a/g=0.2$)*

The singularities at the knuckles have a noticeable effect on the pressure gradients, but to a lesser extent than those of the box body for reason given in Chapter 4.

| Label | a | b | c | d | e | f | g | h | i |
|---|---|---|---|---|---|---|---|---|---|
| Time | 0 | 0.43 | 0.86 | 1.29 | 1.72 | 2.14 | 2.57 | 3.00 | 3.43 |

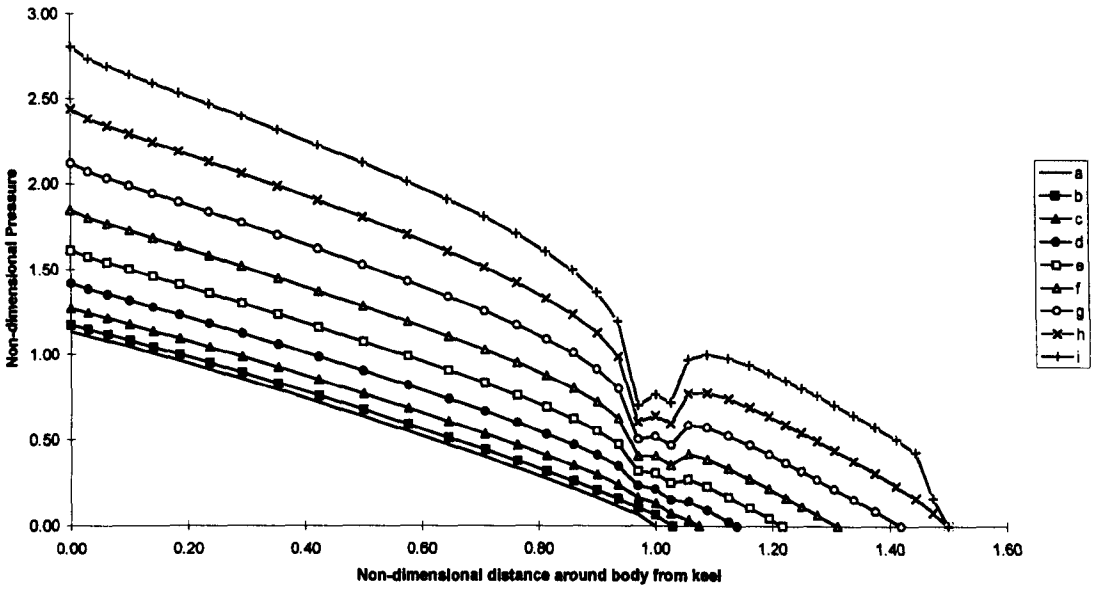


*Graph 5.19 Non-dimensional initial pressure on half wetted surface of entering knuckle ($\alpha=\pi/4$, $a/g=0.2$)*

The surface profiles can be related to those of the box body, as would be expected since the intersection point is always on the wall-sided part of the body. We do see an effect not seen in the box body profiles, at stage *g* the beginnings of a radiated wave can just be distinguished from the general "up-rise" of the surface.

We see that at stage *i* the top of the body is below the free surface. At this point we enforce an artificial condition fixing the intersection point to the top corner of the body. This produces a false free-surface profile but has no significant impact on the force calculations and so enables us to continue for several more time-steps.

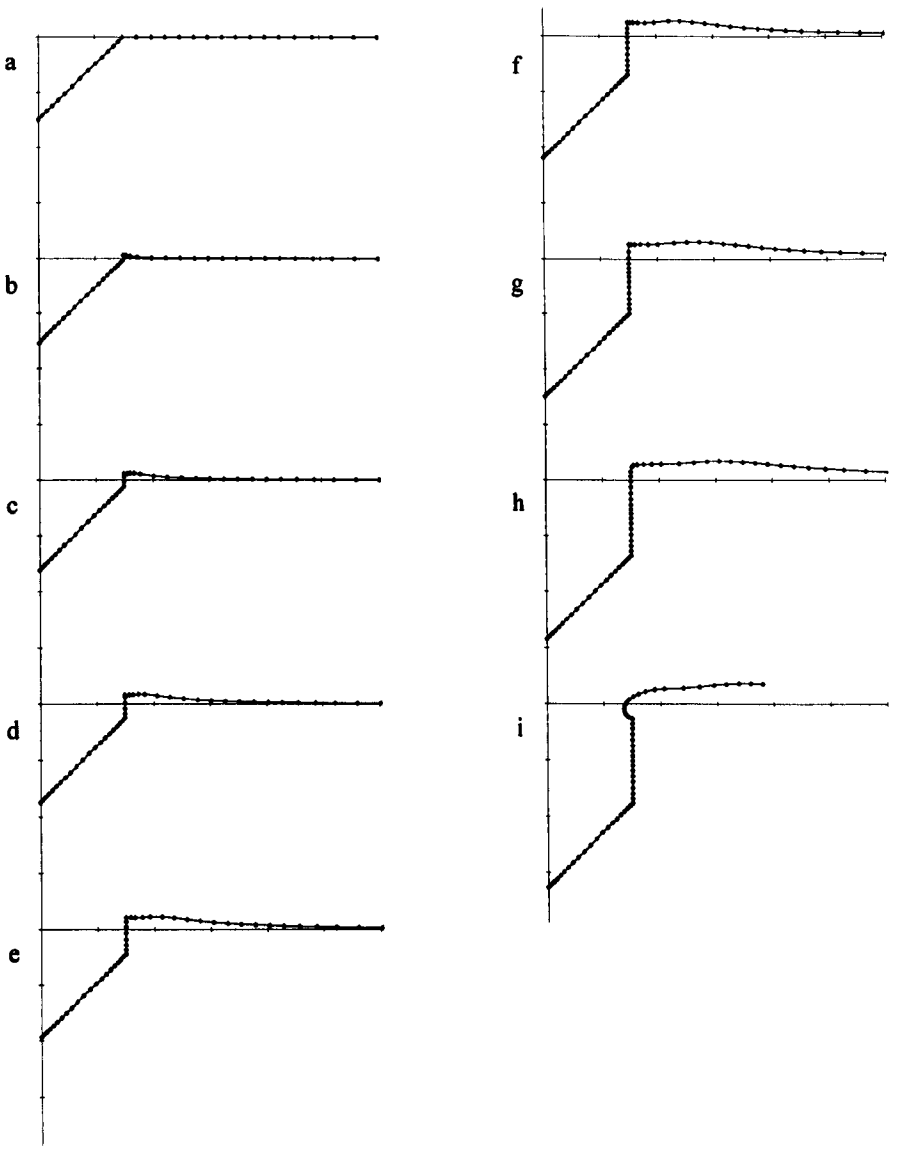


*Graph 5.20 Free-surface profile for entering knuckle ($\alpha=\pi/4$, $a/g=0.2$)*

Let us follow with the higher acceleration case, the body dimensions and initial depth remain the same but this time acceleration is $g/2$.

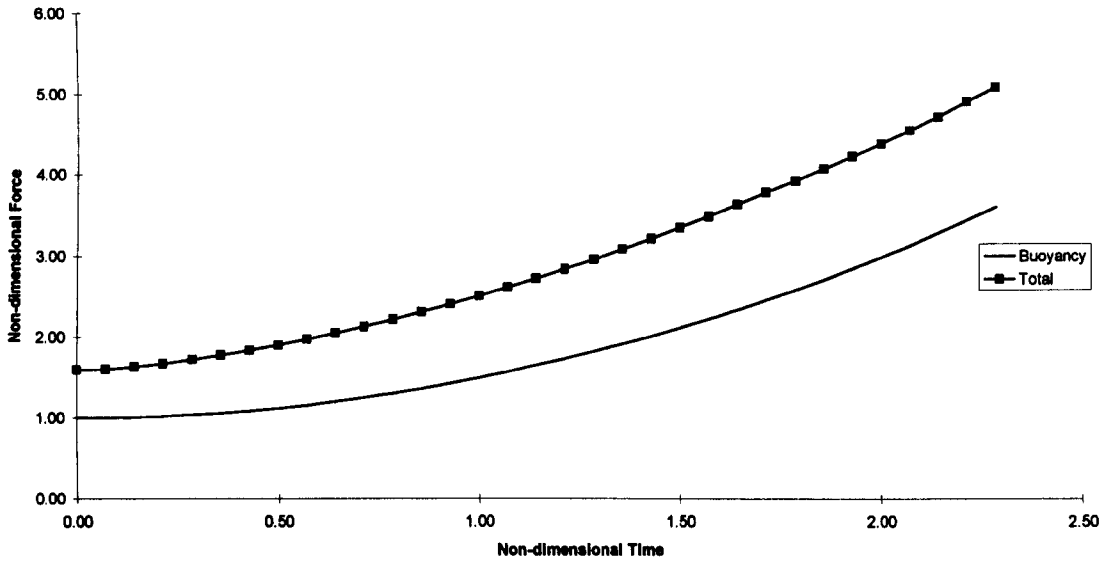


*Graph 5.21 Comparison of Total Force and Buoyancy Force - Entering Knuckle ($\alpha=\pi/4$, $a/g=0.5$)*

Again the gradients are very similar, this in turn means the added mass has a better chance of approximating the difference. As can been seen from previous cases if the buoyancy performs well then the added mass model then performs better. It follows since if the gradients are very similar the difference between the total force and buoyancy force will be almost constant, indicating a smooth, non-violent fluid motion. In turn the added-mass model performs better when fluid motion is not violent.

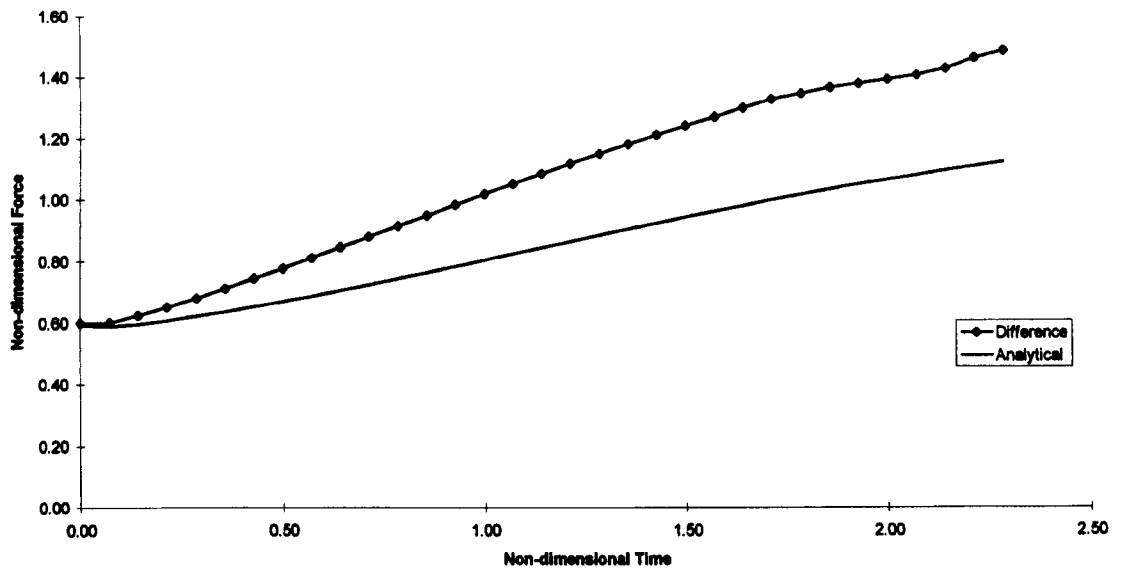


*Graph 5.22 Comparison of Analytical Added Mass and Force Difference - Entering Knuckle ($\alpha=\pi/4$, $a/g=0.5$)*

The knuckle has a more pronounced effect on the pressure gradient at this higher acceleration. We also see the development of negative pressures close to the surface for large $t$, an indication of numerical problems approaching rather than jet formation.

| Label | a | b | c | d | e | f | g | h | i |
|---|---|---|---|---|---|---|---|---|---|
| Time | 0 | 0.29 | 0.57 | 0.86 | 1.14 | 1.43 | 1.72 | 2.00 | 2.29 |

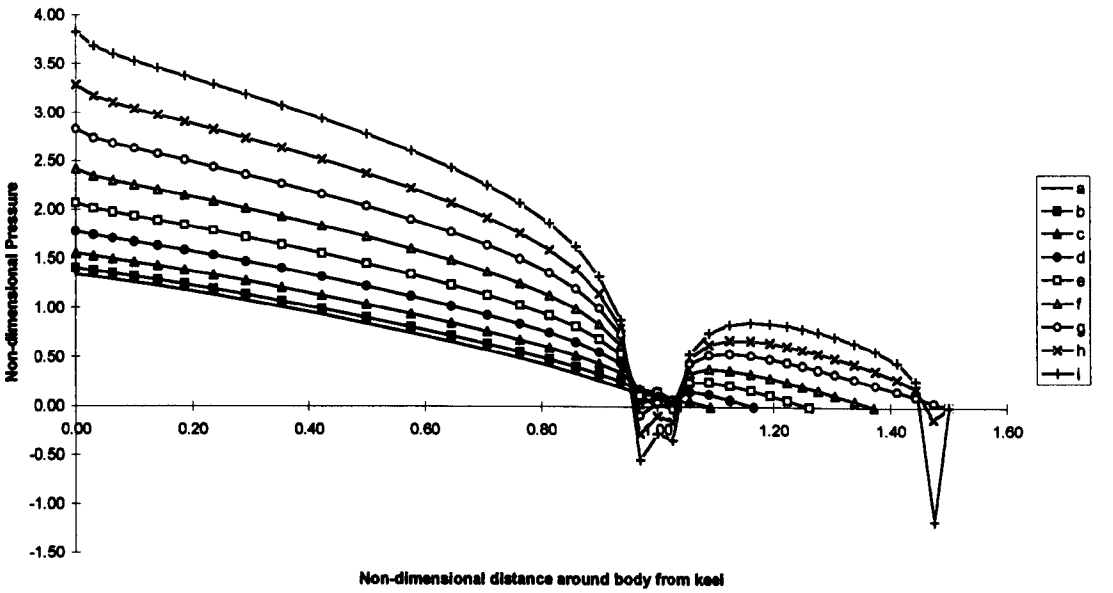


*Graph 5.23 Non-dimensional initial pressure on half wetted surface of entering knuckle ($\alpha=\pi/4$, $a/g=0.5$)*

As in the previous case the development of a radiating wave is definitely noticeable in the final stages of the motion.

In stages *h* and *i* we again have an engulfment situation that we have avoided by fixing the intersection point to the top corner of the body as we did in Graph 5.20.

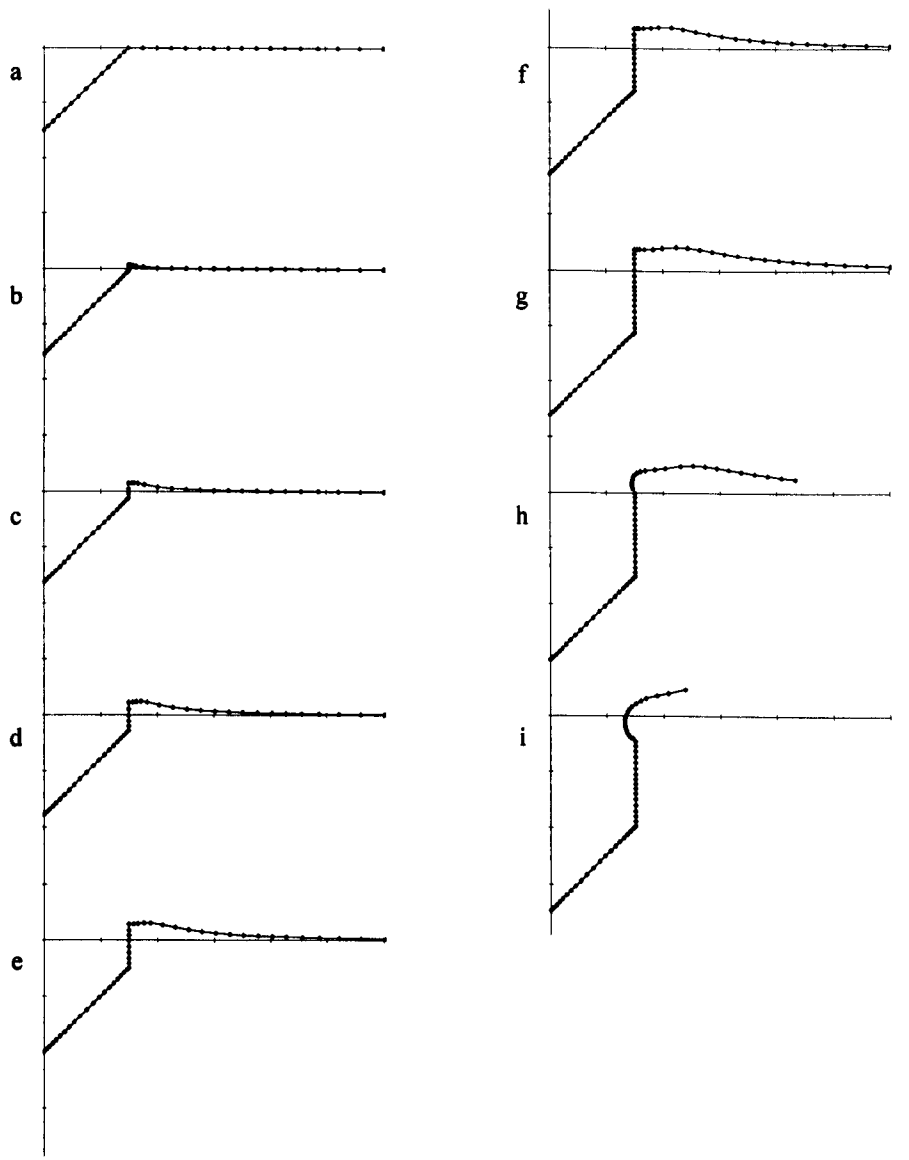


*Graph 5.24 Free-surface profile for entering knuckle ($\alpha=\pi/4$, $a/g=0.5$)*

## Constant velocity

Once again we consider the case of constant velocity exit.

### *Wedge*

Let us return to the wedge case first. Consider a wedge of half angle $\pi/4$, height 1.7 and initial depth -0.33 entering the fluid domain at a constant velocity, Froude number 0.117.

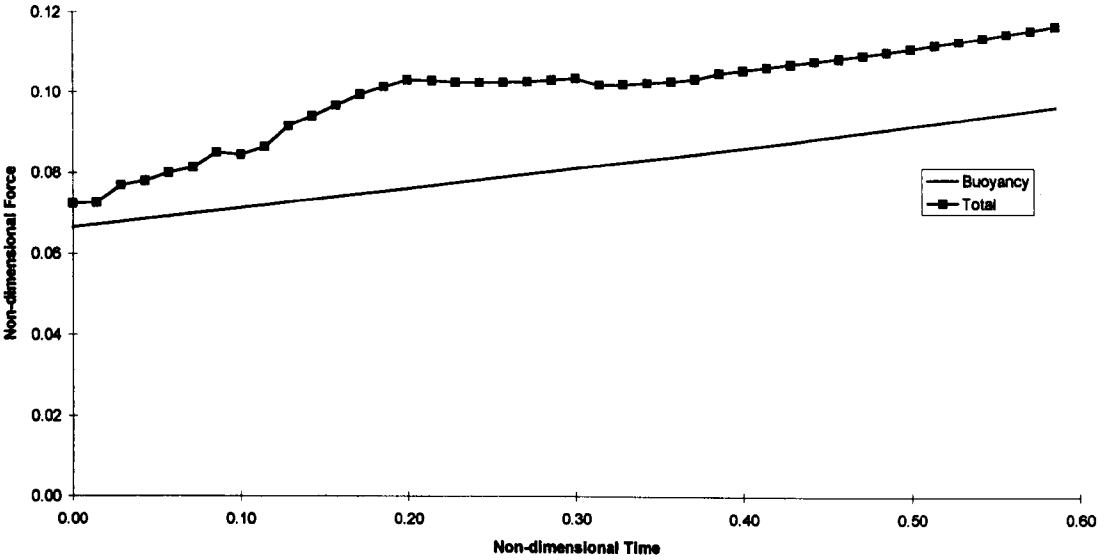


*Graph 5.25 Comparison of Total Force and Buoyancy Force - Entering Wedge ($\alpha=\pi/4$, Fr=0.117)*

We see in Graph 5.25 that the buoyancy still provides a reasonable approximation of the forces on the body. However, Graph 5.26 leaves us in no doubt that the analytical method does not handle the zero acceleration case at all. The results show a virtually constant added mass contribution.

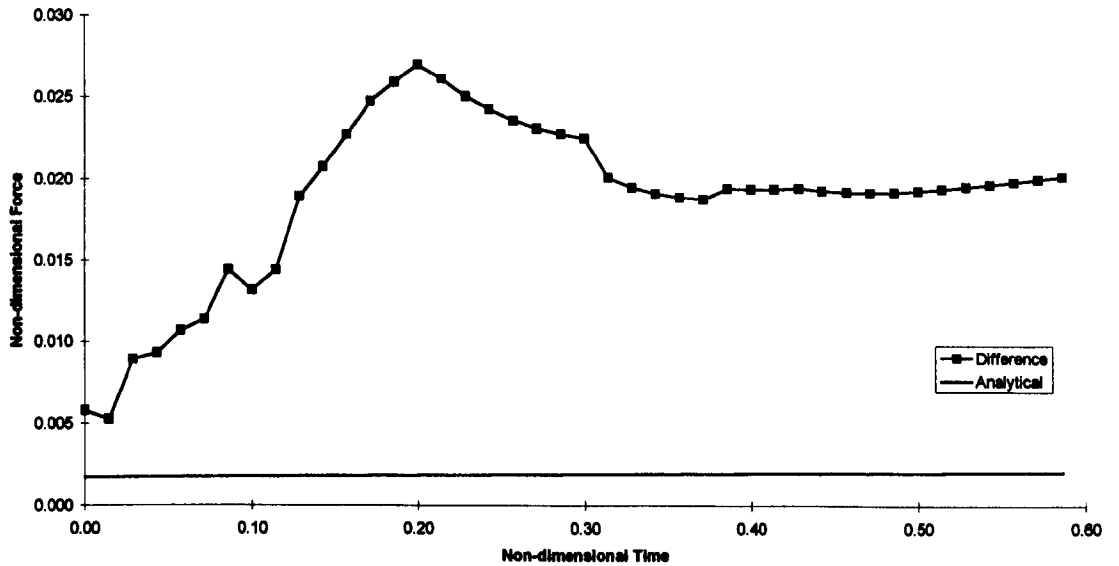


*Graph 5.26 Comparison of Analytical Added Mass and Force Difference - Entering Wedge ($\alpha=\pi/4$, Fr=0.117)*

If we consider the pressure gradients on the body we can see why the method is failing.

| Label | a | b | c | d | e | f | g | h |
|---|---|---|---|---|---|---|---|---|
| Time | 0 | 0.09 | 0.17 | 0.26 | 0.34 | 0.43 | 0.51 | 0.60 |

The pressures become negative at an early stage in the motion, as we have seen in previous examples this usually indicates the formation of a jet. This is confirmed when we study Graph 5.28, by stage *d* we can clearly see the beginnings of a jet. When we reach stage *f* the jet is ready to fall away from the body (a situation we artificially restrict) and so the calculations start to break down. A similar effect was noted by Greenhow (1987).

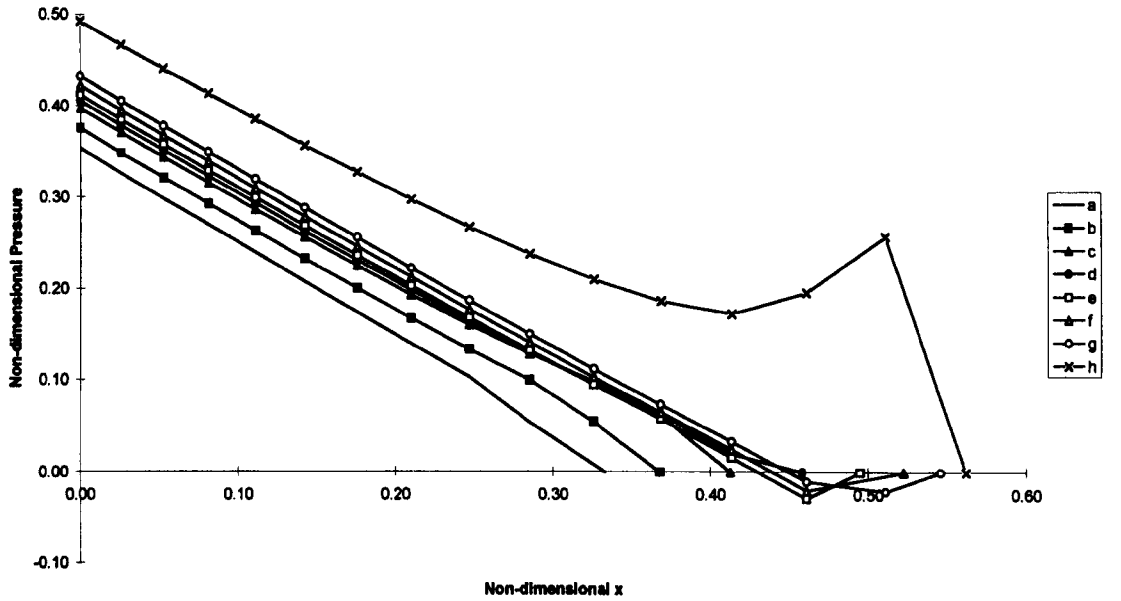


*Graph 5.27 Non-dimensional initial pressure on half wetted surface of entering wedge ($\alpha=\pi/4$, $Fr=0.117$)*

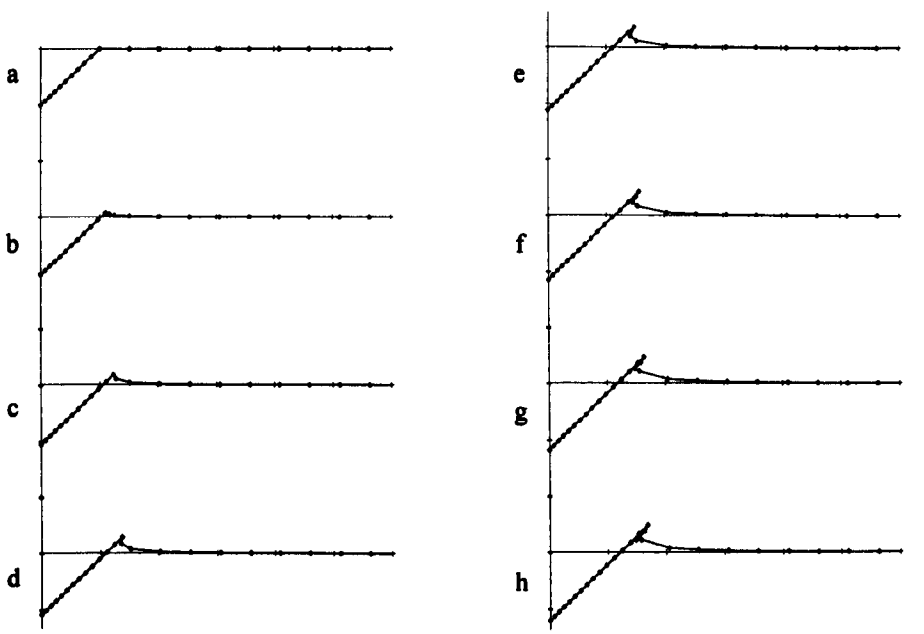


*Graph 5.28 Free-surface profile for entering wedge ($\alpha=\pi/4$, $Fr=0.117$)*

Next is another wedge this time of half angle $\pi/4$, height 1.7 and initial depth -1.0. This body is entering at twice the speed of the previous example, Froude number 0.233.

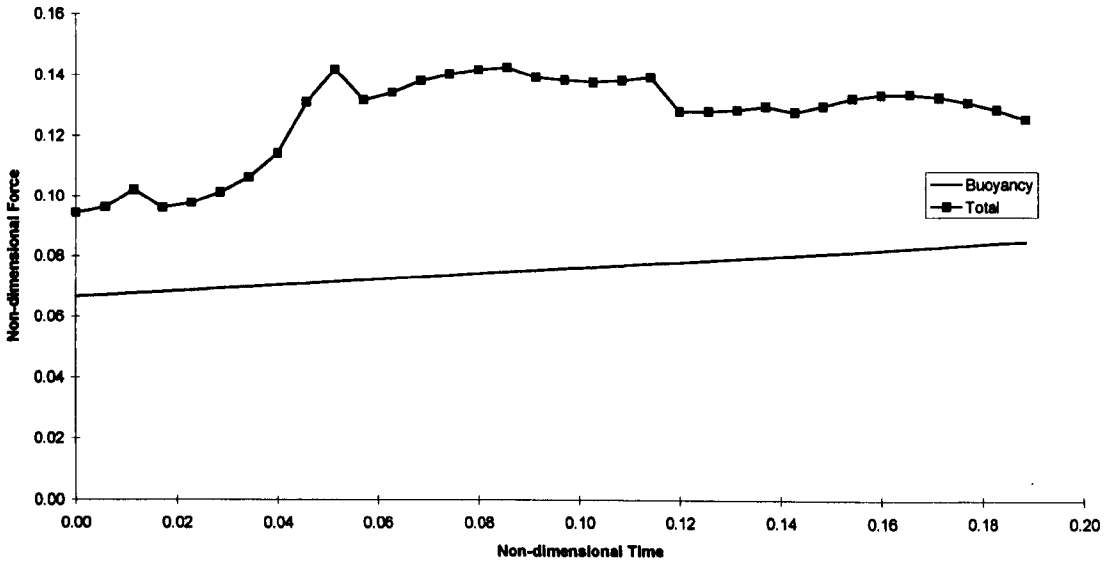


*Graph 5.29 Comparison of Total Force and Buoyancy Force - Entering Wedge ($\alpha=\pi/4$, Fr=0.233)*

We can see just from the force results in Graph 5.29 that the method is having considerable trouble controlling the intersection point, this is reflected in the jagged profile of the total force curve.

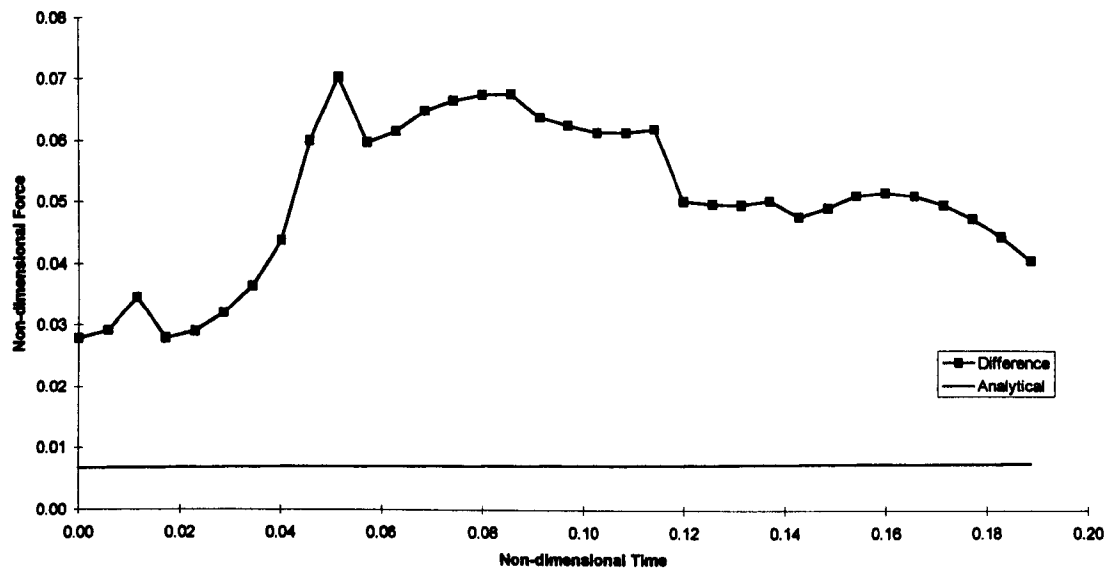


*Graph 5.30 Comparison of Analytical Added Mass and Force Difference - Entering Wedge ($\alpha=\pi/4$, Fr=0.233)*

The initial difference cannot be attributed to draw-down (up-rise) as is testified by Chapter 6.

As in the previous example we see the analytical method is inadequate at approximating the force difference. Also we have a negative pressure next to the surface on the first step ($t = 0$), it is suggested this is a numerical symptom of the impulsive start.

| Label | a | b | c | d | e | f | g | h | i |
|---|---|---|---|---|---|---|---|---|---|
| Time | 0 | 0.02 | 0.05 | 0.07 | 0.09 | 0.11 | 0.14 | 0.16 | 0.18 |

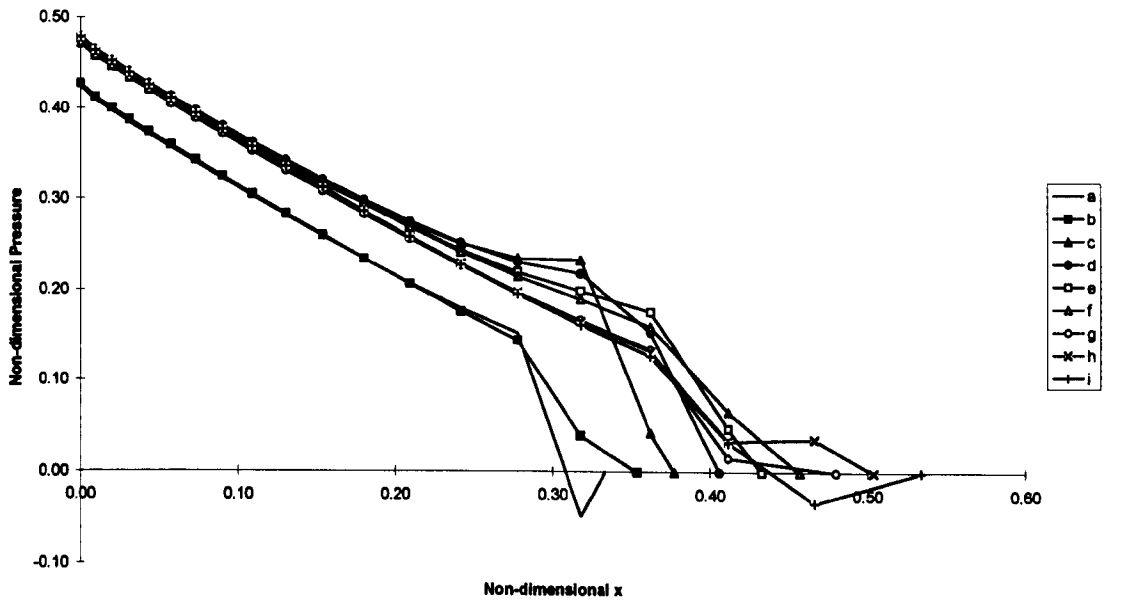


*Graph 5.31 Non-dimensional initial pressure on half wetted surface of entering wedge ($\alpha=\pi/4$, $Fr=0.233$)*

The surface profiles confirm that jet formation is present at an early stage.

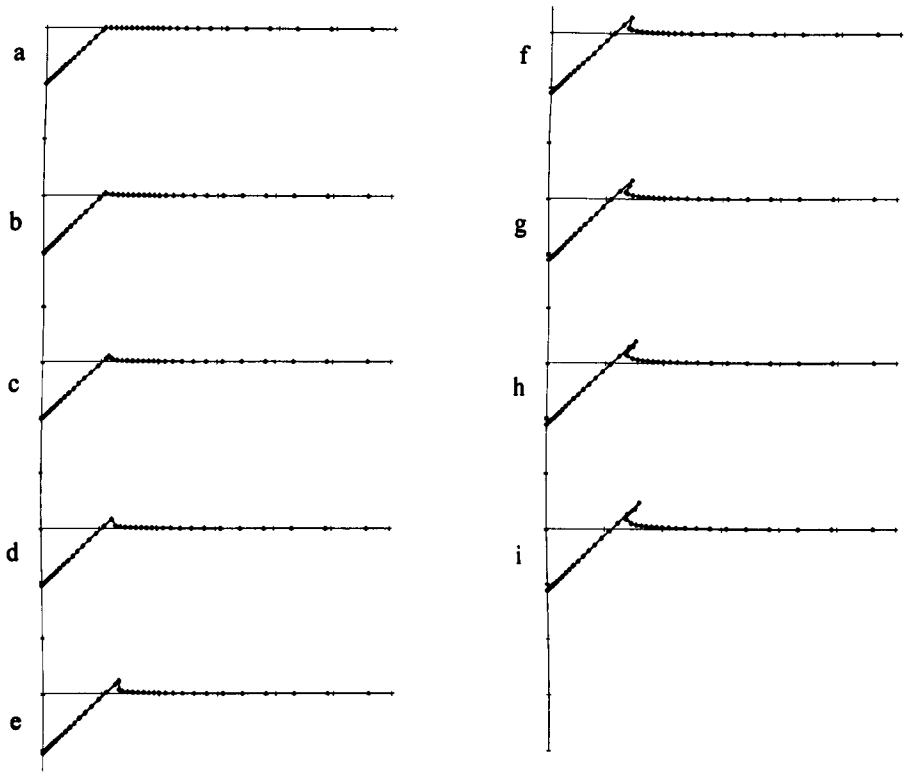


*Graph 5.32 Free-surface profile for entering wedge ($\alpha=\pi/4$, Fr=0.233)*

Further wedge runs are omitted since the above examples have already demonstrated a trend, one which results in very early breakdown of the calculations.

## *Box*

Instead we move our attention on to the box body. Here we have a box of height 2, width 0.33 at an initial submergence of -0.33 and Froude 0.117.

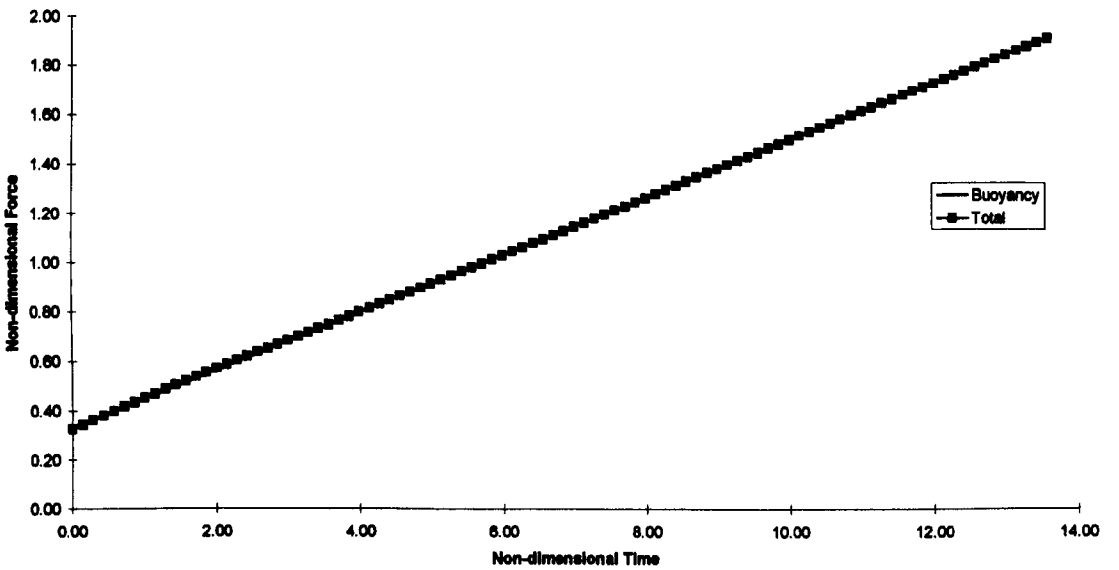


*Graph 5.33 Comparison of Total Force and Buoyancy Force - Entering Box (Fr=0.117)*

The buoyancy force and the numerical force coincide, from Graph 5.33 they look identical however inspection of the following graph shows there is a slight difference. The agreement is to be expected considering that the body is thin and the Froude number is low.

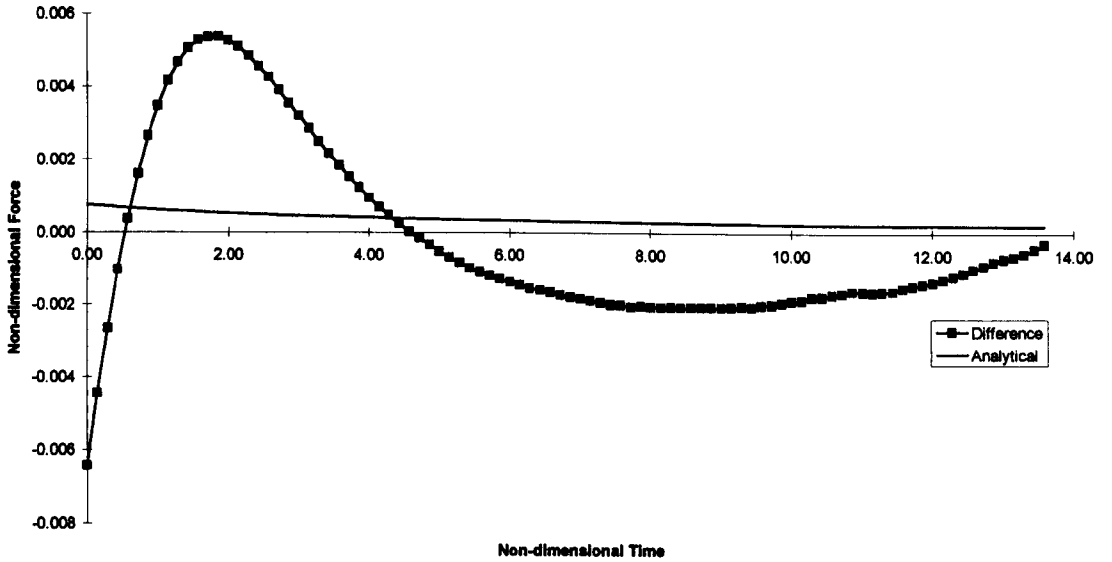


*Graph 5.34 Comparison of Analytical Added Mass and Force Difference - Entering Box (Fr=0.117)*

We have a difference between the two curves at t=0, as in the wedge examples we believe this is attributable to the impulsive start of the body. This is not a physical problem, that is, the numerics should agree with the correct analytical result. So we conclude it is the numerics which cannot handle the impulsive start and the analytical theory is correct at $t = 0$.

The pressure gradients in Graph 5.35 are dominated by hydrostatics.

| Label | a | b | c | d | e | f | g | h | i | j | k |
|---|---|---|---|---|---|---|---|---|---|---|---|
| Time | 0 | 1.29 | 2.57 | 3.86 | 5.15 | 6.43 | 7.72 | 9.01 | 10.29 | 11.58 | 12.87 |

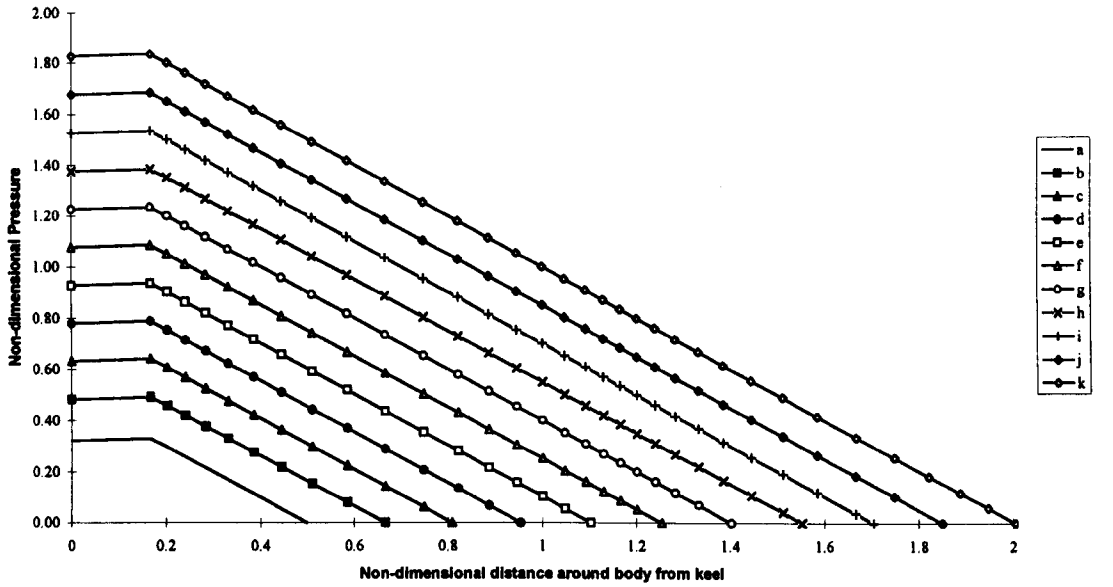


*Graph 5.35 Non-dimensional initial pressure on half wetted surface of entering box (Fr=0.117)*

The surface profiles are just as uneventful, with very little surface movement throughout the body motion.

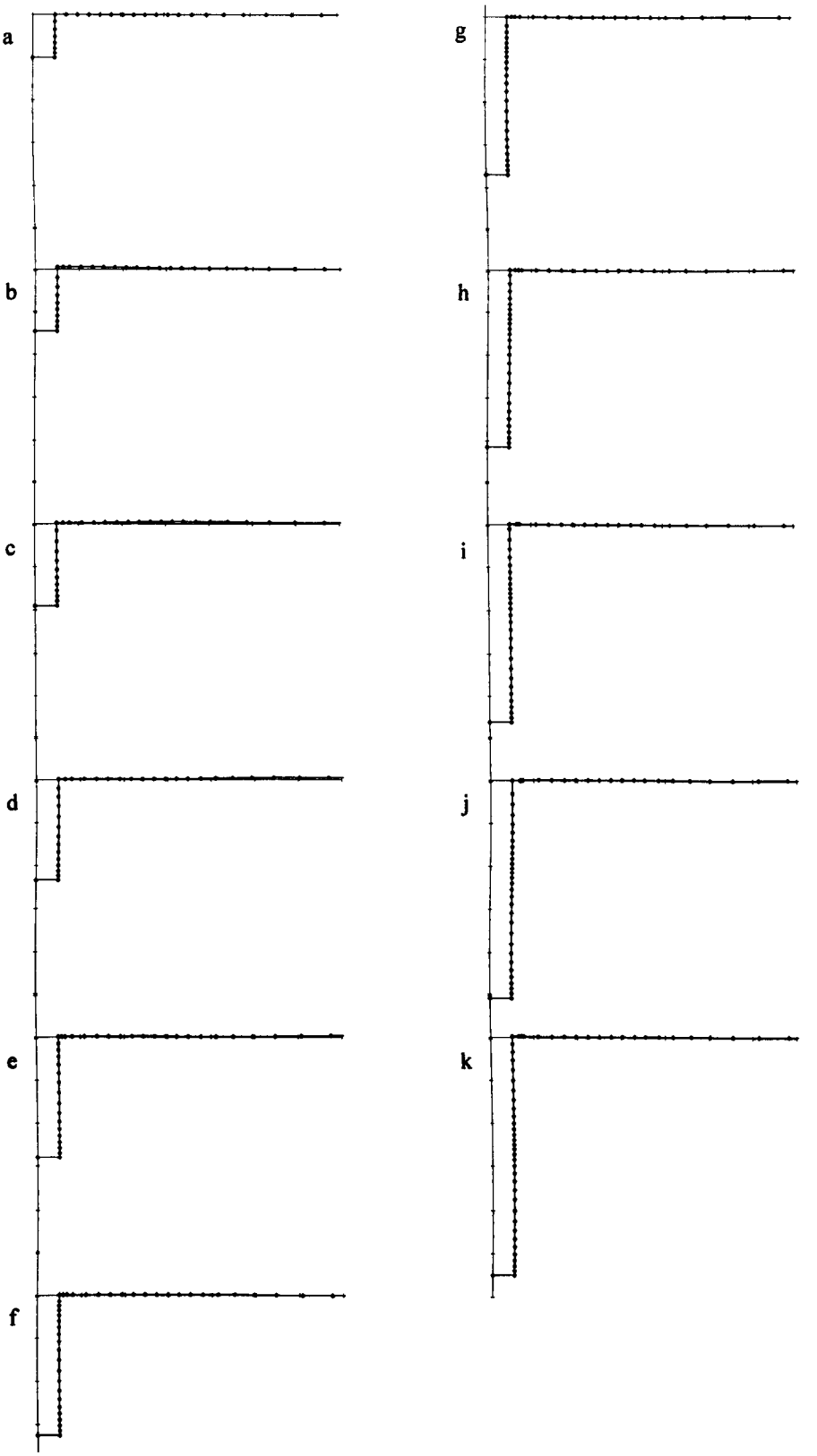


*Graph 5.36 Free-surface profile for entering box (Fr=0.117)*

If we increase the entry velocity and change the body width to 2, raising the Froude number to 0.233 the buoyancy force matches the total force closely.

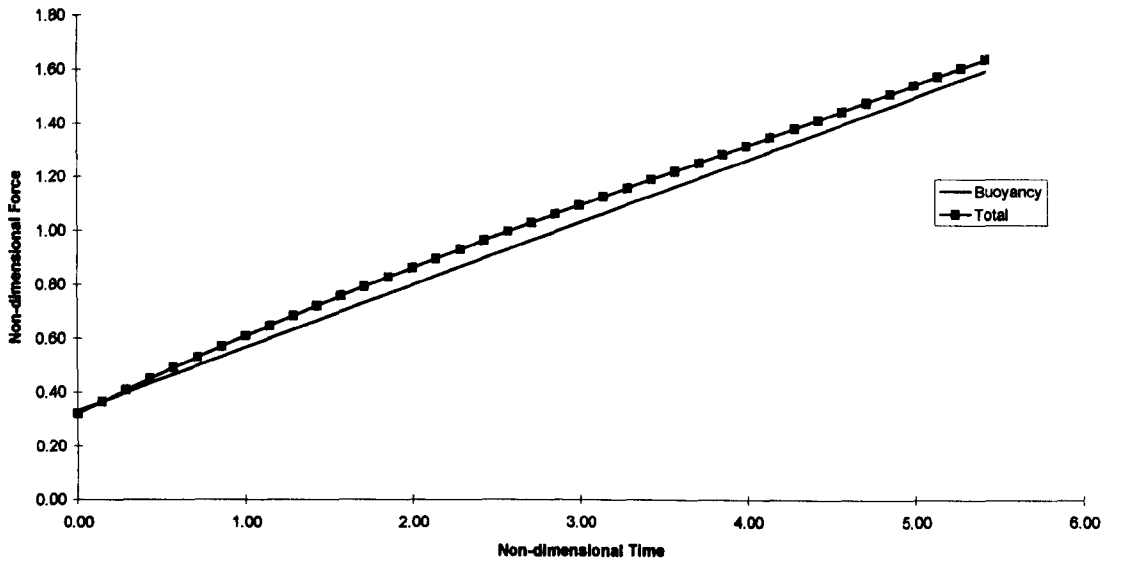


*Graph 5.37 Comparison of Total Force and Buoyancy Force - Entering Box (Fr=0.233)*

However, the analytical added mass and force difference still disagree.

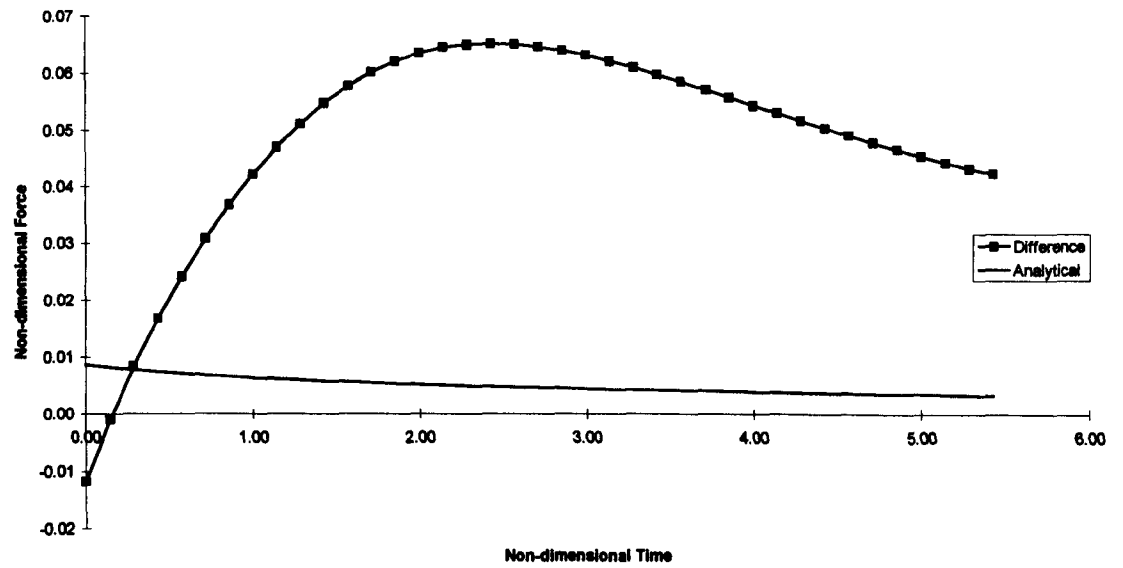


*Graph 5.38 Comparison of Analytical Added Mass and Force Difference - Entering Box (Fr=0.233)*

In the case of $F_r$=0.117 the body motion is slow enough to make the contribution of the singularity to the pressure negligible. Here we see that the singularities present on the body corner appearing in the pressure gradient, Graph 5.39

| Label | a | b | c | d | e | f | g | h | I | j |
|---|---|---|---|---|---|---|---|---|---|---|
| Time | 0 | 0.57 | 1.14 | 1.72 | 2.29 | 2.86 | 3.43 | 4.00 | 4.59 | 5.15 |

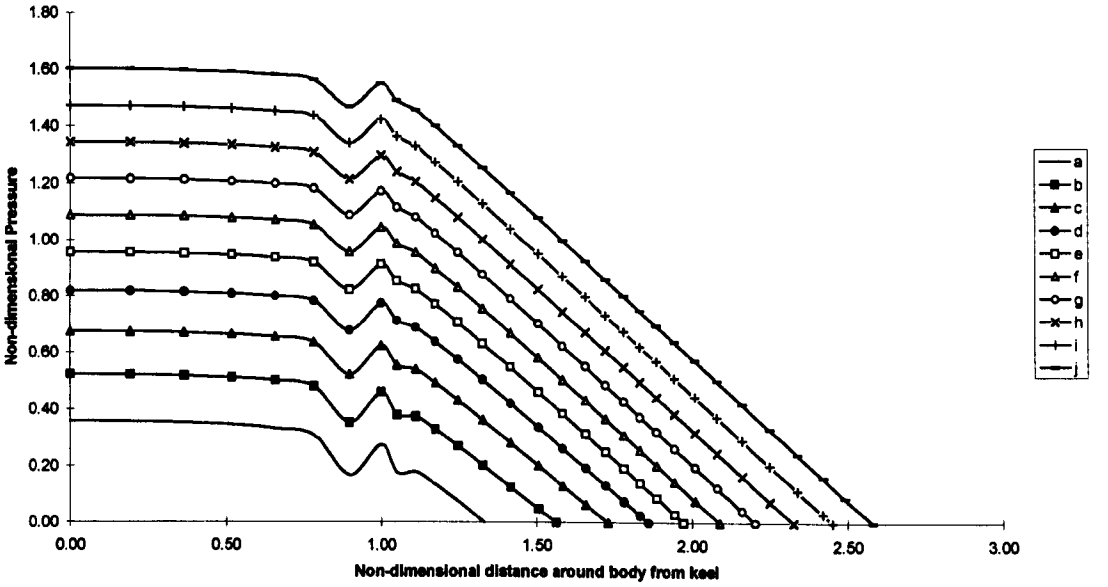


*Graph 5.39 Non-dimensional initial pressure on half wetted surface of entering box (Fr=0.233)*

The surface profiles show motion on the free-surface as it rises up the body and then returns in a full wave motion.

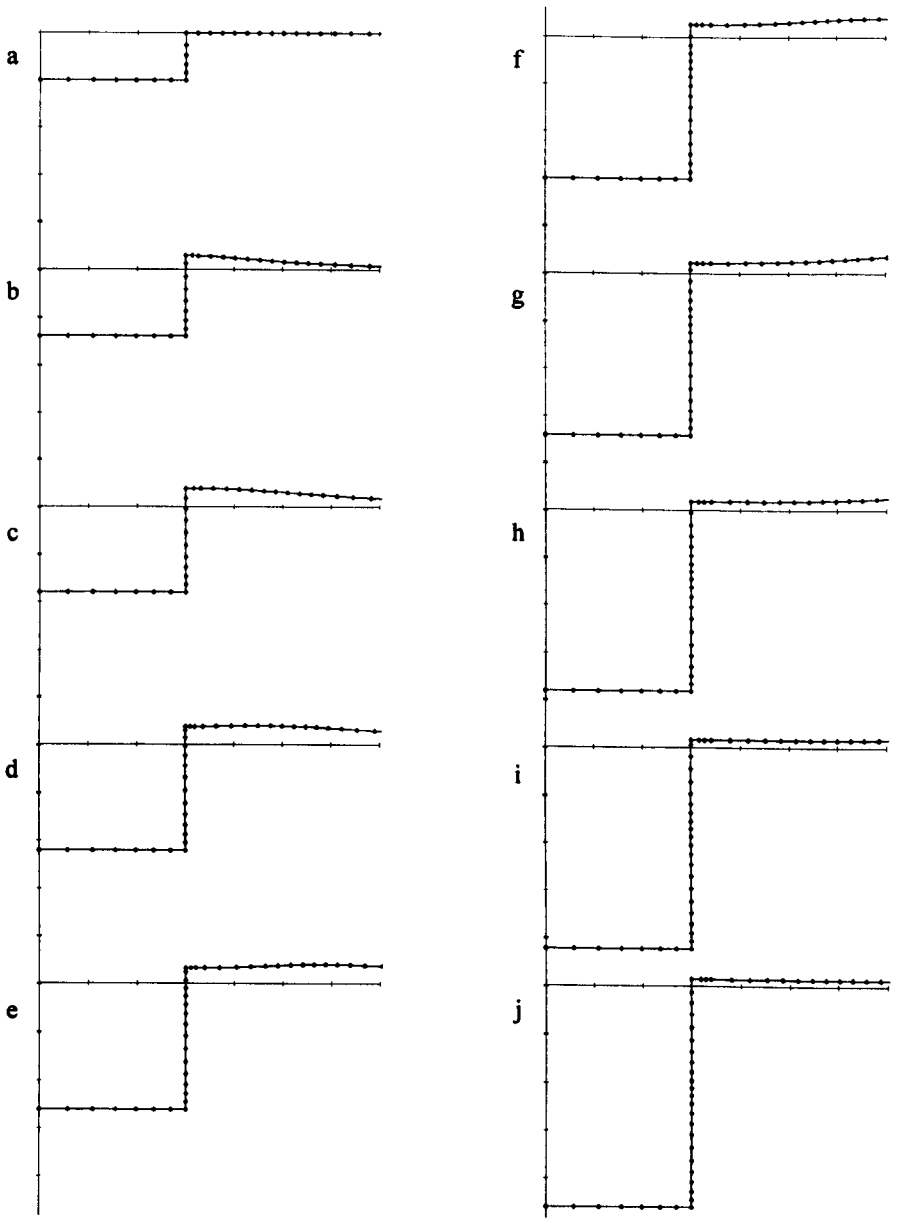


*Graph 5.40 Free-surface profile for entering box (Fr=0.233)*

Let us move the box faster with a Froude of 0.583, a significant increase.

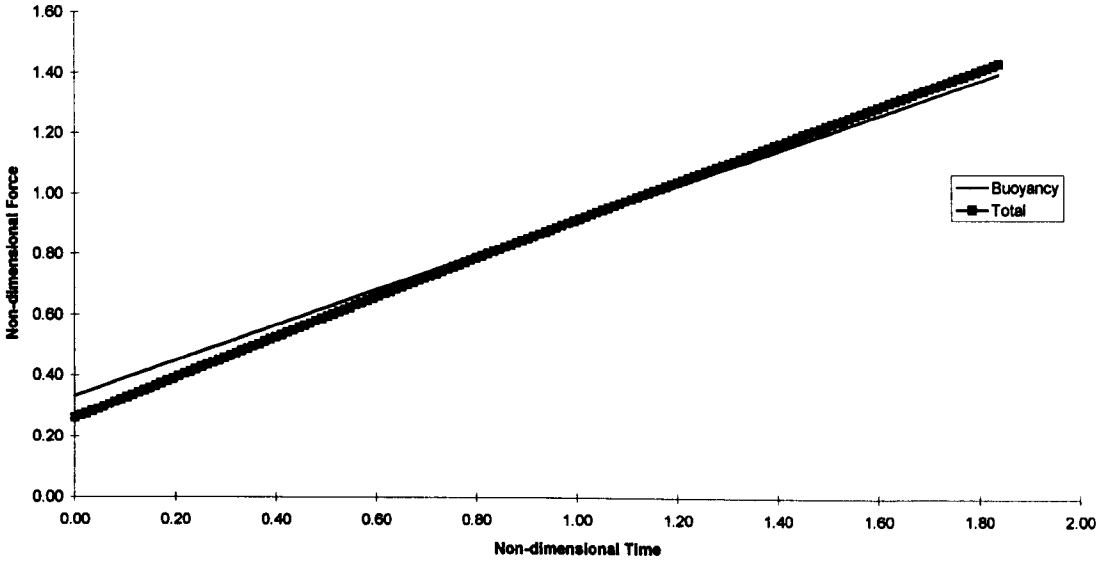


*Graph 5.41 Comparison of Total Force and Buoyancy Force - Entering Box (Fr=0.583)*

The buoyancy and total force continue to attain good agreement at this higher Froude number. However, the discrepancy between the analytical added mass and the force difference is increasing as does the Froude number this can be seen in Graph 5.42. This indicates a breakdown of the method, the combined difficulties of high Froude number and constant velocity motion has rendered the analytical model unsuitable, the surface profiles however are still of use for reference.

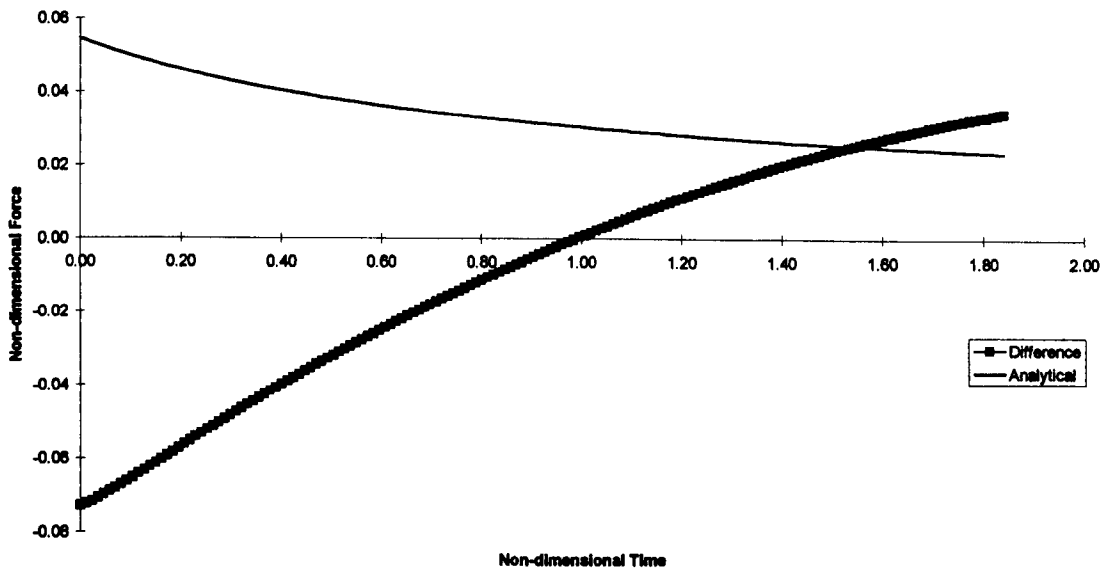


*Graph 5.42 Comparison of Analytical Added Mass and Force Difference - Entering Box (Fr=0.583)*

Obviously with the higher velocity the singularities make a major impression on the pressure gradient as their field of influence increases.

| Label | a | b | c | d | e | f | g | h | i |
|---|---|---|---|---|---|---|---|---|---|
| Time | 0 | 0.23 | 0.46 | 0.69 | 0.91 | 1.14 | 1.37 | 1.60 | 1.83 |

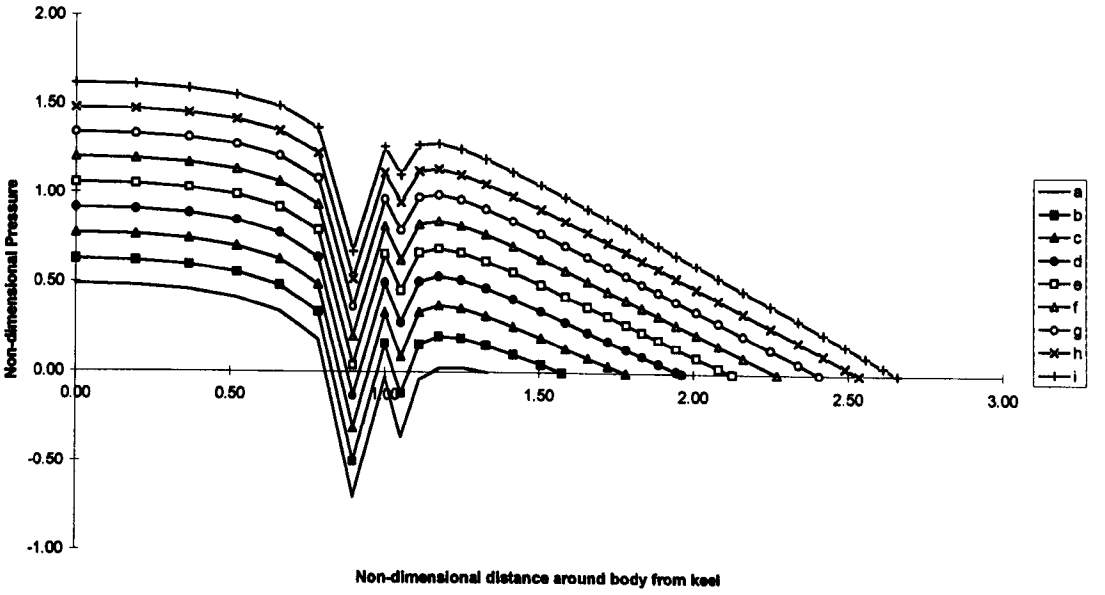


*Graph 5.43 Non-dimensional initial pressure on half wetted surface of entering box (Fr=0.583)*

A large "up-rise" of the surface is apparent in the surface profiles.

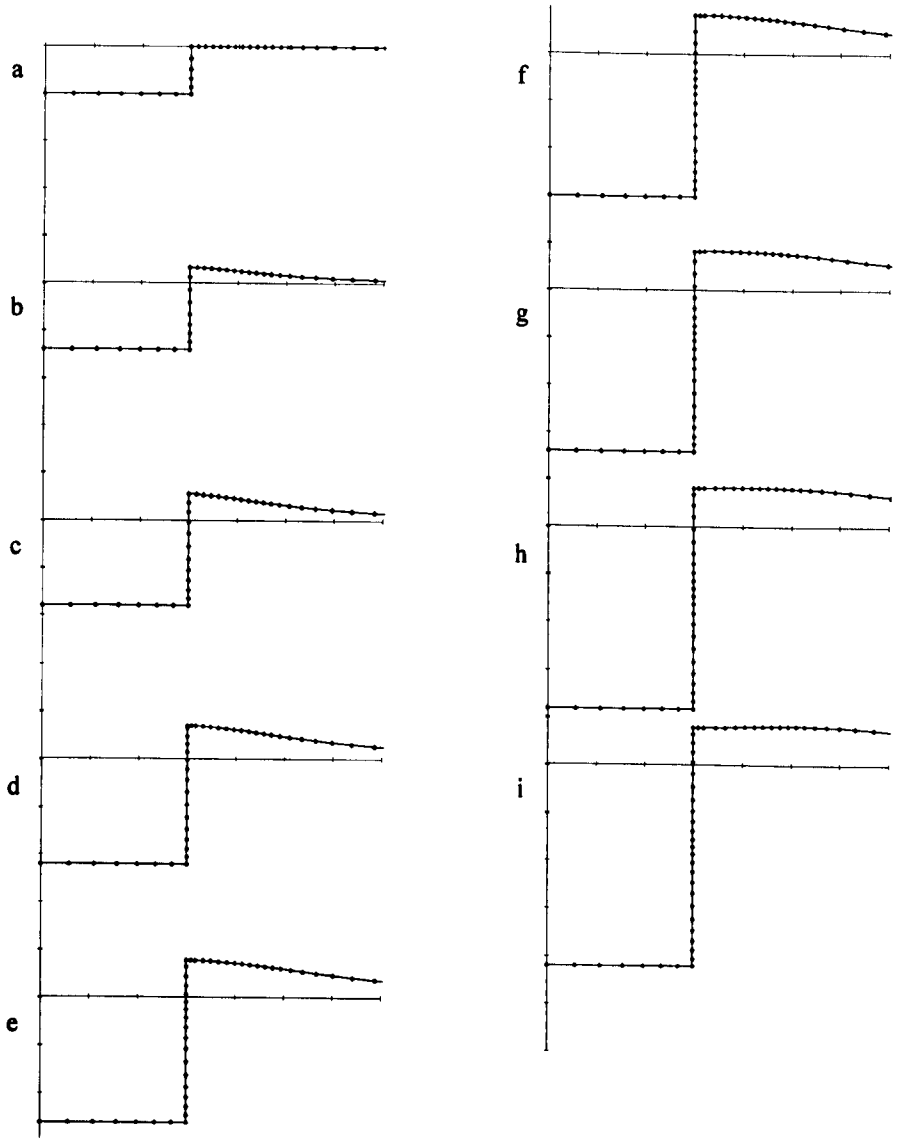


*Graph 5.44 Free-surface profile for entering box (Fr=0.583)*

For reference we also present the free-surface profiles, Graph 5.45, for the same body entering with Froude number 2.915. The non-dimensional times are given in the table below.

| Label | a | b | c | d | e | f | g | h | I |
|---|---|---|---|---|---|---|---|---|---|
| Time | 0 | 0.03 | 0.07 | 0.10 | 0.14 | 0.17 | 0.21 | 0.24 | 0.27 |

The surface profile demonstrates the effect such a large Froude number has on the surface motion. The intersection point moves rapidly up the side of the body, which would effectively result in a jet.

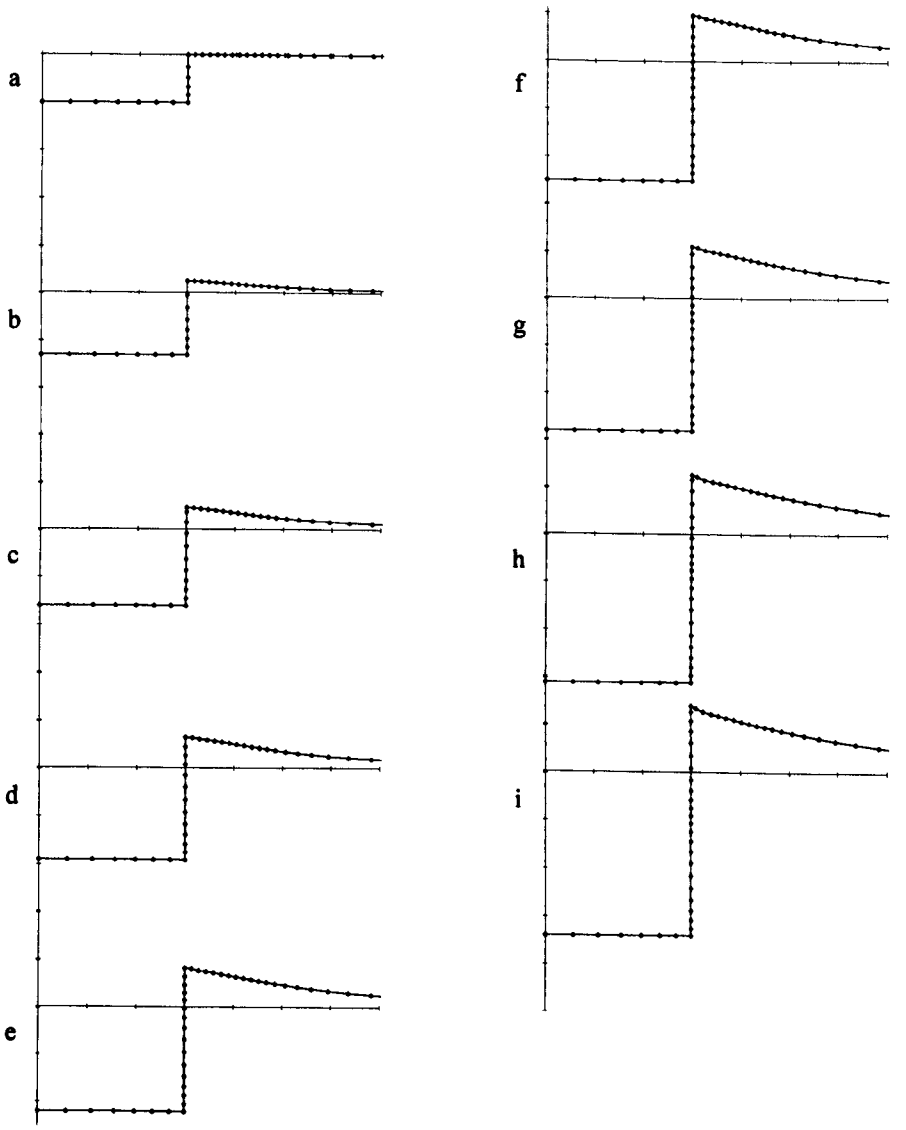


*Graph 5.45 Free-surface profile for entering box (Fr=2.915)*

## *Knuckle*

Finally we consider the constant velocity case of the knuckled body of height 2, vertex height 1, half angle $\pi/4$ and initial depth -1.0, starting with a very small Froude of 0.058.

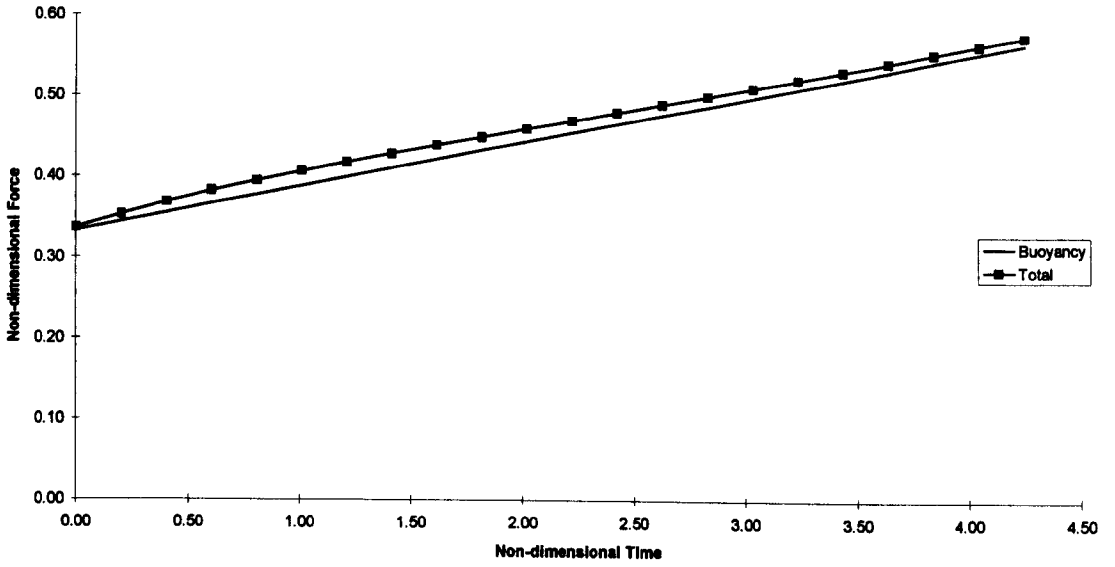


*Graph 5.46 Comparison of Total Force and Buoyancy Force - Entering Knuckle ($\alpha=\pi/4$, Fr=0.058)*

For such a low Froude number the two force calculations compare favourably. And considering the difference as represented in Graph 5.47 the contribution made by the analytical added mass is a bonus but hardly significant considering the numerical magnitude of the difference.

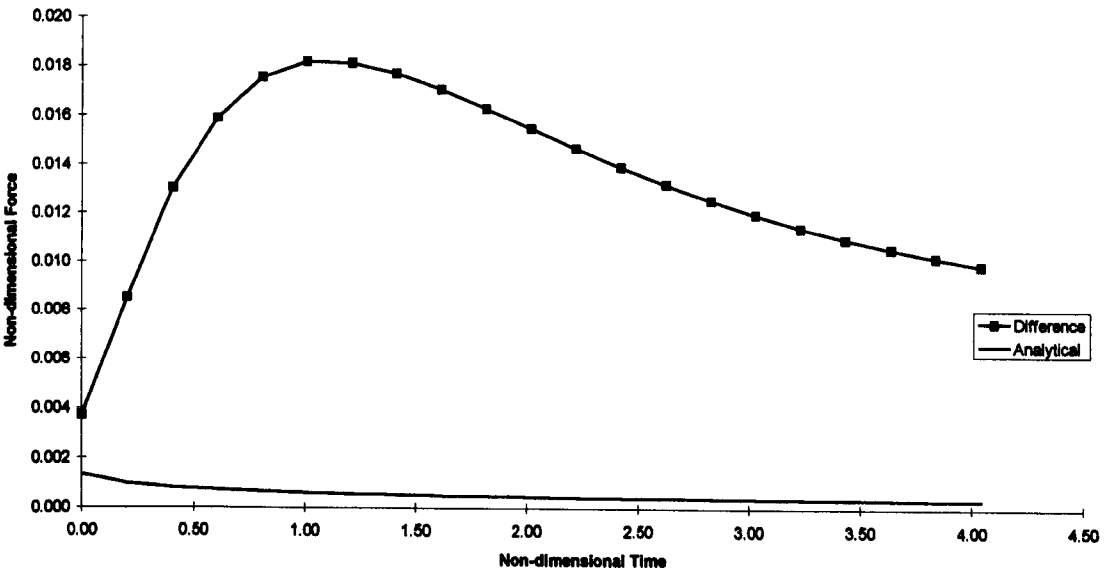


*Graph 5.47 Comparison of Analytical Added Mass and Force Difference - Entering Knuckle ($\alpha=\pi/4$, Fr=0.058)*

The pressure distribution along the body is linear as could be expected from previous evidence.

| Label | a | b | c | d | e | f | g | h | I | j |
|---|---|---|---|---|---|---|---|---|---|---|
| Time | 0 | 0.81 | 1.62 | 2.43 | 3.23 | 4.04 | 4.85 | 5.66 | 6.47 | 7.28 |

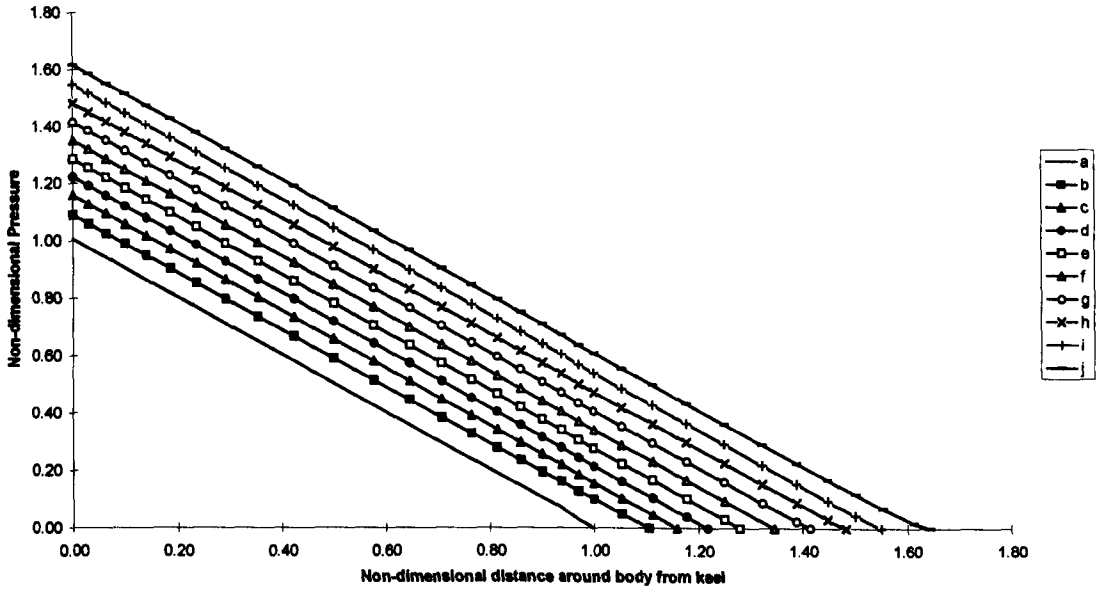


*Graph 5.48 Non-dimensional initial pressure on half wetted surface of entering knuckle ($\alpha=\pi/4$, $Fr=0.058$)*

The surface profile is similarly uneventful at such low Froude number, with minimal surface disturbance in the form of a radiated wave.

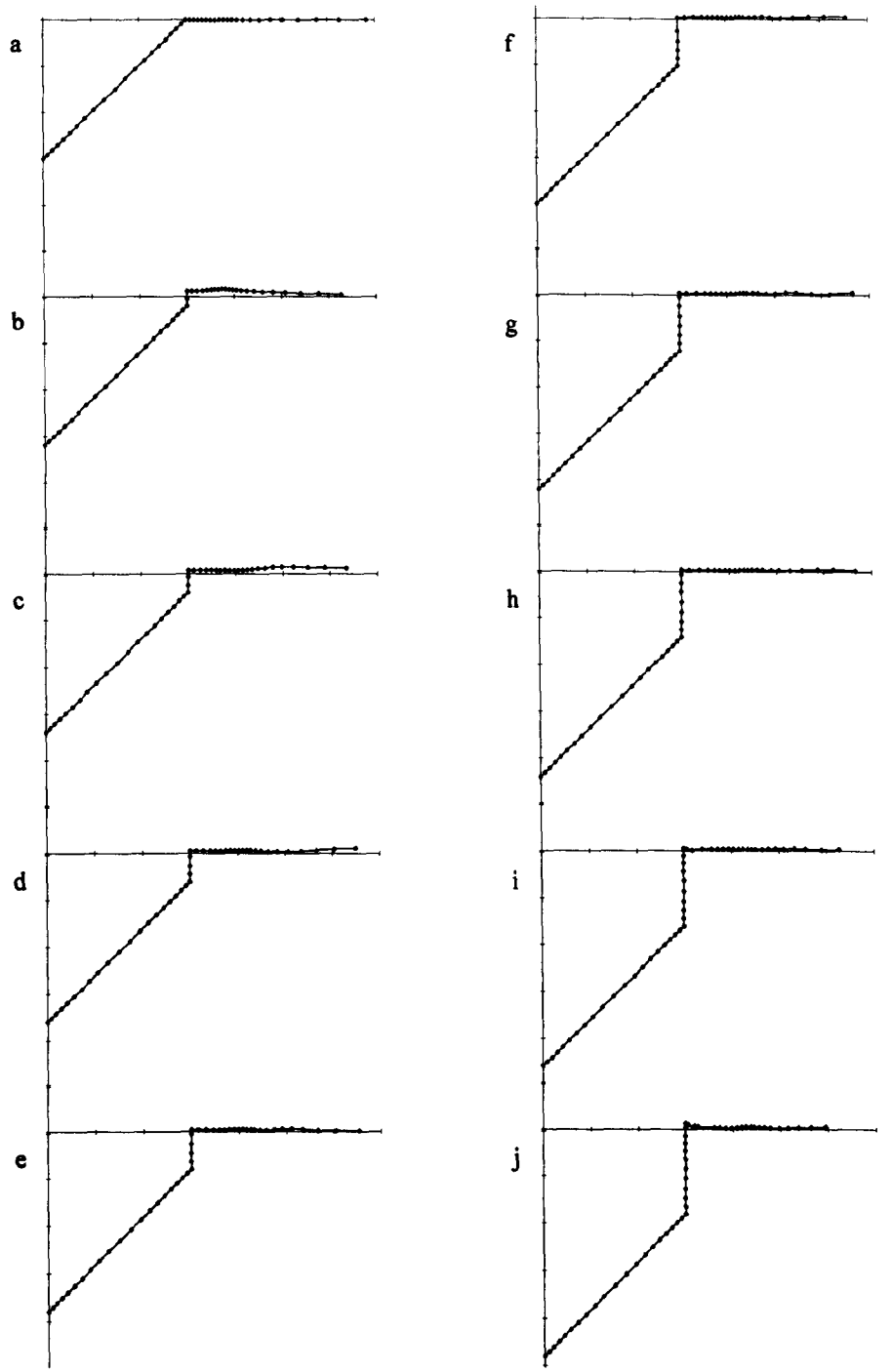


*Graph 5.49 Free-surface profile for entering knuckle ($\alpha=\pi/4$, $Fr=0.058$)*

If we double the Froude number (effectively doubling the velocity) the results begin to move apart (further runs, not presented here, continue the trend).

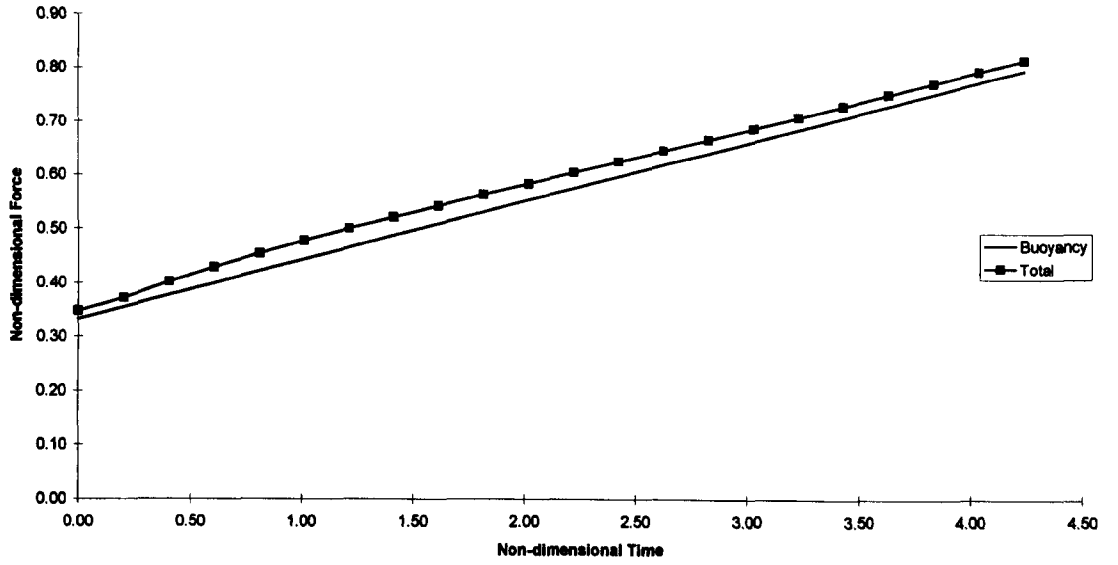


*Graph 5.50 Comparison of Total Force and Buoyancy Force - Entering Knuckle ($\alpha=\pi/4$, Fr=0.117)*

The buoyancy force still provides a reasonable approximation of the total force. The differences shown in Graph 5.51 are five times those in the previous Froude number considered, so the analytical method fails drastically.

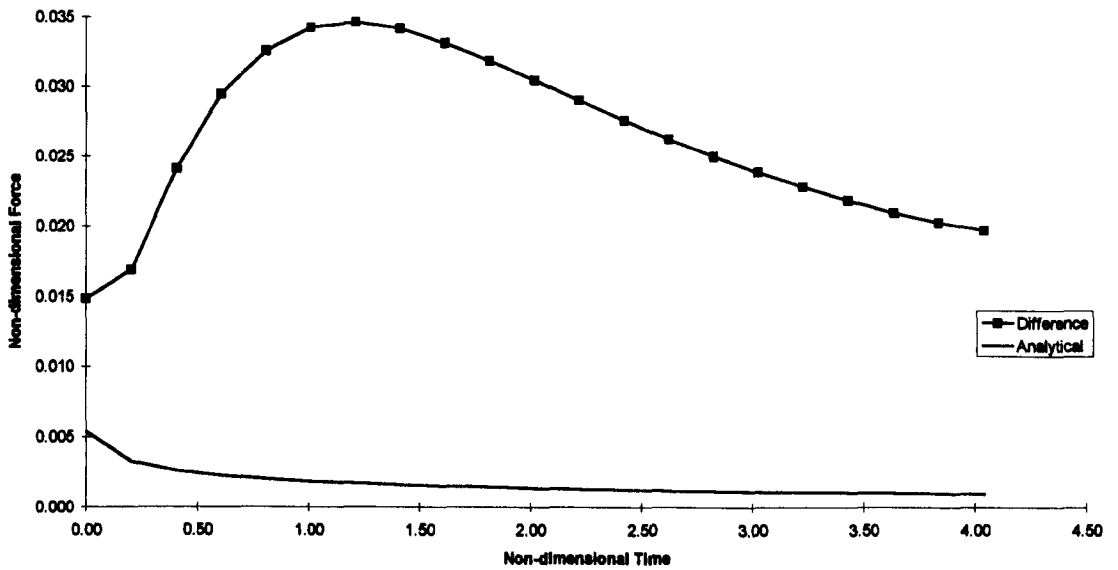


*Graph 5.51 Comparison of Analytical Added Mass and Force Difference - Entering Knuckle ($\alpha=\pi/4$, Fr=0.117)*

| Label | a | b | c | d | e | f | g | h | i | j | k |
|---|---|---|---|---|---|---|---|---|---|---|---|
| Time | 0 | 0.61 | 1.21 | 1.82 | 2.43 | 3.03 | 3.64 | 4.25 | 4.85 | 5.46 | 6.07 |

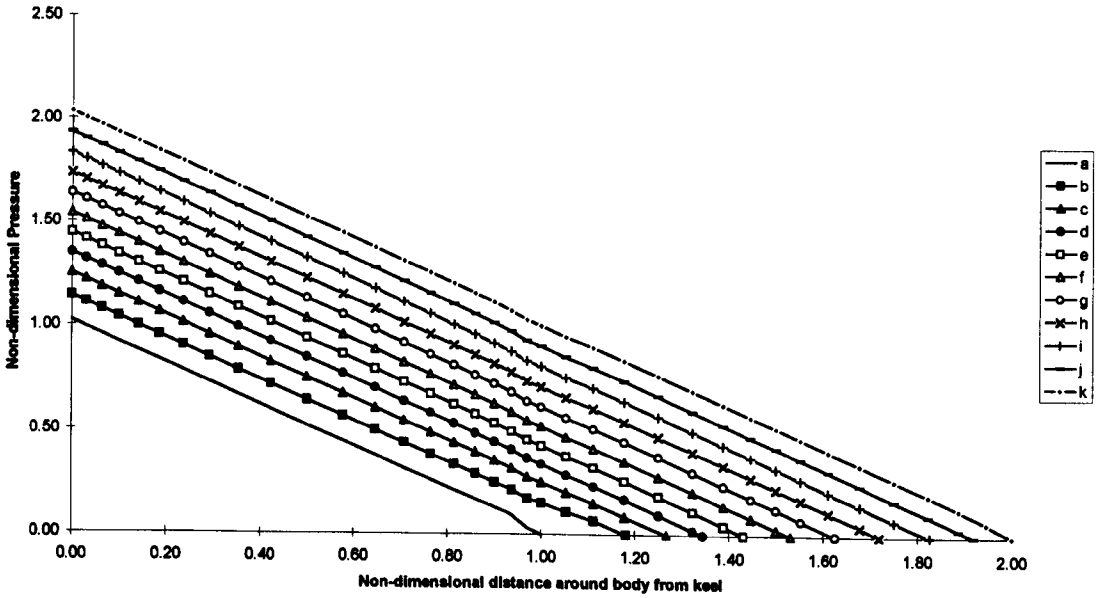


*Graph 5.52 Non-dimensional initial pressure on half wetted surface of entering knuckle ($\alpha=\pi/4$, $Fr=0.117$)*

The pressure graph is still practically linear, contributing again to the evidence that it is the analytical theory that is unsuitable for these cases.

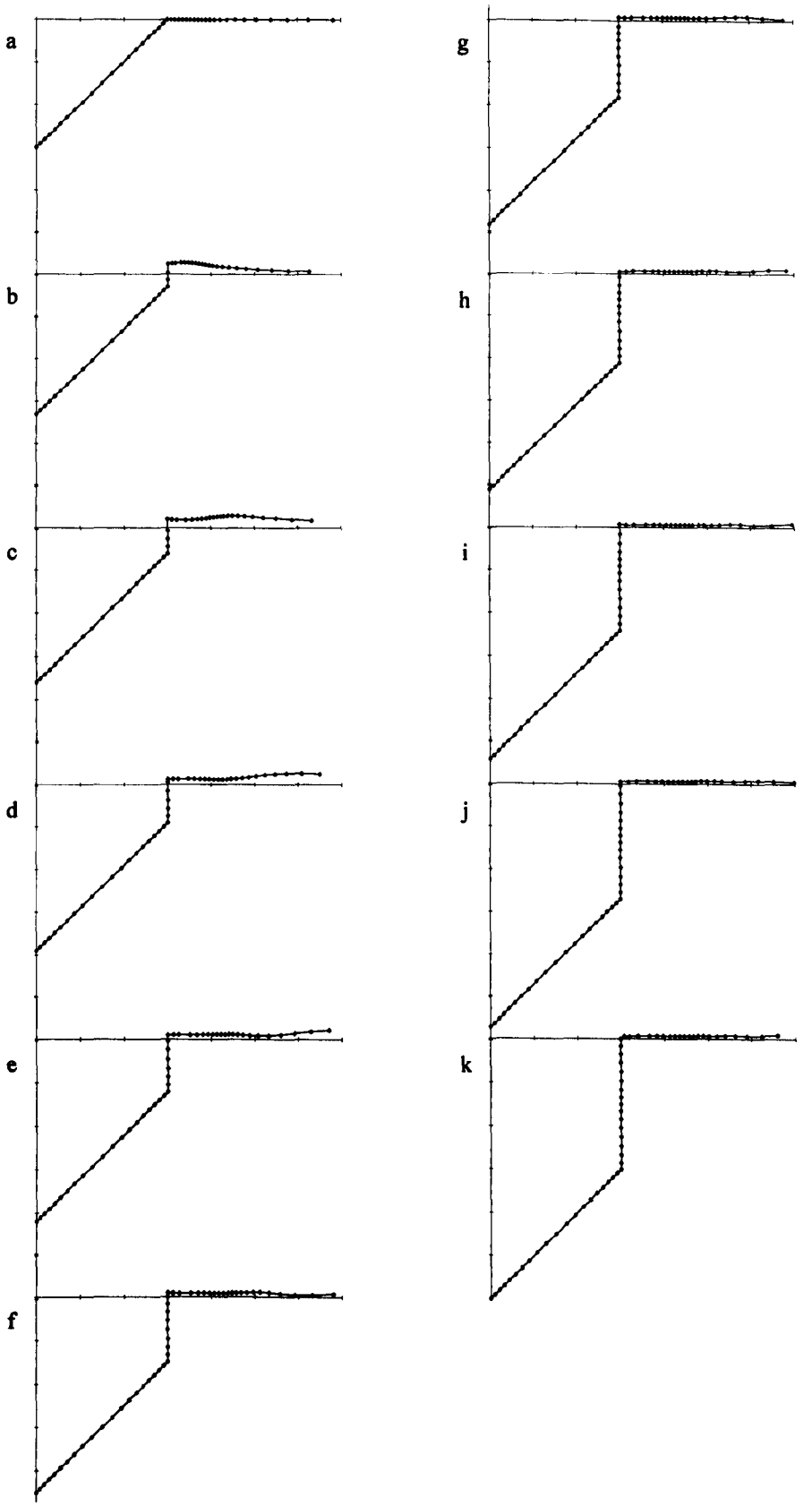


*Graph 5.53 Free-surface profile for entering knuckle ($\alpha=\pi/4$, $Fr=0.117$)*

## Conclusions

We have shown in this chapter that the analytical method can achieve significant results for small time in the case of accelerated motion. However, with constant velocity the results are far from adequate. This eliminates the use of the analytical method for any constant velocity cases of a body entering the fluid domain. Although this may be considered a limitation we have still shown significant progress for the "real" world situation of a body accelerating into a fluid as applicable to ship slamming.

# Chapter 6 Draw-down Analysis

*An examination of the draw-down effect on added mass calculations.*


## Abstract

The effects of including draw-down in the calculations for buoyancy and added mass are demonstrated.


## Introduction

It is proposed that many of the differences encountered between the numerical and analytical schemes described in Chapter 4 and Chapter 5 can be attributed to the effect of draw-down/up-rise of the free surface adjacent to the body. In this Chapter we will examine the effect of including the draw-down in the calculations used in the aforementioned chapters. This is a purely empirical method as currently there exists no way of predicting the draw-down short of fully non-linear numerical calculation. However draw-down might easily be measured from film of model experiments. This chapter uses the numerically-calculated free surfaces presented in Chapters 4 and Chapter 5 to quantify the draw-down and use it in the force calculations.

We recall from Chapter 3 that for a wedge in an ideal fluid the buoyancy force can be calculated as

$$F_b = \rho g \forall(t)$$

where $\forall(t) = b^2 \tan\alpha$ is the submerged body volume. The added mass force is

$$F_a = \rho G \tan\alpha \left(-bv^2 + b^2\dot{v}\right)$$

where $b$ is the submerged depth of the body.

These forces are calculated on the basis of a flat free-surface of equipotential; we must adjust them to take account of the draw-down (up-rise) that occurs. The changes proposed here all relate to the effect the draw-down has on the submerged depth of the body as demonstrated in Figure 6.1.

In Figure 6.1 both $b$ and $\delta$ are assumed to be negative, obviously if the case is that of up-rise then the $\delta$ value would be positive.

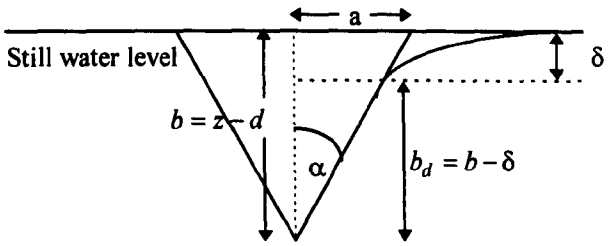


*Figure 6.1 Effects of draw-down δ on the submerged depth*

If we replace $b$ with $b_d$ in the force calculations, we obtain values that include draw-down. The same procedure is used for the box and knuckled body calculations.

We consider the following body/speed configurations for exiting and entering bodies

| | |
|---|---|
| Wedge | constant acceleration $\frac{g}{5}$ and $\frac{g}{2}$ m/s$^2$<br>constant velocity 0.2 m/s |
| Box | constant acceleration $\frac{g}{5}$ and $\frac{g}{2}$ m/s$^2$<br>constant velocity 0.2 m/s |
| Knuckle | constant acceleration $\frac{g}{5}$ and $\frac{g}{2}$ m/s$^2$<br>constant velocity 0.2 m/s |

Graphs of the "Total Force vs. Buoyancy" and "Added mass vs. Force difference" will be provided to compare against those already presented in Chapter 4 and Chapter 5.

For cases where jets are produced an additional correction has been implemented. If we use the body-surface intersection point to determine the up-rise we will over-compensate drastically since the jet is very rapid and thin. Instead we cut-off the jet at the point where the free surface is vertical, in a similar manner to the method used by Zhao & Faltinsen (1993), refer to Figure 6.2 for clarification. When this correction has been implemented the results will be presented on the force graphs together with the uncorrected data.

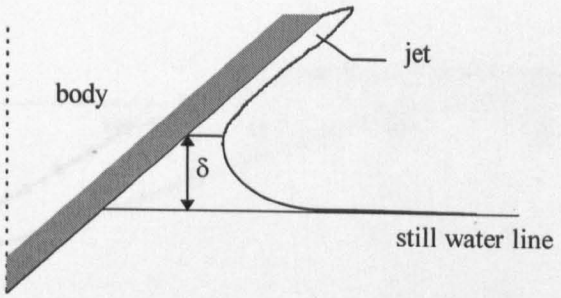


*Figure 6.2 Up-rise correction for jets*

## Wedge

### *Exit*

***Constant accelerated exit at $\frac{g}{5}$ ms².***

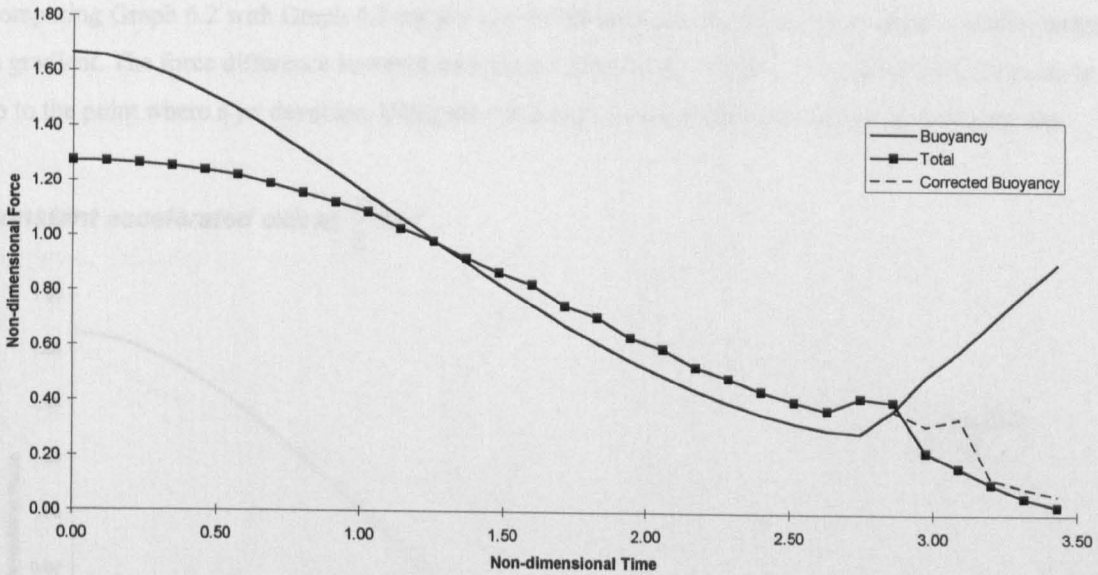


*Graph 6.1 Buoyancy and Total force, a/g=0.2*

Comparison of this graph with Graph 4.1 shows a marked improvement in the buoyancy forces estimation of the total force. Although the initial difference (at t=0) is obviously the same, since we start with a flat free-surface, the difference between the two curves reduces as time increases. Note also that the local maxima at t~2.75 in the total force curve coincides with the sudden gradient change in the buoyancy at this point a jet is beginning to form, causing rapid up-rise. We have introduced the correction cutting of the jet at its highest vertical point as in Figure 6.2. This correction brings the buoyancy closer to the total force.

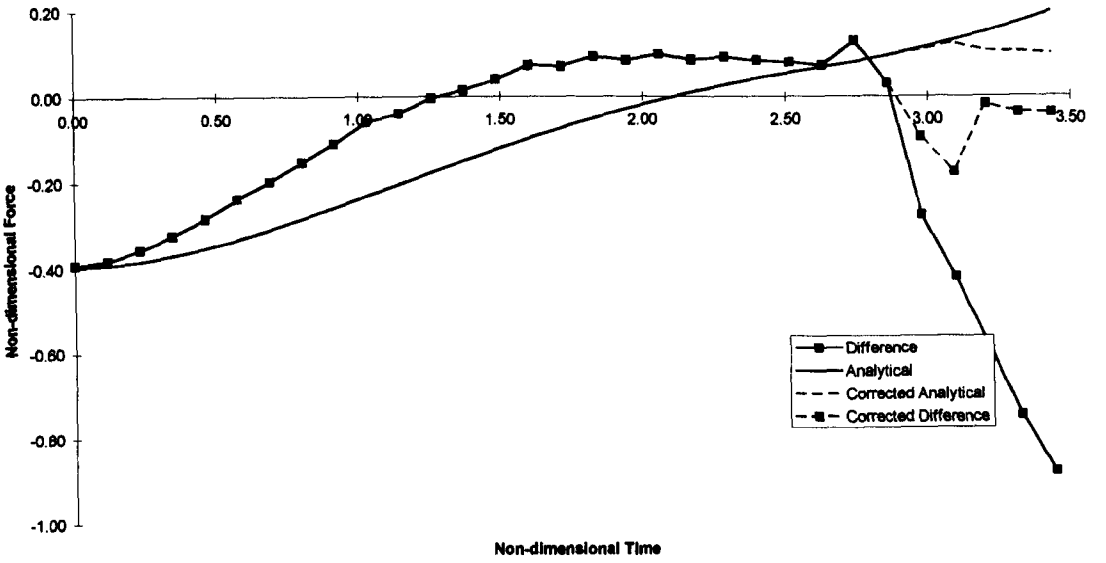


*Graph 6.2 Added mass force and force difference, a/g=0.2*

Comparing Graph 6.2 with Graph 4.2 we see that the added mass force has experienced a small change in gradient. The force difference however now has a similar slope to that of the added mass force curve, up to the point where a jet develops. Using the correction we maintain proximity of the two data sets.

***Constant accelerated exit at*** $\frac{g}{2}$ $ms^2$.

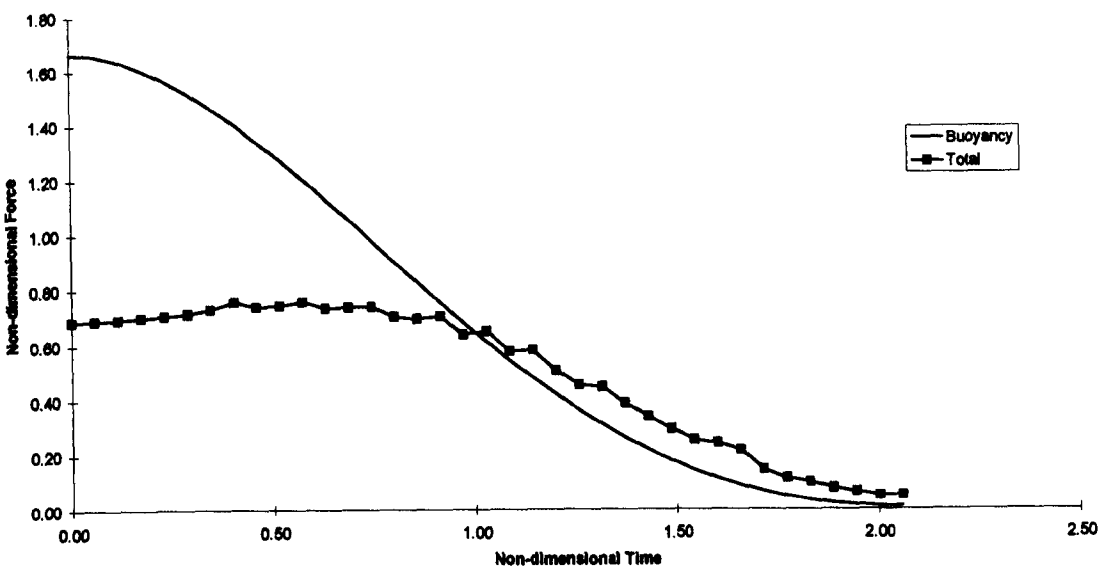


*Graph 6.3 Buoyancy and Total force, a/g=0.5*

Compare with Graph 4.5. We see a similar picture here to the a/g=0.2 case. The buoyancy still has the initial difference, as we would expect, but compares favourably with the total force at the later stages of the motion. Unlike the previous example we have no jet creation this time and so the large time results are far better.

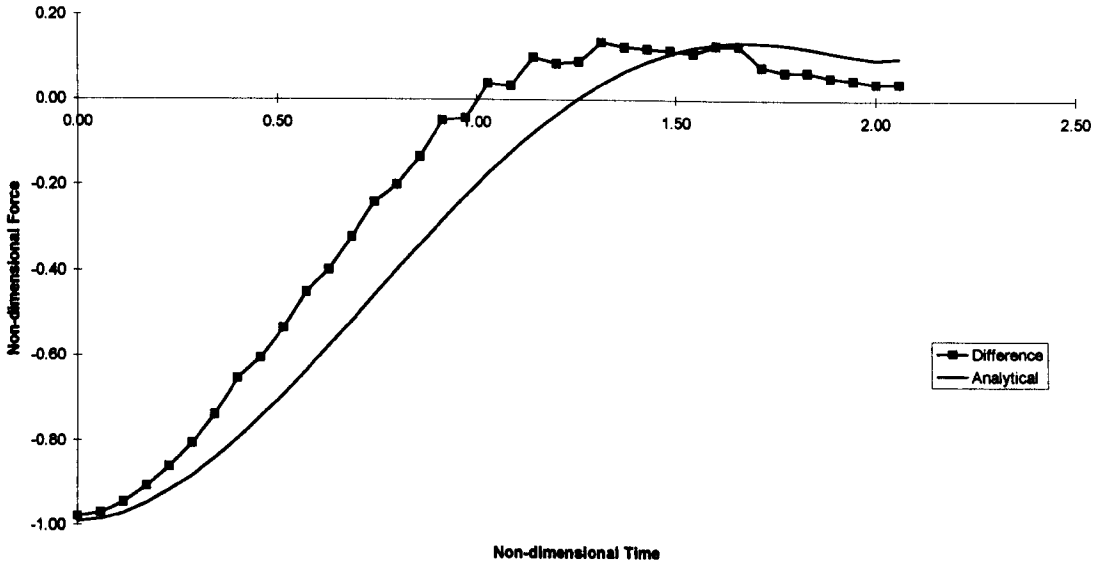


*Graph 6.4 Added mass force and force difference, a/g=0.5*

Compare with Graph 4.6. Over the complete motion the actual improvement on the approximation of the force difference by the added mass force is not that great compared to the method excluding draw-down. However, the most notable difference is that the two curves, again, have very similar gradients unlike those in Graph 4.6.

### Constant velocity exit at 0.2 $ms^{-1}$.

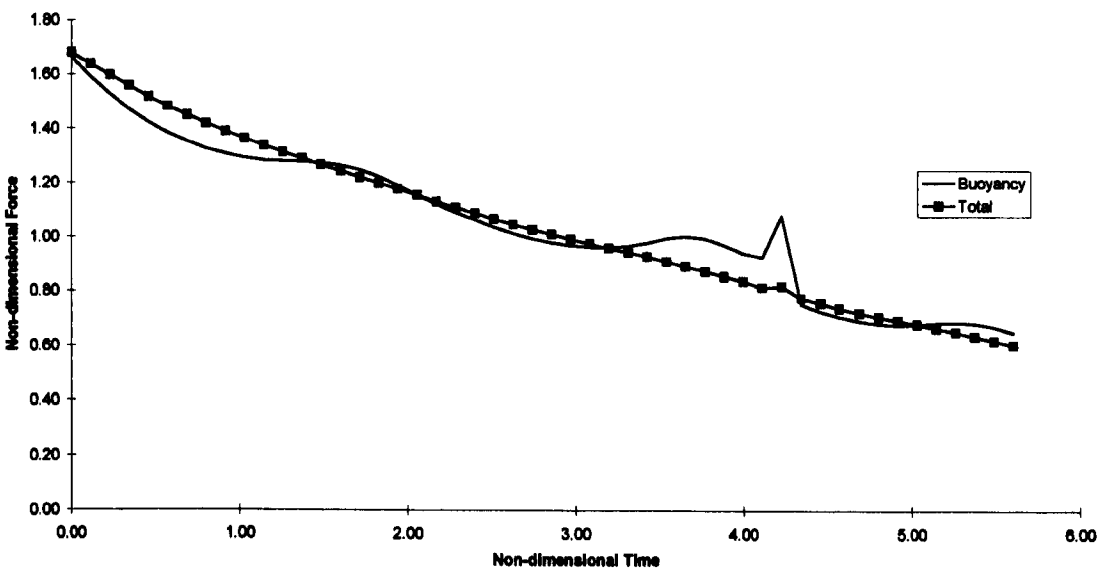


*Graph 6.5 Buoyancy force and Total force, Froude Number 0.117*

Compare with Graph 4.26. There is no real marked improvement here, suffice to note that the small "blip" in the total force is mimicked and accentuated by the buoyancy force curve. Surface profiles of the model show the intersection point moving rapidly from a position slightly above the mean free-

surface to a position below the mean free-surface. This will obviously cause a sudden change in the draw-down and thus the "blip" in the buoyancy force curve that is not on the original graph.

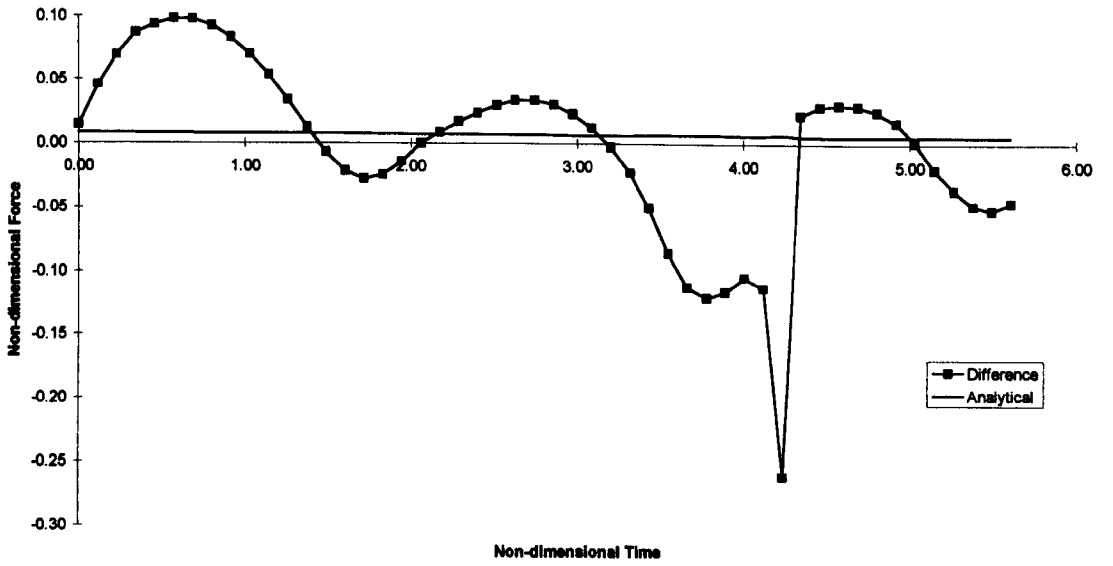


*Graph 6.6 Added mass force and force difference, Froude Number 0.117*

There is a notable degeneration in the results for Graph 6.6 compared those in Graph 4.27. The added mass force has decreased and is now negligible, whereas the difference between the total force and buoyancy has actually increased and now fluctuates around the zero force line.

## *Entry*

We will now consider the same cases for body entry.

***Constant accelerated entry at $\frac{g}{5}$ $ms^{-2}$.***

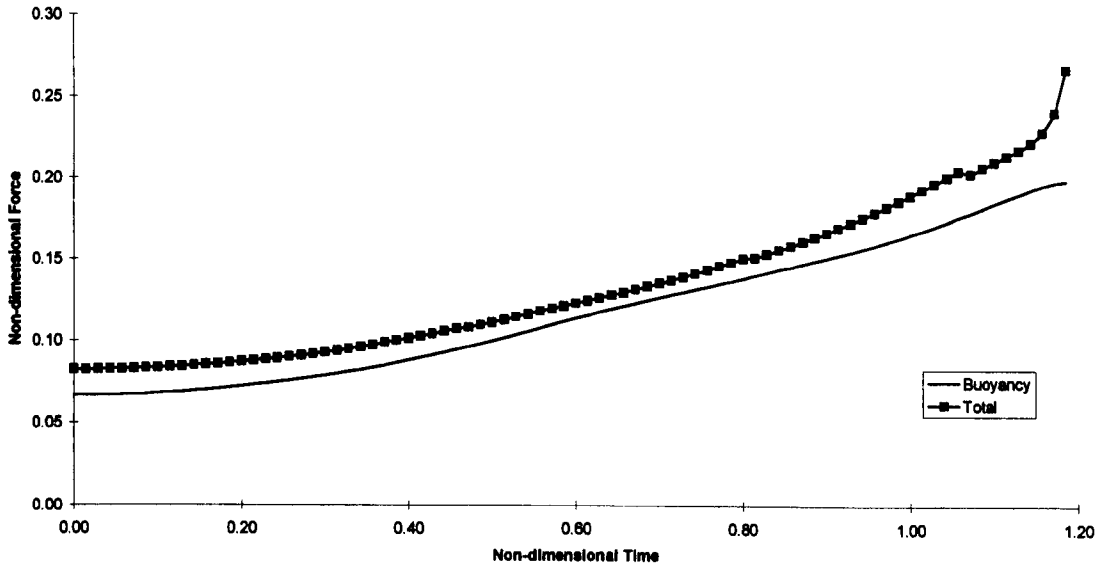


*Graph 6.7 Buoyancy and Total force, a/g=0.2*

Compare with Graph 5.1. As in the exit case, there is an improvement in the buoyancy forces approximation of the Total force. The initial difference remains the same as in Graph 5.1 but the gradient now matches the Total force curve.

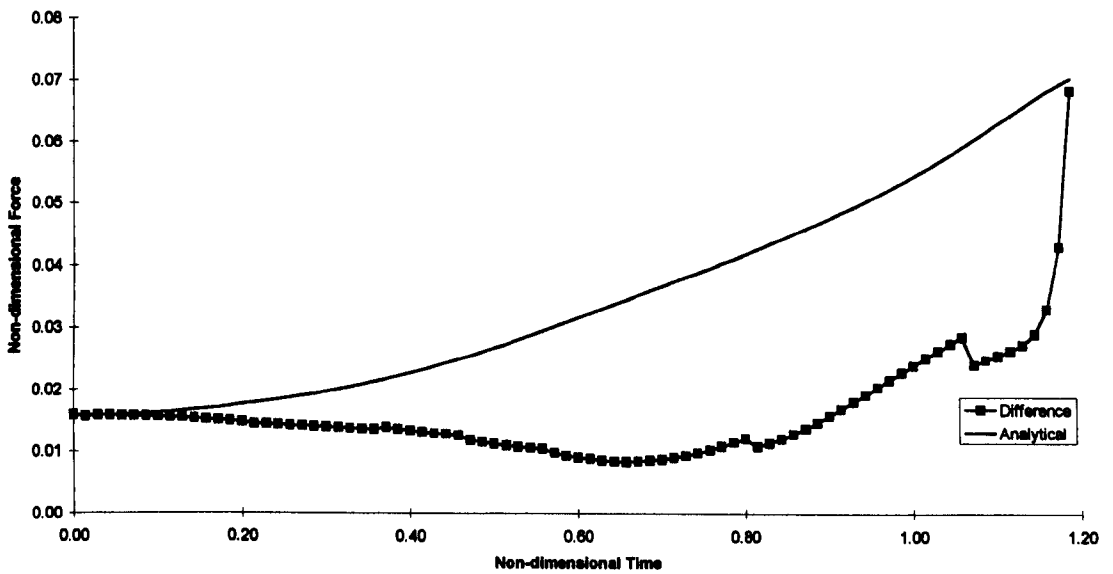


*Graph 6.8 Added mass force and force difference, a/g=0.2*

Compare with Graph 5.2. Due largely to the improvement in the buoyancy force approximation we now have better agreement between the added mass force and the force difference.

***Constant accelerated entry at $\frac{g}{2}$ ms$^{-2}$.***

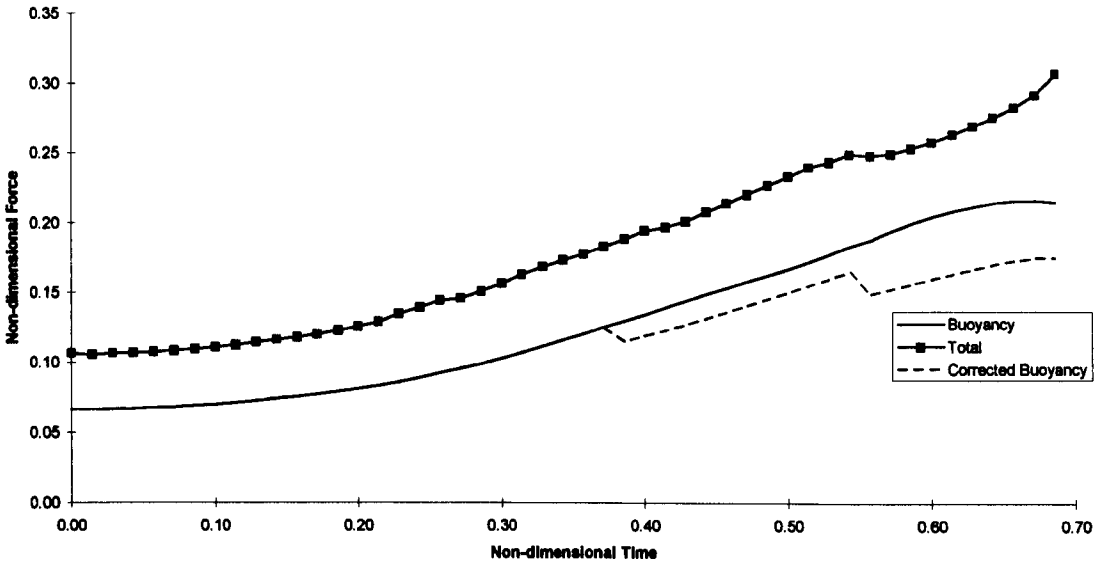


*Graph 6.9 Buoyancy and Total force, a/g=0.5*

Compare with Graph 5.5. The gradient of the buoyancy curve now more closely matches that of the Total force.

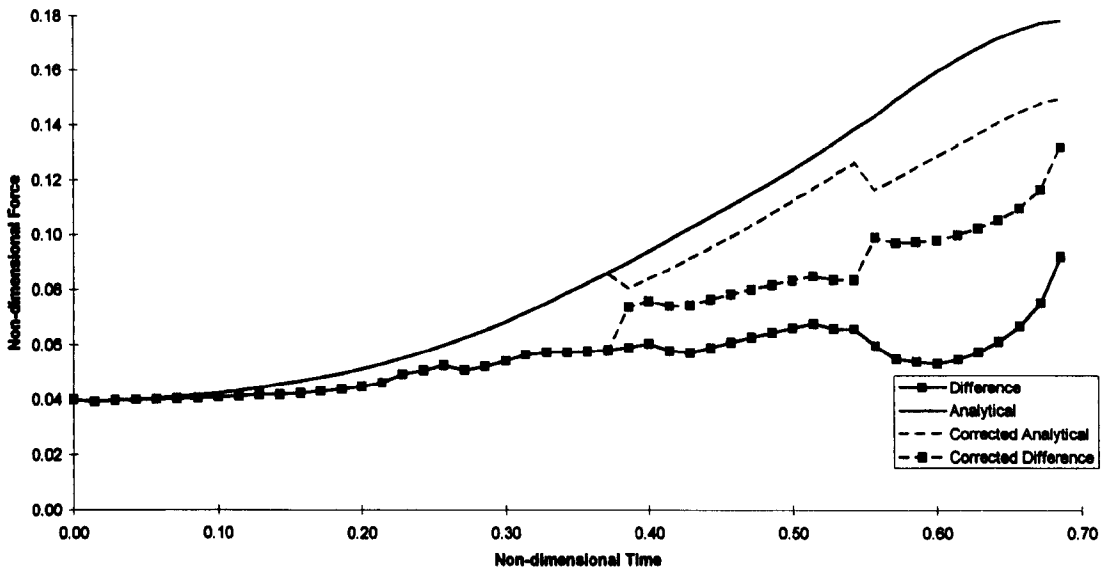


*Graph 6.10 Added mass force and force difference curves, a/g=0.5*

Compare with Graph 5.6. The gradient of the added mass force curve has changed by a large amount. The overall improvement in the approximation of the force difference is minimal. If we include the additional correction, where the draw-down is measured to the point where the jet becomes vertical rather than to the peak of the jet, we see some improvement. This indicates that inclusion of the jet peak in the draw-down evaluation is erroneous.

***constant velocity entry at 0.2 $ms^{-1}$.***

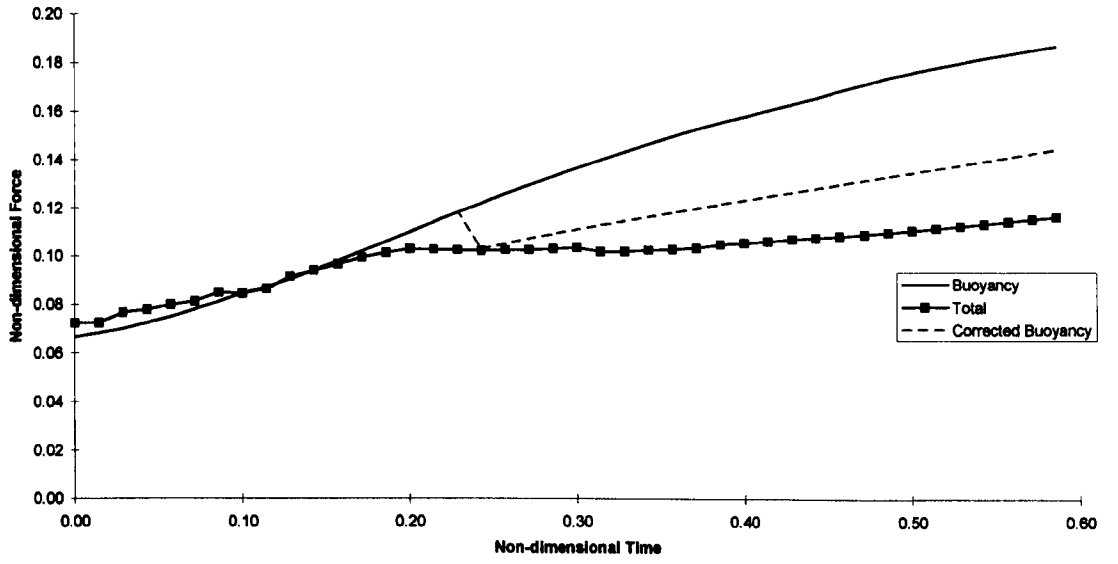


*Graph 6.11 Buoyancy and Total force, Froude Number 0.117*

Compare with Graph 5.25. The curves improve in their proximity to one another in the early time steps but at later time the differences are greater than those in the non-draw-down case. When the correction is also included we find there is an overall improvement on the original results.

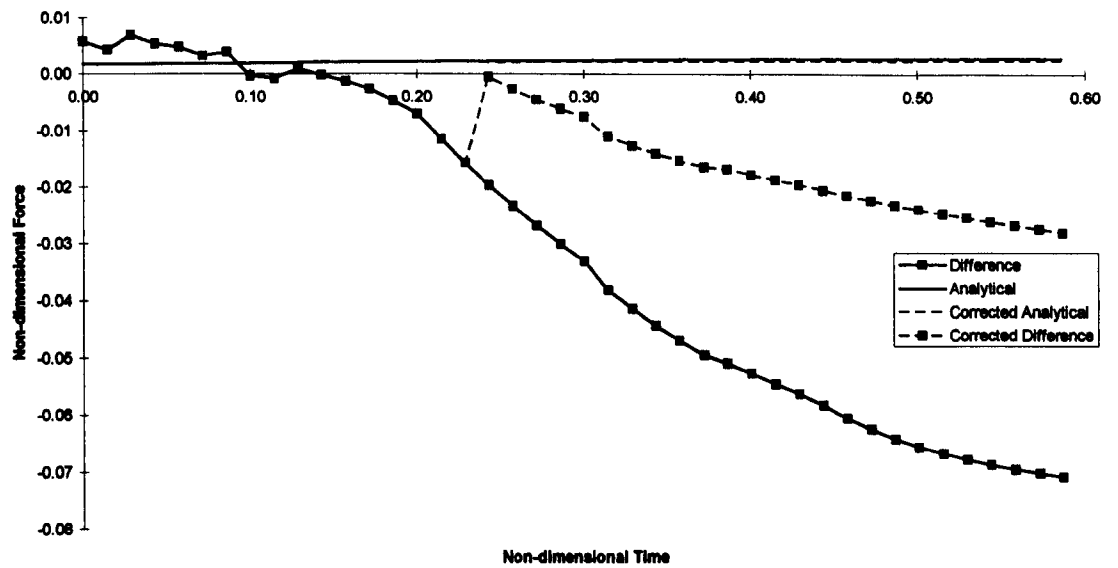


*Graph 6.12 Added mass force and force difference, Froude Number 0.117*

Compare with Graph 5.26. There is a slight improvement on the original result, this is more pronounced before $t = 0.2$. The correction has significant impact on result after $t = 0.2$. The added mass force, as demonstrated in Chapter 5, has little impact in the constant velocity case.

## Box

### *Exit*

***Constant accelerated exit at $\frac{g}{5}$ $ms^{-2}$.***

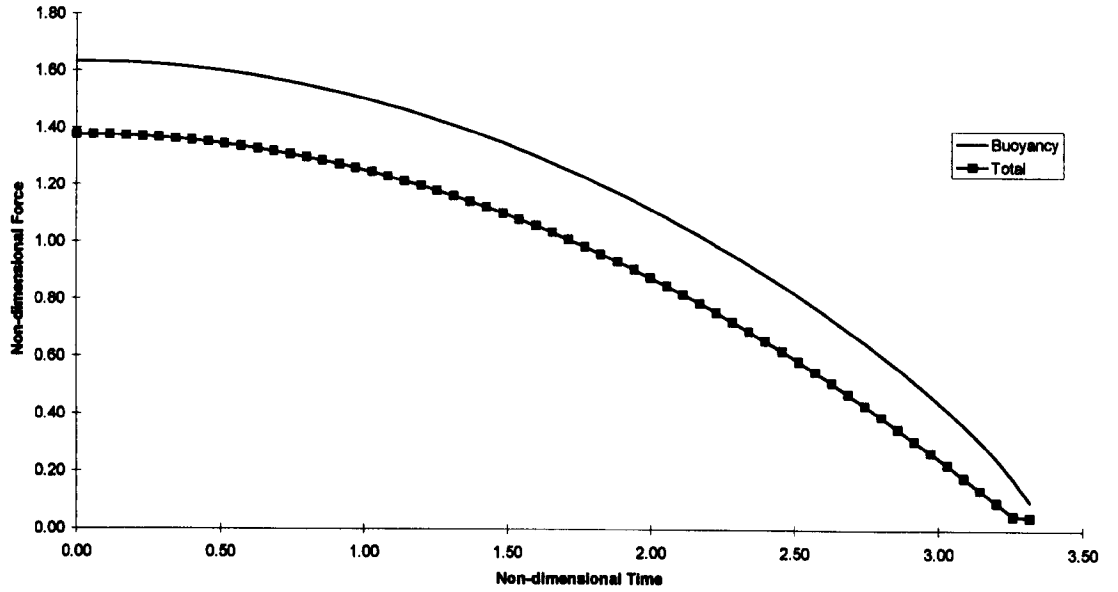


*Graph 6.13 Buoyancy force and Total force, a/g=0.2*

Compare with Graph 4.9. Agreement was good for the original case excluding draw-down, because on the wall-sided body we do not see as much surface movement in the area local to the intersection point. One slight difference is that in later stages of the motion the buoyancy curve approaches the total force curve.

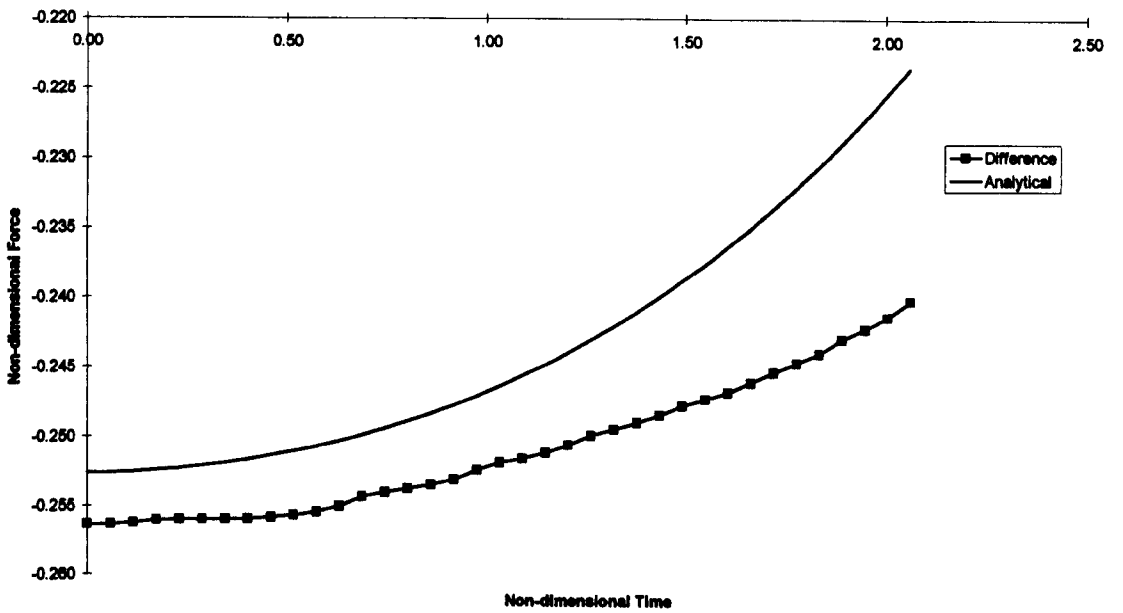


*Graph 6.14Added mass force and force difference, a/g=0.2*

Compare with Graph 4.10. Here the difference is more apparent. The slight change in Graph 6.14 causes the difference curve to take on a positive gradient. A similar change occurs in the added mass force and so we have better agreement.

***Constant accelerated exit at $\frac{g}{2}$ ms$^{-2}$.***

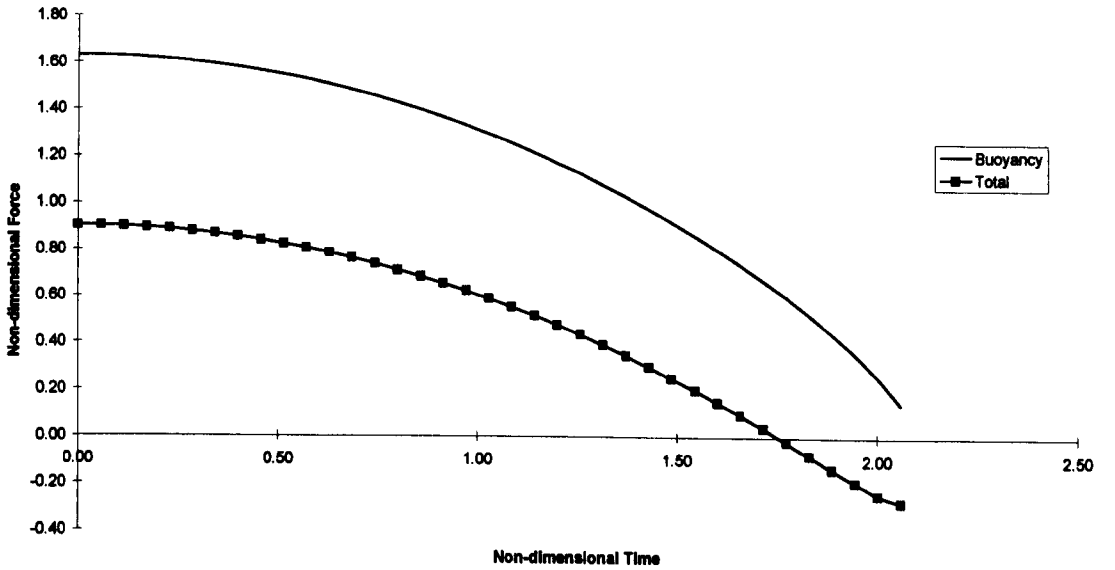


*Graph 6.15 Buoyancy force and Total force, a/g=0.5*

Compare with Graph 4.13. This is very similar situation to the previous example, with a slight change in the gradient of the buoyancy curve at larger time.

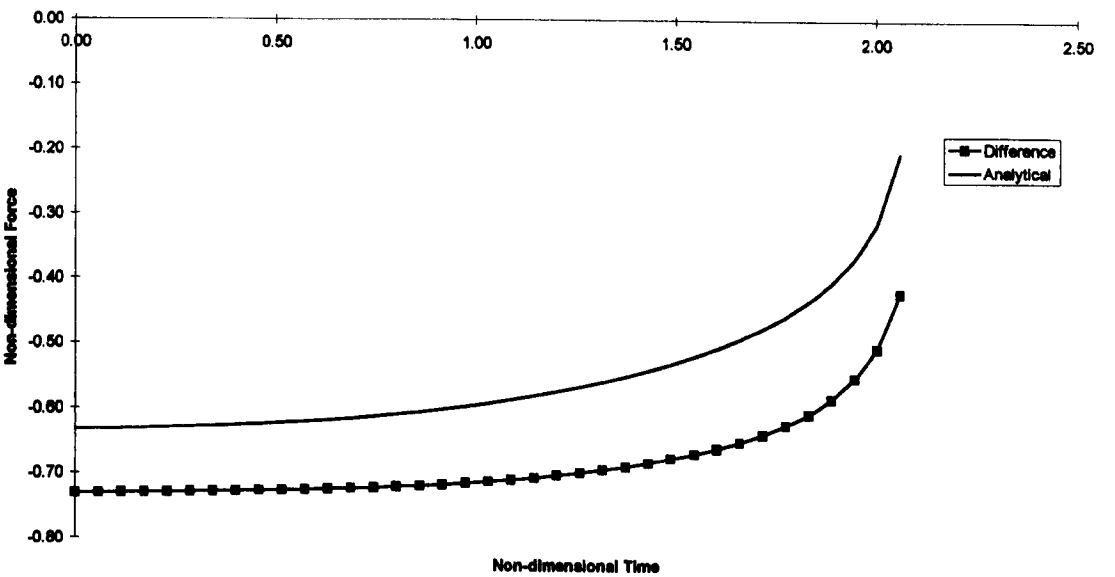


*Graph 6.16 Added mass force and force difference, a/g=0.5*

Compare with Graph 4.14. Again as in the previous example the small change in the buoyancy has had significant impact on the force difference and its comparison with the added mass force. The forces in Graph 4.14 differed in the later time stages, whereas now there is agreement throughout the motion.

***Constant velocity exit at 0.2 ms$^{-1}$.***

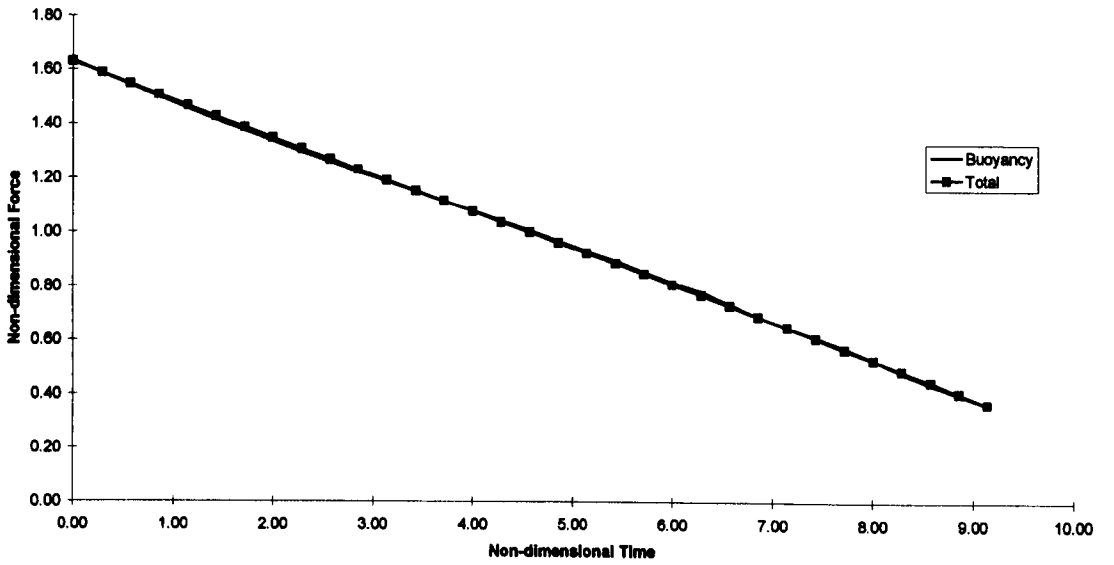


*Graph 6.17 Buoyancy force and Total force, Froude Number 0.117*

Compare with Graph 4.42. The buoyancy force almost completely accounts for the Total force in this case.

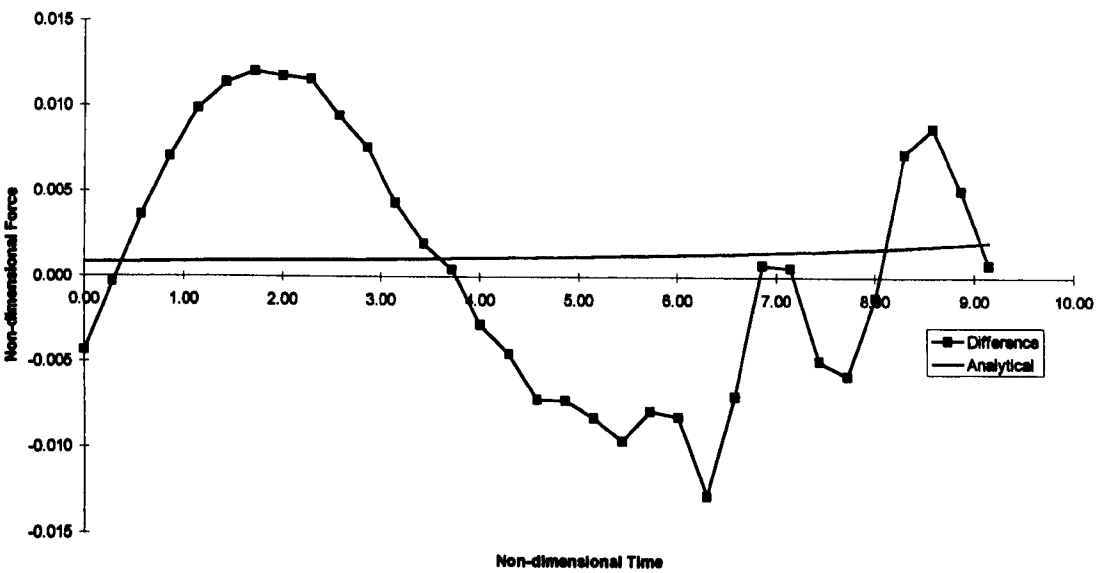


*Graph 6.18 Added mass force and force difference, Froude Number 0.117*

The force difference curve is less linear than in Graph 4.43 but the values remain in the locality of the analytical approximation, making the draw-down inclusion beneficial.

## *Entry*

### *Constant accelerated entry at $\frac{g}{5}$ $ms^{-2}$.*

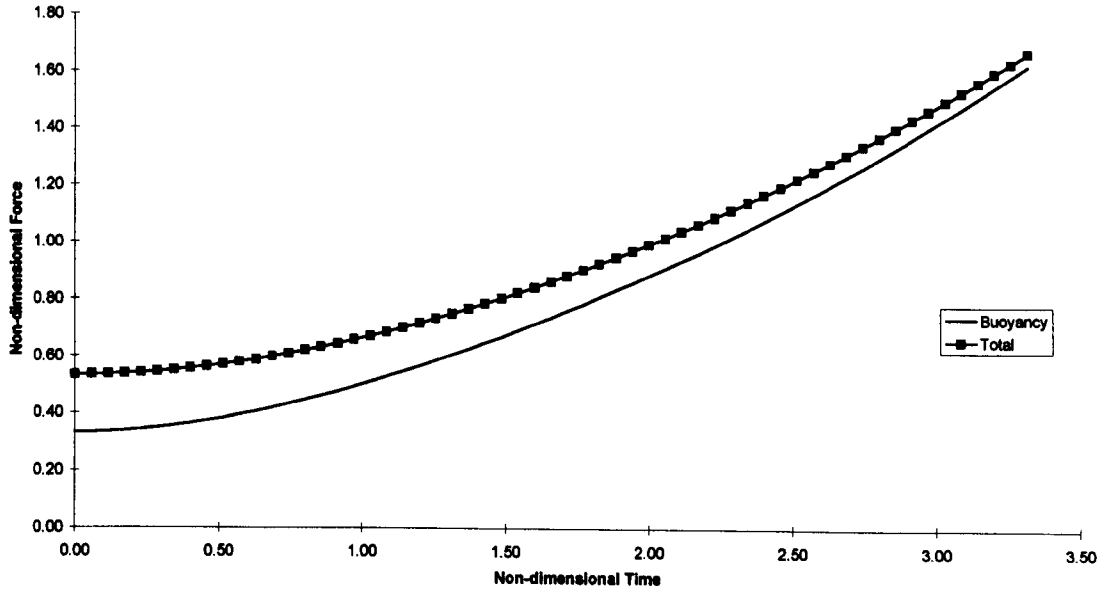


*Graph 6.19 Buoyancy force and Total force, a/g=0.2*

Compare with Graph 5.9. The buoyancy tends toward the total force, an improvement for larger time.

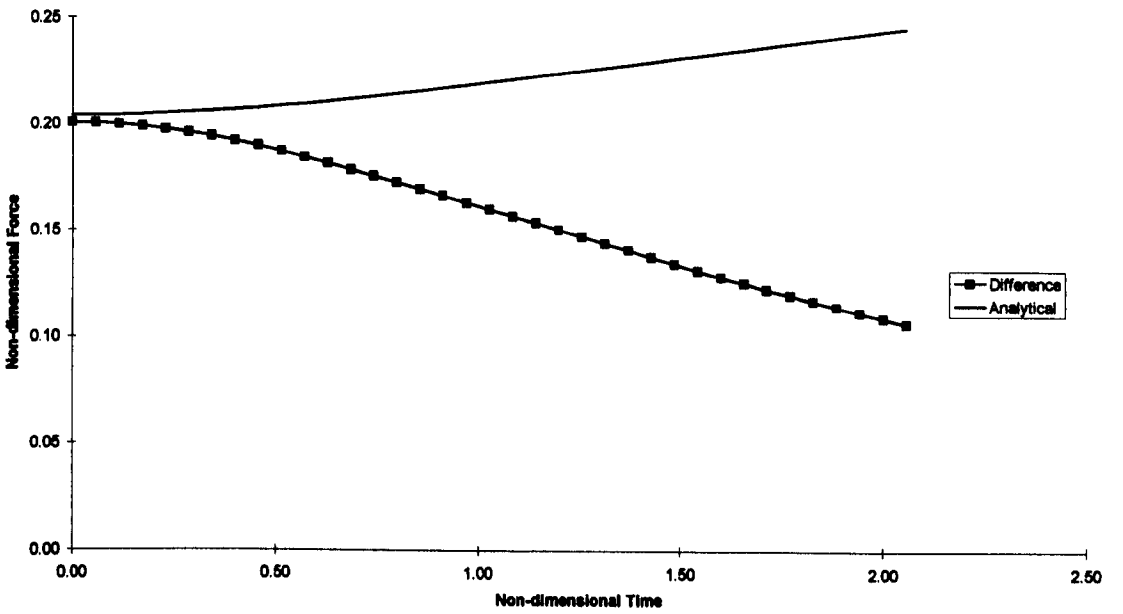


*Graph 6.20 Added mass force and force difference, a/g=0.2,*

Compare with Graph 5.10. There is no improvement here at all, in fact the results are better in the non-draw-down case. The improvement in the buoyancy forces approximation has been to the added mass forces detriment.

***Constant accelerated entry at $\frac{g}{2}$ $ms^{-2}$.***

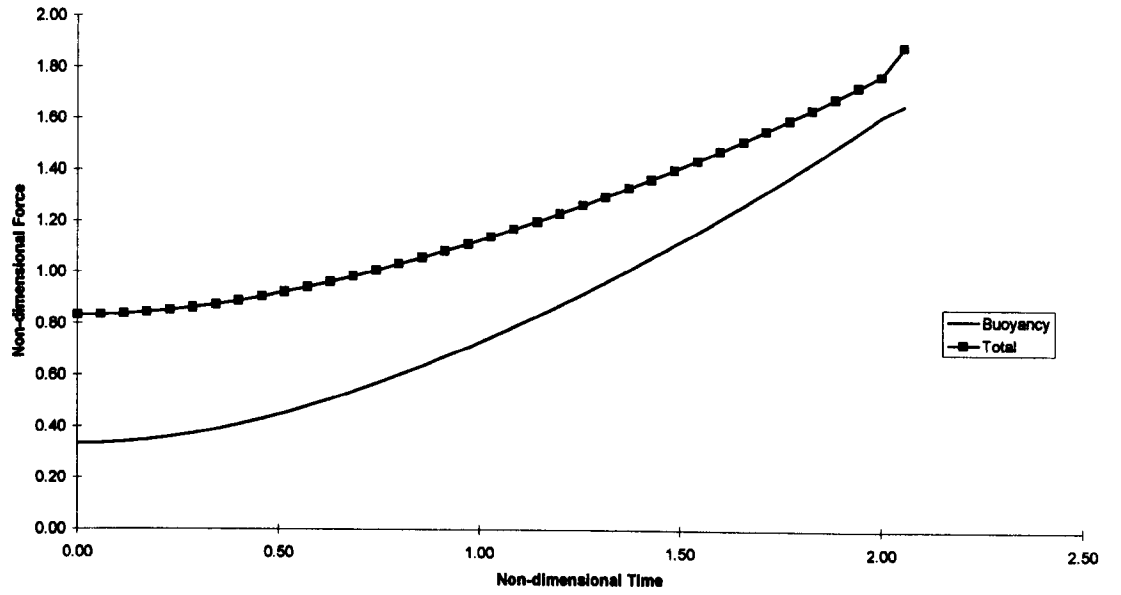


*Graph 6.21 Buoyancy force and Total force, a/g=0.5*

A small improvement on Graph 5.13 at large time can be seen.

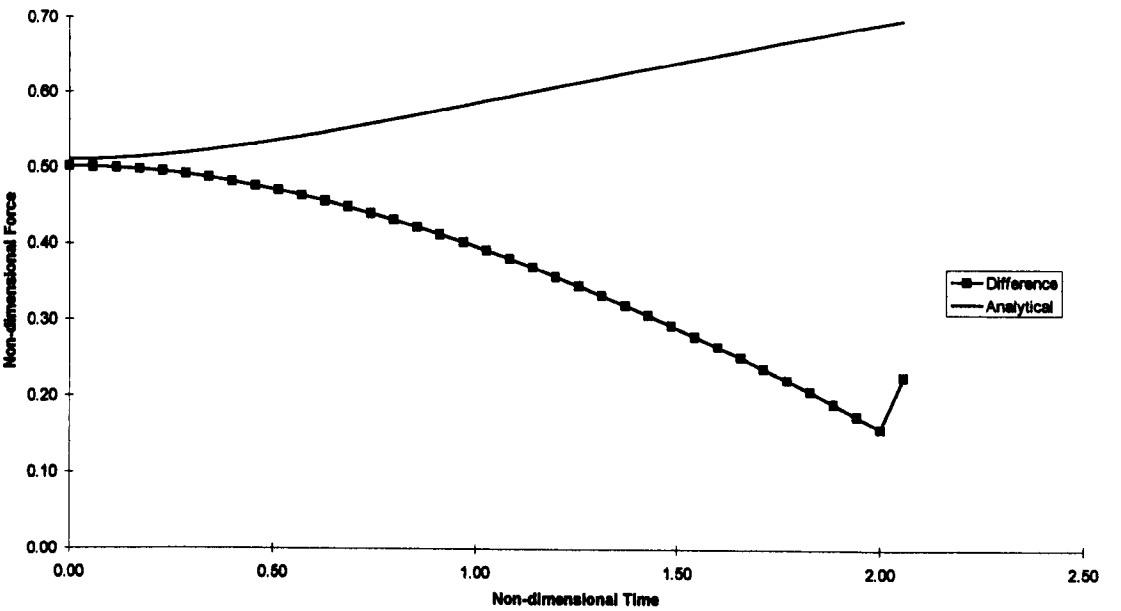


*Graph 6.22 Added mass force and force difference, a/g=0.5*

Compare with Graph 5.14. The added mass force has changed little from the case in Graph 5.14 but due to the buoyancy force improvement the approximation is not as good.

***Constant velocity entry at 0.2 ms$^{-1}$***

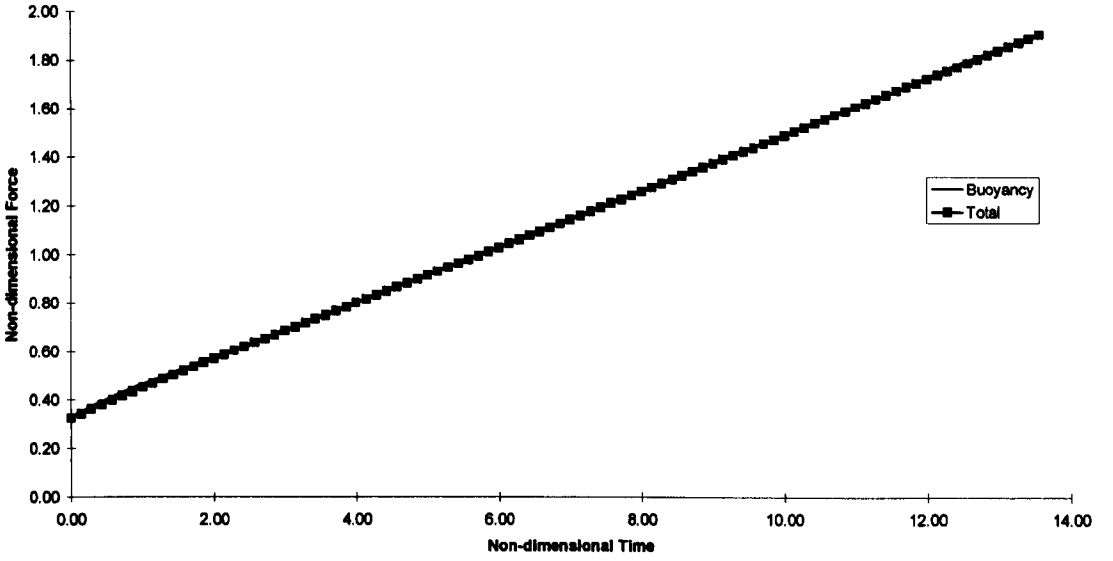


*Graph 6.23 Buoyancy force and total force, Froude Number 0.117*

Compare with Graph 5.34. The original produced very good results, so improvement would be hard, however, let us consider the difference.

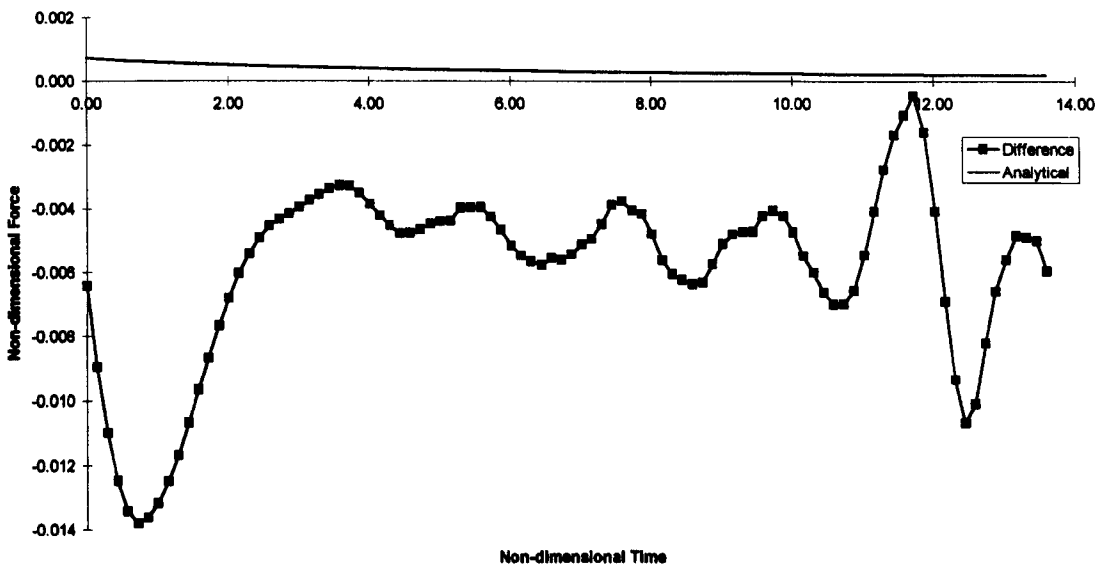


*Graph 6.24 Added mass force and force difference, Froude Number 0.117*

Compare with Graph 5.34. The difference between the buoyancy force and total force produces a different curve in this case but the nett improvement, of including the draw-down, is nil.

## Knuckle

### *Exit*

***Constant accelerated exit at $\frac{g}{5}$ $ms^{-2}$.***

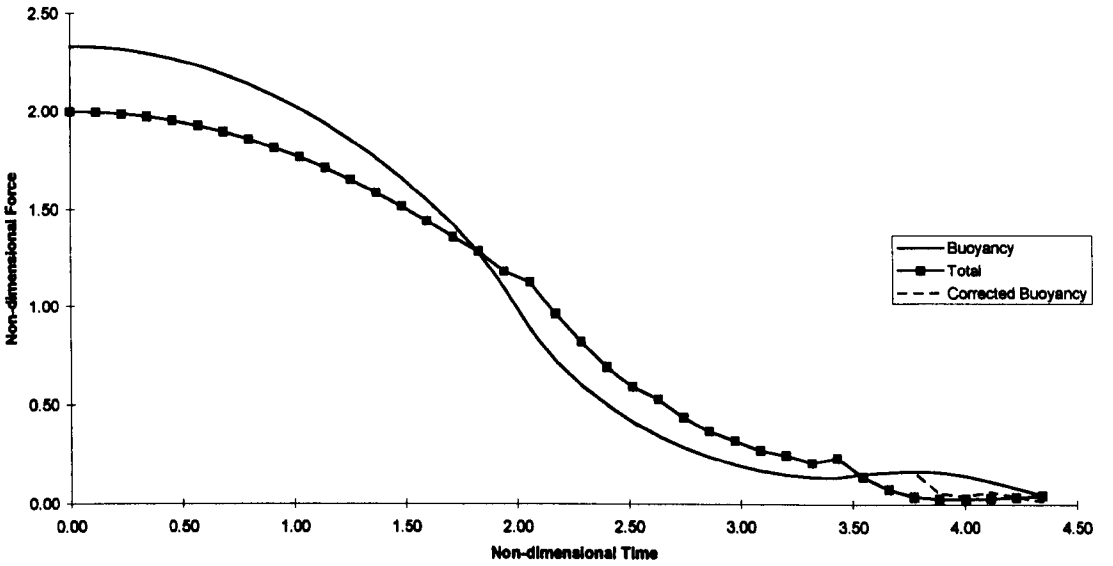


*Graph 6.25 Buoyancy and Total force, a/g=0.2*

This shows slight improvement over Graph 4.18, with the curves intersecting at two points. A further improvement is noticeable with the inclusion of the jet correction.

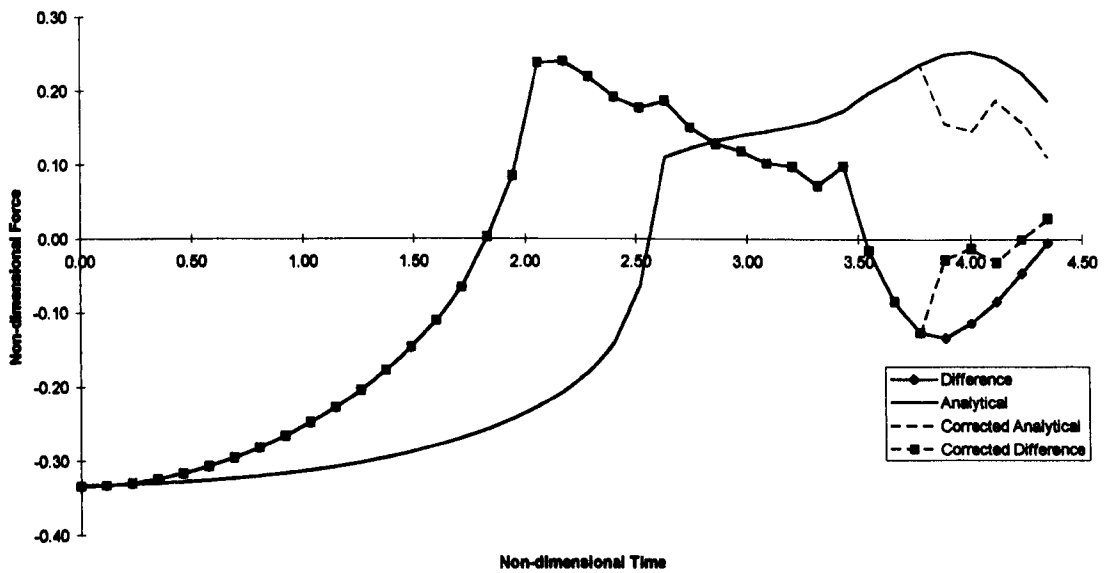


*Graph 6.26 Added mass force and force difference, a/g=0.2*

Compare with Graph 4.19. The curves have a similar appearance but the differences between the two curves are in the same range as those without the inclusion of draw-down.

***Constant accelerated exit at $\frac{g}{2}$ $ms^{-2}$.***

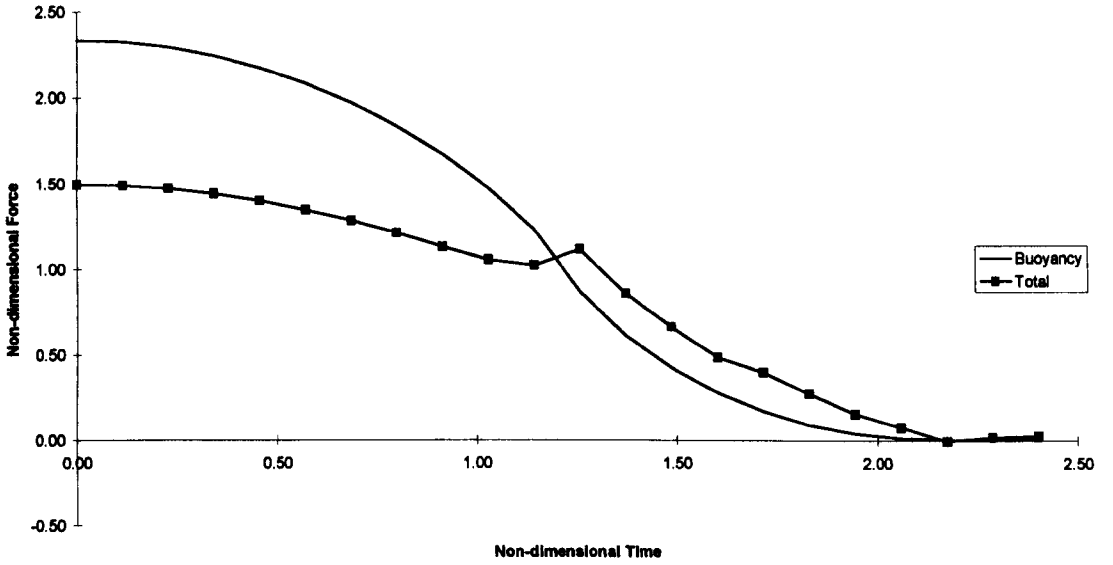


*Graph 6.27 Buoyancy and total force, a/g=0.5*

Compare with Graph 4.22. Here the draw-down result is smooth and so the benefits are apparent. There is more agreement between the two curves at later time than in Graph 4.22.

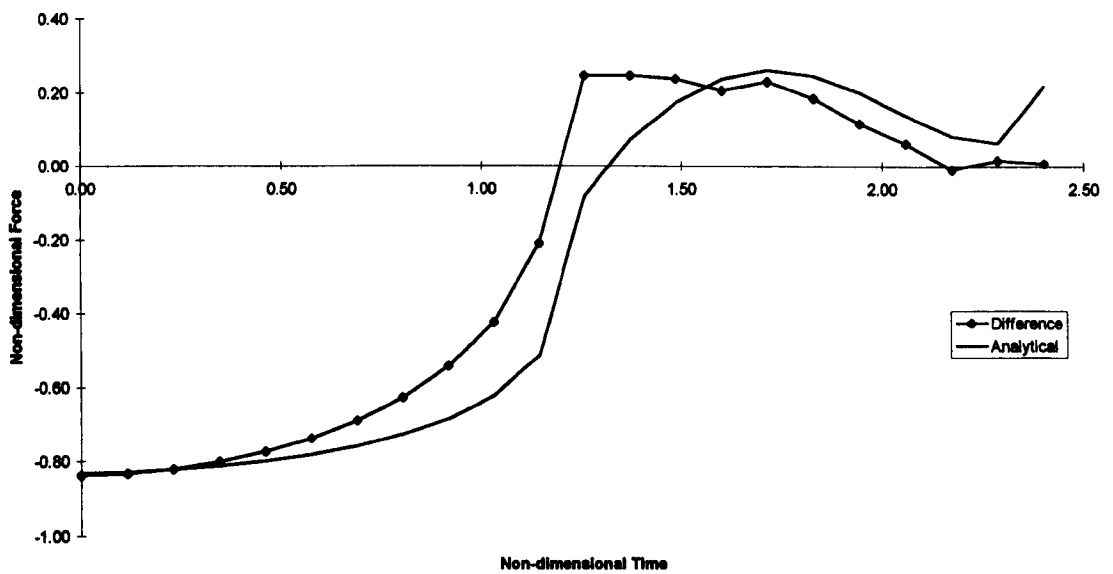


*Graph 6.28 Added mass force and force difference, a/g=0.5*

Compare with Graph 4.23. This result is very encouraging, showing the benefits of draw-down inclusion and the need for some empirical/heuristic method of obtaining such draw-down values.

***Constant velocity exit at 0.2 $ms^{-1}$.***

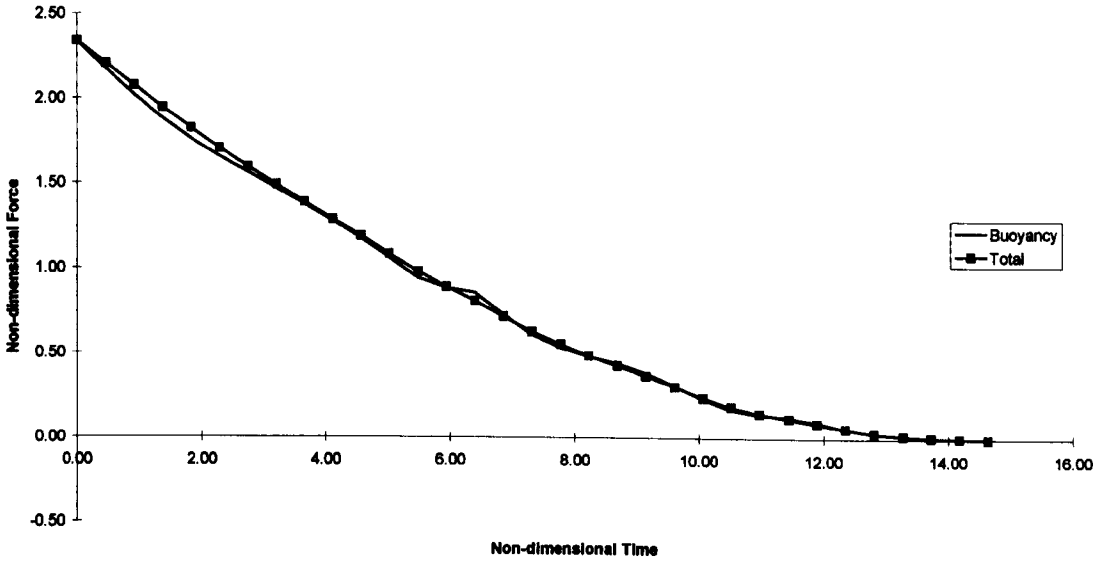


*Graph 6.29 Buoyancy and Total force, Froude Number 0.117*

Here we have no real improvement on Graph 4.59. The continual fluctuations of the draw-down data cause the buoyancy calculations to meander around the total force values.

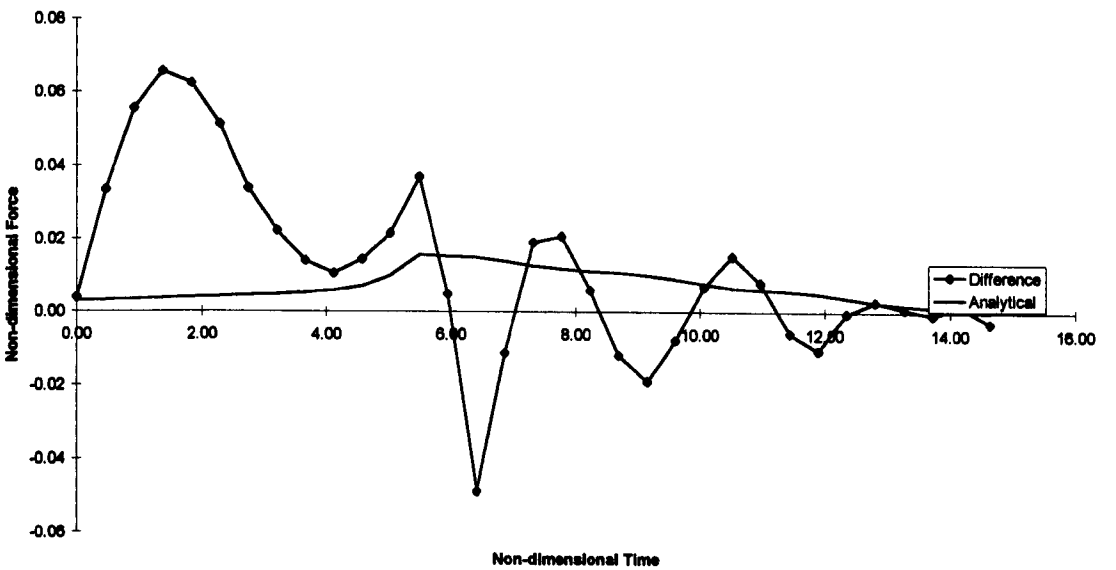


*Graph 6.30 Added mass force and force difference, Froude Number 0.117*

Until t=6 we have an improvement on Graph 4.60, with a maximum difference of 0.05 (a 50% improvement). However the later fluctuations of the intersection point affect the draw-down figures (see Chapter 4 for further explanation).

## *Entry*

### *Constant accelerated entry at $\frac{g}{5}$ $ms^{-2}$.*

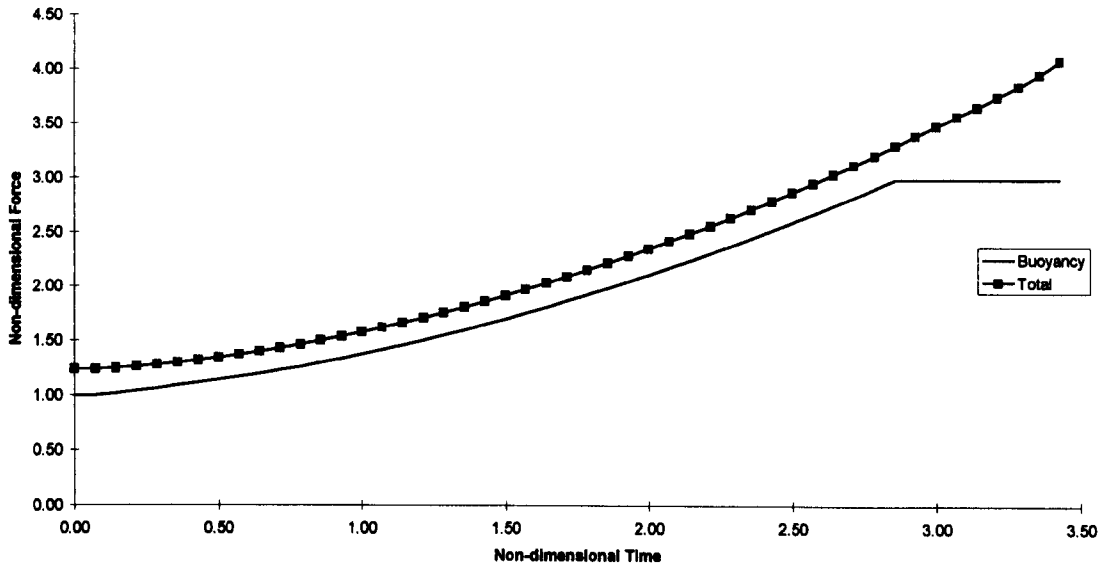


*Graph 6.31 Buoyancy and Total force, a/g=0.2*

There is a slight improvement on the buoyancy forces approximation of the Total force compared with Graph 5.17. The gradients are very close until t~3 when a plateau in the results appears, the plateau is a result of the intersection point reaching the top of the body, from that time the buoyancy force will be constant.

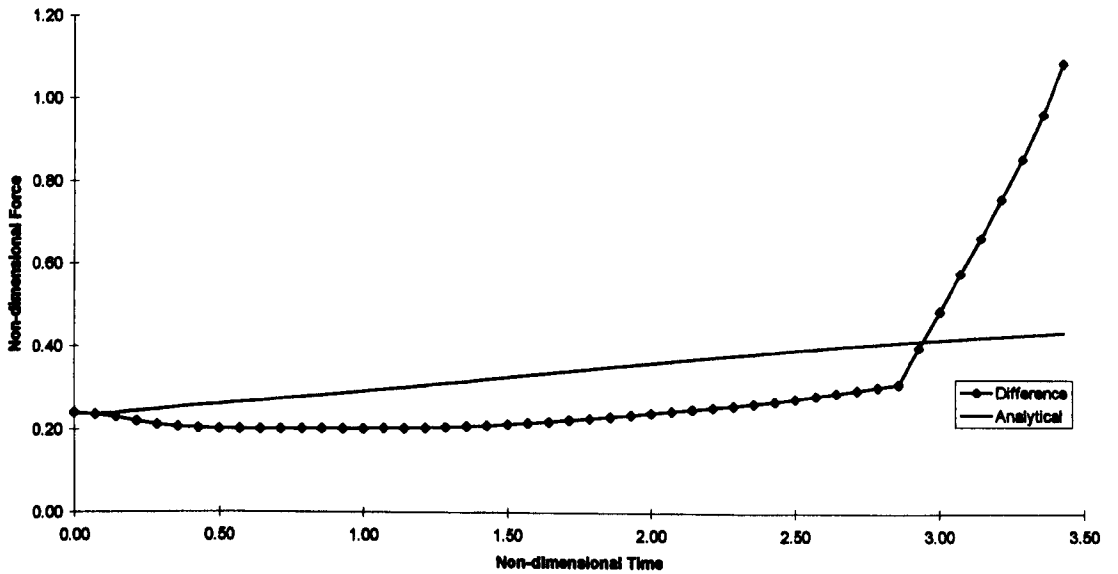


*Graph 6.32 Added mass force and force difference, a/g=0.2*

Compare with Graph 5.18. The difference between the results has reduced significantly. At t~3 the constant buoyancy effects the results, this is included for completeness but should be neglected since it is due to the numerical implementation.

***Constant accelerated entry at $\frac{g}{2}$ $ms^{-2}$.***

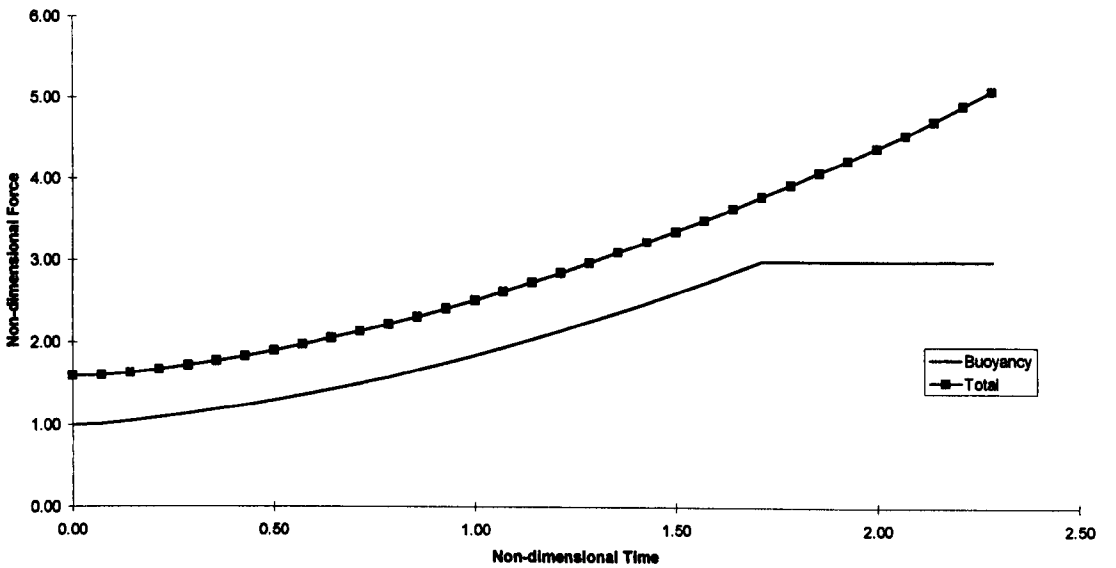


*Graph 6.33 Buoyancy and Total force, a/g=0.5*

Compare with Graph 5.21. The gradients compare favourably until t~1.75, here we see a similar plateau caused by the fluid surface reaching the top of the body.

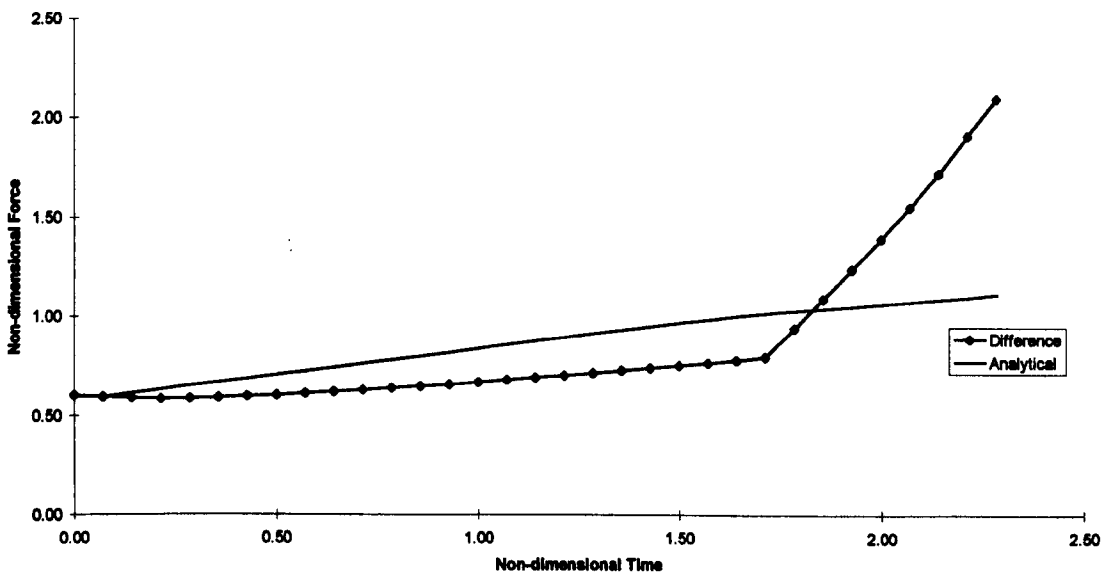


*Graph 6.34 Added mass force and force difference, a/g=0.5*

We see a slight improvement on the non-draw-down results in Graph 5.22.

***Constant velocity entry at 0.2 $ms^{-1}$.***

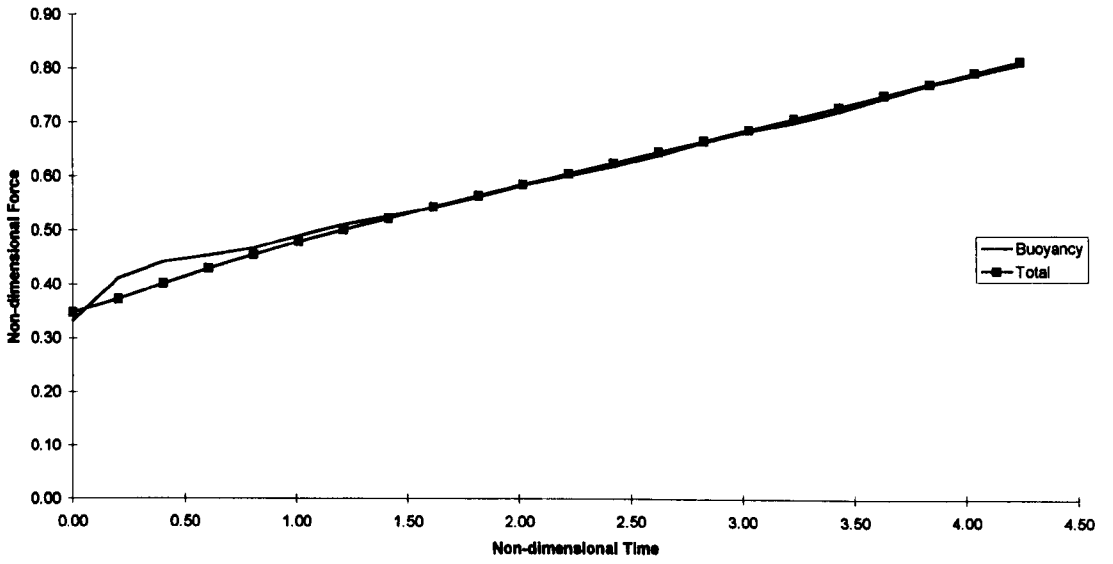


*Graph 6.35 Buoyancy force and Total force, Froude Number 0.117*

The results improve on those in Graph 5.50 in the later time stages.

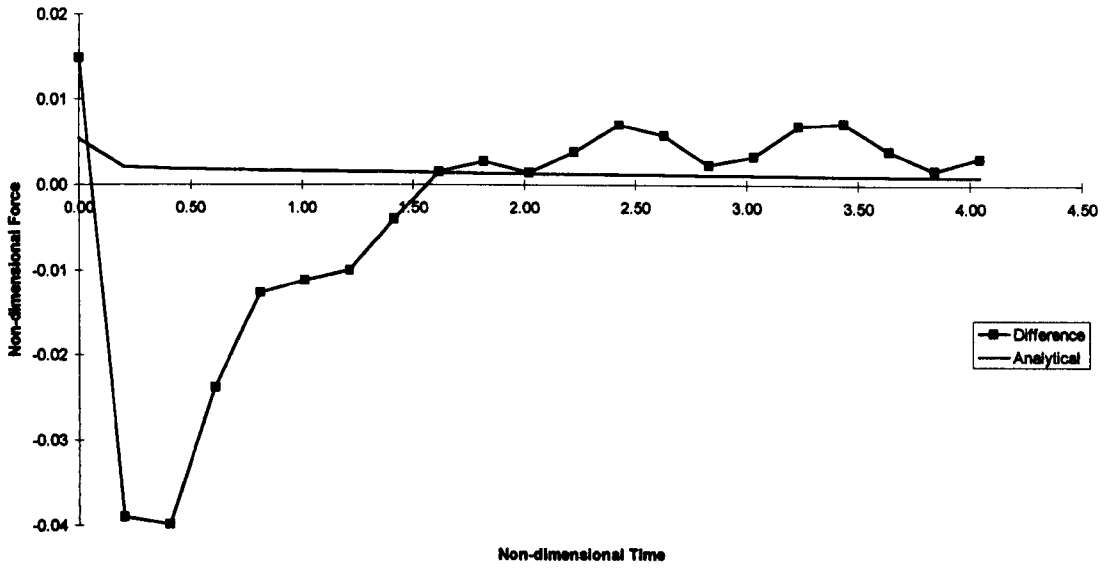


*Graph 6.36 Added mass force and force difference, Froude Number 0.117*

The initial steps result in a difference as large as those seen in Graph 5.51. At later time the results are a good improvement on the non-draw-down case. Since the added mass force is so small this is purely reliant on the buoyancy forces approximation of the total force.

## Conclusion

It appears that draw-down has, as we expected, significantly enhanced our results. The current theory assumes a surface at $\phi = 0$ and so all body volume calculations rely on that assumption. We

have shown in the free surface profiles of Chapter 4 and Chapter 5 that draw-down (and up-rise) can be large, and so will have a significant impact on the actual submerged body volume.

Generally, there is a marked improvement when draw-down is included, except in the constant velocity cases. We have established that the added mass model is ineffective in the constant velocity cases, so it is difficult to ascertain whether the draw-down correction enhances the results. One measure we can use is the improvement of the buoyancy force when compared with the total force calculation. Since this does benefit from the inclusion of draw-down, which has been true for all other cases presented, we may conclude that draw-down does enhance the calculations for constant velocity cases, and so for all cases considered.

Since such improvements can be made by using a draw-down value then when any such model is utilised an approximation of draw-down should be included, this could be obtained by empirical methods, i.e. filming a scale model, or an analytical/heuristic approach.

# Conclusion

In Chapter 1 we described the nature of the boundary-value problem for the motion of a body in inviscid irrotational fluid with a free surface. Existing linear and non-linear theories were discussed with particular reference to the topics of this thesis, namely water entry and exit problems which arise during extreme motions of bow sections of ships during slamming. The need for fully non-linear calculations was outlined, and how the results might be used in practical calculations.

Chapter 2 demonstrated that the numerical method we have employed provides us with a description of a body interacting with the free surface which is sufficiently precise to allow us to use it as a measure for the analytical theory presented in Chapter 3 and possible future numerical codes. The implementation and extension of the code was extensively tested for stability and accuracy, with variations of the discretisation of space and time, for a range of transient motions. Also the self-similar flow resulting from zero-gravity entry of a wedge was briefly checked.

The bulk of the numerical results are given in Chapters 4 and 5 which present an extensive set of runs for constant velocity or constant acceleration exit and entry of a wedge, box and knuckle-shaped body. These demonstrate the versatility and the limitations of the numerical scheme. Specifically we consider the free-surface profiles, the pressure distribution around the body and the resulting body force throughout the motion. For the box and, to a lesser extent, the knuckle-shaped body, the pressure profiles highlight the singularities at the body corners, which result in infinite pressures at these points. This is, of course, a weakness of the inviscid model itself; in reality vortices will be shed from the corners to satisfy a Kutta condition here. However it is stressed that the pressure singularities are integrable, and do result in finite forces on the body, so that a comparison with added mass theory is still possible.

Current methods for approximating the forces experienced by a body cross-section entering and exiting the fluid domain rely on the buoyancy force to be a suitable approximation. In Chapter 4 and 5 it can be clearly seen that the buoyancy force, calculated on the basis of a flat free-surface, only loosely approximates the forces involved, and then only in situations where the surface remains reasonably undisturbed. This analytical model is extended in Chapter 3 by calculating the added mass coefficient through the application of the Schwartz-Christoffel mapping the flow in the complex plane to uniform flow in the mapped plane and solving the resulting equations. This added mass coefficient is incorporated into the force equation and, while still applying the flat free-surface equipotential condition, we augment the buoyancy model. Result show that in the small time the added mass model can greatly improve the body force approximation, and we note that the small time is where the largest forces will be experienced. Thus the methods effectiveness is demonstrated for the immediate application to the approximation of forces experienced in the initial stages of motion. This applies to both the exit and entry cases.

The later stages of the motion are not approximated as well as the initial stages. The later stages are of particular relevance to the exiting case, since the final stages of exit motion would define the starting conditions of the following entry phase. Consideration of the free surface reveals that the intersection of the free-surface and the body does not remain static at the flat free-surface as we have assumed; in fact in the high speed cases we experience large movement both up (up-rise) and down (draw-down) the body. This has a significant effect on both the buoyancy model and our enhanced model, which consider the submerged body volume used in both calculations to be that part of the body below the flat free-surface. The non-linear calculations obviously show that this is not the case.

The numerical results highlighted that especially in the more violent (higher speed) motions, a large degree of draw-down/up-rise was observed on the surface profiles, where the body-surface intersection point moves rapidly down/up the body surface. In contrast to jet formation for an entering body, the rapid downwards free-surface ventilation of an exiting body does not appear to have been previously calculated. Both effects are of particular importance since as the current analytical methods are based on the assumption of a flat free surface, the larger the draw-down/up-rise observed, the more detrimental such an assumption will be. In the box-body cases it can be seen that this draw-down/up-rise is a local effect of a more widespread free-surface motion resulting in radiated waves; here the body-surface intersection point is moving with this wave motion. A more severe form of up-rise is that of jets. This is mostly exhibited in the wedge cases we considered, both in entry and in the last stages of exit, and is caused by the rapid up-rise of water on the body surface. As in the case of draw-down/up-rise this would also have a significant effect on the analytical models employed here. However, using the pressure profiles in conjunction with the free-surface profiles, we may predict that the jet would sometimes leave the body by determining the time when the pressure becomes negative in that region. Moreover, even in cases where this does not happen, it is noted that the pressures within the jets are almost zero and hence make no significant contribution to the force on the body. Thus using the actual intersection point (as calculated by the numerical code here) in the present analytical theories when jetting occurs is both inaccurate and misleading; chapter 6 therefore provides a pragmatic modification to the theory by removing the jets from consideration. We note that this approach also allows the early stages of complete immersion (when only spray jets rise above the freeboard) to be studied.

These results prompted an investigation into the possible improvements resulting from the inclusion of such draw-down/up-rise in the analytical model, Chapter 6. To illustrate the impact the inclusion of the deviations from the flat free-surface can have on the presented analytical models, we present results that include such draw-down/up-rise values in the calculations. The results are very encouraging. The buoyancy force experiences a large improvement when the submerged body volume is re-evaluated with regard to the draw-down/up-rise, and in some cases can virtually account for the total experienced body force. In the more extreme motions the added-mass model is still required (it should still be included in the other cases for consistency), and the contribution can be clearly seen. We conclude that draw-down/up-rise inclusion is very desirable, but jets need special treatment. However there is a problem in general: there is currently no way to predict the position of the free surface *a priori* without

the use of a fully non-linear model to calculate the free-surface, exactly the complication we are striving to avoid. In situations where one lacks exact calculations, one could estimate the draw-down/up-rise through the use of scale model simulations, and apply the correction empirically to the analytical model.

The methods presented within this thesis have demonstrated that exact calculation of the interaction of a two-dimensional ship section with a non-linear free surface reveals interesting hydrodynamic effects such as radiated waves, spray jets and rapid draw-down, but may be too costly for routine calculations. We have seen that such calculations can be provided by the analytical methods based on added-mass provided that draw-down/up-rise of the free surface local to the body is included. This appears to open the way to the application of a modified strip theory in existing codes to extreme ship motions in random seas. Within this context, it would be interesting for future workers to examine the sensitivity of extremes in such quantities as bow acceleration, bow displacement, shear forces and bending moments in the ship's structure, to the choice of analytical model (i.e. buoyancy only, buoyancy plus added mass, buoyancy plus added mass with draw-down/rise-up correction).

# Recommendations

There are four areas the author would like to see future work directed towards.

1. **Constant velocity added mass**

   The poor performance of the added mass at constant velocity has been demonstrated. It would be desirable to refine the $dm_a/dy$ calculation to take account of the draw-down (up-rise) of the free surface during exit (entry). The present calculations have done this by considering the instantaneous free surface position taken from the numerical calculations; such calculations fully solve the problem and will not be generally available. It is possible that data from model-scale experiments or some sort of empirical rule could be used instead, and further work is needed here.

2. **John's equation**

   The extension of John's equation to build analytical models for high Froude number (high speed or zero gravity) wedge entry remains an intriguing possibility. Knowing the r-function allows John's equation to be solved for a range of solution types, the simplest being polynomials. Adding these linear solutions together to satisfy the body-boundary condition would be straightforward, but annulling singularities within the fluid could be difficult (Greenhow(1983)).

3. **Corner flow**

   Can the analytical model of flow around the corner singularity be matched to an outer numerical flow, and would this improve the force calculations? For consistency, the matching would need to be carried out at every time step during the calculation, rather than retrospectively, since the free surface is, in principle, dependent on the calculation of the whole flow.

4. **Vortices**

   In reality the flow past sharp corners must separate and this would make comparison with experiments difficult. An attempt to model the shed vortices, possibly by single or multiple point vortex models, should be made taking into account their coupling with the non-linear free surface.

# Appendix A Numerical Results

*A selection of input and output data for the wedge body simulations.*

## Abstract

Input and output data is provided for reference and to assist in the future use of the model.

## Introduction

We present the data used and obtained in a selection of the wedge runs examined in Chapter 4 and Chapter 5. The information is provided with the intention of simplifying the use of the model and providing a reference for any future results from this and other models.

The information is provided in three tables

1. The input data. The setting of each variable is indicated. For flags I have interpreted their meaning, for a full description of the role of each variable in the input file refer to Appendix E.
2. Here we present the force, time, step number for each selected step and the pressure and position of each body node.
3. Finally we provide the surface and body profile for each of the selected steps. Twenty one surface points are given.

Each set of results span two pages and are headed by the particular runs details.

## Wedge exiting fluid domain with acceleration $g/5$

| | | | |
|---|---|---|---|
| number of steps | 2000 | position of cog (horizontal, vertical) | (0.0, -0.2) |
| time step size | 0.002 | surface width | 20 |
| height step size | 0.1 | water depth | 10 |
| print only | main steps | number of points in surface | 80 |
| print hamming predictor | NO | wave length | 1 |
| start type | normal | wave amplitude | 0 |
| jets leave body | NO | still water line | 0 |
| steps till jet leaves body | 10 | mass density ratio | 0.0075 |
| acceleration | 1.962 | moment of inertia density ratio | 0.001 |
| print every nth step | 10 | forward water line | 0 |
| sway allowed | NO | rear water line | 0 |
| heave allowed | YES | body type | 0 |
| roll allowed | NO | surface point ratio | 0.87 |
| node removal limit | 3 | number of body points | 60 |
| node addition limit | 1 | body point ratio | 0.9 |
| center of rotation (horizontal, vertical) | (0.0, -0.2) | distance of cog to vertex | 0.3 |
| velocity of cog (horizontal, vertical) | (0.0, 0.0) | wedge height | 0.5 |
| angle of body to vertical | 0 | right wedge angle to vertical | 45 |
| angular velocity about cog | 0 | total wedge angle | 90 |

*Table A.1 Input data*

| force | time | step | force | time | step | force | time | step | force | time | step | force | time | step |
|---|---|---|---|---|---|---|---|---|---|---|---|---|---|---|
| 1.79820 | 0.1 | 50 | 1.51330 | 0.2 | 100 | 1.10350 | 0.3 | 150 | 0.72329 | 0.4 | 200 | 0.60172 | 0.5 | 250 |
| Nodes | | | Nodes | | | Nodes | | | Nodes | | | Nodes | | |
| x | y | Pressure | x | y | Pressure | x | y | Pressure | x | y | Pressure | x | y | Pressure |
| 0.46803 | -0.02216 | 0.00000 | 0.40029 | -0.06047 | 0.00000 | 0.31914 | -0.09257 | 0.00000 | 0.24484 | -0.09820 | 0.00000 | 0.23846 | -0.01629 | 0.00000 |
| 0.44753 | -0.04266 | 0.04127 | 0.35780 | -0.10296 | 0.34220 | 0.28512 | -0.12659 | 0.34726 | 0.22625 | -0.11679 | 0.26929 | 0.22625 | -0.02850 | 0.72374 |
| 0.40030 | -0.08989 | 0.45291 | 0.31955 | -0.14121 | 0.74469 | 0.25414 | -0.15757 | 0.74637 | 0.20116 | -0.14188 | 0.60982 | 0.20116 | -0.05359 | 0.70380 |
| 0.35780 | -0.13239 | 0.78479 | 0.28512 | -0.17564 | 1.06060 | 0.22625 | -0.18546 | 1.03840 | 0.17857 | -0.16447 | 0.86036 | 0.17857 | -0.07618 | 0.69837 |
| 0.31955 | -0.17064 | 1.10230 | 0.25414 | -0.20662 | 1.34910 | 0.20116 | -0.21055 | 1.29640 | 0.15824 | -0.18480 | 1.08420 | 0.15824 | -0.09651 | 0.62272 |
| 0.28512 | -0.20507 | 1.39940 | 0.22625 | -0.23451 | 1.61220 | 0.17857 | -0.23314 | 1.53190 | 0.13995 | -0.20309 | 1.28460 | 0.13995 | -0.11480 | 0.95845 |
| 0.25414 | -0.23605 | 1.67440 | 0.20116 | -0.25960 | 1.85200 | 0.15824 | -0.25347 | 1.74260 | 0.12348 | -0.21956 | 1.46640 | 0.12348 | -0.13127 | 1.09720 |
| 0.22625 | -0.26394 | 1.92760 | 0.17857 | -0.28219 | 2.07070 | 0.13995 | -0.27176 | 1.93320 | 0.10866 | -0.23438 | 1.63050 | 0.10866 | -0.14609 | 1.23220 |
| 0.20116 | -0.28903 | 2.15990 | 0.15824 | -0.30252 | 2.26970 | 0.12348 | -0.28823 | 2.10590 | 0.09532 | -0.24772 | 1.77850 | 0.09532 | -0.15943 | 1.36110 |
| 0.17857 | -0.31162 | 2.37230 | 0.13995 | -0.32081 | 2.45080 | 0.10866 | -0.30305 | 2.26210 | 0.08332 | -0.25972 | 1.91300 | 0.08332 | -0.17143 | 1.48220 |
| 0.15824 | -0.33195 | 2.56630 | 0.12348 | -0.33728 | 2.61540 | 0.09532 | -0.31639 | 2.40360 | 0.07252 | -0.27052 | 2.03430 | 0.07252 | -0.18223 | 1.59490 |
| 0.13995 | -0.35024 | 2.74300 | 0.10866 | -0.35210 | 2.76500 | 0.08332 | -0.32839 | 2.53220 | 0.06279 | -0.28025 | 2.14430 | 0.06279 | -0.19196 | 1.69930 |
| 0.12348 | -0.36671 | 2.90390 | 0.09532 | -0.36544 | 2.90100 | 0.07252 | -0.33919 | 2.64890 | 0.05404 | -0.28900 | 2.24480 | 0.05404 | -0.20071 | 1.79530 |
| 0.10866 | -0.38153 | 3.05030 | 0.08332 | -0.37744 | 3.02450 | 0.06279 | -0.34892 | 2.75480 | 0.04617 | -0.29687 | 2.33590 | 0.04617 | -0.20858 | 1.88360 |
| 0.09532 | -0.39487 | 3.18330 | 0.07252 | -0.38824 | 3.13660 | 0.05404 | -0.35767 | 2.85100 | 0.03908 | -0.30396 | 2.41920 | 0.03908 | -0.21567 | 1.96530 |
| 0.08332 | -0.40687 | 3.30420 | 0.06279 | -0.39797 | 3.23840 | 0.04617 | -0.36554 | 2.93830 | 0.03270 | -0.31034 | 2.49530 | 0.03270 | -0.22205 | 2.04070 |
| 0.07252 | -0.41767 | 3.41390 | 0.05404 | -0.40672 | 3.33060 | 0.03908 | -0.37263 | 3.01770 | 0.02696 | -0.31608 | 2.56540 | 0.02696 | -0.22779 | 2.10950 |
| 0.06279 | -0.42740 | 3.51340 | 0.04617 | -0.41459 | 3.41460 | 0.03270 | -0.37901 | 3.09010 | 0.02179 | -0.32125 | 2.63250 | 0.02179 | -0.23296 | 2.17280 |
| 0.05404 | -0.43615 | 3.60380 | 0.03908 | -0.42168 | 3.49080 | 0.02696 | -0.38475 | 3.15620 | 0.01714 | -0.32590 | 2.69150 | 0.01714 | -0.23761 | 2.23130 |
| 0.04617 | -0.44402 | 3.68580 | 0.03270 | -0.42806 | 3.56000 | 0.02179 | -0.38992 | 3.21810 | 0.01295 | -0.33009 | 2.73630 | 0.01295 | -0.24180 | 2.28540 |
| 0.03908 | -0.45111 | 3.76010 | 0.02696 | -0.43380 | 3.62300 | 0.01714 | -0.39457 | 3.27330 | 0.00919 | -0.33385 | 2.77630 | 0.00919 | -0.24556 | 2.33610 |
| 0.03270 | -0.45749 | 3.82750 | 0.02179 | -0.43897 | 3.68090 | 0.01295 | -0.39876 | 3.31810 | 0.00580 | -0.33724 | 2.82070 | 0.00580 | -0.24895 | 2.38600 |
| 0.02696 | -0.46323 | 3.88880 | 0.01714 | -0.44362 | 3.73300 | 0.00919 | -0.40252 | 3.35950 | 0.00275 | -0.34029 | 2.86250 | 0.00275 | -0.25200 | 2.43700 |
| 0.02179 | -0.46840 | 3.94440 | 0.01295 | -0.44781 | 3.77810 | 0.00580 | -0.40591 | 3.40110 | 0.00000 | -0.34304 | 2.92880 | 0.00000 | -0.25475 | 2.53220 |
| 0.01714 | -0.47305 | 3.99480 | 0.00919 | -0.45157 | 3.81960 | 0.00275 | -0.40896 | 3.43970 | | | | | | |
| 0.01295 | -0.47724 | 4.04020 | 0.00580 | -0.45496 | 3.85860 | 0.00000 | -0.41171 | 3.49100 | | | | | | |
| 0.00919 | -0.48100 | 4.08160 | 0.00275 | -0.45801 | 3.89500 | | | | | | | | | |
| 0.00580 | -0.48439 | 4.11950 | 0.00000 | -0.46076 | 3.93520 | | | | | | | | | |
| 0.00275 | -0.48744 | 4.15420 | | | | | | | | | | | | |
| 0.00000 | -0.49019 | 4.18770 | | | | | | | | | | | | |

*Table A.2 Step, Time, Force, Pressure and Nodal position.*

| | 50 | | 100 | | 150 | | 200 | | 250 | |
|---|---|---|---|---|---|---|---|---|---|---|
| | x | y | x | y | x | y | x | y | x | y |
| Surface | 1.35E+00 | -9.89E-04 | 1.16E+00 | -5.23E-03 | 9.62E-01 | -1.69E-02 | 8.60E-01 | -3.54E-02 | 9.45E-01 | -4.29E-02 |
| | 1.25E+00 | -1.16E-03 | 1.09E+00 | -6.01E-03 | 9.12E-01 | -1.89E-02 | 8.20E-01 | -3.87E-02 | 8.92E-01 | -4.69E-02 |
| | 1.16E+00 | -1.35E-03 | 1.02E+00 | -6.86E-03 | 8.68E-01 | -2.10E-02 | 7.85E-01 | -4.18E-02 | 8.44E-01 | -5.08E-02 |
| | 1.09E+00 | -1.56E-03 | 9.64E-01 | -7.76E-03 | 8.29E-01 | -2.31E-02 | 7.54E-01 | -4.47E-02 | 8.02E-01 | -5.45E-02 |
| | 1.02E+00 | -1.78E-03 | 9.14E-01 | -8.71E-03 | 7.96E-01 | -2.51E-02 | 7.27E-01 | -4.76E-02 | 7.65E-01 | -5.79E-02 |
| | 9.65E-01 | -2.02E-03 | 8.71E-01 | -9.70E-03 | 7.66E-01 | -2.72E-02 | 6.99E-01 | -5.06E-02 | 7.32E-01 | -6.08E-02 |
| | 9.15E-01 | -2.28E-03 | 8.33E-01 | -1.07E-02 | 7.41E-01 | -2.93E-02 | 6.71E-01 | -5.38E-02 | 7.03E-01 | -6.33E-02 |
| | 8.72E-01 | -2.55E-03 | 8.00E-01 | -1.18E-02 | 7.15E-01 | -3.16E-02 | 6.42E-01 | -5.72E-02 | 6.73E-01 | -6.59E-02 |
| | 8.34E-01 | -2.82E-03 | 7.71E-01 | -1.28E-02 | 6.89E-01 | -3.42E-02 | 6.12E-01 | -6.05E-02 | 6.42E-01 | -6.82E-02 |
| | 8.01E-01 | -3.13E-03 | 7.46E-01 | -1.39E-02 | 6.62E-01 | -3.72E-02 | 5.82E-01 | -6.39E-02 | 6.11E-01 | -7.04E-02 |
| | 7.73E-01 | -3.42E-03 | 7.21E-01 | -1.51E-02 | 6.35E-01 | -4.05E-02 | 5.47E-01 | -6.66E-02 | 5.77E-01 | -7.17E-02 |
| | 7.48E-01 | -3.70E-03 | 6.96E-01 | -1.65E-02 | 6.07E-01 | -4.44E-02 | 5.15E-01 | -6.84E-02 | 5.45E-01 | -7.27E-02 |
| | 7.23E-01 | -4.08E-03 | 6.71E-01 | -1.82E-02 | 5.77E-01 | -4.84E-02 | 4.77E-01 | -7.12E-02 | 5.09E-01 | -7.31E-02 |
| | 6.98E-01 | -4.49E-03 | 6.46E-01 | -2.02E-02 | 5.48E-01 | -5.27E-02 | 4.34E-01 | -7.39E-02 | 4.74E-01 | -7.26E-02 |
| | 6.73E-01 | -4.94E-03 | 6.20E-01 | -2.26E-02 | 5.11E-01 | -5.73E-02 | 3.96E-01 | -7.44E-02 | 4.36E-01 | -7.25E-02 |
| | 6.49E-01 | -5.55E-03 | 5.94E-01 | -2.54E-02 | 4.73E-01 | -5.91E-02 | 3.59E-01 | -7.32E-02 | 3.92E-01 | -7.35E-02 |
| | 6.24E-01 | -6.30E-03 | 5.68E-01 | -2.96E-02 | 4.41E-01 | -6.02E-02 | 3.31E-01 | -7.19E-02 | 3.51E-01 | -7.39E-02 |
| | 5.99E-01 | -7.24E-03 | 5.36E-01 | -3.38E-02 | 4.13E-01 | -6.35E-02 | 3.08E-01 | -7.12E-02 | 3.08E-01 | -7.29E-02 |
| | 5.74E-01 | -8.66E-03 | 5.05E-01 | -3.74E-02 | 3.91E-01 | -6.89E-02 | 2.95E-01 | -7.25E-02 | 2.71E-01 | -7.10E-02 |
| | 5.48E-01 | -1.04E-02 | 4.78E-01 | -4.33E-02 | 3.71E-01 | -7.69E-02 | 2.84E-01 | -7.87E-02 | 2.37E-01 | -5.01E-02 |
| | 5.23E-01 | -1.60E-02 | 4.50E-01 | -5.16E-02 | 3.52E-01 | -8.46E-02 | 2.72E-01 | -8.77E-02 | 2.37E-01 | -3.32E-02 |
| Intersection | 4.68E-01 | -2.22E-02 | 4.00E-01 | -6.05E-02 | 3.19E-01 | -9.26E-02 | 2.45E-01 | -9.82E-02 | 2.38E-01 | -1.63E-02 |
| Body | 4.48E-01 | -4.27E-02 | 3.58E-01 | -1.03E-01 | 2.85E-01 | -1.27E-01 | 2.26E-01 | -1.17E-01 | 2.26E-01 | -2.85E-02 |
| | 4.00E-01 | -8.99E-02 | 3.20E-01 | -1.41E-01 | 2.54E-01 | -1.58E-01 | 2.01E-01 | -1.42E-01 | 2.01E-01 | -5.36E-02 |
| | 3.58E-01 | -1.32E-01 | 2.85E-01 | -1.76E-01 | 2.26E-01 | -1.85E-01 | 1.79E-01 | -1.64E-01 | 1.79E-01 | -7.62E-02 |
| | 3.20E-01 | -1.71E-01 | 2.54E-01 | -2.07E-01 | 2.01E-01 | -2.11E-01 | 1.58E-01 | -1.85E-01 | 1.58E-01 | -9.65E-02 |
| | 2.85E-01 | -2.05E-01 | 2.26E-01 | -2.35E-01 | 1.79E-01 | -2.33E-01 | 1.40E-01 | -2.03E-01 | 1.40E-01 | -1.15E-01 |
| | 2.54E-01 | -2.36E-01 | 2.01E-01 | -2.60E-01 | 1.58E-01 | -2.53E-01 | 1.23E-01 | -2.20E-01 | 1.23E-01 | -1.31E-01 |
| | 2.26E-01 | -2.64E-01 | 1.79E-01 | -2.82E-01 | 1.40E-01 | -2.72E-01 | 1.09E-01 | -2.34E-01 | 1.09E-01 | -1.46E-01 |
| | 2.01E-01 | -2.89E-01 | 1.58E-01 | -3.03E-01 | 1.23E-01 | -2.88E-01 | 9.53E-02 | -2.48E-01 | 9.53E-02 | -1.59E-01 |
| | 1.79E-01 | -3.12E-01 | 1.40E-01 | -3.21E-01 | 1.09E-01 | -3.03E-01 | 8.33E-02 | -2.60E-01 | 8.33E-02 | -1.71E-01 |
| | 1.58E-01 | -3.32E-01 | 1.23E-01 | -3.37E-01 | 9.53E-02 | -3.16E-01 | 7.25E-02 | -2.71E-01 | 7.25E-02 | -1.82E-01 |
| | 1.40E-01 | -3.50E-01 | 1.09E-01 | -3.52E-01 | 8.33E-02 | -3.28E-01 | 6.28E-02 | -2.80E-01 | 6.28E-02 | -1.92E-01 |
| | 1.23E-01 | -3.67E-01 | 9.53E-02 | -3.65E-01 | 7.25E-02 | -3.39E-01 | 5.40E-02 | -2.89E-01 | 5.40E-02 | -2.01E-01 |
| | 1.09E-01 | -3.82E-01 | 8.33E-02 | -3.77E-01 | 6.28E-02 | -3.49E-01 | 4.62E-02 | -2.97E-01 | 4.62E-02 | -2.09E-01 |
| | 9.53E-02 | -3.95E-01 | 7.25E-02 | -3.88E-01 | 5.40E-02 | -3.58E-01 | 3.91E-02 | -3.04E-01 | 3.91E-02 | -2.16E-01 |
| | 8.33E-02 | -4.07E-01 | 6.28E-02 | -3.98E-01 | 4.62E-02 | -3.66E-01 | 3.27E-02 | -3.10E-01 | 3.27E-02 | -2.22E-01 |
| | 7.25E-02 | -4.18E-01 | 5.40E-02 | -4.07E-01 | 3.91E-02 | -3.73E-01 | 2.70E-02 | -3.16E-01 | 2.70E-02 | -2.28E-01 |
| | 6.28E-02 | -4.27E-01 | 4.62E-02 | -4.15E-01 | 3.27E-02 | -3.79E-01 | 2.18E-02 | -3.21E-01 | 2.18E-02 | -2.33E-01 |
| | 5.40E-02 | -4.36E-01 | 3.91E-02 | -4.22E-01 | 2.70E-02 | -3.85E-01 | 1.71E-02 | -3.26E-01 | 1.71E-02 | -2.38E-01 |
| | 4.62E-02 | -4.44E-01 | 3.27E-02 | -4.28E-01 | 2.18E-02 | -3.90E-01 | 1.30E-02 | -3.30E-01 | 1.30E-02 | -2.42E-01 |
| | 3.91E-02 | -4.51E-01 | 2.70E-02 | -4.34E-01 | 1.71E-02 | -3.95E-01 | 9.19E-03 | -3.34E-01 | 9.19E-03 | -2.46E-01 |
| | 3.27E-02 | -4.57E-01 | 2.18E-02 | -4.39E-01 | 1.30E-02 | -3.99E-01 | 5.80E-03 | -3.37E-01 | 5.80E-03 | -2.49E-01 |
| | 2.70E-02 | -4.63E-01 | 1.71E-02 | -4.44E-01 | 9.19E-03 | -4.03E-01 | 2.75E-03 | -3.40E-01 | 2.75E-03 | -2.52E-01 |
| | 2.18E-02 | -4.68E-01 | 1.30E-02 | -4.48E-01 | 5.80E-03 | -4.06E-01 | 0.00E+00 | -3.43E-01 | 0.00E+00 | -2.55E-01 |
| | 1.71E-02 | -4.73E-01 | 9.19E-03 | -4.52E-01 | 2.75E-03 | -4.09E-01 | | | | |
| | 1.30E-02 | -4.77E-01 | 5.80E-03 | -4.55E-01 | 0.00E+00 | -4.12E-01 | | | | |
| | 9.19E-03 | -4.81E-01 | 2.75E-03 | -4.58E-01 | | | | | | |
| | 5.80E-03 | -4.84E-01 | 0.00E+00 | -4.61E-01 | | | | | | |
| | 2.75E-03 | -4.87E-01 | | | | | | | | |
| | 0.00E+00 | -4.90E-01 | | | | | | | | |

*Table A.3 Free-surface profile*

## Wedge exiting fluid domain with Froude number 0.117

| | | | |
|---|---|---|---|
| number of steps | 2000 | position of cog (horizontal, vertical) | (0.0, -0.2) |
| time step size | 0.0005 | surface width | 20 |
| height step size | 0.1 | water depth | 10 |
| print only | main steps | number of points in surface | 80 |
| print hamming predictor | NO | wave length | 1 |
| start type | normal | wave amplitude | 0 |
| jets leave body | NO | still water line | 0 |
| steps till jet leaves body | 10 | mass density ratio | 0.0075 |
| acceleration | 0 | moment of inertia density ratio | 0.001 |
| print every nth step | 40 | forward water line | 0 |
| sway allowed | NO | rear water line | 0 |
| heave allowed | YES | body type | 0 |
| roll allowed | NO | surface point ratio | 0.87 |
| node removal limit | 3 | number of body points | 60 |
| node addition limit | 1 | body point ratio | 0.9 |
| center of rotation (horizontal, vertical) | (0.0, -0.2) | distance of cog to vertex | 0.3 |
| velocity of cog (horizontal, vertical) | (0.0, 0.2) | wedge height | 0.5 |
| angle of body to vertical | 0 | right wedge angle to vertical | 30 |
| angular velocity about cog | 0 | total wedge angle | 60 |

*Table A.4 Input data*

| force | time | step | force | time | step | force | time | step | force | time | step | force | time | step |
|---|---|---|---|---|---|---|---|---|---|---|---|---|---|---|
| 1.18150 | 0.16 | 320 | 1.01650 | 0.32 | 640 | 0.87083 | 0.48 | 960 | 0.75664 | 0.64 | 1280 | 0.62710 | 0.8 | 1600 |
| Nodes | | | Nodes | | | Nodes | | | Nodes | | | Nodes | | |
| x | y | Pressure | x | y | Pressure | x | y | Pressure | x | y | Pressure | x | y | Pressure |
| 0.25566 | -0.02519 | 0.00000 | 0.24710 | -0.00802 | 0.00000 | 0.22259 | -0.01848 | 0.00000 | 0.21616 | 0.00239 | 0.00000 | 0.18811 | -0.01420 | 0.00000 |
| 0.23112 | -0.06770 | 0.49699 | 0.23112 | -0.03570 | 0.20733 | 0.20658 | -0.04620 | 0.31872 | 0.20658 | -0.01420 | 0.09427 | 0.16462 | -0.05488 | 0.45954 |
| 0.20658 | -0.11020 | 0.93849 | 0.20658 | -0.07820 | 0.62246 | 0.18449 | -0.08445 | 0.70333 | 0.18449 | -0.05245 | 0.44951 | 0.14673 | -0.08586 | 0.77139 |
| 0.18449 | -0.14845 | 1.33150 | 0.18449 | -0.11645 | 1.00140 | 0.16462 | -0.11888 | 1.04480 | 0.16462 | -0.08688 | 0.78094 | 0.13063 | -0.11375 | 1.04810 |
| 0.16462 | -0.18288 | 1.68130 | 0.16462 | -0.15088 | 1.34450 | 0.14673 | -0.14966 | 1.35130 | 0.14673 | -0.11786 | 1.08220 | 0.11614 | -0.13885 | 1.29590 |
| 0.14673 | -0.21386 | 1.99430 | 0.14673 | -0.18186 | 1.65360 | 0.13063 | -0.17775 | 1.62700 | 0.13063 | -0.14575 | 1.35430 | 0.10310 | -0.16143 | 1.51850 |
| 0.13063 | -0.24175 | 2.27470 | 0.13063 | -0.20975 | 1.93180 | 0.11614 | -0.20285 | 1.87510 | 0.11614 | -0.17085 | 1.59980 | 0.09136 | -0.18176 | 1.71860 |
| 0.11614 | -0.26684 | 2.52640 | 0.11614 | -0.23484 | 2.18200 | 0.10310 | -0.22543 | 2.09640 | 0.10310 | -0.19343 | 1.82090 | 0.08080 | -0.20006 | 1.89870 |
| 0.10310 | -0.28943 | 2.75240 | 0.10310 | -0.25743 | 2.40710 | 0.09136 | -0.24576 | 2.29940 | 0.09136 | -0.21376 | 2.02010 | 0.07129 | -0.21652 | 2.06060 |
| 0.09136 | -0.30976 | 2.95550 | 0.09136 | -0.27776 | 2.60960 | 0.08080 | -0.26406 | 2.48040 | 0.08080 | -0.23206 | 2.19950 | 0.06274 | -0.23134 | 2.20640 |
| 0.08080 | -0.32805 | 3.13810 | 0.08080 | -0.29606 | 2.79170 | 0.07129 | -0.28052 | 2.64320 | 0.07129 | -0.24852 | 2.36110 | 0.05504 | -0.24468 | 2.33780 |
| 0.07129 | -0.34452 | 3.30230 | 0.07129 | -0.31252 | 2.95560 | 0.06274 | -0.29534 | 2.78970 | 0.06274 | -0.26334 | 2.50670 | 0.04810 | -0.25668 | 2.45570 |
| 0.06274 | -0.35934 | 3.45000 | 0.06274 | -0.32734 | 3.10300 | 0.05504 | -0.30868 | 2.92170 | 0.05504 | -0.27668 | 2.63770 | 0.04187 | -0.26749 | 2.56200 |
| 0.05504 | -0.37268 | 3.58280 | 0.05504 | -0.34068 | 3.23570 | 0.04810 | -0.32068 | 3.04050 | 0.04810 | -0.28868 | 2.75570 | 0.03625 | -0.27721 | 2.65770 |
| 0.04810 | -0.38468 | 3.70240 | 0.04810 | -0.35268 | 3.35510 | 0.04187 | -0.33149 | 3.14740 | 0.04187 | -0.29949 | 2.86200 | 0.03120 | -0.28596 | 2.74390 |
| 0.04187 | -0.39549 | 3.80990 | 0.04187 | -0.36349 | 3.46250 | 0.03625 | -0.34121 | 3.24360 | 0.03625 | -0.30921 | 2.95770 | 0.02665 | -0.29384 | 2.82160 |
| 0.03625 | -0.40521 | 3.90670 | 0.03625 | -0.37321 | 3.55920 | 0.03120 | -0.34996 | 3.33030 | 0.03120 | -0.31796 | 3.04390 | 0.02256 | -0.30093 | 2.89160 |
| 0.03120 | -0.41396 | 3.99390 | 0.03120 | -0.38196 | 3.64630 | 0.02665 | -0.35784 | 3.40830 | 0.02665 | -0.32584 | 3.12150 | 0.01888 | -0.30730 | 2.95430 |
| 0.02665 | -0.42183 | 4.07230 | 0.02665 | -0.38984 | 3.72460 | 0.02256 | -0.36492 | 3.47870 | 0.02256 | -0.33293 | 3.19150 | 0.01556 | -0.31305 | 3.01080 |
| 0.02256 | -0.42892 | 4.14300 | 0.02256 | -0.39692 | 3.79520 | 0.01888 | -0.37130 | 3.54170 | 0.01888 | -0.33930 | 3.25420 | 0.01258 | -0.31821 | 3.06210 |
| 0.01888 | -0.43530 | 4.20650 | 0.01888 | -0.40330 | 3.85860 | 0.01556 | -0.37705 | 3.59650 | 0.01556 | -0.34505 | 3.31070 | 0.00990 | -0.32286 | 3.10830 |
| 0.01556 | -0.44104 | 4.26360 | 0.01556 | -0.40904 | 3.91570 | 0.01258 | -0.38221 | 3.65000 | 0.01258 | -0.35021 | 3.36200 | 0.00748 | -0.32705 | 3.14930 |
| 0.01258 | -0.44621 | 4.31530 | 0.01258 | -0.41421 | 3.96730 | 0.00990 | -0.38686 | 3.69630 | 0.00990 | -0.35486 | 3.40810 | 0.00530 | -0.33082 | 3.18660 |
| 0.00990 | -0.45086 | 4.36190 | 0.00990 | -0.41886 | 4.01380 | 0.00748 | -0.39105 | 3.73770 | 0.00748 | -0.35905 | 3.44920 | 0.00335 | -0.33421 | 3.22050 |
| 0.00748 | -0.45505 | 4.40370 | 0.00748 | -0.42305 | 4.05540 | 0.00530 | -0.39482 | 3.77520 | 0.00530 | -0.36282 | 3.48660 | 0.00159 | -0.33726 | 3.25140 |
| 0.00530 | -0.45881 | 4.44150 | 0.00530 | -0.42681 | 4.09320 | 0.00335 | -0.39821 | 3.80930 | 0.00335 | -0.36621 | 3.52050 | 0.00000 | -0.34000 | 3.28330 |
| 0.00335 | -0.46220 | 4.47560 | 0.00335 | -0.43020 | 4.12740 | 0.00159 | -0.40126 | 3.84040 | 0.00159 | -0.36926 | 3.55130 | | | |
| 0.00159 | -0.46525 | 4.50750 | 0.00159 | -0.43326 | 4.15860 | 0.00000 | -0.40400 | 3.87230 | 0.00000 | -0.37200 | 3.58310 | | | |
| 0.00000 | -0.46800 | 4.53990 | 0.00000 | -0.43600 | 4.19100 | | | | | | | | | |

*Table A.5 Step, Time, Force, Pressure and Nodal position.*

| | 320 | | 640 | | 960 | | 1280 | | 1600 | |
|---|---|---|---|---|---|---|---|---|---|---|
| | x | y | x | y | x | y | x | y | x | y |
| Surface | 1.16E+00 | -1.89E-03 | 1.16E+00 | -4.81E-03 | 1.05E+00 | -1.05E-02 | 1.15E+00 | -1.35E-02 | 9.39E-01 | -1.62E-02 |
| | 1.06E+00 | -2.26E-03 | 1.05E+00 | -5.69E-03 | 9.60E-01 | -1.20E-02 | 1.04E+00 | -1.51E-02 | 8.57E-01 | -1.52E-02 |
| | 9.66E-01 | -2.67E-03 | 9.65E-01 | -6.67E-03 | 8.81E-01 | -1.35E-02 | 9.51E-01 | -1.64E-02 | 7.86E-01 | -1.36E-02 |
| | 8.89E-01 | -3.12E-03 | 8.87E-01 | -7.74E-03 | 8.12E-01 | -1.51E-02 | 8.70E-01 | -1.75E-02 | 7.24E-01 | -1.12E-02 |
| | 8.22E-01 | -3.63E-03 | 8.19E-01 | -8.89E-03 | 7.52E-01 | -1.66E-02 | 8.00E-01 | -1.82E-02 | 6.70E-01 | -8.48E-03 |
| | 7.63E-01 | -4.17E-03 | 7.60E-01 | -1.01E-02 | 6.98E-01 | -1.79E-02 | 7.37E-01 | -1.85E-02 | 6.24E-01 | -5.66E-03 |
| | 7.12E-01 | -4.75E-03 | 7.09E-01 | -1.14E-02 | 6.52E-01 | -1.91E-02 | 6.83E-01 | -1.82E-02 | 5.85E-01 | -3.32E-03 |
| | 6.68E-01 | -5.37E-03 | 6.64E-01 | -1.27E-02 | 6.10E-01 | -2.00E-02 | 6.35E-01 | -1.72E-02 | 5.52E-01 | -1.29E-03 |
| | 6.29E-01 | -6.02E-03 | 6.24E-01 | -1.40E-02 | 5.74E-01 | -2.06E-02 | 5.93E-01 | -1.58E-02 | 5.24E-01 | -8.06E-04 |
| | 5.96E-01 | -6.69E-03 | 5.90E-01 | -1.53E-02 | 5.42E-01 | -2.09E-02 | 5.57E-01 | -1.39E-02 | 4.97E-01 | -4.06E-04 |
| | 5.67E-01 | -7.37E-03 | 5.59E-01 | -1.66E-02 | 5.14E-01 | -2.08E-02 | 5.25E-01 | -1.20E-02 | 4.74E-01 | -7.59E-04 |
| | 5.41E-01 | -8.07E-03 | 5.33E-01 | -1.78E-02 | 4.86E-01 | -2.05E-02 | 4.98E-01 | -9.73E-03 | 4.49E-01 | -3.38E-03 |
| | 5.15E-01 | -8.87E-03 | 5.06E-01 | -1.90E-02 | 4.57E-01 | -1.93E-02 | 4.73E-01 | -8.07E-03 | 4.21E-01 | -5.19E-03 |
| | 4.90E-01 | -9.81E-03 | 4.79E-01 | -2.03E-02 | 4.29E-01 | -1.80E-02 | 4.46E-01 | -5.34E-03 | 3.93E-01 | -6.78E-03 |
| | 4.64E-01 | -1.09E-02 | 4.51E-01 | -2.17E-02 | 4.00E-01 | -1.51E-02 | 4.23E-01 | -3.74E-03 | 3.64E-01 | -8.36E-03 |
| | 4.38E-01 | -1.23E-02 | 4.22E-01 | -2.28E-02 | 3.75E-01 | -1.24E-02 | 3.97E-01 | -4.24E-03 | 3.32E-01 | -6.83E-03 |
| | 4.12E-01 | -1.40E-02 | 3.94E-01 | -2.38E-02 | 3.48E-01 | -1.03E-02 | 3.72E-01 | -4.67E-03 | 3.03E-01 | -4.67E-03 |
| | 3.86E-01 | -1.59E-02 | 3.63E-01 | -2.33E-02 | 3.21E-01 | -7.80E-03 | 3.47E-01 | -6.25E-03 | 2.73E-01 | -1.68E-03 |
| | 3.59E-01 | -1.89E-02 | 3.34E-01 | -2.19E-02 | 2.97E-01 | -6.63E-03 | 3.18E-01 | -9.76E-03 | 2.47E-01 | -9.02E-04 |
| | 3.28E-01 | -2.13E-02 | 3.04E-01 | -2.02E-02 | 2.71E-01 | -1.03E-02 | 2.85E-01 | -1.12E-02 | 2.30E-01 | -5.02E-03 |
| | 2.98E-01 | -2.34E-02 | 2.73E-01 | -1.50E-02 | 2.49E-01 | -1.42E-02 | 2.49E-01 | -8.31E-03 | 2.11E-01 | -1.01E-02 |
| Intersection | 2.56E-01 | -2.52E-02 | 2.47E-01 | -8.02E-03 | 2.23E-01 | -1.85E-02 | 2.16E-01 | 2.39E-03 | 1.88E-01 | -1.42E-02 |
| Body | 2.31E-01 | -6.77E-02 | 2.31E-01 | -3.57E-02 | 2.07E-01 | -4.62E-02 | 2.07E-01 | -1.42E-02 | 1.65E-01 | -5.49E-02 |
| | 2.07E-01 | -1.10E-01 | 2.07E-01 | -7.82E-02 | 1.84E-01 | -8.45E-02 | 1.84E-01 | -5.25E-02 | 1.47E-01 | -8.59E-02 |
| | 1.84E-01 | -1.48E-01 | 1.84E-01 | -1.16E-01 | 1.65E-01 | -1.19E-01 | 1.65E-01 | -8.69E-02 | 1.31E-01 | -1.14E-01 |
| | 1.65E-01 | -1.83E-01 | 1.65E-01 | -1.51E-01 | 1.47E-01 | -1.50E-01 | 1.47E-01 | -1.18E-01 | 1.16E-01 | -1.39E-01 |
| | 1.47E-01 | -2.14E-01 | 1.47E-01 | -1.82E-01 | 1.31E-01 | -1.78E-01 | 1.31E-01 | -1.46E-01 | 1.03E-01 | -1.61E-01 |
| | 1.31E-01 | -2.42E-01 | 1.31E-01 | -2.10E-01 | 1.16E-01 | -2.03E-01 | 1.16E-01 | -1.71E-01 | 9.14E-02 | -1.82E-01 |
| | 1.16E-01 | -2.67E-01 | 1.16E-01 | -2.35E-01 | 1.03E-01 | -2.25E-01 | 1.03E-01 | -1.93E-01 | 8.08E-02 | -2.00E-01 |
| | 1.03E-01 | -2.89E-01 | 1.03E-01 | -2.57E-01 | 9.14E-02 | -2.46E-01 | 9.14E-02 | -2.14E-01 | 7.13E-02 | -2.17E-01 |
| | 9.14E-02 | -3.10E-01 | 9.14E-02 | -2.78E-01 | 8.08E-02 | -2.64E-01 | 8.08E-02 | -2.32E-01 | 6.27E-02 | -2.31E-01 |
| | 8.08E-02 | -3.28E-01 | 8.08E-02 | -2.96E-01 | 7.13E-02 | -2.81E-01 | 7.13E-02 | -2.49E-01 | 5.50E-02 | -2.45E-01 |
| | 7.13E-02 | -3.45E-01 | 7.13E-02 | -3.13E-01 | 6.27E-02 | -2.95E-01 | 6.27E-02 | -2.63E-01 | 4.81E-02 | -2.57E-01 |
| | 6.27E-02 | -3.59E-01 | 6.27E-02 | -3.27E-01 | 5.50E-02 | -3.09E-01 | 5.50E-02 | -2.77E-01 | 4.19E-02 | -2.67E-01 |
| | 5.50E-02 | -3.73E-01 | 5.50E-02 | -3.41E-01 | 4.81E-02 | -3.21E-01 | 4.81E-02 | -2.89E-01 | 3.63E-02 | -2.77E-01 |
| | 4.81E-02 | -3.85E-01 | 4.81E-02 | -3.53E-01 | 4.19E-02 | -3.31E-01 | 4.19E-02 | -2.99E-01 | 3.12E-02 | -2.86E-01 |
| | 4.19E-02 | -3.95E-01 | 4.19E-02 | -3.63E-01 | 3.63E-02 | -3.41E-01 | 3.63E-02 | -3.09E-01 | 2.67E-02 | -2.94E-01 |
| | 3.63E-02 | -4.05E-01 | 3.63E-02 | -3.73E-01 | 3.12E-02 | -3.50E-01 | 3.12E-02 | -3.18E-01 | 2.26E-02 | -3.01E-01 |
| | 3.12E-02 | -4.14E-01 | 3.12E-02 | -3.82E-01 | 2.67E-02 | -3.58E-01 | 2.67E-02 | -3.26E-01 | 1.89E-02 | -3.07E-01 |
| | 2.67E-02 | -4.22E-01 | 2.67E-02 | -3.90E-01 | 2.26E-02 | -3.65E-01 | 2.26E-02 | -3.33E-01 | 1.56E-02 | -3.13E-01 |
| | 2.26E-02 | -4.29E-01 | 2.26E-02 | -3.97E-01 | 1.89E-02 | -3.71E-01 | 1.89E-02 | -3.39E-01 | 1.26E-02 | -3.18E-01 |
| | 1.89E-02 | -4.35E-01 | 1.89E-02 | -4.03E-01 | 1.56E-02 | -3.77E-01 | 1.56E-02 | -3.45E-01 | 9.90E-03 | -3.23E-01 |
| | 1.56E-02 | -4.41E-01 | 1.56E-02 | -4.09E-01 | 1.26E-02 | -3.82E-01 | 1.26E-02 | -3.50E-01 | 7.48E-03 | -3.27E-01 |
| | 1.26E-02 | -4.46E-01 | 1.26E-02 | -4.14E-01 | 9.90E-03 | -3.87E-01 | 9.90E-03 | -3.55E-01 | 5.30E-03 | -3.31E-01 |
| | 9.90E-03 | -4.51E-01 | 9.90E-03 | -4.19E-01 | 7.48E-03 | -3.91E-01 | 7.48E-03 | -3.59E-01 | 3.35E-03 | -3.34E-01 |
| | 7.48E-03 | -4.55E-01 | 7.48E-03 | -4.23E-01 | 5.30E-03 | -3.95E-01 | 5.30E-03 | -3.63E-01 | 1.59E-03 | -3.37E-01 |
| | 5.30E-03 | -4.59E-01 | 5.30E-03 | -4.27E-01 | 3.35E-03 | -3.98E-01 | 3.35E-03 | -3.66E-01 | 0.00E+00 | -3.40E-01 |
| | 3.35E-03 | -4.62E-01 | 3.35E-03 | -4.30E-01 | 1.59E-03 | -4.01E-01 | 1.59E-03 | -3.69E-01 | | |
| | 1.59E-03 | -4.65E-01 | 1.59E-03 | -4.33E-01 | 0.00E+00 | -4.04E-01 | 0.00E+00 | -3.72E-01 | | |
| | 0.00E+00 | -4.68E-01 | 0.00E+00 | -4.36E-01 | | | | | | |

*Table A.6 Free-surface profile*

## Wedge entering fluid domain with acceleration $g/5$

| | | | |
|---|---|---|---|
| number of steps | 1000 | position of cog (horizontal, vertical) | (0.0, 0.2) |
| time step size | 0.0025 | surface width | 20 |
| height step size | 0.1 | water depth | 10 |
| print only | main steps | number of points in surface | 80 |
| print hamming predictor | NO | wave length | 1 |
| start type | normal | wave amplitude | 0 |
| jets leave body | NO | still water line | 0 |
| steps till jet leaves body | 10 | mass density ratio | 0.0075 |
| acceleration | -1.962 | moment of inertia density ratio | 0.001 |
| print every nth step | 1 | forward water line | 0 |
| sway allowed | NO | rear water line | 0 |
| heave allowed | YES | body type | 0 |
| roll allowed | NO | surface point ratio | 0.87 |
| node removal limit | 3 | number of body points | 60 |
| node addition limit | 1 | body point ratio | 0.9 |
| center of rotation (horizontal, vertical) | (0.0, 0.2) | distance of cog to vertex | 0.3 |
| velocity of cog (horizontal, vertical) | (0.0, 0.0) | wedge height | 0.5 |
| angle of body to vertical | 0 | right wedge angle to vertical | 45 |
| angular velocity about cog | 0 | total wedge angle | 90 |

*Table A.7 Input data*

| force | time | step | force | time | step | force | time | step | force | time | step | force | time | step |
|---|---|---|---|---|---|---|---|---|---|---|---|---|---|---|
| 0.12958 | 0.0375 | 15 | 0.15363 | 0.075 | 30 | 0.16884 | 0.1125 | 45 | 0.23413 | 0.15 | 60 | 0.29960 | 0.1875 | 75 |
| Nodes | | | Nodes | | | Nodes | | | Nodes | | | Nodes | | |
| x | y | Pressure | x | y | Pressure | x | y | Pressure | x | y | Pressure | x | y | Pressure |
| 0.10501 | 0.00383 | 0.00000 | 0.11712 | 0.01161 | 0.00000 | 0.13408 | 0.02166 | 0.00000 | 0.14810 | 0.02602 | 0.00000 | 0.16414 | 0.02985 | 0.00000 |
| 0.09532 | -0.00606 | 0.14001 | 0.10666 | 0.00314 | 0.10410 | 0.12348 | 0.01106 | 0.08747 | 0.13995 | 0.01787 | 0.05956 | 0.15824 | 0.02375 | 0.02261 |
| 0.08332 | -0.01806 | 0.29289 | 0.09532 | -0.01020 | 0.27407 | 0.10666 | -0.00376 | 0.27016 | 0.12348 | 0.00141 | 0.25837 | 0.13995 | 0.00546 | 0.28208 |
| 0.07252 | -0.02886 | 0.41676 | 0.08332 | -0.02220 | 0.40721 | 0.09532 | -0.01709 | 0.41755 | 0.10666 | -0.01341 | 0.43322 | 0.12348 | -0.01101 | 0.48703 |
| 0.06279 | -0.03859 | 0.52411 | 0.07252 | -0.03300 | 0.52394 | 0.08332 | -0.02910 | 0.54699 | 0.09532 | -0.02675 | 0.58086 | 0.10666 | -0.02583 | 0.65285 |
| 0.05404 | -0.04734 | 0.61802 | 0.06279 | -0.04273 | 0.62681 | 0.07252 | -0.03990 | 0.66126 | 0.08332 | -0.03875 | 0.71010 | 0.09532 | -0.03917 | 0.79718 |
| 0.04617 | -0.05521 | 0.70059 | 0.05404 | -0.05148 | 0.71782 | 0.06279 | -0.04962 | 0.76231 | 0.07252 | -0.04956 | 0.82417 | 0.08332 | -0.05117 | 0.92464 |
| 0.03908 | -0.06230 | 0.77344 | 0.04617 | -0.05935 | 0.79838 | 0.05404 | -0.05837 | 0.85198 | 0.06279 | -0.05928 | 0.92504 | 0.07252 | -0.06197 | 1.03750 |
| 0.03270 | -0.06868 | 0.83775 | 0.03908 | -0.06644 | 0.86866 | 0.04617 | -0.06625 | 0.93150 | 0.05404 | -0.06803 | 1.01450 | 0.06279 | -0.07170 | 1.13760 |
| 0.02698 | -0.07442 | 0.89472 | 0.03270 | -0.07282 | 0.93300 | 0.03908 | -0.07334 | 1.00230 | 0.04617 | -0.07591 | 1.09430 | 0.05404 | -0.08045 | 1.22690 |
| 0.02179 | -0.07959 | 0.94514 | 0.02698 | -0.07856 | 0.98912 | 0.03270 | -0.07972 | 1.06510 | 0.03908 | -0.08299 | 1.16510 | 0.04617 | -0.08832 | 1.30630 |
| 0.01714 | -0.08424 | 0.98981 | 0.02179 | -0.08373 | 1.03900 | 0.02698 | -0.08546 | 1.12110 | 0.03270 | -0.08937 | 1.22810 | 0.03908 | -0.09541 | 1.37710 |
| 0.01295 | -0.08843 | 1.02930 | 0.01714 | -0.08838 | 1.08340 | 0.02179 | -0.09063 | 1.17100 | 0.02698 | -0.09512 | 1.28430 | 0.03270 | -0.10179 | 1.44020 |
| 0.00919 | -0.09219 | 1.06420 | 0.01295 | -0.09256 | 1.12260 | 0.01714 | -0.09526 | 1.21550 | 0.02179 | -0.10028 | 1.33480 | 0.02698 | -0.10753 | 1.49690 |
| 0.00580 | -0.09558 | 1.09510 | 0.00919 | -0.09633 | 1.15740 | 0.01295 | -0.09946 | 1.25470 | 0.01714 | -0.10493 | 1.37970 | 0.02179 | -0.11270 | 1.54790 |
| 0.00275 | -0.09863 | 1.12230 | 0.00580 | -0.09972 | 1.18840 | 0.00919 | -0.10323 | 1.28960 | 0.01295 | -0.10912 | 1.41920 | 0.01714 | -0.11735 | 1.59330 |
| 0.00000 | -0.10138 | 1.14610 | 0.00275 | -0.10277 | 1.21600 | 0.00580 | -0.10662 | 1.32110 | 0.00919 | -0.11288 | 1.45450 | 0.01295 | -0.12153 | 1.63290 |
| | | | 0.00000 | -0.10552 | 1.24120 | 0.00275 | -0.10967 | 1.34940 | 0.00580 | -0.11628 | 1.48660 | 0.00919 | -0.12530 | 1.66850 |
| | | | | | | 0.00000 | -0.11242 | 1.37690 | 0.00275 | -0.11933 | 1.51580 | 0.00580 | -0.12869 | 1.70140 |
| | | | | | | | | | 0.00000 | -0.12207 | 1.54650 | 0.00275 | -0.13174 | 1.73170 |
| | | | | | | | | | | | | 0.00000 | -0.13449 | 1.76610 |

*Table A.8 Step, Time, Force, Pressure and Nodal position.*

| | 15 | | 30 | | 45 | | 60 | | 75 | |
|---|---|---|---|---|---|---|---|---|---|---|
| | x | y | x | y | x | y | x | y | x | y |
| Surface | 1.00E+01 | 2.52E-07 | 1.00E+01 | 1.14E-06 | 1.00E+01 | 3.02E-06 | 1.00E+01 | 6.42E-06 | 1.00E+01 | 1.21E-05 |
| | 8.92E+00 | 2.56E-07 | 8.92E+00 | 1.15E-06 | 8.92E+00 | 3.07E-06 | 8.92E+00 | 6.52E-06 | 8.92E+00 | 1.22E-05 |
| | 7.96E+00 | 2.74E-07 | 7.96E+00 | 1.24E-06 | 7.96E+00 | 3.28E-06 | 7.96E+00 | 6.98E-06 | 7.96E+00 | 1.31E-05 |
| | 7.10E+00 | 3.08E-07 | 7.10E+00 | 1.39E-06 | 7.10E+00 | 3.68E-06 | 7.10E+00 | 7.83E-06 | 7.10E+00 | 1.47E-05 |
| | 6.34E+00 | 3.53E-07 | 6.34E+00 | 1.59E-06 | 6.34E+00 | 4.23E-06 | 6.34E+00 | 9.00E-06 | 6.34E+00 | 1.69E-05 |
| | 5.66E+00 | 4.14E-07 | 5.66E+00 | 1.86E-06 | 5.66E+00 | 4.95E-06 | 5.66E+00 | 1.05E-05 | 5.66E+00 | 1.98E-05 |
| | 5.06E+00 | 4.91E-07 | 5.06E+00 | 2.21E-06 | 5.06E+00 | 5.88E-06 | 5.06E+00 | 1.25E-05 | 5.06E+00 | 2.35E-05 |
| | 4.52E+00 | 5.89E-07 | 4.52E+00 | 2.65E-06 | 4.52E+00 | 7.05E-06 | 4.52E+00 | 1.50E-05 | 4.52E+00 | 2.81E-05 |
| | 4.05E+00 | 7.12E-07 | 4.05E+00 | 3.21E-06 | 4.05E+00 | 8.52E-06 | 4.05E+00 | 1.81E-05 | 4.05E+00 | 3.40E-05 |
| | 3.62E+00 | 8.66E-07 | 3.62E+00 | 3.90E-06 | 3.62E+00 | 1.04E-05 | 3.62E+00 | 2.21E-05 | 3.62E+00 | 4.14E-05 |
| | 3.24E+00 | 1.06E-06 | 3.24E+00 | 4.77E-06 | 3.24E+00 | 1.27E-05 | 3.24E+00 | 2.69E-05 | 3.24E+00 | 5.05E-05 |
| | 2.90E+00 | 1.29E-06 | 2.90E+00 | 5.84E-06 | 2.90E+00 | 1.55E-05 | 2.90E+00 | 3.30E-05 | 2.90E+00 | 6.19E-05 |
| | 2.60E+00 | 1.59E-06 | 2.60E+00 | 7.16E-06 | 2.60E+00 | 1.90E-05 | 2.60E+00 | 4.04E-05 | 2.60E+00 | 7.59E-05 |
| | 2.34E+00 | 1.95E-06 | 2.34E+00 | 8.79E-06 | 2.34E+00 | 2.33E-05 | 2.34E+00 | 4.97E-05 | 2.34E+00 | 9.32E-05 |
| | 2.10E+00 | 2.39E-06 | 2.10E+00 | 1.08E-05 | 2.10E+00 | 2.87E-05 | 2.10E+00 | 6.10E-05 | 2.10E+00 | 1.14E-04 |
| | 1.89E+00 | 2.94E-06 | 1.89E+00 | 1.32E-05 | 1.89E+00 | 3.52E-05 | 1.89E+00 | 7.49E-05 | 1.89E+00 | 1.41E-04 |
| | 1.70E+00 | 3.60E-06 | 1.70E+00 | 1.62E-05 | 1.70E+00 | 4.32E-05 | 1.70E+00 | 9.19E-05 | 1.70E+00 | 1.72E-04 |
| | 1.53E+00 | 4.41E-06 | 1.53E+00 | 1.99E-05 | 1.53E+00 | 5.29E-05 | 1.53E+00 | 1.13E-04 | 1.53E+00 | 2.11E-04 |
| | 1.38E+00 | 5.40E-06 | 1.38E+00 | 2.43E-05 | 1.38E+00 | 6.47E-05 | 1.38E+00 | 1.38E-04 | 1.38E+00 | 2.58E-04 |
| | 1.25E+00 | 6.58E-06 | 1.25E+00 | 2.97E-05 | 1.25E+00 | 7.89E-05 | 1.25E+00 | 1.68E-04 | 1.25E+00 | 3.15E-04 |
| | 1.13E+00 | 8.01E-06 | 1.13E+00 | 3.61E-05 | 1.13E+00 | 9.60E-05 | 1.13E+00 | 2.04E-04 | 1.13E+00 | 3.84E-04 |
| Intersection | 1.03E+00 | 9.71E-06 | 1.03E+00 | 4.38E-05 | 1.03E+00 | 1.16E-04 | 1.03E+00 | 2.48E-04 | 1.03E+00 | 4.66E-04 |
| Body | 9.35E-01 | 1.17E-05 | 9.35E-01 | 5.29E-05 | 9.35E-01 | 1.41E-04 | 9.35E-01 | 3.00E-04 | 9.35E-01 | 5.64E-04 |
| | 8.52E-01 | 1.41E-05 | 8.52E-01 | 6.37E-05 | 8.52E-01 | 1.70E-04 | 8.52E-01 | 3.62E-04 | 8.52E-01 | 6.80E-04 |
| | 7.78E-01 | 1.69E-05 | 7.78E-01 | 7.64E-05 | 7.78E-01 | 2.04E-04 | 7.78E-01 | 4.34E-04 | 7.78E-01 | 8.16E-04 |
| | 7.12E-01 | 2.02E-05 | 7.12E-01 | 9.13E-05 | 7.12E-01 | 2.43E-04 | 7.12E-01 | 5.19E-04 | 7.12E-01 | 9.76E-04 |
| | 6.54E-01 | 2.40E-05 | 6.54E-01 | 1.09E-04 | 6.54E-01 | 2.89E-04 | 6.54E-01 | 6.17E-04 | 6.54E-01 | 1.16E-03 |
| | 6.01E-01 | 2.84E-05 | 6.01E-01 | 1.28E-04 | 6.01E-01 | 3.42E-04 | 6.01E-01 | 7.31E-04 | 6.01E-01 | 1.38E-03 |
| | 5.55E-01 | 3.34E-05 | 5.55E-01 | 1.51E-04 | 5.55E-01 | 4.03E-04 | 5.55E-01 | 8.62E-04 | 5.55E-01 | 1.63E-03 |
| | 5.14E-01 | 3.91E-05 | 5.14E-01 | 1.77E-04 | 5.14E-01 | 4.73E-04 | 5.14E-01 | 1.01E-03 | 5.14E-01 | 1.91E-03 |
| | 4.72E-01 | 4.64E-05 | 4.72E-01 | 2.10E-04 | 4.72E-01 | 5.62E-04 | 4.72E-01 | 1.21E-03 | 4.72E-01 | 2.28E-03 |
| | 4.31E-01 | 5.60E-05 | 4.31E-01 | 2.54E-04 | 4.31E-01 | 6.81E-04 | 4.31E-01 | 1.46E-03 | 4.31E-01 | 2.76E-03 |
| | 3.89E-01 | 6.90E-05 | 3.89E-01 | 3.13E-04 | 3.89E-01 | 8.42E-04 | 3.90E-01 | 1.81E-03 | 3.90E-01 | 3.43E-03 |
| | 3.48E-01 | 8.73E-05 | 3.48E-01 | 3.97E-04 | 3.48E-01 | 1.07E-03 | 3.48E-01 | 2.31E-03 | 3.49E-01 | 4.39E-03 |
| | 3.07E-01 | 1.14E-04 | 3.07E-01 | 5.22E-04 | 3.07E-01 | 1.41E-03 | 3.07E-01 | 3.07E-03 | 3.08E-01 | 5.83E-03 |
| | 2.65E-01 | 1.56E-04 | 2.65E-01 | 7.19E-04 | 2.66E-01 | 1.97E-03 | 2.66E-01 | 4.31E-03 | 2.67E-01 | 8.23E-03 |
| | 2.24E-01 | 2.29E-04 | 2.24E-01 | 1.07E-03 | 2.24E-01 | 2.97E-03 | 2.25E-01 | 6.46E-03 | 2.28E-01 | 1.18E-02 |
| | 1.83E-01 | 3.82E-04 | 1.83E-01 | 1.81E-03 | 1.84E-01 | 5.30E-03 | 1.86E-01 | 1.21E-02 | 1.87E-01 | 2.27E-02 |
| | 1.41E-01 | 7.68E-04 | 1.42E-01 | 3.93E-03 | 1.47E-01 | 1.03E-02 | 1.58E-01 | 1.53E-02 | 1.72E-01 | 2.03E-02 |
| | 1.21E-01 | 1.31E-03 | 1.23E-01 | 7.90E-03 | 1.34E-01 | 2.17E-02 | 1.48E-01 | 2.60E-02 | 1.64E-01 | 2.96E-02 |
| | 1.05E-01 | 3.63E-03 | 1.17E-01 | 1.16E-02 | 1.23E-01 | 1.11E-02 | 1.40E-01 | 1.79E-02 | 1.58E-01 | 2.38E-02 |
| | 9.53E-02 | -6.06E-03 | 1.09E-01 | 3.14E-03 | 1.09E-01 | -3.76E-03 | 1.23E-01 | 1.41E-03 | 1.40E-01 | 5.46E-03 |
| | 8.33E-02 | -1.81E-02 | 9.53E-02 | -1.02E-02 | 9.53E-02 | -1.71E-02 | 1.09E-01 | -1.34E-02 | 1.23E-01 | -1.10E-02 |
| | 7.25E-02 | -2.89E-02 | 8.33E-02 | -2.22E-02 | 8.33E-02 | -2.91E-02 | 9.53E-02 | -2.67E-02 | 1.09E-01 | -2.58E-02 |
| | 6.28E-02 | -3.86E-02 | 7.25E-02 | -3.30E-02 | 7.25E-02 | -3.99E-02 | 8.33E-02 | -3.88E-02 | 9.53E-02 | -3.92E-02 |
| | 5.40E-02 | -4.73E-02 | 6.28E-02 | -4.27E-02 | 6.28E-02 | -4.96E-02 | 7.25E-02 | -4.96E-02 | 8.33E-02 | -5.12E-02 |
| | 4.62E-02 | -5.52E-02 | 5.40E-02 | -5.15E-02 | 5.40E-02 | -5.84E-02 | 6.28E-02 | -5.93E-02 | 7.25E-02 | -6.20E-02 |
| | 3.91E-02 | -6.23E-02 | 4.62E-02 | -5.94E-02 | 4.62E-02 | -6.62E-02 | 5.40E-02 | -6.80E-02 | 6.28E-02 | -7.17E-02 |
| | 3.27E-02 | -6.87E-02 | 3.91E-02 | -6.64E-02 | 3.91E-02 | -7.33E-02 | 4.62E-02 | -7.59E-02 | 5.40E-02 | -8.04E-02 |
| | 2.70E-02 | -7.44E-02 | 3.27E-02 | -7.28E-02 | 3.27E-02 | -7.97E-02 | 3.91E-02 | -8.30E-02 | 4.62E-02 | -8.83E-02 |
| | 2.18E-02 | -7.96E-02 | 2.70E-02 | -7.86E-02 | 2.70E-02 | -8.55E-02 | 3.27E-02 | -8.94E-02 | 3.91E-02 | -9.54E-02 |
| | 1.71E-02 | -8.42E-02 | 2.18E-02 | -8.37E-02 | 2.18E-02 | -9.06E-02 | 2.70E-02 | -9.51E-02 | 3.27E-02 | -1.02E-01 |
| | 1.30E-02 | -8.84E-02 | 1.71E-02 | -8.84E-02 | 1.71E-02 | -9.53E-02 | 2.18E-02 | -1.00E-01 | 2.70E-02 | -1.08E-01 |
| | 9.19E-03 | -9.22E-02 | 1.30E-02 | -9.26E-02 | 1.30E-02 | -9.95E-02 | 1.71E-02 | -1.05E-01 | 2.18E-02 | -1.13E-01 |
| | 5.80E-03 | -9.56E-02 | 9.19E-03 | -9.63E-02 | 9.19E-03 | -1.03E-01 | 1.30E-02 | -1.09E-01 | 1.71E-02 | -1.17E-01 |
| | 2.75E-03 | -9.86E-02 | 5.80E-03 | -9.97E-02 | 5.80E-03 | -1.07E-01 | 9.19E-03 | -1.13E-01 | 1.30E-02 | -1.22E-01 |
| | 0.00E+00 | -1.01E-01 | 2.75E-03 | -1.03E-01 | 2.75E-03 | -1.10E-01 | 5.80E-03 | -1.16E-01 | 9.19E-03 | -1.25E-01 |
| | | | 0.00E+00 | -1.06E-01 | 0.00E+00 | -1.12E-01 | 2.75E-03 | -1.19E-01 | 5.80E-03 | -1.29E-01 |
| | | | | | | | 0.00E+00 | -1.22E-01 | 2.75E-03 | -1.32E-01 |
| | | | | | | | | | 0.00E+00 | -1.34E-01 |

*Table A.9 Free-surface profile*

## Wedge entering fluid domain with Froude number 0.117

| | | | |
|---|---|---|---|
| number of steps | 800 | position of cog (horizontal, vertical) | (0.0, 0.2) |
| time step size | 0.0025 | surface width | 20 |
| height step size | 0.1 | water depth | 10 |
| print only | main steps | number of points in surface | 80 |
| print hamming predictor | NO | wave length | 1 |
| start type | normal | wave amplitude | 0 |
| jets leave body | NO | still water line | 0 |
| steps till jet leaves body | 10 | mass density ratio | 0.0075 |
| acceleration | 0 | moment of inertia density ratio | 0.001 |
| print every nth step | 1 | forward water line | 0 |
| sway allowed | NO | rear water line | 0 |
| heave allowed | YES | body type | 0 |
| roll allowed | NO | surface point ratio | 0.9 |
| node removal limit | 3 | number of body points | 60 |
| node addition limit | 1 | body point ratio | 0.95 |
| center of rotation (horizontal, vertical) | (0.0, 0.2) | distance of cog to vertex | 0.3 |
| velocity of cog (horizontal, vertical) | (0.0, -0.2) | wedge height | 0.5 |
| angle of body to vertical | 0 | right wedge angle to vertical | 45 |
| angular velocity about cog | 0 | total wedge angle | 90 |

*Table A.10 Input data*

| force | time | step | force | time | step | force | time | step | force | time | step | force | time | step |
|---|---|---|---|---|---|---|---|---|---|---|---|---|---|---|
| 0.12738 | 0.02 | 8 | 0.15127 | 0.04 | 16 | 0.15121 | 0.06 | 24 | 0.16036 | 0.08 | 32 | 0.17080 | 0.1 | 40 |
| Nodes | | | Nodes | | | Nodes | | | Nodes | | | Nodes | | |
| x | y | Pressure | x | y | Pressure | x | y | Pressure | x | y | Pressure | x | y | Pressure |
| 0.11447 | 0.01047 | 0.00000 | 0.13333 | 0.02533 | 0.00000 | 0.14882 | 0.03652 | 0.00000 | 0.15936 | 0.04338 | 0.00000 | 0.16708 | 0.04708 | 0.00000 |
| 0.09781 | -0.00619 | 0.16279 | 0.12414 | 0.01614 | 0.06559 | 0.13835 | 0.02636 | -0.06464 | 0.15332 | 0.03732 | -0.03785 | 0.15332 | 0.03332 | -0.05934 |
| 0.08562 | -0.01838 | 0.29498 | 0.11084 | 0.00264 | 0.20106 | 0.12414 | 0.01214 | 0.04658 | 0.13635 | 0.02236 | -0.05384 | 0.13835 | 0.01836 | -0.01020 |
| 0.07404 | -0.02996 | 0.39819 | 0.09781 | -0.01019 | 0.28904 | 0.11084 | -0.00136 | 0.17047 | 0.12414 | 0.00814 | 0.08087 | 0.12414 | 0.00414 | 0.11600 |
| 0.06304 | -0.04096 | 0.49983 | 0.08562 | -0.02238 | 0.38518 | 0.09781 | -0.01419 | 0.28021 | 0.11084 | -0.00536 | 0.19850 | 0.11084 | -0.00936 | 0.23345 |
| 0.05259 | -0.05141 | 0.59820 | 0.07404 | -0.03396 | 0.48404 | 0.08562 | -0.02638 | 0.38883 | 0.09781 | -0.01819 | 0.31239 | 0.09781 | -0.02219 | 0.34914 |
| 0.04267 | -0.06133 | 0.69300 | 0.06304 | -0.04496 | 0.58211 | 0.07404 | -0.03796 | 0.49488 | 0.08562 | -0.03038 | 0.42364 | 0.08562 | -0.03438 | 0.46162 |
| 0.03324 | -0.07076 | 0.78398 | 0.05259 | -0.05541 | 0.67776 | 0.06304 | -0.04896 | 0.59746 | 0.07404 | -0.04196 | 0.53131 | 0.07404 | -0.04596 | 0.57011 |
| 0.02428 | -0.07972 | 0.87099 | 0.04267 | -0.06533 | 0.77034 | 0.05259 | -0.05941 | 0.69620 | 0.06304 | -0.05296 | 0.63496 | 0.06304 | -0.05696 | 0.67431 |
| 0.01577 | -0.08823 | 0.95459 | 0.03324 | -0.07476 | 0.85953 | 0.04267 | -0.06933 | 0.79093 | 0.05259 | -0.06341 | 0.73440 | 0.05259 | -0.06741 | 0.77412 |
| 0.00768 | -0.09632 | 1.03520 | 0.02428 | -0.08372 | 0.94533 | 0.03324 | -0.07876 | 0.88170 | 0.04267 | -0.07333 | 0.82963 | 0.04267 | -0.07733 | 0.86962 |
| 0.00000 | -0.10400 | 1.11500 | 0.01577 | -0.09223 | 1.02800 | 0.02428 | -0.08772 | 0.96863 | 0.03324 | -0.08276 | 0.92073 | 0.03324 | -0.08676 | 0.96091 |
| | | | 0.00768 | -0.10032 | 1.10780 | 0.01577 | -0.09623 | 1.05210 | 0.02428 | -0.09172 | 1.00790 | 0.02428 | -0.09572 | 1.04820 |
| | | | 0.00000 | -0.10800 | 1.18700 | 0.00768 | -0.10432 | 1.13240 | 0.01577 | -0.10023 | 1.09150 | 0.01577 | -0.10423 | 1.13180 |
| | | | | | | 0.00000 | -0.11200 | 1.21190 | 0.00768 | -0.10832 | 1.17180 | 0.00768 | -0.11232 | 1.21220 |
| | | | | | | | | | 0.00000 | -0.11600 | 1.25130 | 0.00000 | -0.12000 | 1.29150 |

*Table A.11 Step, Time, Force, Pressure and Nodal position.*

| | 8 | | 16 | | 24 | | 32 | | 40 | |
|---|---|---|---|---|---|---|---|---|---|---|
| | x | y | x | y | x | y | x | y | x | y |
| Surface | 1.48E+00 | 1.41E-05 | 1.48E+00 | 3.09E-05 | 1.48E+00 | 5.10E-05 | 1.35E+00 | 9.06E-05 | 1.35E+00 | 1.26E-04 |
| | 1.35E+00 | 1.69E-05 | 1.35E+00 | 3.72E-05 | 1.35E+00 | 6.14E-05 | 1.23E+00 | 1.09E-04 | 1.23E+00 | 1.51E-04 |
| | 1.23E+00 | 2.04E-05 | 1.23E+00 | 4.47E-05 | 1.23E+00 | 7.37E-05 | 1.12E+00 | 1.31E-04 | 1.12E+00 | 1.81E-04 |
| | 1.12E+00 | 2.44E-05 | 1.12E+00 | 5.36E-05 | 1.12E+00 | 8.84E-05 | 1.02E+00 | 1.56E-04 | 1.02E+00 | 2.17E-04 |
| | 1.02E+00 | 2.92E-05 | 1.02E+00 | 6.42E-05 | 1.02E+00 | 1.06E-04 | 9.37E-01 | 1.87E-04 | 9.37E-01 | 2.59E-04 |
| | 9.37E-01 | 3.49E-05 | 9.37E-01 | 7.66E-05 | 9.37E-01 | 1.26E-04 | 8.59E-01 | 2.23E-04 | 8.59E-01 | 3.09E-04 |
| | 8.59E-01 | 4.15E-05 | 8.59E-01 | 9.12E-05 | 8.59E-01 | 1.51E-04 | 7.88E-01 | 2.64E-04 | 7.88E-01 | 3.67E-04 |
| | 7.88E-01 | 4.93E-05 | 7.88E-01 | 1.08E-04 | 7.88E-01 | 1.79E-04 | 7.24E-01 | 3.13E-04 | 7.24E-01 | 4.35E-04 |
| | 7.24E-01 | 5.84E-05 | 7.24E-01 | 1.28E-04 | 7.24E-01 | 2.12E-04 | 6.67E-01 | 3.70E-04 | 6.67E-01 | 5.14E-04 |
| | 6.67E-01 | 6.89E-05 | 6.67E-01 | 1.51E-04 | 6.67E-01 | 2.50E-04 | 6.15E-01 | 4.36E-04 | 6.15E-01 | 6.05E-04 |
| | 6.15E-01 | 8.10E-05 | 6.15E-01 | 1.78E-04 | 6.15E-01 | 2.95E-04 | 5.64E-01 | 5.22E-04 | 5.64E-01 | 7.25E-04 |
| | 5.64E-01 | 9.68E-05 | 5.64E-01 | 2.13E-04 | 5.64E-01 | 3.52E-04 | 5.12E-01 | 6.36E-04 | 5.12E-01 | 8.85E-04 |
| | 5.12E-01 | 1.18E-04 | 5.12E-01 | 2.59E-04 | 5.12E-01 | 4.29E-04 | 4.61E-01 | 7.94E-04 | 4.61E-01 | 1.11E-03 |
| | 4.61E-01 | 1.46E-04 | 4.61E-01 | 3.23E-04 | 4.61E-01 | 5.35E-04 | 4.09E-01 | 1.02E-03 | 4.09E-01 | 1.42E-03 |
| | 4.09E-01 | 1.87E-04 | 4.09E-01 | 4.14E-04 | 4.09E-01 | 6.87E-04 | 3.58E-01 | 1.36E-03 | 3.58E-01 | 1.91E-03 |
| | 3.58E-01 | 2.49E-04 | 3.58E-01 | 5.51E-04 | 3.58E-01 | 9.16E-04 | 3.06E-01 | 1.93E-03 | 3.06E-01 | 2.71E-03 |
| | 3.06E-01 | 3.48E-04 | 3.06E-01 | 7.73E-04 | 3.06E-01 | 1.29E-03 | 2.55E-01 | 2.99E-03 | 2.55E-01 | 4.25E-03 |
| | 2.55E-01 | 5.25E-04 | 2.55E-01 | 1.18E-03 | 2.55E-01 | 1.98E-03 | 2.04E-01 | 5.35E-03 | 2.05E-01 | 7.32E-03 |
| | 2.03E-01 | 9.09E-04 | 2.03E-01 | 2.07E-03 | 2.03E-01 | 3.53E-03 | 1.55E-01 | 1.82E-02 | 1.58E-01 | 2.38E-02 |
| | 1.52E-01 | 2.06E-03 | 1.52E-01 | 5.66E-03 | 1.53E-01 | 1.17E-02 | 1.46E-01 | 2.39E-02 | 1.48E-01 | 2.67E-02 |
| | 1.26E-01 | 4.85E-03 | 1.33E-01 | 1.50E-02 | 1.41E-01 | 2.04E-02 | 1.54E-01 | 3.43E-02 | 1.62E-01 | 3.74E-02 |
| Intersection | 1.14E-01 | 1.05E-02 | 1.33E-01 | 2.53E-02 | 1.49E-01 | 3.65E-02 | 1.59E-01 | 4.34E-02 | 1.67E-01 | 4.71E-02 |
| Body | 9.78E-02 | -6.19E-03 | 1.24E-01 | 1.61E-02 | 1.38E-01 | 2.64E-02 | 1.53E-01 | 3.73E-02 | 1.53E-01 | 3.33E-02 |
| | 8.56E-02 | -1.84E-02 | 1.11E-01 | 2.64E-03 | 1.24E-01 | 1.21E-02 | 1.38E-01 | 2.24E-02 | 1.38E-01 | 1.84E-02 |
| | 7.40E-02 | -3.00E-02 | 9.78E-02 | -1.02E-02 | 1.11E-01 | -1.36E-03 | 1.24E-01 | 8.14E-03 | 1.24E-01 | 4.14E-03 |
| | 6.30E-02 | -4.10E-02 | 8.56E-02 | -2.24E-02 | 9.78E-02 | -1.42E-02 | 1.11E-01 | -5.36E-03 | 1.11E-01 | -9.36E-03 |
| | 5.26E-02 | -5.14E-02 | 7.40E-02 | -3.40E-02 | 8.56E-02 | -2.64E-02 | 9.78E-02 | -1.82E-02 | 9.78E-02 | -2.22E-02 |
| | 4.27E-02 | -6.13E-02 | 6.30E-02 | -4.50E-02 | 7.40E-02 | -3.80E-02 | 8.56E-02 | -3.04E-02 | 8.56E-02 | -3.44E-02 |
| | 3.32E-02 | -7.08E-02 | 5.26E-02 | -5.54E-02 | 6.30E-02 | -4.90E-02 | 7.40E-02 | -4.20E-02 | 7.40E-02 | -4.60E-02 |
| | 2.43E-02 | -7.97E-02 | 4.27E-02 | -6.53E-02 | 5.26E-02 | -5.94E-02 | 6.30E-02 | -5.30E-02 | 6.30E-02 | -5.70E-02 |
| | 1.58E-02 | -8.82E-02 | 3.32E-02 | -7.48E-02 | 4.27E-02 | -6.93E-02 | 5.26E-02 | -6.34E-02 | 5.26E-02 | -6.74E-02 |
| | 7.68E-03 | -9.63E-02 | 2.43E-02 | -8.37E-02 | 3.32E-02 | -7.88E-02 | 4.27E-02 | -7.33E-02 | 4.27E-02 | -7.73E-02 |
| | 0.00E+00 | -1.04E-01 | 1.58E-02 | -9.22E-02 | 2.43E-02 | -8.77E-02 | 3.32E-02 | -8.28E-02 | 3.32E-02 | -8.68E-02 |
| | | | 7.68E-03 | -1.00E-01 | 1.58E-02 | -9.62E-02 | 2.43E-02 | -9.17E-02 | 2.43E-02 | -9.57E-02 |
| | | | 0.00E+00 | -1.08E-01 | 7.68E-03 | -1.04E-01 | 1.58E-02 | -1.00E-01 | 1.58E-02 | -1.04E-01 |
| | | | | | 0.00E+00 | -1.12E-01 | 7.68E-03 | -1.08E-01 | 7.68E-03 | -1.12E-01 |
| | | | | | | | 0.00E+00 | -1.16E-01 | 0.00E+00 | -1.20E-01 |

*Table A.12 Free-surface profile*

# Appendix B Added Mass Derivation from Dipole Moment

*A derivation of the added mass from the equation of a dipole moment.*


## Abstract

A two-dimensional derivation of the added mass from the dipole moment is given.


## Introduction

Through the use of Green's theorem we demonstrate the relationship between the heave added mass for a body in an unbounded fluid and the two-dimensional dipole moment. A three-dimensional derivation can be found in Newman (1977).

## Green's Theorem

The external flow around a body may be represented by a distribution of sinks and sources along the body surface. To demonstrate this let us first consider two solutions of Laplace's equation in a volume V of fluid bounded by a closed surface S. We use $\phi$ and $\varphi$ for the two potentials. Application of the divergence theorem gives

$$\int_S \left[\phi\frac{\partial\varphi}{\partial n}-\varphi\frac{\partial\phi}{\partial n}\right]dS=\iiint_V \nabla.\left(\phi\nabla\varphi-\varphi\nabla\phi\right)dV=\iiint_V\left(\phi\nabla^2\varphi+\nabla\phi.\nabla\varphi-\varphi\nabla^2\phi-\nabla\varphi.\nabla\phi\right)dV=0 \tag{B.1}$$

We replace $\varphi$ with a source of strength $m=1$. We define the source point as $\xi=(\xi,\eta,0)$ as the position of the source. For a unit source the potential at the field point $x=(x,y,z)$ is

$$\varphi=\frac{\ln r}{2\pi}=\frac{\ln\left[\left((x-\xi)^2+(y-\eta)^2\right)^{1/2}\right]}{2\pi} \tag{B.2}$$

We substitute (B.2) into (B.1).However, care must be taken since the source potential does not satisfy Laplace's equation at the singular point $r=0$, and so is not valid when the source point is within $V$. We circumvent this by surrounding the source point by a circle of radius $\varepsilon$ (Figure B.1).

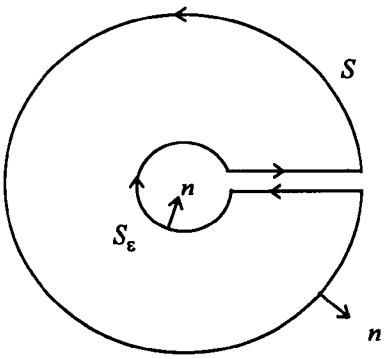


*Figure B.1*

Thus

$$\frac{1}{2\pi}\int_{S+S_\varepsilon}\left(\phi\frac{\partial(\ln r)}{\partial n}-\ln r\frac{\partial\phi}{\partial n}\right)dS=0$$

or

$$\frac{1}{2\pi}\int_{S}\left(\phi\frac{\partial(\ln r)}{\partial n}-\ln r\frac{\partial\phi}{\partial n}\right)dS=-\frac{1}{2\pi}\int_{S_\varepsilon}\left(\phi\frac{\partial(\ln r)}{\partial n}-\ln r\frac{\partial\phi}{\partial n}\right)dS \tag{B.3}$$

We consider the integrand on the right of (B.3) in the limit as $\varepsilon\to 0$. The length of $S_\varepsilon=2\pi r$. The normal derivative of $\ln r$ can be evaluated as $\frac{\partial(\ln r)}{\partial r}=-\frac{1}{r}$, this is negative since the normal is in the opposite direction to $r$. So, the first term is singular in proportion to $\frac{1}{r}$, and when multiplied by the area $2\pi r$, a finite limit will result as $\varepsilon\to 0$. The weaker singularity of the second term will give no contribution, because in the limit as $\varepsilon\to 0$

$$\int_{S_\varepsilon}\ln r\frac{\partial\phi}{\partial n}dS$$

becomes

$$\lim_{\varepsilon\to 0}\int_0^{2\pi}\varepsilon\ln\varepsilon\frac{\partial\phi}{\partial n}d\theta=\int_0^{2\pi}\lim_{\varepsilon\to 0}(\varepsilon\ln\varepsilon)\frac{\partial\phi}{\partial n}d\theta=0$$

since $\lim_{\varepsilon\to 0}(\varepsilon\ln\varepsilon)=0$

For sufficiently small $\varepsilon$ the potential can be assumed constant and taken outside of the integral sign, so the final limiting value of the right-hand side of (B.3) is

$$-\frac{1}{2\pi}\phi(x,y)\int_{S_\varepsilon}\frac{\partial(\ln r)}{\partial n}dS=\phi(x,y)$$

Thus if (x, y) is inside S

$$\phi(x,y) = -\frac{1}{2\pi}\int_S \left(\phi\frac{\partial(\ln r)}{\partial n} - \ln r\frac{\partial\phi}{\partial n}\right)dS \tag{B.4}$$

## Derivation

We consider the relation between the translational added-mass coefficient and the dipole moment describing the fluid motion at distances from the body moving in the $i = 1$ direction. For sufficiently large radial distances $r$ from the body, the disturbance due to the body can be written in the form

$$\phi_1 = \phi = A_0 \ln r + \mathbf{A}.\nabla(\ln r) + O(\ln r^2) = A_0 \ln r + \frac{A_1}{r} + O\left(\frac{1}{r^2}\right) \tag{B.5}$$

where $A_0$ is the net source strength, $\mathbf{A} = A_1\hat{i} + 0\hat{j}$ the dipole moment, and the omitted terms are higher order multi-poles which arise from the separable solutions of Laplace's equation when written in polar co-ordinates. Since the body is rigid there will be no nett flux through the body surface and hence no flux through any other closed surface and so the source strength $A_0 = 0$. Thus

$$\phi \cong \mathbf{A}.\nabla(\ln r) = \frac{\mathrm{A}_1}{\mathrm{r}} \text{ as } r \to \infty \tag{B.6}$$

So the leading order far-field disturbance is identical to that of a dipole. Physically this makes sense since far away from the body the body detail will not be "seen" and the body will look like a distant circle.

We can now re-examine equation (B.4) in the light of (B.6). Suppose $S$ is given by $S = S_\infty \cup S_B \cup c_1 \cup c_2$ as in Figure B.2

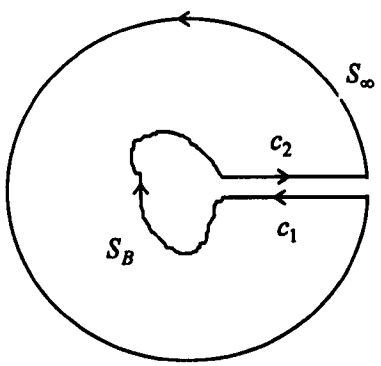


*Figure B.2*

Integrations along the cuts cancel, while

$$-\frac{1}{2\pi}\int_{S_\infty}\left(\phi\frac{\partial \ln r}{\partial n} - \ln r\frac{\partial\phi}{\partial n}\right)dS \to 0 \text{ from (B.6)}$$

Hence integrating the remaining contribution around $S_B$ in the anticlockwise direction gives

$$\phi(x,y) = \frac{1}{2\pi}\int_{S_B} \ln\left[(x-\xi)^2+(y-\eta)^2\right]^{1/2}\frac{\partial\phi}{\partial n} - \phi\frac{\partial}{\partial n}\ln\left[(x-\xi)^2+(y-\eta)^2\right]^{1/2} dS \tag{B.7}$$

where the first term is a distribution of sources and the second a distribution of normal dipoles. If $r=\sqrt{x^2+y^2}$ is large compared to the body dimensions and we neglect terms of order $r^{-2}$, then from Taylor expansions we can write

$$\ln\left[(x-\xi)^2+(y-\eta)^2\right]^{1/2} \cong \ln r - \xi\cdot\nabla(\ln r)$$

where $\xi = \xi\hat{i}+\eta\hat{j}$ and $\nabla$ refers to the $(\xi,\eta)$ co-ordinates, i.e. $\nabla = \frac{\partial}{\partial\xi}\hat{i}+\frac{\partial}{\partial\eta}\hat{j}$ and

$$\frac{\partial}{\partial n}\left(\ln\left[(x-\xi)^2+(y-\eta)^2\right]^{1/2}\right) \cong -\mathbf{n}\cdot\nabla(\ln r)$$

and $\mathbf{n} = n_1\hat{i}+n_2\hat{j}$.

And so the potential at large distances is

$$\phi = \frac{1}{2\pi}\int_{S_B}\frac{\partial\phi}{\partial n}dS\ln r - \frac{1}{2\pi}\int_{S_B}\left(\xi\frac{\partial\phi}{\partial n}-\phi\mathbf{n}\right)dS\cdot\nabla(\ln r) \tag{B.8}$$

where the first term represents a source and hence vanishes since there is no net flux through $S_B$.

Comparing this with (B.5) we see the terms can be equated as

$$\phi = -\frac{1}{2\pi}\int\left(\xi\frac{\partial\phi}{\partial n}-\phi\mathbf{n}\right)dS\cdot\nabla(\ln r) \equiv \mathbf{A}\cdot\nabla(\ln r)$$

Since $\mathbf{A} = A_1\hat{i}+0\hat{j}$ then

$$A_1 = -\frac{1}{2\pi}\int\left(\xi\frac{\partial\phi}{\partial n}-\phi n_1\right)dS \tag{B.9}$$

The potential must satisfy the body boundary condition so $n_1 = \frac{\partial\phi}{\partial n}$. Hence

$$A_1 = -\frac{1}{2\pi}\int_{S_B}\left(\xi n_1 - \phi\frac{\partial\phi}{\partial n}\right)dS$$

and we know that

$$m_a = \rho \int \phi \frac{\partial \phi}{\partial n} dS$$

Hence we can write

$$A_1 = \frac{1}{2\pi}\left( \forall + \frac{m_a}{\rho} \right) \tag{B.10}$$

where $\forall = -\int_{S_B} \xi n_1 dS$ is the area of the body.

Thus, we have shown that the far-field disturbance and associated dipole moment $A$ are directly related to the body volume and the added-mass coefficient $m_a$.

# Appendix C Simplification of Added Mass Equations

## *Using Mathematica® to create simplified expressions for the added mass equations for a box and knuckled body*


### Abstract

A full explanation is given of the methods used and commands implemented to produced a numerically amenable solution to the added mass equations for a box and knuckled body.


### Introduction

For both the box and knuckled body analytical theories we encountered problems when required to produce an equation that is amenable to a simple time step algorithm. This suggest looking for an alternative method of evaluating the integrals involved, an explanation of which follows.

### Box Body

In Chapter 3 we developed an equation for the added mass of a box body, quoted as

$$\frac{m_a}{\rho\pi a^2} = \frac{m}{2\left[E(m)-(1-m)K(m)\right]^2} - \frac{2}{\pi}\left[\frac{E'(m)-mK'(m)}{E(m)-(1-m)K(m)}\right] \tag{C.1}$$

The method used to convert the equation for added mass into one that can be easily implemented in an algorithm are as follows

#### *Evaluate Elliptic Integrals*

Mathematica® has built-in functions to numerically evaluate elliptic integrals, these have been used to assist in the linear approximation of the added mass equation.

Define Mathematica® equations

```
ellip1=EllipticE[m]-(1-m) EllipticK[m]

ellip2=EllipticE[1-m]-m EllipticK[1-m]

ratio[m_]=ellip2/ellip1

ma[m_]=m/(2 ellip1^2)-2 ratio[m]/Pi
```

#### *Tabulate, Graph and Fit*

We evaluate `ratio` and `m` for values $0.1 \le m \le 0.99$ in steps of 0.01. The results are stored in data

```
data=Table[{N[ratio[m]],N[ma[m]]},{m,0.001,0.999,0.001}]
```

and plotted

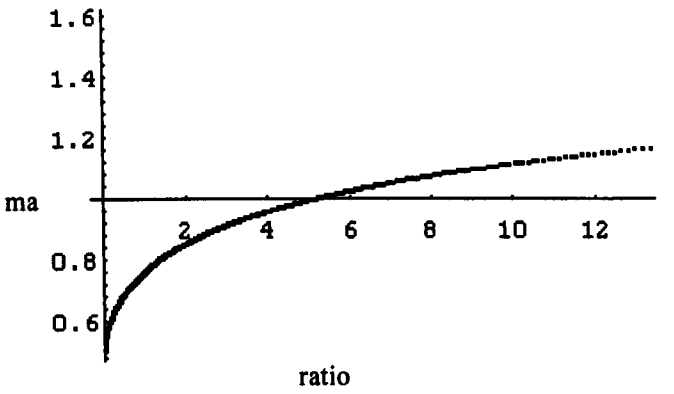


*Graph C.1 Functions ratio vs. ma using elliptic integral evaluation*

Fit a function to this data using constants, $\sqrt{r}$ , r, $r^{3/2}$ and $r^2$

```
fitma[r_]=Fit[data,{1,Sqrt[r],r,Sqrt[r]^3,r^2},r]
```

$$=0.505589+0.26405\sqrt{r}-0.0251687r+0.00104839r^{3/2}-0.000014487r^2$$

Plot this fitted function

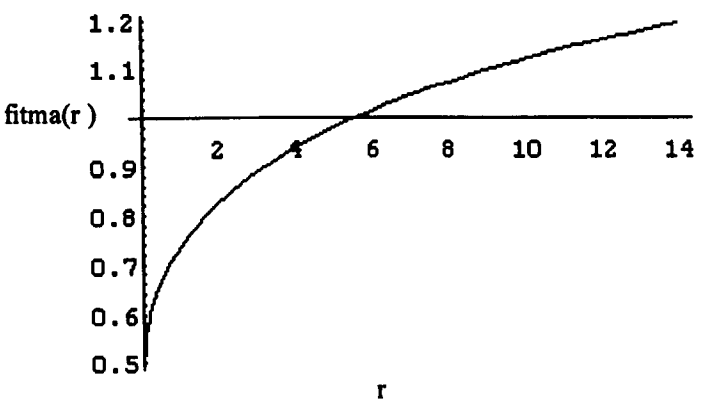


*Graph C.2 Fitted function* `fitma` *for a range or* `r` *values*

Compare the two graphs

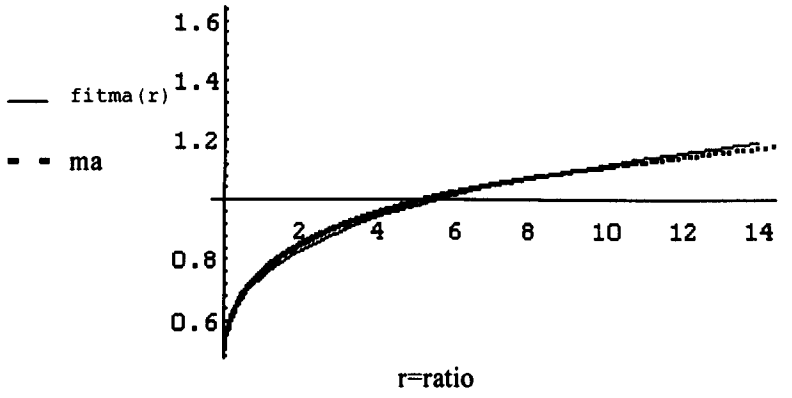


*Graph C.3*

*Graph C.4 Comparison of fitted function* `fitma` *and elliptic integral equation*

Clearly the fitted function `fitma` approximates the equation (C.1) suitably and so, replacing $r$ with depth ratio $\frac{y}{a}$, we define the linear approximation as

$$\frac{m_a}{\rho\pi a^2} = M_a = 0.505589 + 0.26405\sqrt{\frac{y}{a}} - 0.0251687\frac{y}{a} + 0.00104839\left(\frac{y}{a}\right)^{\frac{3}{2}} - 0.000014487\left(\frac{y}{a}\right)^2$$

as quoted in Chapter 3.

## Knuckled Body

In Chapter 3 we developed an equation for the added mass of a knuckled body as

$$\frac{M_a}{\rho\pi a^2} = \frac{\alpha}{\pi}(p^2-1)\frac{K^2}{a^2} - \frac{(b+c)}{\pi a} \tag{C.2}$$

where

$$K\int_1^p \left(\frac{\zeta^2-1}{p^2-\zeta^2}\right)^{\frac{\alpha}{\pi}} d\zeta = \frac{c-b}{\cos\alpha} = \frac{a}{\sin\alpha} \tag{C.3}$$

and the ratio $G$ can be defined as

$$G(p,\alpha) = \frac{c-b}{b\cos\alpha} = \frac{a}{b\sin\alpha} = \frac{\int_1^p \left(\frac{\zeta^2-1}{p^2-\zeta^2}\right)^{\frac{\alpha}{\pi}} d\zeta}{\int_0^1 \left(\frac{1-\zeta^2}{p^2-\zeta^2}\right)^{\frac{\alpha}{\pi}} d\zeta} \tag{C.4}$$

where $p$ is a parameter resulting from the conformal mapping and $b$, $a$ and $\alpha$ define the body.

The method used to convert this equation into one that can be easily implemented in an algorithm is as follows

### *Numerically integrate*

Each of the integrals in (C.2) must be numerically integrated in Mathematica®.

$\int_0^1 \left(\frac{1-\zeta^2}{p^2-\zeta^2}\right)^{\frac{\alpha}{\pi}} d\zeta$ is evaluated using the command

```
int01[a_,p_]=Nintegrate[((1-z^2)/(p^2-z^2))^a,{z,0,1}]
```

$\int_1^p \left(\frac{\zeta^2-1}{p^2-\zeta^2}\right)^{\frac{\alpha}{\pi}} d\zeta$ is evaluated using the command

```
int1p[a_,p_]=Nintegrate[(((z/1000)^2-1)/(p^2-(z/1000)^2))^a/1000,{z,1000,1000
p},WorkingPrecision->20]
```

Note the z/1000 term, this is used to improve the precision and prevent underflow in the calculation.

### *Tabulate*

The results of the numerical integration are tabulated and manipulated.

```
data=Table[{p,int01[1/4,p],int1p[1/4,p]},{p,1,2.0,0.01}]
```

will tabulate the results of the numerical integration for $1 \leq p \geq 2$ in steps of 0.01, placing the result in `data`. Depending on the computer system you are using it may be required to slice this up into bite sizes pieces (i.e. `{p,1,1.1,0.01},{p,1.1,1.2,0.01},...`)

```
data2=Table[{data[[i,2]]/data[[i,3]],N[(data[[i,1]]^2-
1)/2*(1/data[[i,3]])^2]},{i,1,97}]
```

This re-tabulates the previous `data` into a more useful form, $\left(\frac{1}{G}, \frac{M_a}{\rho\pi a^2} + \frac{b+c}{\pi a}\right)$, placing the results in `data2`.

### *Visualise and Fit*

Plotting the resulting data helps to visualise the equations (C.2) and (C.4), we can then attempt to fit a linear equation to these results, and evaluating its precision using graphs.

We plot `data2`

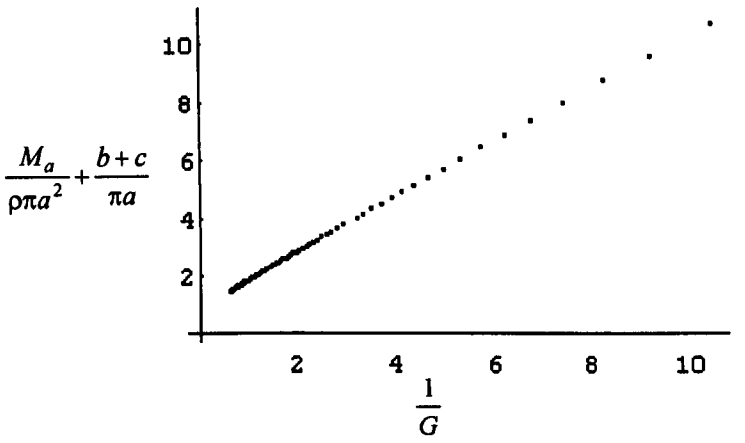


*Graph C.5 The contents of* `data2`

In a similar manner we calculate the data for the range $2 \leq p \leq 100$ in larger steps of 1. This is then combined with `data2` to produce one large data set `dataall`

plot this

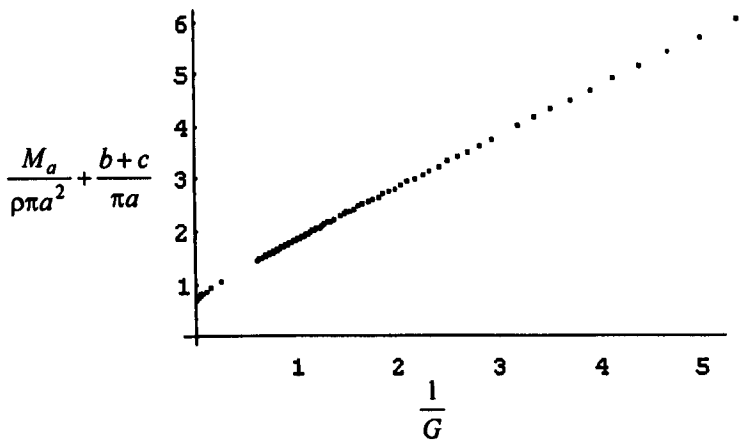


*Graph C.6 Depiction of the data set* `datall`

Fit a function containing constants, $x$ and $\sqrt{x}$ to this curve

```
allfit[x_]=Fit[dataall,{1,x,Sqrt[x]},x]
```

$$= 0.0690022 + 0.246738\sqrt{x} + 0.884717x$$

plot the resultant function

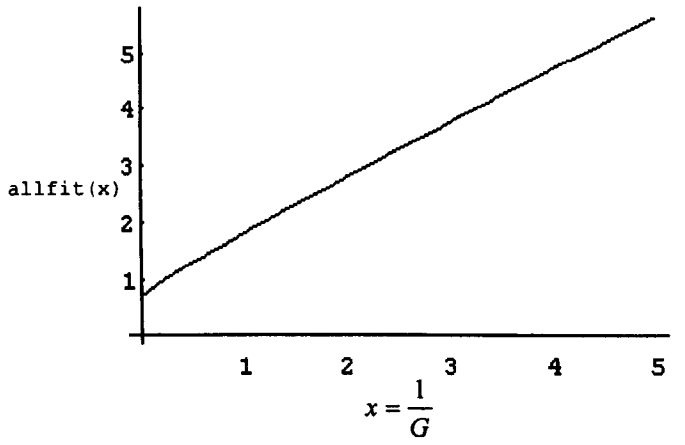


*Graph C.7Fitted function* `allfit`

compare the original data with the fitted function

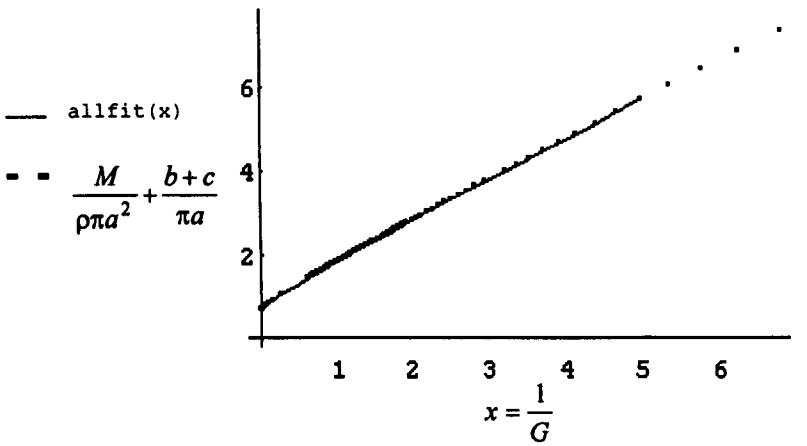


*Graph C.8 Comparison of* `dataall` *and fitted function* `allfit`

calculate the difference error between the data and the fitted function

```
error=Table[{dataall[[i,1]],dataall[[i,2]]-allfit[dataall[[i,1]]]},{i,1,195}]
```

plot this error

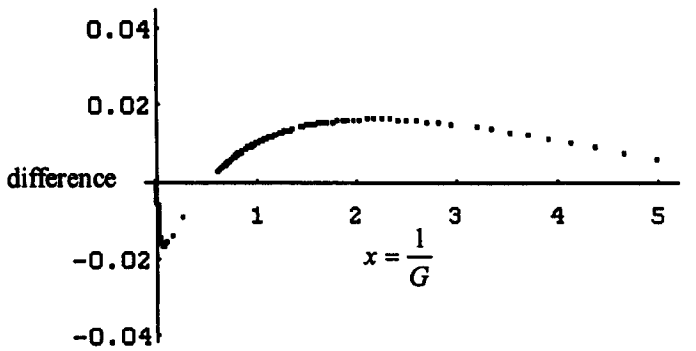


*Graph C.9 Difference error between* `dataall` *and fitted function* `allfit`

Let us concentrate on the data between 0 and 1 since $\frac{b}{\sqrt{2}a}$ will fall mainly in this range. We will define the small scale data from dataall as smlscale, where $0 \le \frac{1}{G} \le 1$.

The small scale data looks like

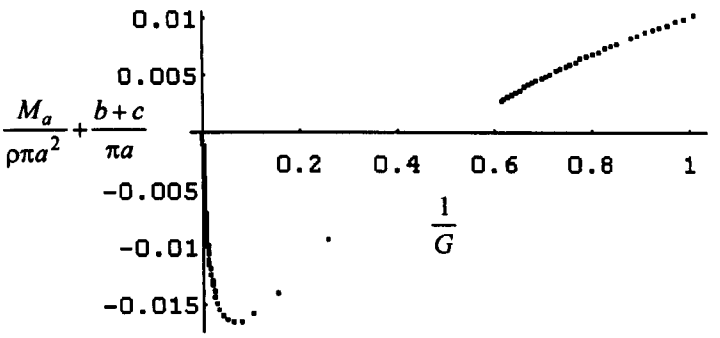


*Graph C.10 Small time* `dataall`

Fit a function to `smlscale` data using constants, $x$, $x^2$ and $\ln x$.

```
smlerr[x_]=Fit[smlscale,{1,x,x^2,Log[x]},x]
```

$$= -0.03401 + 0.0734954x - 0.0297166x^2 - 0.00500196 \ln x$$

and plot

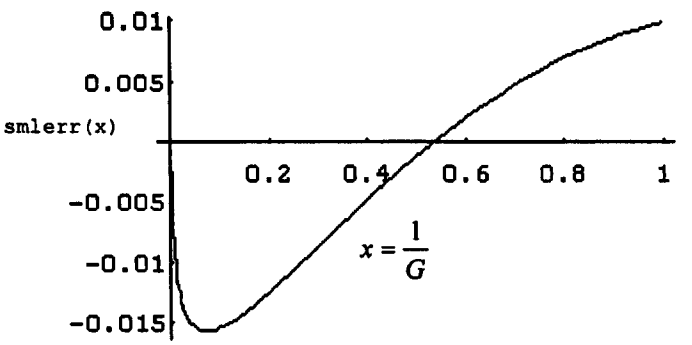


*Graph C.11 Function fitted to* `smlscale` *data*

compare fitted function `smlerr` with `smlscale` data

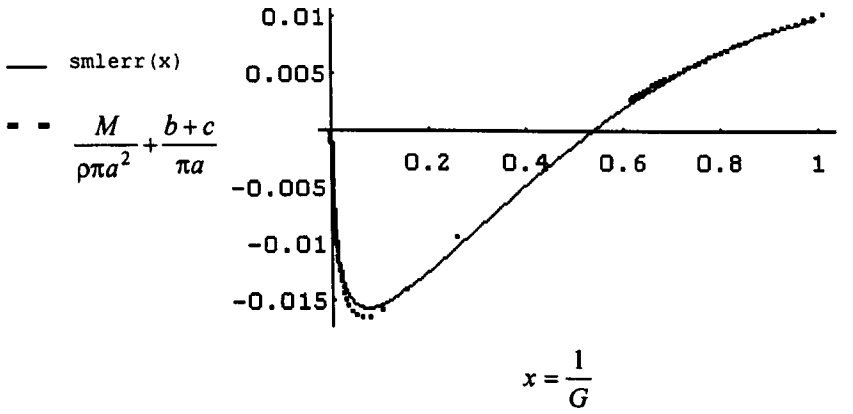


*Graph C.12 Comparison of* `smlscale` *data and function* `smlerr`

define complete fitted function as the original plus small scale fit

```
totalfit[x_]=0.6900219732802933+0.246738328479538*x^(1/2)+0.884717431182508*x-
0.03400997269789174+0.07349543073816949*x-0.02971659513399275*x^2-
0.005001961506839604*Log[x]
```

plot `totalfit`

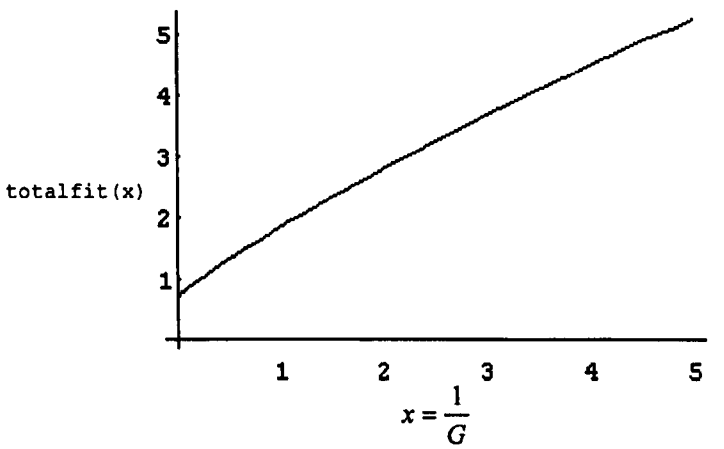


*Graph C.13 Combined fitted function* `totalfit`

overlay on original `dataall` data

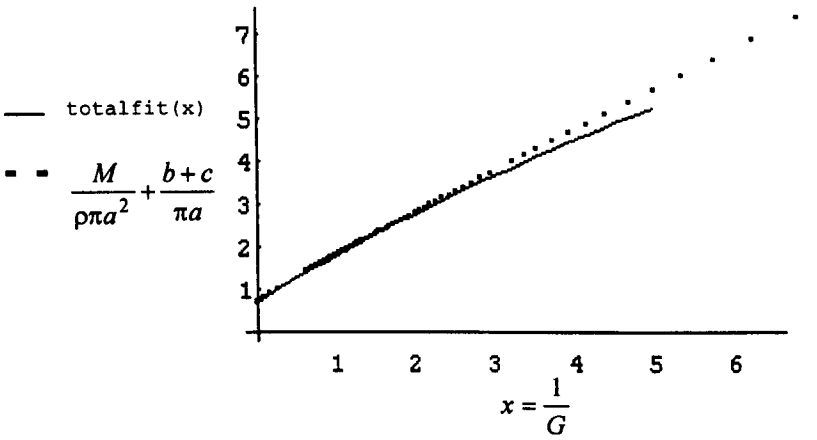


*Graph C.14 Comparison of* `totalfit` *function and* `dataall`

find difference error between them

```
totalerr=Table[{dataall[[i,1]],dataall[[i,2]]-totalfit[dataall[[i,1]]]},{i,1,195}]
```

plot this error

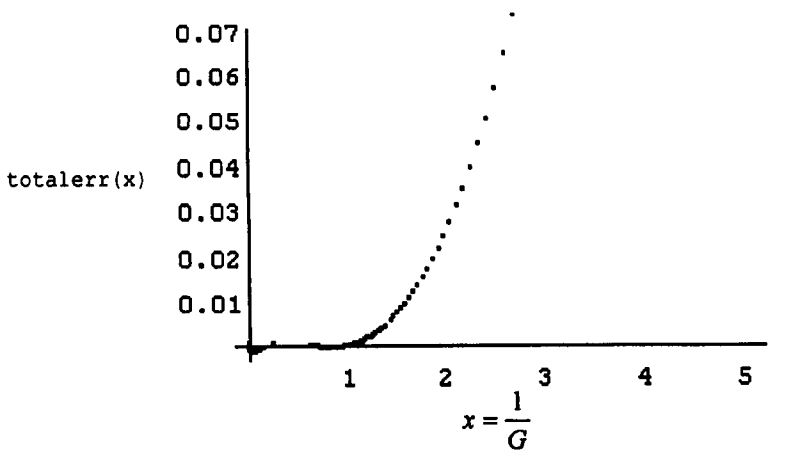


*Graph C.15 Difference error between* `totalfit` *function and* `dataall`

Within the range that we have interest the error is suitable small to make this linear approximation acceptable.

## *Evaluate and Simplify*

Evaluate function when $x=\frac{b}{\sqrt{2}a}$

```
N[totalfit[x]/.x->b(Sqrt[2]*a)]
```

$$-0.656012+\frac{0.677559b}{a}-\frac{0.0148583b^2}{a^2}+0.207481\sqrt{\frac{b}{a}}-0.00500196\ln\frac{\sqrt{2}b}{a}$$

now find $\frac{M_a}{\rho\pi a^2}$ using `N[%-(2b+a)/(Pi*a)]`

$$= 0.656012 + \frac{0.677559b}{a} - \frac{0.0148583b^2}{a^2} + 0.207481\sqrt{\frac{b}{a}} - 0.00500196\ln\frac{\sqrt{2}b}{a} - \frac{2b+a}{\pi a}$$

simplify the resultant equation with `Simplify[%]`

$$= 0.337702 + 0.040939\frac{b}{a} - 0.0148583\left(\frac{b}{a}\right)^2 + 0.207481\sqrt{\frac{b}{a}} - 0.00500196\ln\left(\frac{b\sqrt{2}}{a}\right)$$

which is, replacing $b$ for the depth variable $y$.

$$\frac{M_a}{\rho\pi a^2} = 0.337702 + 0.040939\frac{y}{a} - 0.0148583\left(\frac{y}{a}\right)^2 + 0.207481\sqrt{\frac{y}{a}} - 0.00500196\ln\left(\frac{y\sqrt{2}}{a}\right)$$

as in Chapter 3.

# Appendix D John's Equation

*Derivation and presentation of results obtained from John's equation.*


## Abstract

A derivation of John's equation and it application to high speed wedge entry into the fluid domain. Graphical results are presented for reference.


## Introduction

Time dependent non-linear free surface flows are generally beyond the scope of analysis, even in zero gravity. Nevertheless some progress was made in the early 1980's using the semi-Lagrangian approach of John (1953) whereby exact solutions relating to the jet, loop and combined jet and loop overturning region of a breaking wave were discovered by Longuet-Higgins (1983), New (1983) and Greenhow (1983) respectively. Calculation of these flows depends crucially on knowledge of John's r-function, see below.

Although somewhat outside the more practically-orientated scope of this thesis it is interesting to look at the self-similar flow arising from zero gravity wedge entry from the semi-Lagrangian point of view. Garabedian's (1953) result for the constancy of arc length arises in an extremely simple way and has some consequences for a number of other relations derived here. Perhaps more importantly, we exploit these relations and the numerical results of Chapter 2 to calculate numerically the r-function. Future work might be able to utilise these results to build semi-Lagrangian analytical models whereby free-surface solutions could be added in such a way as to satisfy the wedge symmetry and far field conditions.

## Constancy of arc length

If we consider a free surface described by $z(s,t)$ where $s$ is a parameter which is real on the free surface (a Lagrangian marker) and $t$ is time. Below the free surface $z$ is complex and is not a Lagrangian marker, hence the term semi-Lagrangian (see e.g. Longuet-Higgins 1982)

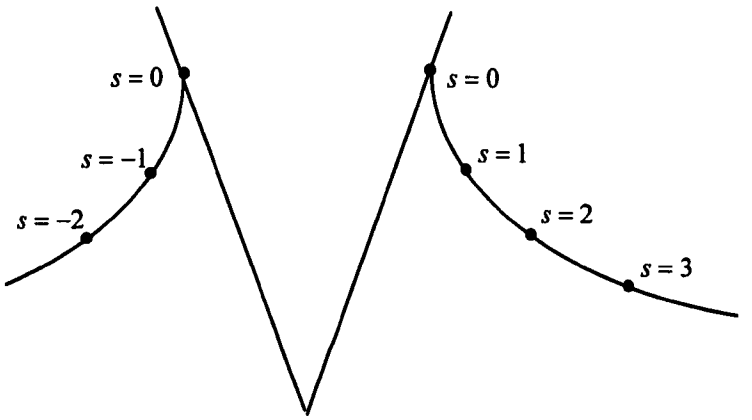


We require self-similarity. Following Garabedian's (1953) notation we therefore have

$$\lambda z(s,t) = z(\lambda s, \lambda t) = z(\varsigma, \tau) \tag{D.1}$$

where $\varsigma = \lambda s$ and $\tau = \lambda t$. We see this relationship explicitly in Graph 2.3, where it is used as a stringent check on the numerical results.

Differentiating with respect to $\lambda$

$$z(s,t) = sz_{\varsigma} + tz_{\tau}$$

and putting $\lambda = 1$

$$z(s,t) = sz_{s} + tz_{t}$$

differentiate with respect to $t$

$$z_{t} = sz_{st} + tz_{tt} + z_{t}$$

so

$$sz_{st} + tz_{tt} = 0 \tag{D.2}$$

and we know $z_{s} = z_{s} + sz_{ss} + tz_{ts}$, then

$$sz_{ss} + tz_{ts} = 0 \tag{D.3}$$

The dynamic condition of John (1953) states that in zero gravity the free-surface particle acceleration is normal to the free-surface. Hence

$$z_{tt} = irz_{s} \tag{D.4}$$

with real $r$. The big advantage of equation (D.4) is that it is linear; any solutions with the same r-function may be added to give the required free-surface. The difficulties lie in satisfying the body boundary condition and avoiding singularities within the flow. Multiplying (D.4) through gives

$$z_{tt}\overline{z_{tt}} = irz_s\overline{z_{tt}}$$

The left hand side is real so

$$\Re(z_s\overline{z_{tt}}) = 0$$

so we can say

$$\Re(z_s\overline{z_{st}}) = 0$$

$$\Rightarrow \frac{\partial|z_s|^2}{\partial t} = 0 \tag{D.5}$$

$$\Rightarrow |z_s|^2 = f(s) = [g(s)]^2$$
$$\text{or } |z| = \int_s g(s)ds$$

which states that the arc length $|z_s|$ is constant with respect to $t$. Alternatively consider the change in $|z|^2$ between two markers $s_1$ and $s_2$ i.e. $|z|^2\Big|_{z_2}^{z_1}$, this is independent of time $t$. This result was shown by Wagner (1932) and a more complicated proof was given by Garabedian (1953).

## Application of John's equation

As we have already stated in equation (D.4)

$$z_{tt} = irz_s$$

in the $(\varsigma,\tau)$ system this becomes $z_{tt} = \lambda^2 z_{\tau\tau}$ and $z_s = \lambda z_\varsigma$, thus

$$z_{\tau\tau} = \frac{iR(\varsigma,\tau)}{\lambda} z_\varsigma$$

Using $z_{tt} = \frac{-s^2}{t^2} z_{ss} = irz_s$ we can deduce $z_{ss} = -ir\frac{t^2}{s^2} z_s \Rightarrow z_{ss}\overline{z_s} = ir\frac{t^2}{s^2}$, hence

$$\Re(z_{ss}\overline{z_s}) = 0 \Rightarrow \frac{\partial|s|^2}{\partial s} = 0$$

i.e. at any time the (arc length)$^2$ between $s_1$ and $s_2$ does not change as $s_1 \to s_1 + \partial s$ and $s_2 \to s_2 + \partial s$. Note if $s$ is initial distance from origin, i.e. particles are labelled by this, then $z = s$ initially. So

$z_s = 1 \ \forall s$ at $t = 0$ and $|z_s|^2 = 1 \ \forall t$ also.

At intersection point $z = (A)t$ where $A$ is complex and $\arg(A + iv) = \delta$ on right hand side of wedge $\Re(A) > 0$ and $\Im(A) > 0$.

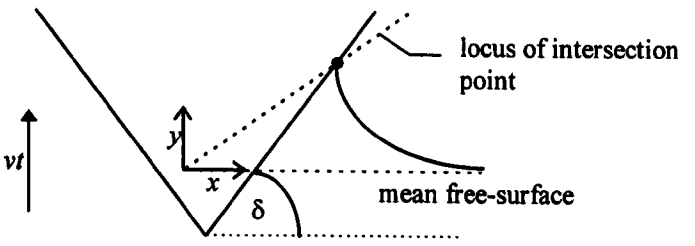


So $z_{tt} = 0$ i.e. $r(0,t) = 0 \ \forall t > 0$. This feature is shown in the numerical results of Graph D.1.

At $\infty$ $z_{tt} \to 0$ i.e. $\lim_{s \to \infty} r(s,t) = 0 \ \forall t > 0$. Again this feature is shown in the numerical results of Graph D.1.

From equations (D.2) and (D.4) we have

$z_{tt} = \frac{-s}{t} z_{st} = irz_s$ which suggests a new variable $z_s = \Lambda(s,t)$ with $|\Lambda| = 1 \ \forall t > 0$ from equation (D.5).

$$\Lambda_t = -ir\frac{t}{s}\Lambda$$

Note $\Lambda_t \overline{\Lambda_t} = -ir\frac{t}{s}\Lambda\Lambda_t \Rightarrow \Re(\Lambda\Lambda_t) = 0$ i.e. $\frac{\partial}{\partial t}|\Lambda|^2 = 0$ as before.

Suppose $\Lambda = e^{i\theta}$ since $|\Lambda| = 1$, $\Lambda_t = i\theta_t e^{i\theta} = ir\frac{t}{s}e^{i\theta}$

$$\theta_t = -r\frac{t}{s}$$

$$r = \frac{-s}{t}\theta_t \tag{D.6}$$

Since $r(0,t) = 0$ then this is automatically satisfied. As $s \to \infty$, $\theta_t \to 0$ i.e. surface slope far from the wedge stays flat with time.

The geometrical significance of $\theta$ can be explained as follows. Firstly

$$z_s = \Lambda = e^{i\theta(s,t)} \Rightarrow z = \int_0^s e^{i\theta(\sigma,t)} d\sigma + At$$

Since $z = At$ when $s = 0$ i.e. at the intersection point. Notice that fluid particles follow the free surface as if they are particles on a string. This arises from the kinematic condition plus the conservation of arc length.

Furthermore

$$z_s = \lim_{\delta s \to 0} \frac{z(s+\delta s,t) - z(s,t)}{\delta s}$$

And we know $|z_s| = 1$. So $\theta = \arg(z_s)$, so $\theta$ is angle between the x-axis and the tangent at $s$ i.e. the slope.

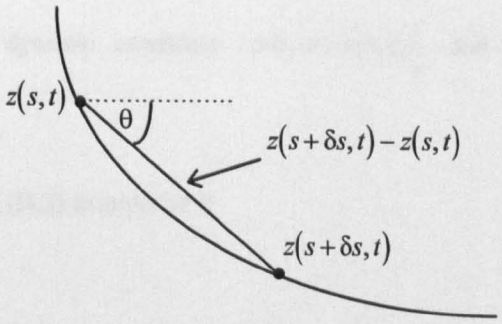


Further $-(\pi - \delta) < \theta < 0$, with equality if the contact angle is zero.

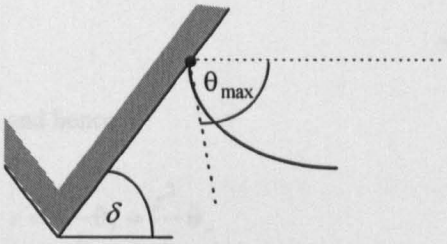


As $s \to \infty$

$$z = \int_0^\infty e^{i\theta(\sigma,t)} d\sigma + \left[\Re(A) + i\Im(A)\right]t$$

but $\Im(z) \to 0$ as $s \to \infty$ so that

$$\Im\left[\int_0^\infty e^{i\theta(\sigma,t)} d\sigma\right] - \Im(A)t = 0$$

$$\int_0^\infty \sin\left[\theta(\sigma,t)\right] d\sigma + \Im(A)t = 0$$

## *Particle dynamics*

Assuming $\theta$ and $\theta_t$ are known

$$z = \int_0^s e^{i\theta(\sigma,y)} d\sigma + At$$

$$z_t = \int_0^s e^{i\theta(\sigma,y)} \theta_t(\sigma,t) d\sigma + A$$

$$z_{tt} = irz_s \Rightarrow z_{tt} = ire^{i\theta} = i\left(\frac{-s}{t}\theta_t\right)e^{i\theta}$$

i.e. $z_{tt} = -i\frac{s}{t}\theta_t e^{i\theta}$

If $r(s,t)$ is known then dynamic condition $\Rightarrow \theta_t = -r(s,t)\frac{t}{s}$ and $\theta = -\frac{1}{s}\int_0^t \tau \cdot r(s,t) d\tau$ when $t = 0$, $\theta = 0$ for $s > 0$

Let us look again at equation (D.3) in terms of $\theta$

$$s\frac{\partial(z_s)}{\partial s} + t\frac{\partial(z_s)}{\partial t} = 0$$

But $z_s = e^{i\theta(s,t)}$ so

$$s\theta_s + t\theta_t = 0 \tag{D.7}$$

and hence

$$r = -\frac{s}{t}\theta_t = \frac{s^2}{t}\theta_s$$

From (D.7) we see that since $\theta_s > 0$ then $\theta_t < 0$ i.e. the free-surface particles move up towards the wedge with increasing slope as the flow develops. Notice that when $s = 0$, $\theta_t = 0$ so the contact angle stays constant. More generally we expect from self-similarity that

$$\theta(s,t) = \theta(\lambda s, \lambda t) \tag{D.8}$$

(D.7) follows from this trivially since (with $\lambda = 1 + \varepsilon$)

$$\theta_t = \lim_{\varepsilon \to 0}\left\{\frac{\theta(s,t+\varepsilon t) - \theta(s,t)}{\varepsilon t}\right\} = \lim_{\varepsilon \to 0}\left\{\frac{\theta(s,t+\varepsilon t) - \theta(s+\varepsilon s, t+\varepsilon t)}{\varepsilon t}\right\}$$

So $\frac{t}{s}\theta_t = \lim_{\varepsilon \to 0}\left\{\frac{\theta(s,t+\varepsilon t) - \theta(s+\varepsilon s, t+\varepsilon t)}{\varepsilon s}\right\} = -\theta_s$

But it is also true that (D.7)$\Rightarrow$ (D.8) since if $\zeta = \frac{s}{t}$ as suggested by (D.8) is a constant and the orthogonal variable

$$\eta = \sqrt{\zeta^2 + t^2} = t\sqrt{\zeta^2 + 1} = s\sqrt{\frac{1}{\zeta^2} + 1}$$

thus

$$\frac{d\theta}{d\eta} = \theta_t \frac{dt}{d\eta} + \theta_s \frac{ds}{d\eta} = \frac{t\theta_t + s\theta_s}{\sqrt{\zeta^s + 1}} = 0$$

on the line where $\zeta = \frac{s}{t}$ is a constant.

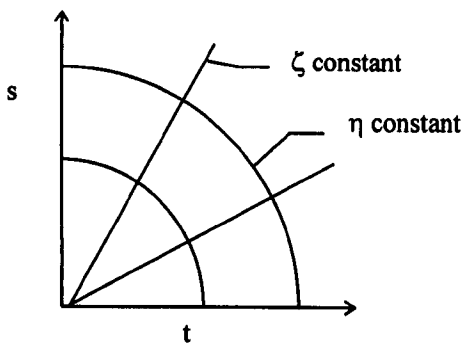


*Figure D.1 Self-similarity variables*

So

$$t\theta_t + s\theta_s = 0 \Leftrightarrow \theta(s,t) = \theta(\lambda s, \lambda t) \qquad \text{(D.9)}$$

## Numerical calculation of r-function

To make further progress we need to know the r-function, which we calculate from the time derivative of the surface i.e. from (D.6).

We obtain values of the r-function using the numerical data for the entry of a wedge, half angle $\pi/10$, with a high enough Froude number (0.583) for the flow to be essentially gravity free.

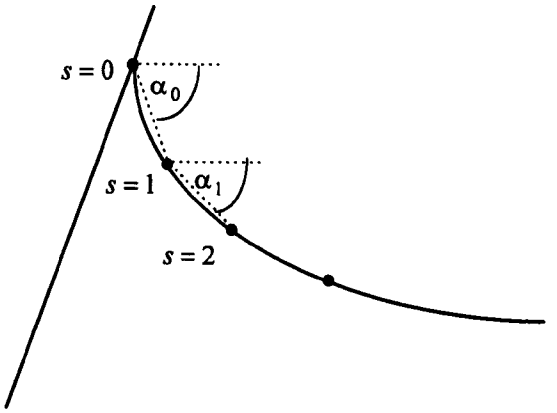


We calculate the angles $\alpha_0$ and $\alpha_1$ using

$$\alpha_n = \tan^{-1}\left(\frac{y_{n+1} - y_n}{x_{n+1} - x_n}\right)$$

then finding

$$\theta(s_n, t) = \frac{\alpha_n + \alpha_{n+1}}{2}$$

then using the centred difference theorem to calculate

$$\theta_t = \frac{\theta(s_n, t+1) - \theta(s_n, t)}{2t}$$

This can then be applied to the equation

$$r = \frac{-s}{t}\theta_t$$

The r-function values are plotted against time for all Lagrangian markers.

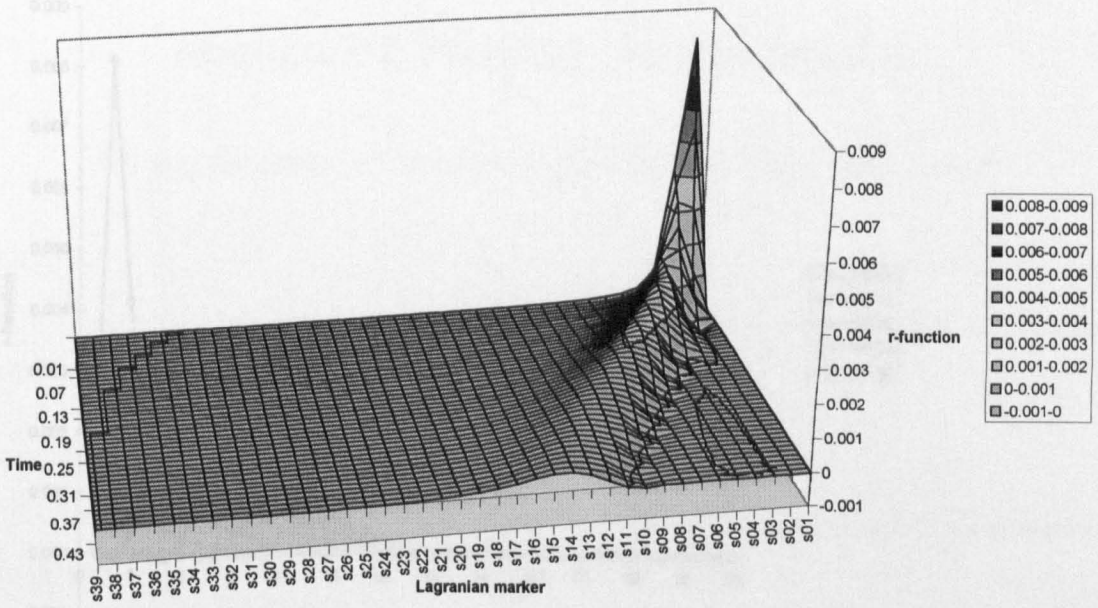


*Graph D.1 r-function plotted against time for all Lagrangian markers (COLOUR)*

To simplify obtaining values from the r-function graph a selection of results are presented below in a two-dimensional format.

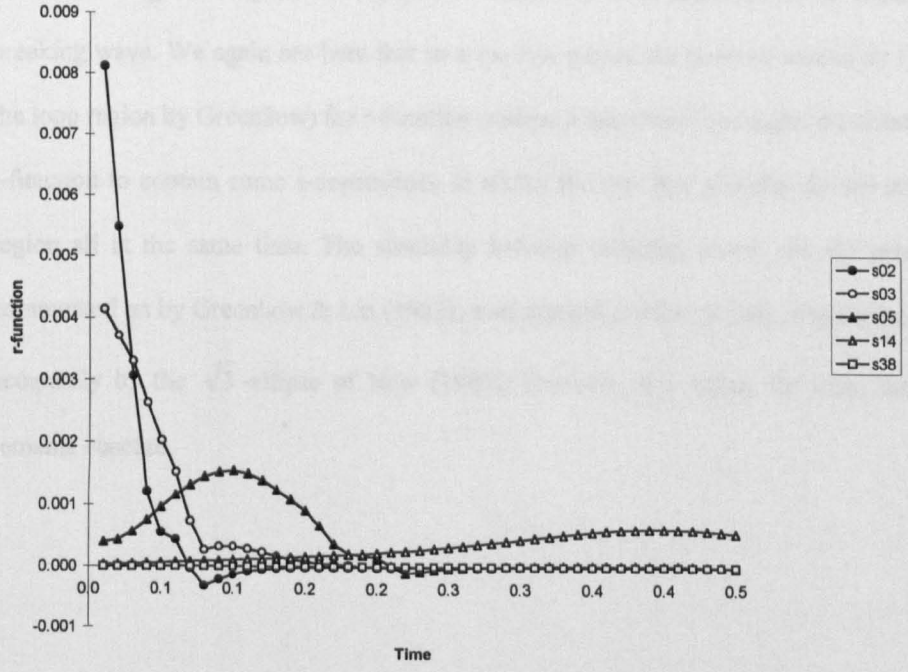


*Graph D.2 r-function against time for a selection of Lagrangian markers.*

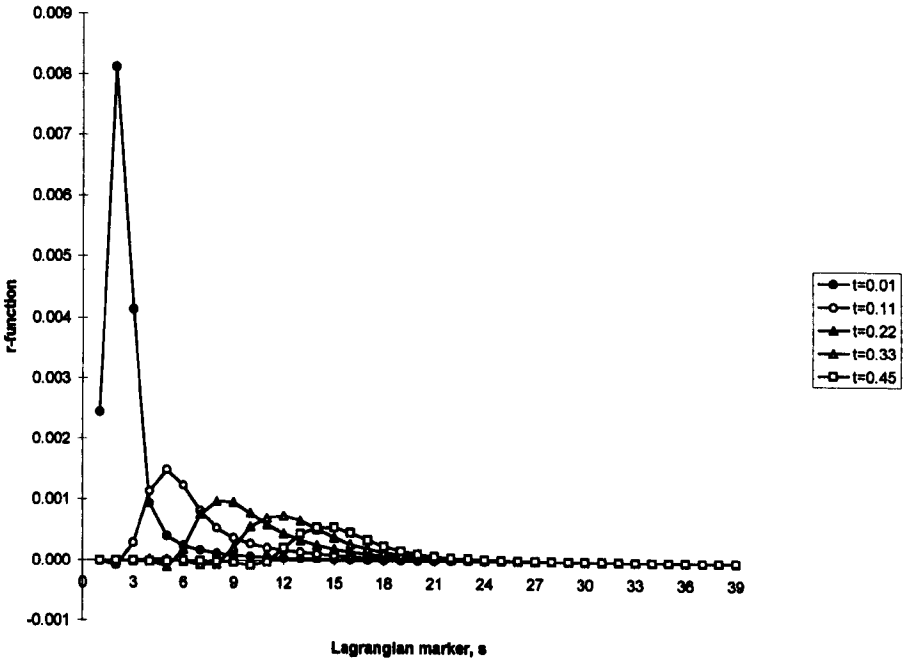


*Graph D.3 r-function against Lagrangian marker for a range of times.*

It is interesting to compare the results of Graph D.3 with those shown in Greenhow (1983) for a breaking wave. We again see here that as a particle passes the point of verticality ( called the node of the loop region by Greenhow) the r-function reaches a maximum, and again we observe the need for the r-function to contain some s-dependence to model the fact that particles do not enter the overturning region all at the same time. The similarity between breaking waves and the present case was also commented on by Greenhow & Lin (1983); a substantial portion of both loop regions can be fitted very accurately by the $\sqrt{3}$ -ellipse of New (1983). However, the reason for these intriguing similarities remains obscure.

# Appendix E Program Documentation

*An explanation of the input and output data files used.*

## Abstract

Input and output files are broken down into their constituent parts and explained, the objective being to simplify future use of the system.

## Introduction

We present each of the files used by the system. Input variables are explained. The dimensions and physical interpretation of output data is described.

## Input

The input file format is in the form

| | | | | | | | | | |
|---|---|---|---|---|---|---|---|---|---|
| nstep, | dt, | dp, | iprint, | iwrite, | istart, | ilcng, | ncng, | acctype, | jump, |
| isway, | iheave, | iroll, | divout, | divin, | | | | | |
| zg, | vzg, | teta, | tetad, | zcg, | | | | | |
| cvlgth, | hwat, | nf, | | | | | | | |
| rlambd, | etaa, | swl, | | | | | | | |
| smass, | smint, | | | | | | | | |
| fwl, | rwl, | r, | | | | | | | |
| ratio, | | | | | | | | | |
| nbody, | | | | | | | | | |
| ratbod, | vertex, | hwedge, | angwed, | angver, | | | | | *if r=0* |
| ratbod, | vertex, | hbox, | wbox, | angwed, | | | | | *if r=-1* |
| ratbod , | vertex, | hbox, | wpen, | angwed, | angver | | | | *if r=-2* |

Each variable is now described , included are indications of reasonable values and interpretation.

| | |
|---|---|
| nstep | The number of integration steps to perform |
| dt | Time step size |
| dp | Size of height step (used in point spacing) |
| iprint | Define the amount of output sent to file. Defined values are:<br>19 Print Gamma functions<br>18 Print calculation matrices A & B<br>17 Print Gaussian elimination steps |

| | |
|---|---|
| | 16 Print solution vectors |
| | 14 Print results of main steps |
| iwrite | Print predicted Hamming values if set to 1 |
| istart | Start up method: |
| | 0 Restart from present file |
| | 11 Perform standard run |
| ilcng | Allow jet to leave body : |
| | 0 No jet may leave body |
| | $x$>0 First jet may leave body after $x$ steps |
| ncng | Number of steps till subsequent jets may leave body |
| acctype | Type of accelerated motion: |
| | 0 constant velocity |
| | -100 Transient motion |
| | $x$ Constant acceleration at $x$ m/s$^2$ |
| jump | Print every n$^{th}$ step |
| isway | Allow sway motion if 1 |
| iheave | Allow heave motion if 1 |
| iroll | Allow roll motion if 1 |
| divout | Ratio of surface to body elements required before a surface point is removed |
| divin | Ratio of surface to body elements required before a surface point is added |
| zg | Co-ordinates of body's centre of rotation |
| vzg | Velocity of centre of gravity |
| teta | Angle of the body motion to vertical |
| tetad | Angular velocity about centre of gravity |
| zcg | Co-ordinates of centre of gravity |

| | |
|---|---|
| cvlgth | Length of control volume |
| hwat | Depth of control volume. Should be six to ten times the body submergence to prevent interference with control volume bottom. |
| nf | Number of control points on the free-surface |
| rlambd | Wave length. Used for waves at $t$=0, should be a multiple of cvlgth. |
| etaa | Wave amplitude |
| swl | Still water length |
| smass | Mass density ratio (effectively volume of body below free-surface at equilibrium). Has no effect in forced motion. |
| smint | Moment of inertia density ratio |
| fwl | Forward water line |
| rwl | Rear water line |
| r | Radius of body:<br>0 wedge body<br>-1 box body<br>-2 knuckled body<br>$x$>0 circular body |
| ratio | Ratio of points on free-surface:<br><1 clusters points near body<br>1 even distribution<br>>1 clusters points away from body |
| nbody | Number of control points of body |
| ratbod | Ratio of points on body:<br><1 clusters points near vertex<br>in the case of a box/knuckle points are clustered near corners |

| | |
|---|---|
| vertex | Distance of vertex/bottom from centre of gravity |
| hwedge (wedge only) | Height of body |
| angwed | Angle of body to vertical.<br>Wedge : angle of right hand side wedge face to vertical (for vertical motion use half-angle)<br>Other : tilt of body about centre of gravity |
| angver (wedge only) | Total angle of wedge vertex |
| hbox (box and knuckle only) | Height of box |
| wbox (box only) | Width of box |
| wpen (knuckle only) | Width of knuckled body |

## Output

### *Surface data*

Data is output in the format

| point co-ordinate $(x, y)$ | Complex potential $(\Re, \Im)$ | Time derivative of complex potential $(\Re, \Im)$ | Point identifier<br>N1 indicates intersection point | Step number |
|---|---|---|---|---|
| | | | | |

### *Depth data*

Data is output in the format

| Step number | Time | Centre of gravity $(x, y)$ | Acceleration of c.o.g. $(x, y)$ | Velocity of c.o.g. $(x, y)$ | Draw-down |
|---|---|---|---|---|---|
| | | | | | |

### *Pressure data*

Data is output in the format

| Body point co-ordinates $(x, y)$ | Pressure | Step number |
|---|---|---|
| | | |

## *Force data*

Data is output in the format

| Step number | Force number | Force | Hydrodynamic force |
|---|---|---|---|
| | | $(x, y)$ | |

## *Plot data*

Data is output in the format

| **Comments** | |
|---|---|
| Step number | INTEGRATION STEP NO: 0<br>TIME : T= 0.00000SECS<br>********** |
| | ACCELERATION; AZG= 0 -1.962 (M/SECS**2)<br>VELOCITY ; VZG= 0 0 (M/SECS)<br>COORDINATES ; ZG= 0 0.2 (M) |
| Point number i.e. point N1 is the 40th point. See Figure E.1 for marker references. | N1= 40<br>N2= 70<br>N3=109<br>N4=116<br>N5=127<br>N =133 |
| Number of surface points. | NF= 80 |
| Point insertion/ removal notes. | INSERTED AN EXTRA POINT ON RHS<br>INSERTED EXTRA POINT ON LHS |

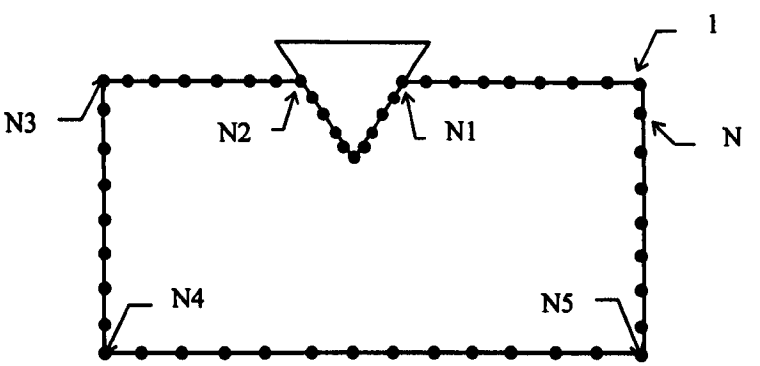


*Figure E.1 Marker definition*

# References

Abramowitz, M. & Stegun, I. A. (1965) Handbook of mathematical functions, with formulas, graphs, and mathematical tables. *Dover Publications, inc., New York.* ISBN 0-486-61272-4.

Armand, J. L. & Cointe, R. (1986) Hydrodynamic impact analysis of a cylinder. *Proc. 5th Int. Offshore Mech. and Arctic Engng. Symp., Tokyo.* Vol. 1, pp. 609-634.

Baker, R. G. Merion, D. I. & Orzag, S. A. (1981) Generalised vortex methods for free-surface flow problems. *J. Fluid Mech.* Vol. 123, pp. 477-501.

Bassett, A. B. (1888) A treatise on hydrodynamics. *Reprinted 1961.Dover, New York.*

Belik, O. Bishop, R.E.D. & Price, W.G. (1983) A simulation of ship responses due to slamming in irregular head seas. *Trans. RINA.* Vol. 125, pp. 237-253.

Blackmore, P. A. & Hewson, P. J. (1984) Experiments on full-scale wave impact pressures. *Coastal Engineering.* Vol. 8, pp. 311-346.

Borg, S. F. (1957) Some contributions to the water entry problem. *Proc. Am. Soc. Civil Eng. J. Eng. Mech. Div.* Vol. 83, # EM2, paper 1214, pp. 1-28.

Brevig, P. Greenhow, M. & Vinje, T. (1981) Extreme wave forces on submerged cylinders. *Proc. B.H.R.A. 2nd Int. Symp. on wave and tidal energy, Cambridge.* pp. 143-166.

Campbell, I. M. C. & Weynberg, P. A. (1980) Measurement of parameters affecting slamming. *Final report, Wolfson Unit for Marine Tech. Southampton University.* Report no. 440.

Chaplear, J. E. (1961) Direct numerical calculation of wave properties. *J. Geophys. Res.* Vol. 66, pp. 501-508.

Chaplin, J. R. (1984) Non-linear forces on a horizontal cylinder beneath waves. *J. Fluid Mech.* Vol. 147, pp. 449-464.

Chaplin, J. R. (1988) Loading on a cylinder in uniform oscillatory flow: part II - Elliptical orbital flow. *Appl. Ocean Res.* Vol. 10, # 4, pp. 199-206.

Chaplin, J. R. Rainey, R.C.T. & Yemm R.W. (1997) Ringing of a vertical cylinder in waves. *J. Fluid Mech.* Vol. 350 pp. 119-147.

Chapman, R. B. (1979) Large amplitude motion of two-dimensional floating bodies. *J. Ship Research.* Vol. 23, #1, pp. 20.

Chuang, S-L. (1967) Experiments on slamming of wedge-shaped bodies. *J. Ship Res.* Vol. 11, # 3, pp. 190-194.

Cointe, R. (1991) Free surface flows close to a surface piercing body. *Mathematical approaches in hydrodynamics, Soc. Ind. Appl. Math. USA.* pp. 319-334.

Cointe, R. Molin, B. & Nays, P. (1988) Non-linear and second-order transient waves in a rectangular tank. *B.O.S.S Trondheim,* pp. 705-720.

Cokelet, E. D. (1978) Breaking waves - the plunging jet and interior flow-field. *Proc. Symp. Mech. Wave-induced forces on cylinders, Bristol.* pp. 1-17.

Cooker, M. (1990) The interaction between steep water waves and coastal structures. *PhD Thesis, University of Bristol, Dept. of Math.*

Cross, N. (1993) Motion of a cylinder below the free-surface. *4th yr. undergraduate project, Brunel University.*

Dean, R. G. (1965) Stream function representation of non-linear ocean waves. *J. Geophys. Res.* Vol. 70, #18, pp. 4561-4572.

Dean, R. G. & Dalrymple, R. A. (1984) Water wave mechanics for engineers and scientists. *Prentice-Hall Inc.* ISBN 981-02-0420-5.

Dean, W. R. (1948) On the reflection of surface waves from a submerged circular cylinder. *Proc. Camb. Phil. Soc.* Vol. 44, pp. 483-491.

Dobrovol'skaya, Z. (1969) On some problems of singularity flow of a fluid with a free-surface. *J. Fluid Mech.* Vol. 36, pp. 805.

Dold, J. W. and Peregrine, D. H. (1986) An efficient boundary-integral method for steep unsteady water waves. In Numerical methods for fluid dynamics II (ed. Morton ,K. W. and Baines, M. J. ). *Oxford University Press.* Vol. II, pp. 657-679.

Dommermuth, D. G. Yue, D. K. P. Lin, W-M. Rapp, R. J. Chan, E. S. & Melville, W. K. (1988) Deep water plunging breakers: a comparison between potential theory and experiments. *J. Fluid Mech.* Vol. 189, pp. 423-442.

Evans, D. V. Jeffery, D. C. Salter, S. H. & Taylor, J. R. M. (1979) Submerged cylinder wave energy device; theory and experiment. *Appl. Ocean Res.* Vol. 1, pp. 3-12.

Fabula, A. G. (1957) Ellipse-fitting approximation of two-dimensional normal symmetric impact of rigid bodies on water. *Proc. 5th Mid-Western Conf. Fluid Mech.* pp. 299-315.

Faltinsen, O. Kjærland, O. Nøttveit, A. and Vinje, T. (1977) Water impact loads and dynamic response of horizontal circular cylinders in offshore structures. *OTC paper 2741, Texas.*

Faltinsen, O. & Sortland, B. (1987) Slow drift eddy-making damping of a ship. *Applied Ocean Research.* Vol. 9, #4, pp. 37-46.

Fraenkel, E. & McLeod, J.B. (1997) Some results for the entry of a blunt wedge into water. *Phil. Trans. Roy. Soc. Series A.* Vol. 355, pp. 523-535.

Garabedian, P. R. (1953) Oblique water entry of a wedge. *Comm. Pure Appl. Math.* Vol. 1 pp157.

Gerald, C. F. & Wheatley, P. O. (1994) Applied Numerical Analysis. *Addison-Wesley.* 5th Edition, §5. ISBN 0-201-56553-6.

Gradshteyn, I. S. & Ryzhik, I. M. (1994). Tables of Integrals, Series and Products. *5th ed. Academic Press.*

Greenhow, M. (1983) Free-surface flows related to breaking waves. *J. Fluid Mech.* Vol. 134, pp. 259-275.

Greenhow, M. (1987) Wedge entry into initially calm water. *Applied Ocean Research.* Vol. 9, #4, pp. 214-223.

Greenhow, M. (1988) Water entry and exit of a horizontal circular cylinder. *Appl. Ocean Res.* Vol. 10, # 4, pp. 191-198.

Greenhow, M. (1993) A complex variable method for the floating body boundary-value problem. *J. Comp. Appl. Math.* Vol. 46, pp. 115-128.

Greenhow, M. & Li, Y. (1987) Added masses for circular cylinders near or penetrating fluid boundaries - review, extension and application to water entry, exit and slamming. *Ocean Engineering.* Vol. 4, pp. 325-348.

Greenhow, M. & Lin, W-M. (1983) Non-linear free-surface effects: experiments and theory. *Dept. Ocean Engineering, MIT.* Report no. 83-19.

Greenhow, M. & Lin, W-M. (1985) Numerical simulation of non-linear free-surface flows generated by wedge entry and wavemaker motion. *Proc. 4th Int. Conf. Num. Ship Hydro., Washington.* pp. 94-106.

Greenhow, M. & Moyo, S. (1997) Water entry and exit of horizontal circular cylinders. *Phil. Trans. R. Soc. London.* Ser. A Vol. 355 pp. 551-563.

Hepworth, T. (1991) An investigation of the motion of a submerged cylinder moving below a free-surface with constant velocity. *4th year undergraduate project, Dept. Math. & Statistics, Brunel University.*

Howison, S. D. Ockendon, J. R. & Wilson, S. K. (1991) Incompressible water entry problems at small deadrise angles. *J. Fluid Mech.* Vol. 222, pp. 215-230.

Hughes, O.F. (1972) Solution of the wedge entry problem by numerical conformal mapping. *J. Fluid Mech.* Vol. 56, pp. 173-192.

Isaacson, M. de St. Q. (1981) Non-linear wave effects on fixed and floating bodies. *J. Fluid Mech.* Vol. 120, pp. 267-281.

John, F. (1953) Two-dimensional potential flows with a free boundary. *Comm. Pure Appl. Math.* Vol. 6, pp. 497-503.

Kaplan, P. & Silbert, M. N. (1976) Impact forces on platform horizontal members in the splash zone. *OTC, Dallas.* Vol. 1, paper no. 2498.

Keady, G. (1998) A numerical study of the wedge-water-entry problem: fixed points of separable and mixed-monotone positive operators. *http://maths.uwa.edu.au/~keady/wedgeD/index.html.*

King, A. C. & Needham, D. J. (1994) The initial development of a jet caused by fluid, body and free-surface interaction. 1. A uniformly accelerating plate. *J. Fluid Mech.* Vol. 268, pp. 89-101.

Kjeldsen, P. (1981) Shock pressures from deep water breaking waves. *Proc. Int. Symp. Hydrodynamics, Trondheim.* pp. 567-584.

Korobkin, A. A. & Pukhnochov, V. V. (1988) Initial stage of water impact. *Ann. Rev. Fluid Mech.* Vol. 10, pp. 159-185.

Longuet-Higgins, M. S. (1978a) The instabilities of gravity waves of finite amplitude in deep water. I. Superharmonics. *Proc. Roy. Soc. London.* Vol. 360, pp. 471-488.

Longuet-Higgins, M. S. (1978b) The instabilities of gravity waves of finite amplitude in deep water. II. Subharmonics. *Proc. Roy. Soc. London.* Vol. 360, pp. 489-505.

Longuet-Higgins, M. S. (1982) Parametric solution for breaking waves. *J. Fluid Mech.* Vol. 121, pp. 403-424.

Longuet-Higgins, M. S. (1983) Rotating hyperbolic flows: particle paths and parametric representation. *Quart. J. Mech. Appl. Math.* Vol. 36, pp. 247-270.

Longuet-Higgins, M. S. & Cokelet, E. D. (1976) The deformation of steep surface waves on water. I. A numerical method of computation. *Proc. Roy. Soc. London.* Ser. A, Vol. 350, pp. 1-26.

Longuet-Higgins, M. S. & Dommermuth D. G. (1997) Crest instabilities of gravity waves. Part 3. Non-linear development and breaking. *J. Fluid Mech.* Vol. 336, pp. 33-50.

Longuet-Higgins, M. S. & Tanaka, M. (1997) On the crest instabilities of steep surface waves. *J. Fluid Mech.* Vol. 336, pp. 51-68.

Lundgren, H. (1969) Wave shock forces: an analysis of deformations and forces on the wave and in the foundation. *Proc. Symp. Wave Action, Delft.* Paper 4.

Mackie, A. G. (1962) A linearised theory of the water entry problem. *Q. J. Mech. Appl. Math.* Vol. XV, pp. 137.

Mackie, A. G. (1965) Gravity effects in the water entry problem. *J. Aust. Math. Soc.* Vol. 5, pp. 4-27

Mackie, A. G. (1969) The water entry problem. *Q. J. Mech. Appl. Math.* Vol. 22, pp. 1-17.

Milne-Thompson, L.M. (1986) Theoretical Hydrodynamics. *Macmillan New York 5th ed.*

Miloh, T. (1981) Wave slam on a sphere penetrating a free-surface. *J. Eng. Math.* Vol. 15, pp. 221-240.

Miyata, H. & Lee, Y. (1990)Vortex motion about a horizontal cylinder in waves. *Ocean Engineering.* Vol. 17, # 3, pp. 77-92.

Moran, J. P. (1965) The vertical water-exit and entry of slender symmetric bodies. *J. Aerospace Sciences.* Vol. 803.

Moutzouris, C. (1979) Some scaling parameters of loading from wave breaking on rigid inclined structures. *Mechanics of wave induced forces on cylinders, edited by T Shaw. Pitman.* pp. 714-727.

New, A. (1983) A class of elliptic free-surface slows. *J. Fluid Mech.* Vol. 130, pp. 219-239.

New, A. L. McIver, P. & Peregrine, D. H. (1985) Computations of overturning waves. *J. Fluid Mech.* Vol. 150, pp. 233-251.

Newman, J. N. (1977) Marine Hydrodynamics. *The MIT Press.* ISBN 0-262-14026-8.

Nichols, B. D. & Hirt, C. W. (1977) Non-linear hydrodynamic forces on floating bodies. *International conference on Numerical Ship Hydrodynamics, Berkley.* pp. 382-394.

Ogilvie, F. (1963) First and second order forces on a cylinder submerged under a free-surface. *J. Fluid Mech.* Vol. 16, pp. 451-472.

Øristland, O. (1987) Wave forces on sub-sea modules during lifting in the splash zone. *Marintek.* report 532013.18.

Partensky, H. W. (1988) Dynamic forces due to breaking waves at vertical coastal structures. *Proc. 21st Int. Conf. Coastal Engineering.* Vol. 3, pp. 2504-2518.

Patterson, A.R. (1976) A first course in fluid dynamics. *Cambridge University Press.*

Peregrine, D H. & Thais L. (1996) The effect of entrained air in violent water wave impacts. *J. Fluid Mech.* Vol. 325, pp. 377-397.

Pierson, J. D. (1951) On the virtual mass of water associated with an immersing wedge. *J. Aeronautical Sciences.* June, 430.

Rainey, R. T. C. (1989) A new equation for calculating wave loads on offshore structures. *J. Fluid Mech.* Vol. 204, pp. 295-324.

Riabouchinski, D. (1920) Sur la résistance des fluides. *Congress of Math. Strasbourg.* pp. 568-585.

Ridley, J. A. (1982) A study of some theoretical aspects of slamming. *N.M.I. Report No. R158.*

Rienecker, M. M. & Fenton, J. D. (1981) A Fourier approximation method for steady water waves. *J. Fluid Mech.* Vol. 104, pp. 119-137.

Scott, J. C. (1975) The role of salt in whitecap persistence. *Deep-sea research.* Vol. 22, pp. 653-657

Shiffman, M. & Spencer, D. C. (1951) The force of impact of a cone striking a water surface (vertical entry). *Communs. Pure Appl. Math.* Vol. 4, pp. 379.

Skourup, J. & Jonsson, I. G. (1992) Computations of forces on, and particles orbits around, horizontal cylinders in steep waves. *Ocean Engineering.* Vol. 19, # 6, pp. 527-553.

Takagi , K. et al (1986) The impact load and pressure acting on the circular cylinder. *Proc. Offshore Mech. and Arctic Engineering (OMAE) Symp., Tokyo.* pp. 242-249.

Tanimoto, K. et al (1986) Impact force of breaking waves on an inclined pile. *Proc. Offshore Mech. and Arctic Engineering (OMAE) Symp., Tokyo.* pp. 235-241.

Telste, J. G. (1987) Inviscid flow about a cylinder rising to a free-surface. *J. Fluid Mech.* Vol. 182, pp. 149-168.

Terent'ev, A. G. (1991) Non-stationary motion of bodies in a fluid. *Proc. Steklov Inst. Math.* Vol. 186, pp. 211-221.

Tyvand, P. A. & Miloh, T. (1995 a) Free-surface flow due to impulsive motion of a submerged circular cylinder. *J. Fluid Mech.* Vol. 286, pp. 67-101.

Tyvand, P. A. & Miloh, T. (1995 b) Free-surface flow generated by a small submerged circular cylinder starting from rest. *J. Fluid Mech.* Vol. 286, pp. 103-116.

Ursell, F. (1950) Surface waves on deep water in the presence of a submerged circular cylinder. *Proc. Camb. Phil. Soc.* Vol. 46, pp. 141-158.

Vinje, T. & Brevig, P. (1981a) Breaking waves on finite water depths, a numerical study. *Ship Research Institute of Norway.* R-111.81.

Vinje, T. & Brevig, P. (1981b) Non-linear, two-dimensional ship motions. *Ship Research Institute of Norway.* R-112.81.

von Karman, T. (1929) The impact of seaplane floats during landing . *N.A.C.A. TN 321, Washington.*

Wagner, H. (1932) Über Stöss- und Gleitvorgänge an der Oberflache von Flüssigkeiten. *Z. Angew. Math. Mech.* Vol. 12, pp. 193-215; see also: The Phenomena of Impact and Planning on Water. N.A.C.A. 1936 Translation 1366, pp. 1-57.

Williams, J. M. (1985) Tables of progressive gravity waves. *Pitman.*

Wu , G. X. (1993) Hydrodynamic forces on a submerged circular cylinder undergoing large amplitude motion. *J. Fluid Mech.* Vol. 254, pp. 41-58.

Xu, H. & Yue, D. K. P. (1992) Numerical study of three-dimensional overturning water waves. *Proc. 7th Int. workshop on water waves and floating bodies, May, Val de Rueil, France.* pp. 303-307.

Yamamoto, Y. Iida, K. Fukasawa, T. Murakami, T. Arai, M. & Ando, A. (1985) Structural damage analysis of a fast ship due to bow flare slamming. *International Shipbuilding Program.* Vol. 32, pp. 123.

Zhang, S. Yue, D. K. P. & Tanizawa, K. (1996) Simulation of plunging wave impact on a vertical wall. *J. Fluid Mech.* Vol. 327, pp. 221-254.

Zhao, R. & Faltinsen, O. (1993) Water entry of two-dimensional bodies. *J. Fluid Mech.* Vol.246, pp. 593-612.

Zhou, D. et al (1991) Wave impact pressure on vertical cylinders. *Applied Ocean Res.* Vol. 13, # 5, pp. 220-234.